# GRINDING OF Ti-6Al-4V TITANIUM ALLOY: AN EXPERIMENTAL AND DIMENSIONAL ANALYSIS EVALUATION

by

**JAMES ASHMAN**

A thesis submitted to
The University of Birmingham
for the degree of
DOCTOR OF PHILOSOPHY

School of Engineering
College of Engineering and Physical Sciences
University of Birmingham
May 2022

UNIVERSITY OF
BIRMINGHAM

## University of Birmingham Research Archive

### e-theses repository

This unpublished thesis/dissertation is copyright of the author and/or third parties. The intellectual property rights of the author or third parties in respect of this work are as defined by The Copyright Designs and Patents Act 1988 or as modified by any successor legislation.

Any use made of information contained in this thesis/dissertation must be in accordance with that legislation and must be properly acknowledged. Further distribution or reproduction in any format is prohibited without the permission of the copyright holder.

# SYNOPSIS

The work presented in this thesis deals with the grinding characteristics of aerospace alloy Ti-6Al-4V (Ti64). Firstly, a new and novel approach for evaluating the peak workpiece temperature was conducted and, in addition, the associated cutting forces acting on the grinding wheel were also analysed, alongside the $G$-ratio and subsequent surface integrity of the ground workpiece, i.e., surface roughness, microstructure analysis, microhardness interrogation and induced residual stresses. Secondly, a further dimensional analysis (DA) study of the test programme was then performed to determine if a theoretical approach could be developed for predicting the experimental test programme findings. In summary, the present research was structured into two phases of work.

Phase 1 involved an experimental test programme to investigate the effect of changes in wheel speed, $V_s$, feed rate, $V_w$, and depth of cut, $a$, values on workpiece temperature, over a range of finishing and larger stock removal conditions when using a SiC grinding wheel. The workpiece temperatures were evaluated through a series of three thermocouples implanted in the workpiece near the entry, middle and exit of the cut, whilst the grinding forces were measured using a piezoelectric dynamometer. A key observation was that significant spikes in workpiece temperature were recorded by the thermocouple positioned near the end of the cut when compared to the first two thermocouples in the series; e.g., a maximum workpiece temperature differential, $\Delta$T, of 72.9%. Moreover, a maximum workpiece temperature of approximately 800°C was measured when using the most aggressive parameters, whilst a minimum workpiece temperature of approximately 75°C was observed when grinding using less aggressive parameters. Film boiling of the coolant was proposed as a possible explanation, in addition to the build-up of latent heat within the system. Similarly, higher cutting forces were observed when using more aggressive grinding parameters, with peak cutting forces reaching 1500N, whilst lower grinding parameters observed force traces as low as 500N, i.e., $\Delta$F of 66.7%. Additional post-grinding surface integrity assessment consisting of surface roughness, optical microscopy of the subsurface, microhardness and residual stresses were evaluated regarding the Ti64 workpieces after the experimental test programme had been conducted. Significantly higher $G$-ratios were found when using less aggressive grinding parameters, whilst microhardness values were found to be higher further along the grinding pass by 4.1%, indicating that temperatures are higher again due to the lack of coolant fluid within the grinding zone at this point in the pass. Higher wheel speeds were also found to reduce the peak workpiece temperature, and so this should be considered when grinding components that require high precision finishing. The average

surface roughness, $R_a$, observed a maximum 50% reduction when increasing wheel speeds from 20m.s$^{-1}$ to 30m.s$^{-1}$ whilst keeping the feed rate and the depth of cut constant.

Phase 2 established DA models using the Buckingham-$\pi$ method. Six Buckingham-$\pi$ groups were derived using base unit quantities associated with the workpiece and the tooling material properties, in addition to the machining parameters tested. The Buckingham-$\pi$ groups were then analysed and compared against the experimental results from Phase 1. Results indicated an excellent correlation for predicting both workpiece temperature and cutting forces when comparing depth of cut, feed rate and wheel speed, with the variance between data sets being less than 5%.

For Mom, Dad, Fiona and, on balance, I suppose a little bit for myself too.

Education is not the learning of facts, it's rather the training of the mind to think.

*Albert Einstein*

# ACKNOWLEDGEMENTS

The author would very much like to thank Dr. Richard Hood for his close supervision and assistance throughout the course of the project. Without your enduring support, the research would not have concluded, and I thank you both professionally, and personally, for all your guidance.

Extended thanks also go to Dr. Sein Leung Soo for his supervision throughout the project. Assistance was provided when asked for with both courtesy and poise.

Moreover, the advice and input from Prof. Stefan Dimov in relation to the Dimensional Analysis approach for assessing the grinding process was also appreciated and was received on my behalf with great humility and thanks.

Furthermore, my sincerest appreciation and gratitude go to Mr. and Mrs. Leonard and Janette Hughes for their hospitality and understanding shown towards me throughout. I cannot overstate how much this kind gesture meant to me. I will never forget it.

My dearest thanks go to my Mom, Lorraine, Dad, David and sister, Kathryn, for their endless love and support during the good times and the bad. It was, and always will be, deeply appreciated.

Finally, my unfaltering love and eternal thanks go to my partner, Fiona, for her tireless and unwavering patience, unending optimism and continuous emotional reassurance during such a roller-coaster of a ride. I couldn't have done it without you. I love you more than I can describe. We did it.

# PAPERS IN PREPARATION

Below highlights the series of journal papers which are currently in preparation based on the research outlined in this thesis;

1. “Evaluating the Grindability of Ti-6Al-4V - Part 1: Workpiece Temperature Assessment”.

2. “Evaluating the Grindability of Ti-6Al-4V - Part 2: Cutting Force Assessment”.

3. “Evaluating the Grindability of Ti-6Al-4V - Part 3: Surface Integrity Assessment”.

# Table of Contents

**List of Figures** **xi**

**List of Tables** **xxi**

**Nomenclature** **xxiii**

**1 Introduction** **1**

1.1 Background and Motivation for the Project . . . . . 3

1.2 Aims and Objectives of the Project . . . . . 6

1.3 Organisation of the Research and Thesis Structure . . . . . 7

**2 Literature Review** **10**

2.1 Introduction . . . . . 10

2.2 Grinding Processes . . . . . 13

2.2.1 Mechanics of Grinding . . . . . 14

2.2.1.1 Chip Length . . . . . 15

2.2.1.2 Chip Thickness . . . . . 16

2.2.1.3 Number of Contact Points . . . . . 16

2.2.1.4 Temperature Mechanics . . . . . 17

2.2.1.5 Cutting Force Mechanics . . . . . 20

2.2.2 Grinding Wheel Systems . . . . . 22

2.2.3 Coolant Delivery and Application . . . . . 25

2.2.4 Importance of Wheel Dressing . . . . . 35

2.2.5 Surface Integrity Considerations post-Grinding . . . . . 39

2.2.6 Grinding Operations . . . . . 48
2.2.6.1 Creep Feed Grinding . . . . . 48
2.2.6.2 Speed Stroke Grinding . . . . . 50
2.2.6.3 High Efficiency Deep Grinding . . . . . 51
2.3 Grinding Ti-6Al-4V . . . . . 53
2.4 Grinding other Titanium Alloys . . . . . 54
2.5 Grinding Modelling Methods . . . . . 56
2.5.1 Classical Numerical Solutions . . . . . 56
2.5.2 Dimensional Analysis . . . . . 61
2.6 Temperature Measurement during Grinding . . . . . 70
2.7 Cutting Force Measurement during Grinding . . . . . 75
2.8 Experimental Design Methods . . . . . 76
2.8.1 Components of Experimental Design . . . . . 77
2.8.1.1 Factors, Levels and Responses . . . . . 77
2.8.1.2 Unexplained Variation, Noise Factors, Correlation/Causation and Interactions . . . . . 78
2.8.2 Types of Design of Experiments and Applications to Machining . . . . . 78
2.9 Conclusions from the Literature . . . . . 79

**3 Methodology** **83**

3.1 Phase 1: Experimental Grinding Tests . . . . . 83
3.1.1 Machine Tool and Cutting Fluid . . . . . 83
3.1.1.1 Data Acquisition . . . . . 84
3.1.1.2 Workpiece Preparation . . . . . 85
3.1.1.3 Experimental Test Programme Array . . . . . 91
3.1.2 Surface Integrity and Optical Microscopy Analysis . . . . . 93
3.1.3 *G*-ratio Analysis . . . . . 99
3.2 Phase 2: Dimensional Analysis Numerical Models . . . . . 100

**4 System Stability Tests** **101**

4.1 Results . . . 101

4.2 Discussion . . . 106

**5 Experimental Test Programme** **111**

5.1 Results . . . 111

5.1.1 *G*-ratio . . . 111

5.1.2 Workpiece Temperature . . . 114

5.1.3 Cutting Forces . . . 134

5.1.4 Workpiece Temperature and Cutting Force Comparison . . . 141

5.2 Discussion . . . 144

5.2.1 *G*-ratio . . . 144

5.2.2 Workpiece Temperature . . . 148

5.2.3 Cutting Forces . . . 169

5.2.4 Workpiece Temperature and Cutting Force Comparison . . . 174

**6 Surface Integrity and Optical Microscopy Tests** **179**

6.1 Results . . . 179

6.1.1 Surface Roughness . . . 179

6.1.2 Microstructural Interrogation . . . 184

6.1.2.1 Ground Surface . . . 184

6.1.2.2 Subsurface . . . 185

6.1.2.3 SEM Imaging . . . 192

6.1.3 Microhardness . . . 198

6.1.4 Residual Stress . . . 202

6.2 Discussion . . . 208

6.2.1 Surface Roughness . . . 208

6.2.2 Microstructural Interrogation . . . 212

6.2.2.1 Ground Surface . . . 212

6.2.2.2 Subsurface . . . 213

6.2.2.3 SEM Imaging . . . 217

6.2.3 Microhardness . . . . . 221
6.2.4 Residual Stress . . . . . 226

**7 Dimensional Analysis Numerical Models 231**

7.1 Results . . . . . 231
7.1.1 Peak Workpiece Temperature . . . . . 231
7.1.2 Peak Cutting Forces . . . . . 238
7.2 Discussion . . . . . 242
7.2.1 Peak Workpiece Temperature . . . . . 242
7.2.2 Peak Cutting Forces . . . . . 243

**8 Overall Discussion and Conclusions 245**

**9 Suggestions for Further Work 250**

**10 References 253**

**Appendices A1**

Appendix A: Post Surface Grinding Roughness Results . . . . . A1
A.1 Normal to Grinding Direction . . . . . A1
A.2 Axial to Grinding Direction . . . . . A2
A.3 Position Variance Comparison . . . . . A3
Appendix B: Grinding Wheel Modal Analysis . . . . . B1
B.1 L9a Array . . . . . B2
B.2 L9b Array . . . . . B4
Appendix C: Thermocouple Response Time Tests . . . . . C1
Appendix D: Engineering Drawings . . . . . D1
D.1 Kistler 9257A Dynamometer Platform . . . . . D1
D.2 Thermocouple Extraction Plate . . . . . D2
D.3 Embedded Thermocouple Workpiece . . . . . D3
D.4 Cutting Force and Workpiece Temperature Data Acquisition Sub-Assembly Configuration . . . . . D4

D.5 Cutting Force and Workpiece Temperature Data Acquisition Sub-Assembly Exploded View Configuration . . . . . D5
D.6 SiC Grinding Wheel Tooling . . . . . D6
D.7 Wendt Mk IV Cantilever Dresser Roller Spindle Mounting Points . . . . . D7
Appendix E: Grinding Power Rate Profiles . . . . . E1

# List of Figures


1.1 Official Image of the Lockheed Martin F-22 Raptor Supersonic Fighter Jet (https://www.lockheedmartin.com/en-us/products/f-22.html. Accessed 2023) . 2

1.2 Official Image of the Boeing 777 Long Range Commercial Passenger Twin Jet Airliner (https://www.boeing.com/commercial/777. Accessed 2023) . . . . . 3

1.3 Areas where Titanium (blue) and Nickel superalloys (red) are utilised in Jet Engines (Rugg, 2003) . . . . . 4

1.4 Grinding Process Schematic . . . . . 5

1.5 Research Process Flowchart Schematic . . . . . 9

2.1 Schematic of the Grinding Chip Formation Process (Kalpakjian and Schmid, 2008) . . . . . 15

2.2 Local and Total Sum of the Temperature Profiles across a Ground Workpiece (Rowe, 2009) . . . . . 18

2.3 Comparative Stock Removal Rates for Differing Grinding Processes (Klocke *et al.*, 2016) . . . . . 25

2.4 Coolant Retention Profile on the Grinding Wheel Tooling (Hryniewicz *et al.*, 2000) . . . . . 29

2.5 Workpiece Temperature vs. Dressing Feed Rate (bearing Steel) for fine dressing (a), medium dressing (b) and coarse dressing (c) modes (Shaji and Radhakrishnan, 2002a) . . . . . 32

2.6 Specific Energy vs. Speed Ratio Predictions and Test Values (Baseri *et al.*, 2008b) . . . . . 37

2.7 Numerical and Experimental Normal (a, c) and Tangential (b, d) Cutting Force Model with Ploughing Force Component (Durgumahanti *et al.*, 2010) . . . . . 57
2.8 Conventional (a) and Superabrasive (b) wheel response optimisations during rough grinding (Liu, Chen and Gindy, 2008) . . . . . 59
2.9 Predicted Values from DA vs Test Data from Umino *et al.*, (1972), Umino *et al.*, (1972a) and Umino *et al.*, (1972b) as presented by Zhang *et al.*, (1999) . . 64
2.10 Wear Volume vs. Sliding Speed (Test Data and DA Comparison) for UHMWPE (a) and NBR (b) (Kaelani and Syaifudin, 2021) . . . . . 65
2.11 Dimensional Analysis Data for Surface Roughness (Phate and Toney, 2019) . . 67
2.12 Dimensional Analysis Data for MRR (Phate and Toney, 2019) . . . . . 67
2.13 Dimensional Analysis Data for Cutting Force (Alauddin and Zhang, 2007) . . 68
2.14 Dimensional Analysis Data for MRR (Kumar and Kamba, 2010) . . . . . 69
2.15 Workpiece Temperature v Cutting Time for steel alloy DN 36CrNiMo4 (a) and Workpiece Temperature vs. Cutting Speed for steel alloys DIN 9SMn28, DIN 22CrMoS3-5 and DIN 36CrNiMo4 (b) via a Thermocouple Arrangement during Drilling (Nedić and Erić, 2014) . . . . . 73
2.16 Experimental Design Flowchart regarding the Grinding Process . . . . . 77

3.1 Thermocouple Placement CAD Model . . . . . 87
3.2 Thermocouple Embedded Depth Schematic . . . . . 88
3.3 Embedded Thermocouple Extraction Method . . . . . 89
3.4 Complete Experimental Test Setup detailing grinding wheel (a), mounted workpiece and dynamometer platform (b) and mounting plate and dressing unit (c) . . . . . 90
3.5 Surface Integrity Wire EDM Prepared Sample; Physical (a) and CAD Model (b) 94
3.6 Residual Stress Strain Gauge Setup Example . . . . . 97
3.7 Incremental Drilling Setup (a) and Process (b) for Test [2]a Sample . . . . . 98

4.1 Thermocouple Temperature Measurement System Stability Check 1 - No Grind; No Coolant . . . . . 101
4.2 Cutting Force Measurement System Stability Check 1 - No Grind; No Coolant 102

4.3 Thermocouple Temperature Measurement System Stability Check 2 - No Grind; Low Pressure Coolant . . . . . 102
4.4 Cutting Force Measurement System Stability Check 2 - No Grind; Low Pressure Coolant . . . . . 103
4.5 Thermocouple Temperature Measurement System Stability Check 3 - No Grind; High Pressure Coolant . . . . . 103
4.6 Cutting Force Measurement System Stability Check 3 - No Grind; High Pressure Coolant . . . . . 104
4.7 Stability Test 4: Workpiece Temperature Thermocouple Response - With Grind; High Pressure Coolant . . . . . 104
4.8 Stability Test 4: Cutting Force Response - With Grind; High Pressure Coolant 105

5.1 $G$-ratios for changes in Depth of Cut for Test [1], Test [2] and Test [8] . . . . . 111
5.2 $G$-ratios for changes in Wheel Speed for Test [1] and Test [6] . . . . . 112
5.3 $G$-ratios for changes in Feed Rate for Test [2] and Test [7] . . . . . 112
5.4 $G$-ratio vs. Volume of Workpiece Removed - Test [1] across five passes . . . . . 113
5.5 $G$-ratio vs. Volume of Workpiece Removed - Test [6] across seven passes . . . 113
5.6 Test [1] – 0.97mm Stand Off Distance Workpiece Temperature Measurement (Pass 1) . . . . . 114
5.7 Test [1] – 0.67mm Stand Off Distance Workpiece Temperature Measurement (Pass 2) . . . . . 114
5.8 Test [1] – 0.37mm Stand Off Distance Workpiece Temperature Measurement (Pass 3) . . . . . 115
5.9 Test [1] – 0.07mm Stand Off Distance Workpiece Temperature Measurement (Pass 4) . . . . . 115
5.10 Test [1] – Thermocouple Destruction Workpiece Temperature Measurement (Pass 5) . . . . . 116
5.11 Workpiece Temperature at all Thermocouple Locations vs. Time for all Grinding Passes (Test 1) . . . . . 116
5.12 Microscope Images of Destroyed Thermocouple Nodes . . . . . 117

5.13 Test [1] - Workpiece Temperature vs. Thermocouple Stand Off Distance . . . . 117
5.14 Test [2] - 1.27mm Stand Off Distance Workpiece Temperature Measurement (Pass 1) . . . . . 118
5.15 Test [2] - 0.27mm Stand Off Distance Workpiece Temperature Measurement (Pass 2) . . . . . 118
5.16 Peak Workpiece Temperature at all Thermocouple Locations vs. Time for all Grinding Passes (Test 2) . . . . . 119
5.17 Test [2] - Workpiece Temperature vs. Thermocouple Stand Off Distance . . . . 119
5.18 Test [3] - Repeatability Test for Peak Workpiece Temperature Response . . . . 120
5.19 Test 4 - Pass 1 Radial Workpiece Temperature Reading . . . . . 120
5.20 Example Workpiece Temperature Retention Time Comparison for TC1, TC2 and TC3 for Test [3] and Test [4] . . . . . 121
5.21 Test [4] – 2mm Stand Off Distance Workpiece Temperature Measurement (Pass 2) . . . . . 121
5.22 Test [4] - Thermocouple Destruction Workpiece Temperature Measurement (Pass 3) . . . . . 122
5.23 Peak Workpiece Temperature at all Thermocouple Locations vs. Time for all Grinding Passes (Test 4) . . . . . 122
5.24 Test [5] - 2mm Stand Off Distance Workpiece Temperature Measurement (Pass 1) . . . . . 123
5.25 Test [5] – 1mm Stand Off Distance Workpiece Temperature Measurement (Pass 2) . . . . . 123
5.26 Peak Workpiece Temperature at all Thermocouple Locations for all Grinding Passes (Test 5) . . . . . 124
5.27 Test [5] - Workpiece Temperature vs. Thermocouple Stand Off Distance . . . 124
5.28 Test [6] – 1.68mm Stand Off Distance Workpiece Temperature Measurement (Pass 1) . . . . . 125
5.29 Test [6] – 1.38mm Stand Off Distance Workpiece Temperature Measurement (Pass 2) . . . . . 125

5.30 Test [6] – 1.08mm Stand Off Distance Workpiece Temperature Measurement (Pass 3) . . . 126
5.31 Test [6] – 0.78mm Stand Off Distance Workpiece Temperature Measurement (Pass 4) . . . 126
5.32 Test [6] – 0.48mm Stand Off Distance Workpiece Temperature Measurement (Pass 5) . . . 127
5.33 Test [6] – 0.18mm Stand Off Distance Workpiece Temperature Measurement (Pass 6) . . . 127
5.34 Test [6] – Final Pass/Thermocouple Destruction Workpiece Temperature (Pass 7) . . . 128
5.35 Peak Workpiece Temperature at all Thermocouple Locations for all Grinding Passes (Test 6) . . . 128
5.36 Test [6] - Workpiece Temperature vs. Thermocouple Stand Off Distance . . . 129
5.37 Test [7] – 1.5mm Stand Off Distance Workpiece Temperature Measurement (Pass 1) . . . 129
5.38 Test [7] – 0.5mm Stand Off Distance Workpiece Temperature Measurement (Pass 2) . . . 130
5.39 Peak Workpiece Temperature at all Thermocouple Locations for all Grinding Passes (Test 7) . . . 130
5.40 Test [7] - Workpiece Temperature vs. Thermocouple Stand Off Distance . . . 131
5.41 Test [8] – 0.5mm Stand Off Distance Workpiece Temperature Measurement (Pass 1) . . . 131
5.42 Test [9] – 0.5mm Stand Off Distance Workpiece Temperature Measurement (Pass 1) . . . 132
5.43 Test [10] – 0.5mm Stand Off Distance Workpiece Temperature Measurement (Pass 1) . . . 132
5.44 Test [1] – Cutting Forces vs. Time (Pass 1) . . . 134
5.45 Test [2] – Cutting Forces vs. Time (Pass 2) . . . 134
5.46 Test [3] - Repeatability Test for Peak Cutting Force Response . . . 135
5.47 Test [4] - Cutting Force vs. Time (Pass 3) . . . 135

5.48 Test [5] - Cutting Force vs. Time (Pass 2) . . . . . 136
5.49 Test [6] - Cutting Force vs. Time (Pass 7) . . . . . 136
5.50 Test [7] - Cutting Force vs. Time (Pass 2) . . . . . 137
5.51 Test [8] - Cutting Force vs. Time (Pass 1) . . . . . 137
5.52 Test [9] - Cutting Force vs. Time (Pass 1) . . . . . 138
5.53 Test [10] - Cutting Force vs. Time (Pass 1) . . . . . 138
5.54 Peak Workpiece Temperature and Cutting Force Comparison for Test [1] and Test [2] ($\Delta a$) . . . . . 141
5.55 Peak Workpiece Temperature and Cutting Force Comparison for Test [5] and Test [7] ($\Delta V_w$) . . . . . 141
5.56 Peak Workpiece Temperature and Cutting Force Comparison for Test [3] and Test [4] ($\Delta V_s$) . . . . . 142
5.57 Cutting Forces and Workpiece Temperature for all Tests . . . . . 143
5.58 Typical Boiling Curve for Water at 1bar . . . . . 153

6.1 Average Surface Roughness vs. Position for Grinding Tests Conducted (Parallel) . . . . . 179
6.2 Average Surface Roughness vs. Position for Grinding Tests Conducted (Parallel) . . . . . 180
6.3 Average Surface Roughness Values across all Grinding Test Cases (Parallel) . . 181
6.4 Average Surface Roughness vs. Position for Grinding Tests Conducted (Perpendicular) . . . . . 182
6.5 Average Surface Roughness vs. Position for Grinding Tests Conducted (Perpendicular) . . . . . 182
6.6 Average Surface Roughness Values across all Grinding Tests Conducted (Perpendicular) . . . . . 183
6.7 Ground Surface - Test [1] (Adjacent to TC 3) . . . . . 184
6.8 Ground Surface - Test [2]b (Between TC 2 and TC 3) . . . . . 184
6.9 Ground surface - Test [8] (Adjacent TC 3) . . . . . 185

6.10 Thermocouple 3 Location Microstructure Micrographs for Test [1] at x2.5 magnification (a), x5 magnification (b), x20 magnification (c) and x50 magnification (d) . . . . . 185
6.11 Thermocouple 3 Location Microstructure (a) and Microhardness (b) Comparison for Test [1] . . . . . 186
6.12 Thermocouple 3 Location Wire-EDM Surface Microstructure for Test [1] at x2.5 magnification (a), x5 magnification (b), x20 magnification (c) and x50 magnification (d) . . . . . 186
6.13 Thermocouple 3 Location Microstructure Micrographs for Test [2] at x2.5 magnification (a), x5 magnification (b), x20 magnification (c) and x50 magnification (d) . . . . . 187
6.14 Thermocouple 3 Location Microstructure (a) and Microhardness (b) Comparison for Test [2] . . . . . 187
6.15 Thermocouple 3 Location Wire-EDM Surface Microstructure for Test [2] at x2.5 magnification (a), x5 magnification (b), x20 magnification (c) and x50 magnification (d) . . . . . 188
6.16 Thermocouple 3 Location Microstructure Micrographs for Test [8] at x2.5 magnification (a), x5 magnification (b), x20 magnification (c) and x50 magnification (d) . . . . . 189
6.17 Thermocouple 3 Location Microstructure (a) and Microhardness (b) Comparison for Test [8] . . . . . 189
6.18 Thermocouple 3 Location Microstructure Micrographs for Test [10] at x2.5 magnification (a), x5 magnification (b), x20 magnification (c) and x50 magnification (d) . . . . . 190
6.19 Thermocouple 3 Location Microstructure (a) and Microhardness (b) Comparison for Test [10] . . . . . 191
6.20 SEM Image of Subsurface (a-c) and Ground Surface (d-e) - Test [1] . . . . . 192
6.21 SEM Image of Subsurface - Test [1] . . . . . 193
6.22 SEM Image of the Wire-EDM Subsurface - Test [1] . . . . . 193

6.23 SEM Image of the Subsurface Damage at entry to the workpiece (a) and exit of the workpiece (b) - Test [6] . . . . . 194
6.24 SEM Image of Subsurface Damage at entry to the workpiece x1000Mag (a) and entry of the workpiece x1500Mag (b) - Test [9] . . . . . 195
6.25 Conventional Camera Image of Subsurface Damage for Test [9] at the entry, middle and exit of the workpiece (a-c) and Test [10] (d-f) at locations of TC 1, TC 2 and TC 3 . . . . . 196
6.26 Ground Surface SEM Image for Test [10] (a-c) and Subsurface Damage for Test [10] (d-f) . . . . . 197
6.27 Microhardness vs. Indentation Depth for Test [9] . . . . . 198
6.28 Average Microhardness per Thermocouple Location for Test [9] . . . . . 198
6.29 Microhardness vs. Indentation Depth for Test [8] . . . . . 199
6.30 Average Microhardness per Thermocouple Location for Test [8] . . . . . 199
6.31 Average Microhardness vs. Indentation Depth for all Tests Conducted . . . . . 200
6.32 Average Microhardness vs. Indentation Depth for all Tests Conducted . . . . . 200
6.33 Average Microhardness across all Tests Summary . . . . . 201
6.34 Residual Principal Stress $\sigma_1$ vs. Depth (Grinding Direction) . . . . . 202
6.35 Residual Principal Stresses $\sigma_1$ for all Depths of Cut Analysed (Grinding Direction) . . . . . 203
6.36 Typical Phase Transition Plot for varying percentage Vanadium Content within Ti-6Al-4V (Majumdar *et al.*, 2019) . . . . . 204
6.37 Residual Principal Stress $\sigma_3$ vs. Depth (Transverse Direction) . . . . . 205
6.38 Residual Principal Stresses $\sigma_3$ for all Depths of Cut Analysed (Transverse Direction) . . . . . 205
6.39 Residual Shear Stress vs. Depth . . . . . 206
6.40 Residual Shear Stresses for all Depths of Cut Analysed . . . . . 207

7.1 Dimensional Analysis Workpiece Temperature Prediction Derived Equation ($V_w$ Variable) . . . . . 235

7.2 Dimensional Analysis Workpiece Temperature Prediction Derived Equation ($V_s$ Variable) . . . 236
7.3 Dimensional Analysis Workpiece Temperature Prediction Derived Equation ($a$ Variable) . . . 237
7.4 Dimensional Analysis Cutting Force Prediction Derived Equation ($V_w$ Variable) . . . 240
7.5 Dimensional Analysis Cutting Force Prediction Derived Equation ($V_s$ Variable) . . . 241
7.6 Dimensional Analysis Cutting Force Prediction Derived Equation ($a$ Variable) . . . 241

A1 Normal to Grinding Direction Surface Roughness Measurements ($R_a$; $R_q$) . . . A1
A2 Normal to Grinding Direction Surface Roughness Measurements ($R_z$) . . . A2
A3 Axial to Grinding Direction Surface Roughness Measurements ($R_a$; $R_q$) . . . A2
A4 Axial to Grinding Direction Surface Roughness Measurements ($R_z$) . . . A3
A5 Position Variance of Surface Roughness Measurements ($R_a$)(with grinding pass) A4
A6 Position Variance of Surface Roughness Measurements ($R_q$)(with grinding pass) A4
A7 Position Variance of Surface Roughness Measurements ($R_z$)(with grinding pass) A5
A8 Position Variance of Surface Roughness Measurements ($R_a$)(against grinding pass) A5
A9 Position Variance of Surface Roughness Measurements ($R_q$)(against grinding pass) A6
A10 Position Variance of Surface Roughness Measurements ($R_z$)(against grinding pass) A6
B1 Grinding Wheel Mode Values (L9a OA) . . . B2
B2 Grinding Wheel Mode Values (L9b OA) . . . B4
C1 Low Temperature Thermocouple Response Time Trial Results . . . C1
C2 Laplace Transform System Developed . . . C2
C3 Low Temperature Thermocouple Response Time Trial Results . . . C3
D1 Kistler 9257A Dynamometer Platform . . . D1
D2 Thermocouple Extraction Plate . . . D2
D3 Embedded Thermocouple Workpiece . . . D3

D4 Cutting Force and Workpiece Temperature Data Acquisition Sub-Assembly Configuration . . . . . D4
D5 Cutting Force and Workpiece Temperature Data Acquisition Sub-Assembly Exploded View Configuration . . . . . D5
D6 SiC Grinding Wheel Tooling . . . . . D6
D7 Wendt Mk IV Cantilever Dresser Roller Spindle Mounting Points . . . . . D7
E1 Grinding Power Rate Profiles for all Experimental Tests . . . . . E2

# List of Tables


2.1 Comparative Performances of a Range of Different Grinding Wheel Materials (Malkin, 1989; Morgan *et al.*, 1998; Spriggs, 2002; Xu *et al.*, 2006; Marinescu *et al.*, 2006) . . . . . 23

2.2 Details of Various Oil and Water-Based Coolant Thermal Properties (Vashisht and Kapila, 2008) . . . . . 26

2.3 Comparative Manufacturing Methods of Diamond Profile Roller Dressers; (R - Sintered; PG - Reverse Plated; RG - Electroplated) (Dr. Kaiser, 2012) . . 36

2.4 Comparative Performances of a Range of Workpiece Temperature Measurement Techniques (Conradie *et al.*, 2012) . . . . . 74

3.1 Chemical Composition of Ti-6Al-4V . . . . . 85

3.2 Experimental Test Programme Process Parameters . . . . . 92

3.3 Experimental Dressing Parameters . . . . . 93

3.4 Buehler Alpha-2 Speed Grinder Polisher Operating Parameters . . . . . 95

5.1 Summary of Experimental Workpiece Temperature Data . . . . . 133

5.2 Summary of Experimental Cutting Force Data . . . . . 139

5.3 Summary of Experimental Workpiece Temperature and Cutting Force Data . . 140

7.1 Variables used for Buckingham-$\pi$ Group Derivations . . . . . 231

7.2 Derived Buckingham-$\pi$ Groups for Peak Workpiece Temperature using Dimensional Analysis . . . . . 233

7.3 Variables used for Buckingham-$\pi$ Group Derivations . . . . . 238

7.4 Derived Buckingham-$\pi$ Groups for Peak Cutting Force using Dimensional Analysis . . . . . 239

B1 Grinding Wheel Modal Study Taguchi L9a Array . . . . . B1

B2 Grinding Wheel Modal Study Taguchi L9b Array . . . . . B1

B3 Sample First Six Mode Distributions . . . . . B3

# Nomenclature

## Acronyms/Abbreviations

| | |
|---|---|
| $Al_2O_3$ | Aluminium Oxide |
| ANN | Artificial Neural Network |
| ASTM | American Society for Testing and Materials |
| Au | Gold |
| AWJ | Abrasive Water Jet |
| $BaF_2$ | Barium Fluoride |
| BCC | Body Centred Cubic |
| BNA | Barkhausen Noise Analysis |
| C | CVD Diamond |
| CAD | Computer Aided Design |
| $CaF_2$ | Calcium Fluoride |
| cBN | Cubic Boron Nitride |
| cBN-B | Cubic Boron Nitride (Polycrystalline) |
| cBN-U | Cubic Boron Nitride (Conventional) |
| CDCF | Continuous Dress Creep Feed |
| CFD | Computational Fluid Dynamic |
| CFG | Creep Feed Grinding |
| CFRP | Carbon Fibre Reinforced Plastic |
| CMM | Coordinate Measuring Machine |
| CMSX-4 | Nickel-based Superalloy |
| CNS | Classical Numerical Solutions |
| CoCr | Cobalt-Chromium |
| CVD | Chemical Vapour Deposition |
| dimQ | Dimensionless Quantities |
| *D* | Diamond |
| DA | Dimensional Analysis |

| | |
|---|---|
| DAQ | Data Acquisition |
| DoE | Design of Experiments |
| DT | Destructive Testing |
| EDM | Electrical Discharge Machining |
| EG | Ethylene Glycol |
| EHL | Elastohydrodynamic Lubrication |
| ELID | Electrolytic In-Process Dressing |
| *ERF* | Error Function |
| FE | Finite Element |
| FEA | Finite Element Analysis |
| FFG | Form and Finish Grinding |
| G | Random |
| GUI | Graphical User Interface |
| H | Hand Set |
| HAZ | Heat Affected Zone |
| HCF | High-Cycle Fatigue |
| HCP | Hexagonal Close Packed |
| HEDG | High Efficiency Deep Grinding |
| HF | Hydrofluoric Acid |
| HK | Knoop Hardness |
| $HNO_3$ | Nitric Acid |
| HP | High Pressure |
| HRK | Rockwell K Hardness |
| HSS | High Speed Steel |
| HV | Vickers Hardness |
| K | Natural Diamond |
| LCF | Low-Cycle Fatigue |
| m | Number of Variables |
| MFR | Mass Flow Rate ($kg.s^{-1}$) |

| | |
|---|---|
| MMC | Metal Matrix Composite |
| MoCuSi | Molybdenum Copper Silicon |
| $MoO_3$ | Molybdenum Trioxide |
| MQL | Minimum Quantity Lubrication |
| MRR | Material Removal Rate, Q, ($mm^3.s^{-1}$) |
| n | Number of Dimensionless Quantities |
| NDT | None-Destructive Testing |
| NR | Nitrile Rubber |
| OA | Orthogonal Array |
| PC | Personal Computer |
| PG | Reverse Plated |
| $PG_1$ | Propylene Glycol |
| PLC | Programmable Logic Controller |
| PTFE | Poly Tetra Flouro Ethylene |
| PVD | Physical Vapour Deposition |
| r | Number of Buckingham-$\pi$ Groups |
| rpm | Revolutions per Minute ($rev.min^{-1}$) |
| R | Sintered |
| RG | Electroplated |
| RSM | Response Surface Methodology |
| SEM | Scanning Electron Microscopy |
| SiC | Silicon Carbide |
| SI | Standard Index |
| SPIF | Single Point Incremental Forming |
| SQL | Small Quantity Lubrication |
| SRG | Stock Removal Grinding |
| SSG | Speed Stroke Grinding |
| TC | Thermocouple |
| THC | Thermal History Coatings |

| | |
|---|---|
| THP | Thermal History Paints |
| Ti64 | Ti-6Al-4V |
| TIP | Thermal Image Processing |
| TRL | Technology Readiness Level |
| TVSR | Thermal Vibratory Stress Relief |
| UA | Ultrasonically Assisted |
| UHMWPE | Ultra High Molecular Weight Poly Ethylene |
| USB | Universal Series Bus |
| UV | Ultra-Violet |
| VIPER | Very Impressive Performance Extreme Removal |
| VSR | Vibratory Stress Relief |
| WEDM | Wire Electrode Discharge Machining |
| $WRP_s$ | Work Removal Parameters of the Wheel ($m^3.s^{-1}.N^{-1}$) |
| $WRP_w$ | Work Removal Parameters of the Workpiece ($m^3.s^{-1}.N^{-1}$) |
| XRD | X-Ray Diffraction |

## Roman Symbols

| | |
|---|---|
| $a$ | Depth of Cut (mm) |
| $a_o$ | Constant |
| $a_1$ | Constant |
| $\mathrm{a}_d$ | Dressing Depth (mm) |
| $\mathrm{a}_p$ | Engagement Width (mm) |
| $b$ | Radial Depth of Cut (mm) |
| $b_c$ | Wheel Thickness (mm) |
| $c$ | Specific Heat Capacity ($\mathrm{J.kg^{-1}.K^{-1}}$) |
| $\mathrm{c}_g$ | Number of Active Grits |
| $\mathrm{c}_s$ | Specific Heat Capacity (wheel) ($\mathrm{J.kg^{-1}.K^{-1}}$) |
| $\mathrm{c}_w$ | Specific Heat Capacity (workpiece) ($\mathrm{J.kg^{-1}.K^{-1}}$) |
| $\mathrm{C}_t$ | Capacitance of the Charge Amplifier Range Capacitor (F) |
| d | Thickness of the Workpiece (mm) |
| $d_{100}$ | Diameter of a Grain of Wheel Grade 100 (mm) |
| $d_{g_{av}}$ | Grain Mean Diameter (mm) |
| $\mathrm{d}_g$ | Abrasive Grain Size (mm) |
| E | Young's Modulus (GPa) |
| $\bar{E}$ | Dimensionless Young's Modulus |
| $\mathrm{F}_a$ | Axial Cutting Force (N) |
| $\mathrm{F}_x$ | Cutting Force Component ($x$ Direction) (N) |
| $\mathrm{F}_y$ | Cutting Force Component ($y$ Direction) (N) |
| $\mathrm{F}_z$ | Cutting Force Component ($z$ Direction) (N) |
| $\mathrm{F}_{CrossFeed}$ | Cross Feed Force (N) |
| $\mathrm{F}_{Cutting}$ | Force Solely due to Cutting (No Ploughing or Rubbing) (N) |
| $\mathrm{F}_{Max}$ | Maximum Cutting Force (N) |
| $\mathrm{F}_N$ | Normal Cutting Force (N) |
| $\mathrm{F}_{N_{Ch}}$ | Normal Chip Formation Force (N) |
| $\mathrm{F}_{N_{Grain}}$ | Normal Force Component acting on a Single Grain (N) |

| | |
|---|---|
| $\mathrm{F}_{N_{Sliding}}$ | Normal Sliding Component Force (N) |
| $F(t)$ | Forcing Function |
| $\mathrm{F}_T$ | Tangential Cutting Force (N) |
| $\mathrm{F}_{Total}$ | Resultant Cutting Force (N) |
| $\mathrm{F}_{T_{Ch}}$ | Tangential Chip Formation Force (N) |
| $\mathrm{F}_{T_{Grain}}$ | Tangential Force Component acting on a Single Grain (N) |
| $\mathrm{F}_{T_o}$ | Tangential Cutting Force (threshold) (N) |
| $\mathrm{F}_{T_{Sliding}}$ | Tangential Sliding Component Force (N) |
| $G$-ratio | Grinding Ratio |
| $h_m$ | Maximum Chip thickness (mm) |
| $Hm$ | Hardening Depth ($\mu$m) |
| $H_n$ | Wheel Hardness Number |
| $I$ | Base Quantity for Electric Current |
| $J$ | Base Quantity for Luminous Intensity |
| $\mathrm{k}_1$ | Thermocouple Gain |
| $\mathrm{k}_{constant}$ | Constant |
| $\mathrm{k}_d$ | Thermal Diffusivity ($\mathrm{m}^2.\mathrm{s}^{-1}$) |
| $\mathrm{k}_A$ | Archard Constant |
| $\mathrm{K}_{Nc}$ | Coefficient for Normal Cutting Force (MPa) |
| $\mathrm{K}_{Np}$ | Coefficient for Normal Ploughing Force (MPa) |
| $\mathrm{K}_{Tc}$ | Coefficient for Tangential Cutting Force (MPa) |
| $\mathrm{K}_{Tp}$ | Coefficient for Tangential Ploughing Force (MPa) |
| $\mathrm{l}_c$ | Contact Length (mm) |
| $\mathrm{l}_h$ | Half Contact Zone Length (m) |
| $\mathrm{l}_k$ | Average Chip Length (mm) |
| $L$ | Base Quantity for Length |
| $\dot{m}$ | Mass Flow Rate ($\mathrm{kg}.\mathrm{s}^{-1}$) |
| M | Base Quantity for Mass |
| $\mathrm{M}_b$ | Maximum Bending Moment for failure |

| | |
|---|---|
| N | Base Quantity for Molar Mass |
| $P_c$ | Grinding Processing Power (kW) |
| $P_{SpindleIdle}$ | Idle Spindle Power (kW) |
| $P_{SpindleTotal}$ | Total Spindle Power (kW) |
| $P_w$ | Power Delivered to Workpiece (W) |
| $q$ | Dressing Speed Ratio |
| $q_t$ | Total Heat Flux ($W.m^{-2}$) |
| $Q_w$ | Material Removal Rate ($mm^3.s^{-1}$) |
| $Q'_w$ | Specific Material Removal Rate ($mm^2.s^{-1}$) |
| $r_g$ | Grit Aspect Ratio |
| $R_a$ | Average Surface Roughness ($\mu$m) |
| $R_q$ | Root Mean Square Surface Roughness ($\mu$m) |
| $R_t$ | Charge Amplifier Time Constant Resistance ($\Omega$) |
| $R_t$ | Peak to Trough Surface Roughness ($\mu$m) |
| $R_{wp}$ | Energy Partition to the Workpiece |
| $R_z$ | Mean Surface Roughness Depth ($\mu$m) |
| $S_n$ | Wheel Structure Number |
| $t_c$ | Time taken for Grinding Zone Contact to Stay Stationary (s) |
| $t_{high}$ | High Temperature (°C) |
| $t_{low}$ | Low Temperature (°C) |
| $T$ | Peak Workpiece Temperature (°C) |
| $T_1$ | Base Quantity for Time |
| $\bar{T}$ | Dimensionless Temperature |
| $T_{sub}$ | Subsurface Workpiece Temperature (°C) |
| $T_{Max}$ | Maximum Temperature (°C) |
| $T_{Melt}$ | Melting Temperature (°C) |
| $u_{chip}$ | Specific Energy due to Chip Formation ($J.kg^{-1}$) |
| $u_{plough}$ | Specific Energy due to Ploughing Force ($J.kg^{-1}$) |
| $u_{rub}$ | Specific Energy due to Rubbing Force ($J.kg^{-1}$) |

| | |
|---|---|
| $u_t$ | Total Specific Energy ($J.kg^{-1}$) |
| $V_a$ | Axial Cross-Feed ($mm.min^{-1}$) |
| $V_b$ | Percentage Volume of Bond Material in the Wheel Matrix |
| $V_d$ | Cross Feed Rate ($mm.min^{-1}$) |
| $V_{ds}$ | Dressing Speed ($m.s^{-1}$) |
| $V_g$ | Percentage Volume of Grain Material in the Wheel Matrix |
| $V_s$ | Wheel Speed ($m.s^{-1}$) |
| $V_w$ | Feed Rate ($mm.min^{-1}$) |
| $\dot{V}$ | Volumetric Flow Rate ($mm^3.s^{-1}$) |
| $X_1$ | Buckingham-$\pi$ Group 1 (Zhang *et al.*, 1993) |
| $y(t)$ | Thermocouple Response |
| $z$ | Depth from Cutting Surface (mm) |
| $Z_s$ | Average Material Removal Rate of Wheel ($mm^3.min^{-1}$) |
| $Z_w$ | Average Material Removal Rate of Workpiece ($mm^3.min^{-1}$) |

## Greek Letters

| | |
|---|---|
| $\alpha$ | Rake Angle (°) |
| $\alpha_{t-e}$ | Coefficient of Thermal Expansion ($K^{-1}$) |
| $\gamma$-TiAl | Gamma Titanium Aluminide |
| $\theta_1$ | Base Quantity for Temperature |
| $\theta_d$ | Sum of Collective Temperature Arcs within the Grinding Zone (°C) |
| $\theta_l$ | Localised Abrasive Grain Grinding Temperature (°C) |
| $\lambda$ | Thermal Conductivity ($W.m^{-1}.K^{-1}$) |
| $\lambda_s$ | Thermal Conductivity of the Wheel ($W.m^{-1}.K^{-1}$) |
| $\lambda_w$ | Thermal Conductivity of the Workpiece ($W.m^{-1}.K^{-1}$) |
| $\nu$ | Poisson's Ratio |
| $\pi_1$ | Buckingham-$\pi$ Group 1 |
| $\pi_2$ | Buckingham-$\pi$ Group 2 |
| $\pi_3$ | Buckingham-$\pi$ Group 3 |
| $\pi_4$ | Buckingham-$\pi$ Group 4 |
| $\pi_5$ | Buckingham-$\pi$ Group 5 |
| $\pi_6$ | Buckingham-$\pi$ Group 6 |
| $\rho$ | Density ($kg.m^{-3}$) |
| $\rho_w$ | Density of the Workpiece ($kg.m^{-3}$) |
| $\sigma_1$ | Residual Stress (Grinding Direction) (MPa) |
| $\sigma_3$ | Residual Stress (Transverse Direction) (MPa) |
| $\sigma_{comp}$ | Compressive Stress (MPa) |
| $\sigma_r$ | Compressive Residual Stress (MPa) |
| $\sigma_T$ | Thermal Stress (MPa) |
| $\tau$ | Thermocouple Time Constant (s) |
| $\tau_{13}$ | Residual Shear Stress (MPa) |
| $\tau_s$ | Shear Strength of the Wheel (MPa) |
| $\tau_{tc}$ | Charge Amplifier Time Constant (s) |
| $\tau_w$ | Shear Strength of the Workpiece (MPa) |

$\phi_d$ Dressing Tool Diameter (mm)

$\phi_s$ Wheel Diameter (mm)

## Dimensionless Numbers

| | |
|---|---|
| $P_e$ | Peclet Number |
| $R_e$ | Reynolds Number |

# Chapter 1

# Introduction

Throughout various manufacturing industries, the process of material removal through the use of a variety of machining methods is commonplace. In particular, this thesis concentrates on the machining process of grinding. Grinding can be classified as a conventional material removal process, albeit one which has distinctive differences from other common machining methods. Unlike turning, which relies on a single point cutting tool which causes a cutting chip formation, grinding relies on several abrasive particles to cause wear of the workpiece with little to no visible chip formation (Malkin and Guo, 2007). Grinding wheels are constituted of many abrasive particles held in a composite matrix of varying bond types depending on the wheel type; i.e., resinoid bonds for conventional abrasives, or vitrified bonds for superabrasive types. These differences hold significant challenges for manufacturers, researchers and production engineers who may wish to optimise and utilise the grinding process for differing objectives.

For instance, surface grinding is often used as a 'finishing process' after larger stock removal processes have been employed. This is because surface grinding observes lower workpiece temperatures and cutting forces than other manufacturing processes due to the high speed of the tooling and small depths of cut, which results in better surface roughness and residual compressive stresses (Marinescu *et al.*, 2013); a key factor when manufacturing components that operate in environments where temperature is a critical factor. However,

both workpiece temperature and cutting force can increase significantly as the grinding wheel begins to wear, resulting from an increase in specific energy within the grinding zone.

Titanium is widely utilised throughout the aerospace sector. For example, the material and its alloys consist of 42% of the total weight of Lockheed Martin's F-22 Raptor jet fighter as presented in Fig 1.1 (Cotton, Clarke and Phelps, 2002), and 8.2% of the commercial Boeing-777 passenger aircraft as shown in Fig 1.2 (Williams and Starke, 2003). Specifically, the aerospace grade, alpha-beta titanium alloy Ti-6Al-4V is commonly used in airframe structures having replaced heavier, previously used, steel joints. The alloy consists of titanium (atomic number of 22 and relative atomic mass of 44.87 which is a transition metal in group 4 of the periodic table), aluminium (atomic number of 13 and relative atomic mass of 26.98 which is part of the boron group in group 13 of the periodic table) and vanadium (atomic number of 23 and relative atomic mass of 50.94 which is also a transition metal in group 5 of the periodic table) (Levi, 2000).



**Figure 1.1:** Official Image of the Lockheed Martin F-22 Raptor Supersonic Fighter Jet (https://www.lockheedmartin.com/en-us/products/f-22.html. Accessed 2023)




**Figure 1.2:** Official Image of the Boeing 777 Long Range Commercial Passenger Twin Jet Airliner (https://www.boeing.com/commercial/777. Accessed 2023)

Ti-6Al-4V is also often used for various jet engine components, usually in the colder fan and compressor sections where operating temperatures are lower (≈200°C - 550°C) rather than in the hotter combustion chamber and high-pressure (HP) turbines where operating temperatures are higher, i.e., up to 2000°C. This is due to the possibility of combustion. The widespread utilisation of Ti64 is primarily due to the alloy having an extremely good strength-to-weight ratio and superb corrosive and erosive resistivity. However, despite considerable advancements in machine and cutting tool technology over the past twenty years, the machinability of Ti64 still remains a key issue, especially in relation to the resulting workpiece surface integrity condition. In terms of conventional cutting processes, the grinding of Ti64 is particularly challenging, not least due to its low thermal conductivity ($\approx$6.7W.m$^{-1}$.K$^{-1}$) and relatively high ductility as reported by Whittaker and Hess (2015), which frequently causes heavy loading and rapid wear of the grinding wheel and is thus the basis from which this work builds.

## 1.1 Background and Motivation for the Project

Grinding is a key abrasive manufacturing process used across most industries. However, in the aerospace industry, it is particularly utilised for Ti64 components such as the fan and compressor sections (Rugg, 2003), in addition to the finishing of critical, high temperature exposed nickel-based superalloy sections such as turbine blades. A schematic detailing the areas where both of these materials are utilised within jet engines is detailed in Fig 1.3, where the blue areas refer to titanium components and the red areas refer to nickel-based superalloy components.

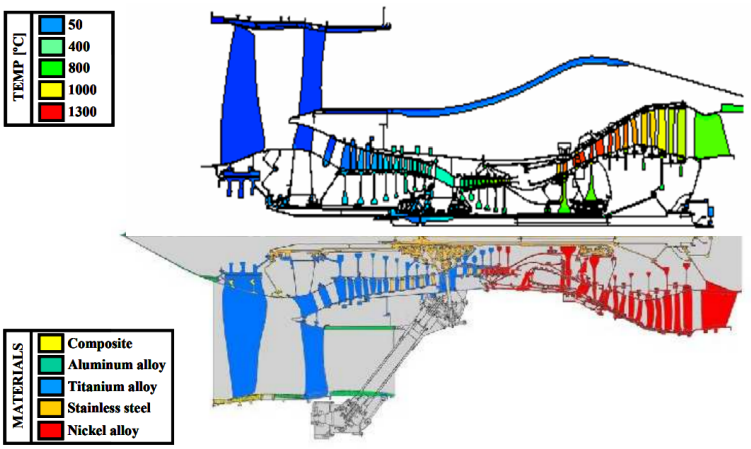



**Figure 1.3:** Areas where Titanium (blue) and Nickel superalloys (red) are utilised in Jet Engines (Rugg, 2003)

One major factor considered is the temperature that occurs in the grinding zone located between the grinding wheel and the workpiece as detailed in Fig 1.4. The temperature induced within the grinding zone can significantly affect the workpiece material properties, and, as such, lower temperatures are highly desirable. Improved surface integrity performance (i.e., low surface roughness and compressive residual stresses) are observed when grinding zone temperatures are lower, resulting in a more mechanically improved component (Kadivar *et al.*, 2020).

Nonetheless, the abrasive machining of conventional titanium alloys (e.g., Ti-6Al-4V) still remains problematic due to the material having an extremely low thermal conductivity ($6.7 \mathrm{W.m^{-1}.K^{-1}}$), high ductility and high chemical reactivity with the grinding wheel tooling. Significant work hardening is also observed when operating at reduced grinding parameter magnitudes, thus decreasing its grindability further (Patil *et al.*, 2016). As such, grinding Ti-6Al-4V is generally more challenging than grinding hard and abrasive materials like hardened steels, glass and ceramics, for instance. Conversely, grinding has been used for the machining of new generation $\gamma$-TiAl intermetallic alloys which are deemed to have significant potential in the future development of thermally critical components in jet engines due to their acceptable yield strength, high specific stiffness and good oxidation resistance (Murtagian, 2004).

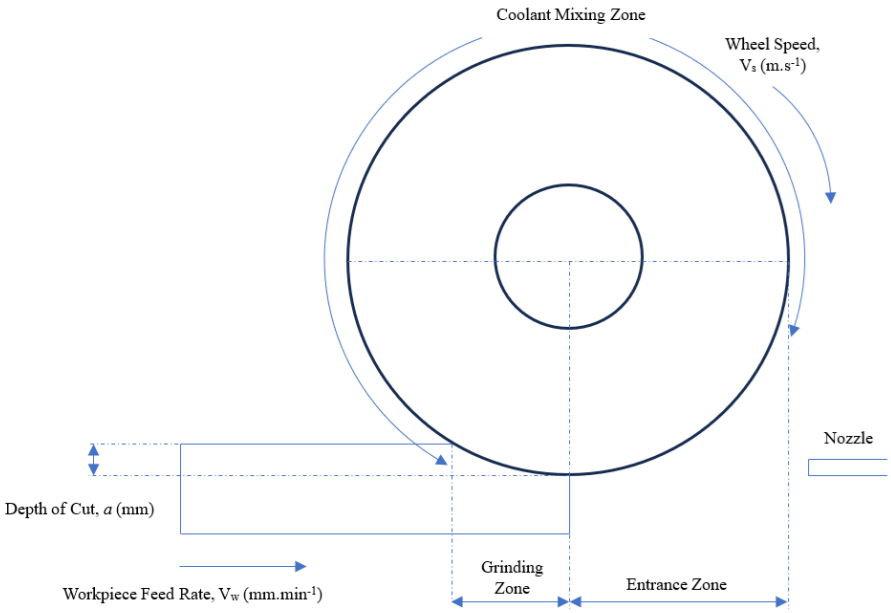



**Figure 1.4:** Grinding Process Schematic

Due to the complexity of the grinding process using undefined cutting edges, the computational modelling via Finite Element (FE) packages is extremely difficult and solve-time intensive, and as such, very little work has been conducted utilising predictive methods to evaluate peak workpiece temperatures and cutting forces via mechanical contact models. This is also apparent in terms of the lack of research regarding experimentally evaluating workpiece temperature outputs via physical testing as temperature measurement within this area of grinding research is scarce.

The following were the principal motivations for the research;

- Very little work is currently being conducted worldwide in respect to grinding and specifically temperature prediction and measurement. This statement is based on initial investigations into the volume of available literature published within this research area.

- Research into grinding processes regarding advanced aerospace alloys is severely underrepresented in the worldwide academic community (Less than ten centres of excellence worldwide).

- Access to aerospace materials and grinding systems/wheels is difficult, and therefore, by default, information from both experimental and numerical modelling activities are highly sought.

- Workpiece surface integrity is an area of high interest for any manufacturing process, especially within the aerospace industry that contains many safety critical components.

- Information is required for industry at low Technology Readiness Levels (TRLs) and therefore the project has potential for significant future impact.

## 1.2 Aims and Objectives of the Project

The overall aim of the project was to assess the grindability of Ti-6Al-4V, with the specific aim of experimentally evaluating the peak workpiece temperature. Additionally, the development of six Buckingham-$\pi$ groups via a Dimensional Analysis (DA) of the grinding process were derived so they could be subsequently assessed against the experimental data to determine if theoretical approaches could be applied during subsequent research.

The following objectives were outlined as being crucial to meet the criteria of the project;

1. Complete a comprehensive literature review of relevant past research on grinding of titanium aerospace alloys such as Ti-6Al-4V, including experimental based studies; specifically, those relating to workpiece temperature, cutting forces and surface integrity assessment and evaluation.

2. Undertake a valid experimental test programme considering a variety of grinding parameters such as wheel speed, feed rate and depth of cut. This would also include measuring the workpiece temperature using a novel thermocouple placement configuration, in addition to the cutting forces and subsequent surface integrity performance.

3. Development of new DA numerical models to simulate the grinding process and thus be able to predict the peak workpiece temperatures and cutting forces under the same experimentally tested operating conditions.

4. Analysis, implementation and integration of state-of-the-art datalogging equipment for workpiece temperature measurement into the manufacturing architecture available at the University of Birmingham.

## 1.3 Organisation of the Research and Thesis Structure

The research was split into three distinct phases of work. A brief description of each is given below, whilst Fig 1.5 displays a flowchart schematic of the programme of work.

The Preparation Phase section, presented in Chapter 2: Literature Review, involved assessing a large volume of previously published academic works relating to state-of-the-art grinding processes, as well as experimental and DA trends for measuring and predicting peak workpiece temperature, cutting forces and the surface integrity performance of the workpiece post-grinding.

The following phases (Phase 1 through to Phase 2) are presented in Chapter 4: Results and Discussion;

Phase 1 of the work considered the experimental testing of a range of grinding variables; namely, wheel speed, $V_s$, feed rate, $V_w$, and depth of cut, $a$. Ti-6Al-4V and SiC were used for the workpiece and tooling respectively, whilst the workpiece temperature, cutting forces, $G$-ratio and subsequent surface integrity performance were the desired

outputs measured. This test programme utilised a Bridgeport Grinding Centre for the machining, six thermocouples for the workpiece temperature measurement, a standard data logger for the workpiece temperature data acquisition, whilst the cutting forces were obtained via a dynamometer. Subsequent surface integrity assessment was undertaken on the ground workpieces which considered the surface roughness, optical microstructure analysis, microhardness and residual stress evaluation.

Phase 2 of the programme applied DA of the grinding parameters used throughout the test programme, in addition to both the workpiece and tooling's material properties. The Buckingham-$\pi$ theorem was applied for the analysis, with six new and unique dimensionless groups being derived to analyse the grinding process via numerical predictions for workpiece temperature and cutting force responses.

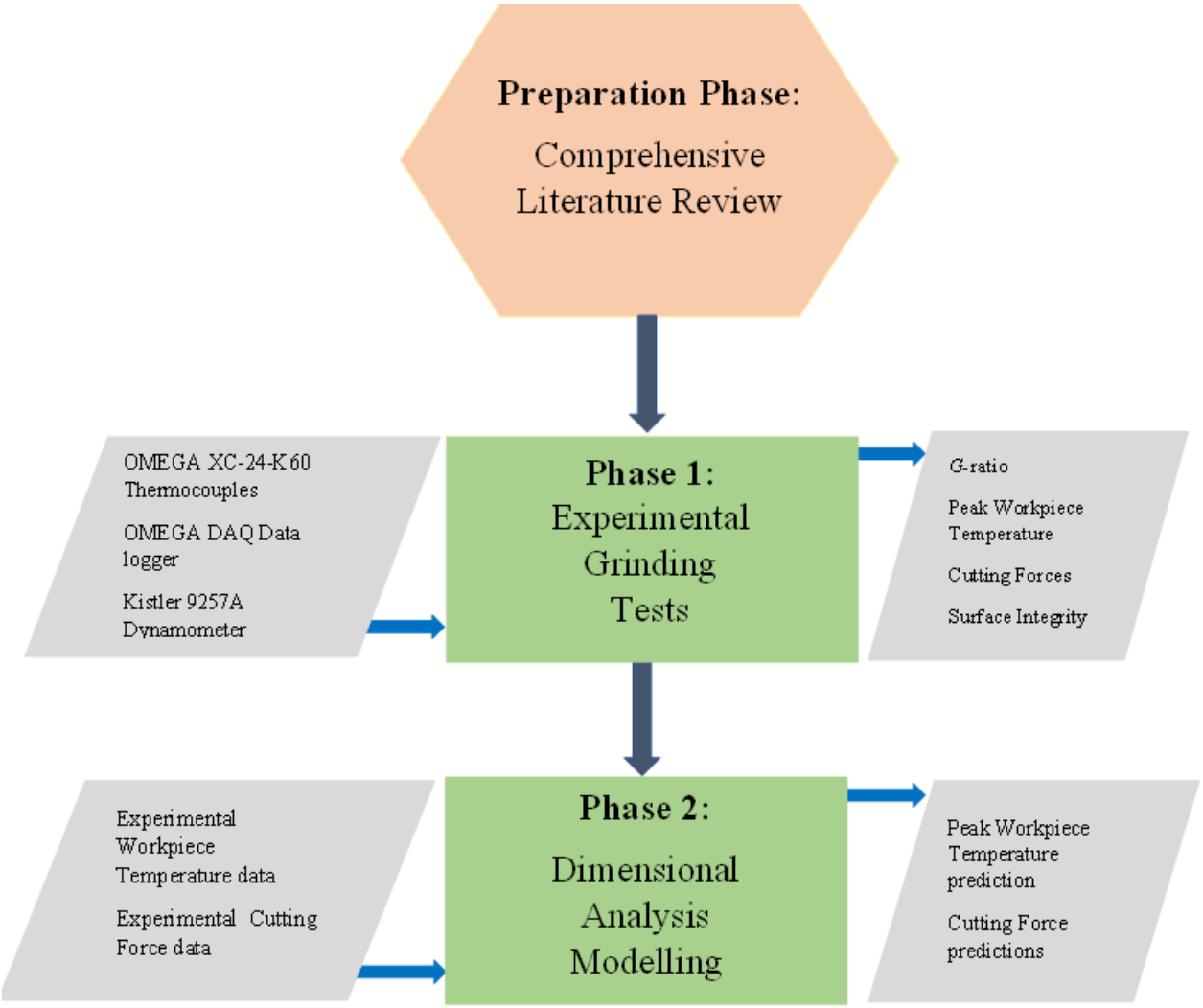



**Figure 1.5:** Research Process Flowchart Schematic

# Chapter 2

# Literature Review

## 2.1 Introduction

Grinding has been used throughout the course of human history, dating back to when pre-historic man used stone to carve materials used for hunting (Malkin, 1989). During the twentieth century, however, $Al_2O_3$ and SiC grinding wheels have been utilised, and, more recently, cubic boron nitride (cBN) and diamond alternatives. Additionally, the grinding process itself has progressed significantly over the past two decades to now include Creep Feed Grinding (CFG), Speed Stroke Grinding (SSG) and High Efficiency Deep Grinding (HEDG) processes. These have enabled increased material removal rates and reduced cycle times whilst retaining the workpiece surface integrity and fatigue life performance. Grinding is now a key machining method employed in the manufacture of turbofan engine components, in addition to airframe applications such a landing gears, throughout the aerospace sector. This has been, in part, as a result of newly developed, highly exotic alloys including that of $\gamma$-titanium being used for turbine blade solutions, whilst the lower operating temperature ($<$500°C) fan and compressor sections using Ti-6Al-4V.

Despite holding such positive properties, titanium alloys display a reduced thermal conductivity, i.e., 6.9W.m$^{-1}$.K$^{-1}$ for Ti-6Al-4V and relatively high ductility (Xu *et al.*, 2003). This ultimately has a negative impact on the ability to machine workpieces formed from Ti64, thus making it more difficult to grind. This has resulted in issues regarding surface

integrity and finish, surface cracking and burn. Due to the extensive nature that grinding has on Ti-6Al-4V for aerospace components, this is a significant problem that needs to be addressed (Caggiano and Teti, 2013). Many previous works have considered how different grinding wheels such as $Al_2O_3$, SiC and cBN can be used to negate this effect including those by Ichida *et al.*, (2006), Aspinwall *et al.*, (2007), Liu, Chen and Gindy (2008) and more recently, Butler-Smith *et al.*, (2011).

In addition, the modelling of the grinding process, especially in terms of FE methods, has been seen to be somewhat limited in its approach. Many numerical models have been developed, most notably the moving heat source model by Jaeger (1942), Hahn (1962) and more contemporary works by Durgumahanti *et al.*, (2010), Shen and Xiao (2011) and Esnault and Roux (2013). However, the FE approach has been limited to macro-scale paradigm models involving stresses, plastic strains and estimated surface temperatures such as those presented by Cook *et al.*, (2007), Öpöz and Chen (2010) and Tahvilian *et al.*, (2013), and not so extensive in terms of microscale modelling of the grain-workpiece interface. This has been due to the highly complex nature of undertaking such an analysis, with much easier and time-effective methods of predicting such outputs being reported within the literature via numerical solutions. Such methods include the DA method. As such, this thesis collates an extensive collection of previous published works concerning experimental testing whilst grinding Ti-6Al-4V, additional titanium alloys and other "hard to grind" materials. Furthermore, the design, development and ultimate implementation of classical numerical and DA models of the grinding process when assessing the Ti-6Al-4V alloy were also critiqued.

Prior to any further discussion, some basic parameters referred to throughout this thesis are established here. Despite the grinding process being one of considerable complexity, three key operating parameters are crucial when wishing to understand both the peak workpiece temperature experienced by the workpiece, as well as the peak cutting forces experienced by the grinding tool. These are as follows;

i) Wheel Speed, $V_s$, ($m.s^{-1}$) – Speed at which the grinding wheel is spinning.

ii) Feed Rate, $V_w$, ($mm.min^{-1}$) – Rate at which the workpiece is fed into the grinding tool.

iii) Depth of Cut, $a$, (mm) – Depth of cut removed from the workpiece.

Other important factors which are considered non-operating parameters which affect both workpiece temperature and cutting forces include;

iv) Wheel Material.

v) Workpiece Material.

vi) Coolant.

vii) Dressing Mode.

As the workpiece material and wheel material were held constant as Ti-6Al-4V and SiC respectively for both the experimental test programme and the theoretical DA modelling derivations, only process parameters i) through to iii) were investigated throughout this thesis. Finally, other parameters referred to in this thesis, although not directly process parameters, include:

viii) Material Removal Rate (MRR), $Q_w$, ($mm^3.s^{-1}$) – Rate at which material is removed from the workpiece.

ix) $G$-ratio – Ratio of volume of workpiece material removed to volume of grinding wheel wear, as is expressed in Eqn. 2.1. Here, the $G$-ratio was evaluated for the grinding tests conducted, as wheel wear has a direct impact on the workpiece temperature and the induced cutting forces.

$$G - ratio = \frac{Volume\ of\ Workpiece\ Material\ Removed}{Volume\ of\ Grinding\ Wheel\ Wear} \qquad \text{(Eqn. 2.1)}$$

## 2.2 Grinding Processes

Grinding is a material removal process that utilises a grinding wheel constructed of abrasive, hard grit materials such as silicon carbide (SiC), aluminium oxide ($Al_2O_3$), cubic boron nitride (cBN) or diamond. These abrasives are held in a weaker, bonded material matrix which can be either organic in nature (i.e., resin), inorganic, such as clay, or metal bonded. The abrasive materials, once held in the bonded matrix, are observed to have spaces between them. This is called the grinding wheel's porosity. The wheel's porosity has an effect on the wheel performance, i.e., it results in fluid being able to navigate across the wheel, and thus remove heat from the system. Porosity can be adjusted depending on wheel application by the addition of several additives, with the example of sawdust being a historical solution. However, according to Chitali and Gupta (2007), any other carbonaceous material will suffice. High friction levels during grinding subsequently cause wear, so periodic dressing of the wheel is necessary, normally through the use of synthetic diamond wheels with vitreous (i.e., glass-like) bonds or via electroplated dressing tools which utilise a single layer of the abrasive held in nickel alloy matrix.

Grinding can be categorised into two key areas; Stock Removal Grinding (SRG) and Form and Finish Grinding (FFG). SRG involves removing a lot of material in a short space of time, with the magnitude of the chip thickness being larger and, as such, regular dressing of the wheel is not deemed necessary. However, for this to be the case, certain conditions need to apply such as utilising wheels with large grain sizes (Shaw, 1988; Shaw, 2003). A typical material removal rate for SRG as quoted by Hou and Komanduri (2003) was $733mm^3.s^{-1}$, whilst for FFG, the stock removal rate is far less, in the region of $6mm^3.s^{-1}$. This stands to reason as in FFG, the grinding wheel speeds are much faster in the order of magnitude of $16m.s^{-1}$ - $32m.s^{-1}$, smaller chip thicknesses are observed and regular dressing is therefore needed. Regular dressing is required due to the level of the wheel wear occurring on the tooling and the need for geometrical accuracy to be maintained. Additionally, the work by Oliveira *et al.*, (2009) discussed at length the current state of grinding in terms of cost and other such parameters within the industrial sphere, with key problems with the method still consisting of there being no in-process roughness measurement, automatic thermal compensation of the grinding tool or better predictability of the process. This work was influenced by previous research conducted some time earlier by Wetton (1969) and Keeg (1983).

### 2.2.1 Mechanics of Grinding

Kalpakjian and Schmid (2008) defined the grinding process as a 'chip removal process' that could be differentiated by four factors when compared to other conventional machining methods. The chips formed by grinding differ from the long, thin, chips produced by orthogonal cutting, i.e., they're 'dust-like'. Key process characteristics/parameters as defined by Kalpakjian and Schmid (2008) are outlined below;

i) The individual grains have irregular geometries and are spaced irregularly along the grinding wheel.

ii) The average rake angle ($\alpha$) of the grain is highly negative (i.e., -60° or lower).

iii) The grains on the periphery of the grinding wheel have different radial positions.

iv) The cutting speed of the grinding wheel is extremely high (around 30m.s$^{-1}$). However, slower wheel speeds than 30m.s$^{-1}$ are used when surface finish is not a requirement, i.e., during SRG.

Grinding can also be considered as a material removal process that includes three distinct processes: rubbing, ploughing and cutting (Hou and Komanduri, 2003). Fig. 2.1 (Kalpakjian and Schmid, 2008) details these processes. The total cutting arc length of an abrasive grain within the grinding wheel is shown with $l_k$, whilst the maximum chip thickness is noted as $h_m$. The grinding wheel speed and workpiece feed rate are $V_s$ and $V_w$ respectively, whilst the cutting depth is represented by $a$. Moreover, the resulting process has been thoroughly analysed by several researchers such as Malkin and Cook (1971a), Shaw (1996a) and Rowe (2009), all of whom dictate the governing equations that relate to being able to numerically predict factors such as depth of cut, average chip thickness and average material removal rate.

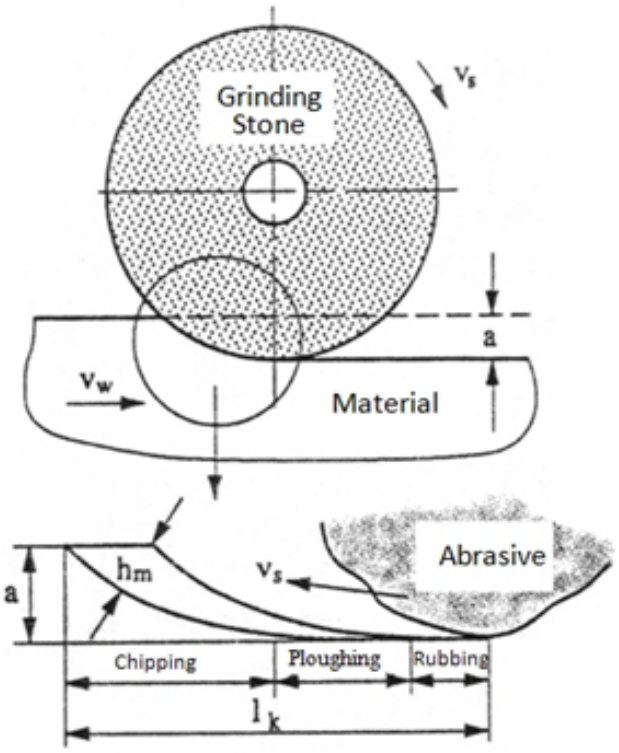



**Figure 2.1:** Schematic of the Grinding Chip Formation Process (Kalpakjian and Schmid, 2008)

#### 2.2.1.1 Chip Length

According to Vinay and Rao (2013), the average chip length, denoted as $l_k$, (mm) and the average material removal rate, $Z_w$ ($mm^3.min^{-1}$), during the grinding process are given in Eqn. 2.2 and Eqn. 2.3, respectively:

$$l_k = \sqrt{a.\phi_s} \qquad \text{(Eqn. 2.2)}$$

and

$$Z_w = a.a_p.V_w \qquad \text{(Eqn. 2.3)}$$

where $a$ is classified as the depth of the cut, (mm), $\phi_s$ is the diameter of the grinding wheel (mm), $a_p$ is the engagement width (mm), and $V_w$ is the feed rate of the workpiece ($mm.min^{-1}$).

Additionally, Vinay and Rao (2013) also stated that when the undeformed chip thickness, $h_m$ (mm), is at a maximum, the force being applied to the grain in the

grinding wheel is at a maximum, whilst the self-sharpening process by the grains within the wheel are observed to behave less coarsely when $V_w$ is decreased or wheel speed, $V_s$ ($mm.s^{-1}$) is increased. This relationship is demonstrated in Eqn. 2.4;

$$h_m = \frac{k_A.V_w}{V_s}.\sqrt{a} \qquad \text{(Eqn. 2.4)}$$

where $k_A$ is the wear coefficient (Archard Constant), as presented by Eqn. 2.5;

$$k_A = \frac{6}{c_g.r_g.\sqrt{\phi_s}} \qquad \text{(Eqn. 2.5)}$$

where, $c_g$ is the number of active grains and $r_g$ is the aspect ratio of the grains.

#### 2.2.1.2 Chip Thickness

Despite the significant work by Vinay and Rao (2013), the estimation of the chip thickness formed during the grinding process has been unpredictable. This has been in part due to the inability to estimate with accuracy the number of contact points being made between the grinding wheel and the workpiece. As described in Fig. 2.1, this total work energy into the system can be separated between rubbing, ploughing and cutting. It has been established for many years that the specific energies involved whilst grinding are much higher than any other machining process. However, Malkin (1989) stated that whilst this is true, a reduction in specific energy can be obtained when the chip thickness of the removed material is reduced. Indeed, this relationship between the specific energy and chip thickness during material removal is called the size effect and was the subject of an intensive key publication by Shaw (1996b).

#### 2.2.1.3 Number of Contact Points

During the grinding process, not all abrasive grains located on the grinding wheel are in contact with the workpiece simultaneously and thus cutting consistently (Vinay and Rao, 2013). As mentioned previously, grinding is made-up of three distinct processes: rubbing,

ploughing and cutting. Due to the nature of these processes, part of the grinding wheel's abrasive grains may not be in contact with the workpiece at all. This obviously has implications when wishing to model the interactions between the grinding wheel and the workpiece. When addressing the specific energies associated with rubbing, ploughing and cutting Malkin (1989) proposed the following relationship regarding the total specific energy within the grinding system, $u_t$, (J.kg$^{-1}$) in Eqn. 2.6:

$$u_t = u_{chip} + u_{plough} + u_{rub} \qquad \text{(Eqn. 2.6)}$$

where $u_{chip}$ is the specific energy lost to the chip formation/cutting, (J.kg$^{-1}$), $u_{plough}$ is the specific energy lost to the ploughing action, (J.kg$^{-1}$) and $u_{rub}$ is the specific energy lost to the rubbing action, (J.kg$^{-1}$).

#### 2.2.1.4 Temperature Mechanics

Due to the nature of FFG, the surface temperature of the workpiece during this grinding process is of greater importance to the final product than that of surface temperature during SRG. However, this is not to say that workpiece temperature during SRG is of negligible importance. For instance, greater levels of surface damage resulting from this initial process has a direct impact on the level of damaged material during finishing which has to be removed. Moreover, it should be noted that the level of tolerances that are required with the finishing grinding method are stricter than during SRG. If workpiece temperature were not considered this could result in localised plastic deformations, over-tempering of the workpiece and thermal cracking. This is in addition to there being much higher specific energies and surface residual stresses in FFG than in SRG (Shaw, 1988). However, ensuring peak workpiece temperatures are kept to a minimum is important for all grinding processes as excessive temperatures have a negative impact on the surface roughness, $R_a$, fatigue life and residual stress profiles of the finished component. It is also important to note that there are both localised and average temperatures acting along the length of the workpiece during the machining process, i.e., localised peaks between the singular abrasive particles and the

average heat induced in the workpiece due to these localised heat profiles. The localised temperature is denoted as $\theta_l$, (°C) whilst $\theta_d$ is the sum of the collective temperatures across the total of the grinding wheel contact region (°C). Fig. 2.2 (Rowe, 2009) demonstrates these profiles.

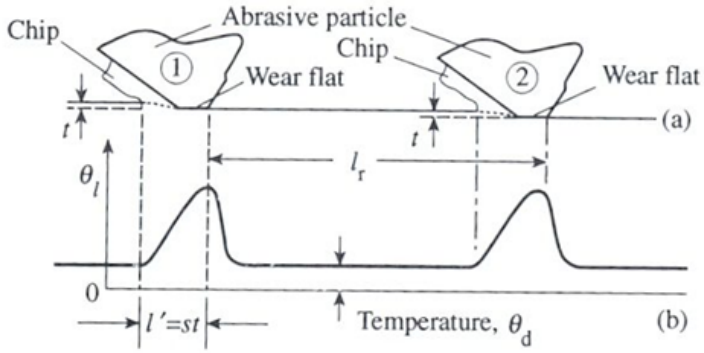



**Figure 2.2:** Local and Total Sum of the Temperature Profiles across a Ground Workpiece (Rowe, 2009)

Grinding temperature predictions are often expressed as a moving heat source function, with different heat distributions that can be used, i.e., triangular or uniform. As most of the thermal energy enters the grinding zone during the grinding operation as proposed by Shaw (1996a), i.e., 80:20 in terms of workpiece to wheel ratio, the temperature distributions can be solved via Bessel functions (Chen and Öpöz, 2016). As such, earlier work by Carslaw and Jaeger (1959) derived predictive formulations regarding subsurface workpiece temperature, $T_{sub}$, (°C) during the grinding process as proposed by Eqn. 2.7.

$$T_{sub} = \frac{2}{\sqrt{\pi}}.\frac{R_{wp}.q_t\sqrt{t_c}}{\sqrt{\lambda_w.\rho_w.c_w}}.e^{\frac{-z^2}{4k_d.t_c}} - \frac{q_t.z}{\lambda_w}[1 - ERF(\frac{z}{2\sqrt{k_d.t_c}})] \qquad \text{(Eqn. 2.7)}$$

where $R_{wp}$ is the energy partition of the total heat flux, $q_t$, (W.m$^{-2}$) to the workpiece within the grinding zone, $z$ is the depth away from the grinding surface (mm), $t_c$ is the total time that the heat source stays stationary at one point within the grinding zone (s), $\lambda_w$ is the thermal conductivity of the workpiece (W.m$^{-1}$.K$^{-1}$), $\rho_w$ is the density of the workpiece (kg.m$^{-3}$), $c_w$ is the specific heat capacity of the workpiece (J.kg$^{-1}$.K$^{-1}$), $ERF$ is the associated error function and $k_d$ is the thermal diffusivity of the workpiece (m$^2$.s$^{-1}$)

which, as Eqn. 2.8 proves, can be expressed as;

$$k_d = \frac{\lambda_w}{\rho_w . c_w} \qquad \text{(Eqn. 2.8)}$$

Additionally, temperature distributions within the workpiece are highly influenced by the Peclet number, $P_e$, which is given in Eqn. 2.9 as;

$$P_e = \frac{V_w . l_h}{2k_d} \qquad \text{(Eqn. 2.9)}$$

where $l_h$ is half the contact zone length (m).

Finally, as the thermal stress induced in the workpiece during grinding causes expansion of the workpiece surface whilst the cooler, subsurface material remains constant, the surface is restricted in its ability to expand. As such, compressive thermal stresses are induced on the surface of the ground workpiece. The elastic stresses are known to be a function of depth into the workpiece, and with thermal stresses also being equal to the elastic stresses as a function of depth, then the thermal stress, $\sigma_T$, can be expressed as Eqn. 2.10 shows;

$$\sigma_T = \frac{1}{1-\nu}[E\alpha_{t-e}T + \frac{1}{d}\int_{\frac{-d}{2}}^{\frac{d}{2}} E\alpha_{t-e}Tdz + \frac{12z}{d^3}\int_{\frac{-d}{2}}^{\frac{d}{2}} E\alpha_{t-e}Tzdz] \qquad \text{(Eqn. 2.10)}$$

where $\nu$ is the Poisson's ratio of the workpiece material, $E$ is the Young's Modulus of the workpiece material (GN.m$^{-2}$), $\alpha_{t-e}$ is the coefficient of thermal expansion, (K$^{-1}$), $d$ is the thickness of the workpiece material (mm), $T$ is the peak workpiece temperature (°C) and $z$ is the distance from the workpiece cutting surface (mm).

#### 2.2.1.5 Cutting Force Mechanics

Much work has been conducted by earlier researchers regarding cutting force mechanics whilst grinding. Hahn (1962) derived expressions for both workpiece MRR as presented in Eqn. 2.11 and tool MRR as presented in Eqn. 2.12;

$$Z_w = WRP_w(F_T - F_{T_o}) \quad \text{(Eqn. 2.11)}$$

&

$$Z_s = WRP_s(F_T - F_{T_o}) \quad \text{(Eqn. 2.12)}$$

where $Z_w$ and $Z_s$ are the material removal rates for the workpiece and grinding wheel respectively ($m^3.s^{-1}$), the $WRP_w$ and $WRP_s$ are the work removal parameters for the workpiece and wheel respectively ($m^3.s^{-1}.N^{-1}$), which was further reinforced by the work of Lindsay & Hahn (1971), $F_T$ is the tangential cutting force (N) and $F_{T_0}$ is the tangential cutting force (threshold) (N). Meanwhile, as also presented by Lindsay & Hahn (1971), the $WRP_w$ is given by Eqn. 2.13;

$$WRP_w = \frac{7.93e^5(\frac{V_w}{V_S})^{0.158}.[1 + (\frac{4a_d}{V_{ds}})].V_s}{\phi_s^{0.14}V_b^{0.147}d_g^{0.13}HRK^{1.42}}\rho \quad \text{(Eqn. 2.13)}$$

where $a_d$ is the dressing depth (m), $V_{ds}$ is the dressing speed ($m.s^{-1}$), $\phi_s$ is the wheel diameter (m), $V_b$ is the percentage volume of bond material present in the wheel matrix, $d_g$ is the grain size (mm) and HRK is the workpiece hardness measured on the Rockwell K Scale.

Furthermore, $d_g$ and $V_b$ are expressed in Eqn. 2.14 and Eqn. 2.15 respectively;

$$d_g = \frac{0.0245}{Grain\ Size} \quad \text{(Eqn. 2.14)}$$

&

$$V_b = 1.33H_n + 2.2S_n - 8 \quad \text{(Eqn. 2.15)}$$

where $H_n$ is the grinding wheel hardness number and $S_n$ is the wheel structure number.

Malkin (1989) expressed the $F_T$ and $F_N$ vectors of the cutting forces as a function of the cutting, ploughing and rubbing force components, which were then simplified when compared against the cutting force approximations derived by Hahn (1962) and Lindsay and Hahn (1971). These are given in Eqn. 2.16 and Eqn. 2.17;

$$F_T = F_{T_{Ch}} + F_{T_{sliding}} \quad \text{(Eqn. 2.16)}$$

&

$$F_N = F_{N_{Ch}} + F_{N_{sliding}} \quad \text{(Eqn. 2.17)}$$

where $F_{T_{Ch}}$ is the tangential chip formation force, (N), $F_{T_{Sliding}}$ is the tangential sliding force, (N), $F_{N_{Ch}}$ is the normal chip formation force, (N) and $F_{N_{Sliding}}$ is the normal sliding force, (N).

Finally, in terms of the cutting forces induced via the grinding process, Aslan and Budak (2014) presented how milling force equations can be used to derive more accurate grinding force expressions as shown in Eqn. 2.18 and Eqn. 2.19;

$$F_{T_{grain}} = K_{T_c} f \sin\theta . a + K_{T_p} . b \quad \text{(Eqn. 2.18)}$$

&

$$F_{N_{grain}} = K_{N_c} f \sin\theta . a + K_{N_p} . b \qquad \text{(Eqn. 2.19)}$$

where $F_{T_{grain}}$ and $F_{N_{grain}}$ are the tangential and normal force components acting on a single grain, (N), $K_{T_c}$ and $K_{T_p}$ are the coefficients for the tangential cutting force and the ploughing force respectively, (N), $K_{N_c}$ and $K_{N_p}$ are the coefficients for the normal cutting force and the ploughing force, (N), both of which are derived empirically, whilst $b$ is the radial depth of cut (mm).

### 2.2.2 Grinding Wheel Systems

Around the turn of the twentieth century, new, synthetic abrasive materials were beginning to emerge for the grinding wheel tooling, such as aluminium oxide ($Al_2O_3$) and silicon carbide (SiC) (Jackson and Davim, 2011). Today, however, even these materials are now becoming outdated as purely synthetic diamond and cubic boron nitride (cBN) wheels are available which are deemed superior when machining difficult to grind materials such as Ti-6Al-4V (Souza and Silva, 2019). However, the use of SiC wheels still remains a suitably cheap and simplistic solution for grinding titanium alloys. Research is also being conducted in the areas of developing more uniform bond structures within grinding wheels and improving control systems which monitor the structure and therefore the manufacture of different abrasive materials. This has resulted in more improved versions of aluminium oxide abrasives, for example. Table 2.1 (Malkin, 1989; Morgan *et al.*, 1998; Spriggs, 2002; Xu *et al.*, 2006; Marinescu *et al.*, 2006) displays a typical comparison between different materials which are used to manufacture grinding wheels.

**Table 2.1:** Comparative Performances of a Range of Different Grinding Wheel Materials (Malkin, 1989; Morgan *et al.*, 1998; Spriggs, 2002; Xu *et al.*, 2006; Marinescu *et al.*, 2006)

| **Property** | **$Al_2O_3$** | **SiC** | **cBN** | **Diamond** |
|---|---|---|---|---|
| Crystal Structure | Hex | Hex | Cubic | Cubic |
| Density, $\rho$, (kg.m$^{-3}$) | 3098 | 3200 | 3480 | 3520 |
| Melting Temperature, $T_{Melt}$, (°C) | 2040 | 2860 | 3200 | 3700 |
| Knoop Hardness, $HK$ | 2100 | 2400 | 4700 | 8000 |
| Thermal Conductivity, $\lambda$, (W.m$^{-1}$.K$^{-1}$) | 30 | 120 | 740 | 2200 |

Rowe *et al.*, (1995) experimentally tested and compared both an alumina and cBN grinding wheel on hardened steel. Measurements included the surface temperature of the workpiece, partition ratio of heat flux transferred to the workpiece and specific energies within the grinding zone. In addition, theoretical models for predicting the partition ratios which also included the heat emission out of the system via the chip formation and coolant were proposed. The two data sets were found to be reasonably accurate when plotted and contrasted. It was found that the cBN wheel induced lower workpiece temperatures (≈27%) and partition ratios (≈33.3%) when compared to the alumina alternative due to its higher thermal conductivity. Although the work was able to develop models for predicting all heat transfer in the system, the experimental data did not consider other metals. Therefore, the accuracy of this approach for different workpiece materials remains uncertain.

The industrial sector has made advances in grinding wheel tooling development in more recent years. This has been a result of the need for longer wheel life tools in light of the increase in the grinding of aerospace alloys such as Ti-6Al-4V. An example of which is the development of the Cubitron II grinding wheel system as reported by 3M (2015). Benefits include precisely shaped grains for improved performance and prolonged wheel life via having a rigid, reinforced, resin bonded wheel structure consisting of a blend of $Al_2O_3$ and precision-shaped ceramic grains.

Ichida *et al.*, (2006) experimentally tested and compared both a conventional cBN wheel (denoted as cBN-B) and a polycrystalline (cBN-U or ultrafine cBN) alternative when grinding a v-shaped groove in a nickel-based superalloy (Nimonic 80A) workpiece via a single pass. Depth of cut and wheel speed were held constant (1.5mm and 30m.s$^{-1}$ respectively),

whilst the feed rate was varied (0.25mm.s$^{-1}$ - 1.0mm.s$^{-1}$). Cutting forces and wheel wear were thus measured. Results indicated that cBN-U wheels experienced less wheel wear and as such, had a higher $G$-ratio ($\approx$ x10 higher than cBN-B wheels). Additionally, cutting forces appeared lower for cBN-B wheels than for cBN-U wheels (20% - 30%). However, the research did not consider developing a predictive model of wheel wear for either type of wheel.

Liu, Chen and Gindy (2008) established experimental research into the grinding of CMSX4 and Inconel 718 superalloys ground with $Al_2O_3$, cBN and diamond grinding wheels. Grinding vibration, cutting forces, spindle power and grinding zone temperatures were thus measured. A Taguchi based experiment was conducted, with $R_a$, $F_N$, $F_T$ and $G$-ratio being the investigated responses. Several optimisation models were developed including those for $Al_2O_3$ and superabrasive grinding wheels during SRG. The depth of cut was varied between 0.01mm and 2.5mm, whilst the feed rate was varied between 500mm.min$^{-1}$ and 2000mm.min$^{-1}$. Additionally, the wheel speed was varied between 30m.s$^{-1}$ and 55m.s$^{-1}$. Results indicated that during SRG, diamond grinding wheels were more efficient than cBN and $Al_2O_3$ grinding wheels across the range of materials analysed. Despite an optimisation method being undertaken regarding grinding wheels, materials and a range of responses, no mention was made of simulating the data presented. Further in relation to Liu, Chen and Gindy (2008), Fig 2.3 details a range of stock removal rates for differing grinding processes (Klocke *et al.*, 2016). It should be noted that despite most of the previous discussion concentrating on nickel-based superalloys (mainly due to lack of available research on grinding Ti-6Al-4V specifically), the two material groups are both considered "hard to grind" substrates which encounter similar problems, i.e., low thermal conductivity as discussed by Jadam, Rakesh and Datta (2020).

Earlier research was conducted by Xu *et al.*, (2003) who analysed the abrasive wear of $Al_2O_3$, SiC and cBN grinding wheels when grinding both titanium alloy TC4 and nickel-superalloy K417. Experimental tests were conducted and the wear of the wheels compared. Results indicated that cBN wheels can increase the maximum possible depth of cut for superalloys ($\approx$76%), whilst still retaining a low workpiece temperature of 100°C.

For the TC4 workpiece, the surface texture appeared to become highly complex as the grinding temperature increased, with scale like markings becoming increasingly obvious up to a maximum at 1000°C. Other findings were that both $Al_2O_3$ and SiC grinding wheels had observable adhesion between the spent abrasive material tooling and the workpiece material. This was proposed to be due to greater chemical interactions occurring within the grinding zone at higher grinding temperatures. Limitations of the work, however, prevented them going further by way of developing a numerical model, as all data collected was experimental.

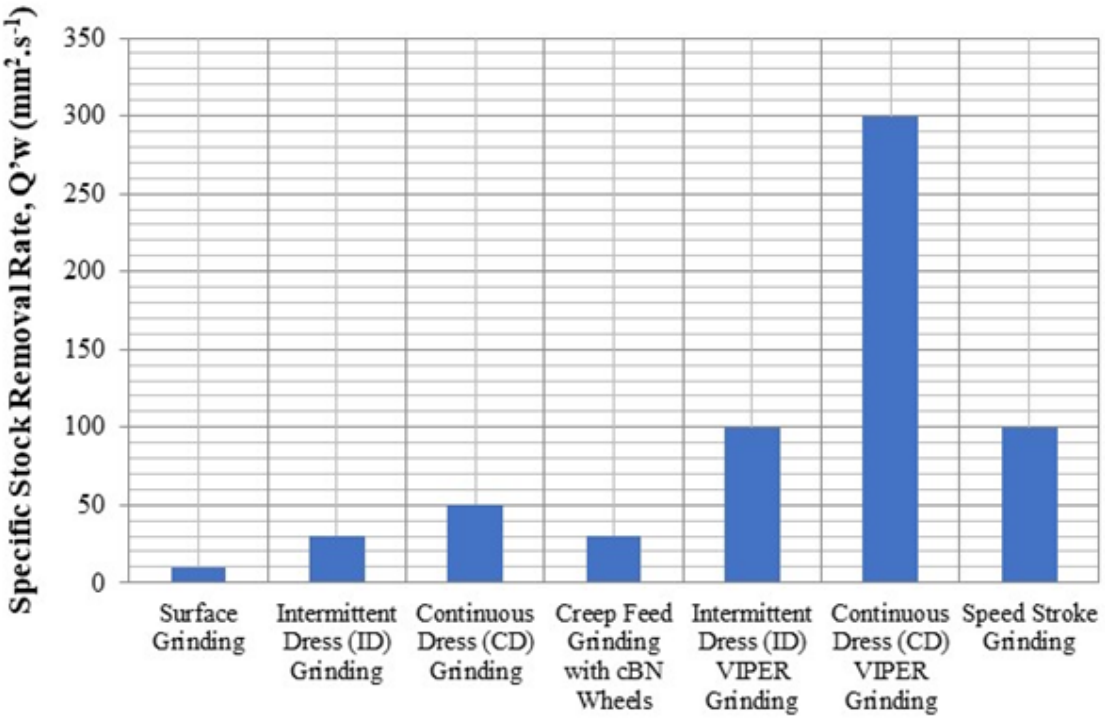



**Figure 2.3:** Comparative Stock Removal Rates for Differing Grinding Processes (Klocke *et al.*, 2016)

### 2.2.3 Coolant Delivery and Application

Normally, the metalworking fluid used within the grinding process is either water or oil based. Coolants are used for several purposes; they produce lubrication between the workpiece and the grinding wheel, in addition to enabling good heat transfer out of the wheel-workpiece system. Again, this is highly dependent on the coolant's specific heat capacity, $c$, and its thermal conductivity, $\lambda$. Table 2.2 (Vashisht and Kapila, 2008) details

these properties including the relevant densities of several water and oil-based coolants, with Methanol/Water combinations being the most effective. Here, EG-water is *Ethylene Glycol*-Water and $PG_1$-water is *Propylene Glycol*-Water. More recent investigations using methanol/ethanol coolants include those by McManus and Haddad (2014) who assessed using methanol coolant when machining aluminium.

**Table 2.2:** Details of Various Oil and Water-Based Coolant Thermal Properties (Vashisht and Kapila, 2008)

| **Property and Coolant** | EG -Water | $PG_1$ -Water | Methanol -Water | Ethanol -Water | Sunflower oil | Synthetic oil |
|---|---|---|---|---|---|---|
| Thermal Conductivity, $\lambda$, ($W.m^{-1}.K^{-1}$) | 0.37 | 0.36 | 0.4 | 0.38 | 0.168 | 0.159 |
| Specific Heat Capacity, c, ($J.kg^{-1}.K^{-1}$) | 3285 | 3400 | 3560 | 3500 | 2300 | 5680 |
| Density, $\rho$, ($kg.m^{-3}$) | 1087 | 1062 | 935 | 927 | 890 | 986 |

However, when grinding titanium alloys such as Ti-6Al-4V, a water-based coolant is preferred (Shaw, 1996a). One reason for this is that the sparks and swarf off the workpiece are hot and are normally covered with the coolant fluid. If the coolant fluid was therefore of an oil-based nature, there is a significant risk for rapid combustion of the swarf to occur, and thus endanger the operator. This is even more pronounced when grinding titanium with current trends moving towards higher wheel speeds and higher coolant supply pressures. Since water-based fluids have a far lower viscosity than oil-based ones, using them in a demanding process like CFG can seriously affect the integrity of the workpiece and shorten the life of the grinding wheel. When utilising a standard nozzle design, this leads to a lower $R_e$ number, which encourages a dispersed jet and necessitates positioning the nozzle as closely as possible to the grinding arc to reduce overspray (Steffen *et al.*, 2005). Several studies have been conducted to ascertain to what extent adding additional additives to the coolant used when grinding aerospace alloys has upon the process. Examples of additives used within coolants include dilute, inorganic salts which have been found to be the most effective in grinding performance improvement.

Irani *et al.*, (2005) reported a bibliography of current and emerging grinding coolant/lubricant trends. This study regarded previous work in the field, and namely considered what factors affect the performance of the fluid such as the design of the nozzle,

the placement of the nozzle and the exit velocities of the fluid. The research also considered solid lubricant and radial coolant streams. Findings suggested that the currently utilised coherent jet nozzles offer the best solution for fluid application, as other designs such as shoe or radial jet nozzles are currently too unstable to be integrated into the production grade grinding process, in addition to the associated increase in cost. Similar suggestions were also made several years earlier by Bienkowski (1993) in terms of the classification of differently available fluid types, i.e., synthetics, semi-synthetics, soluble oils and straight oils.

Work by Webster *et al.*, (2002) considered how effective the application of coolant is during continuous-dress creep feed grinding when monitoring wheel speed and MRR. The flow rate of the coolant was also varied. Results from the study indicated utilising an inclined workpiece whilst grinding yields a more convenient method for identifying parameters which cause surface burn. Secondly, different models for predicting optimum flow rates were compared. However, the study did not compare different coolant variants for analysis.

Hadad and Sadeghi (2012) experimentally evaluated the heat transfer characteristics of Minimum Quantity Lubrication (MQL) in grinding. This was in turn compared against a newly developed thermal model of the MQL approach which did not assume that when the coolant reaches boiling point, the energy partition entering the coolant is zero. Two separate grinding wheels were used (cBN and an $Al_2O_3$ alternative), whilst the volumetric flow rate and supply pressures were varied ($0.0007 m^3.s^{-1}$ - $0.031 m^3.s^{-1}$ and 2bar-10bar respectively). Although some positive results were found, experimental results indicated that MQL cannot achieve the low temperatures found when compared to using conventional, large volume, fluid coolant methods. Additionally, with MQL grinding, the average heat transfer coefficient was lower than when compared to fluid grinding ($900 W.m^{-1}.K^{-1}$ - $1200 W.m^{-1}.K^{-1}$ and $3.7e^4 W.m^{-1}.K^{-1}$ respectively). Conclusions from the study suggested that MQL cooling methods were not as efficient as conventional methods due to the reduced metalworking fluid being present in both the grinding zone and the trailing edge of the tooling. Although an interesting study, the research solely concentrated on steel workpieces.

Sai *et al.*, (2015) considered the effect of Small Quantity Lubrication (SQL) during the grinding process. SQL can be considered a version of MQL, but one whereby a wider range of cutting fluid volumetric flow rate, $\dot{V}$ ($mm^3.s^{-1}$), is considered, i.e., $1ml.h^{-1} < \dot{V} < 1000ml.h^{-1}$. Similar to Hadad and Sadeghi (2012), both computational models, as well as experimental data, were obtained. The numerical model's input parameters were then altered (mass flow rate, supply pressures and stand off distance) to determine the effect of the SQL approach. An alumina grinding wheel was used for the experimental tests, whilst steel was used as the workpiece material. The study found that both an increase in supply pressure and the mass flow rate of the lubricant caused an increase in both the grinding forces acting on the wheel, in addition to the induced residual stress within the workpiece and is therefore something which should be considered when designing experiments. The results also suggested that when utilising SQL, the mass flow rate can be reduced significantly without compromising quality of the surface by using nanofluids. Again, the workpiece material analysed was steel, and so no confirmation can be made regarding whether the same effects would be observed when grinding the Ti-6Al-4V titanium alloy.

Earlier research by Hryniewicz *et al.*, (2000) regarded the flow of the coolant when grinding with non-porous grinding wheels. Experimental tests were conducted on an aluminium grinding wheel whilst a numerical study was also established to verify the physical test data. Test parameters measured included the coolant flow rate and supply pressure through the system, in addition to the coolant retention on the grinding wheel as shown in Fig 2.4 (Hryniewicz *et al.*, 2000). Additionally, the flow profiles of the coolant outside of the grinding zone were also measured, whilst secondary testing used a resin-bonded wheel instead of the initially used aluminium wheel. Results from the study enabled the researchers to claim a critical wheel speed exists for which no fluid can be ejected from the grinding zone, with this value being inversely proportional to the maximum protrusion height of the abrasive grain from the grinding wheel's surface. The amount of fluid which is ejected from the wheel is related to the initial thickness of the fluid on the wheel and the critical thickness of the fluid on the wheel. More research will be needed, however, in

relation to harder to grind materials such as Ti-6Al-4V to determine whether the findings of their research hold for these more complex materials.

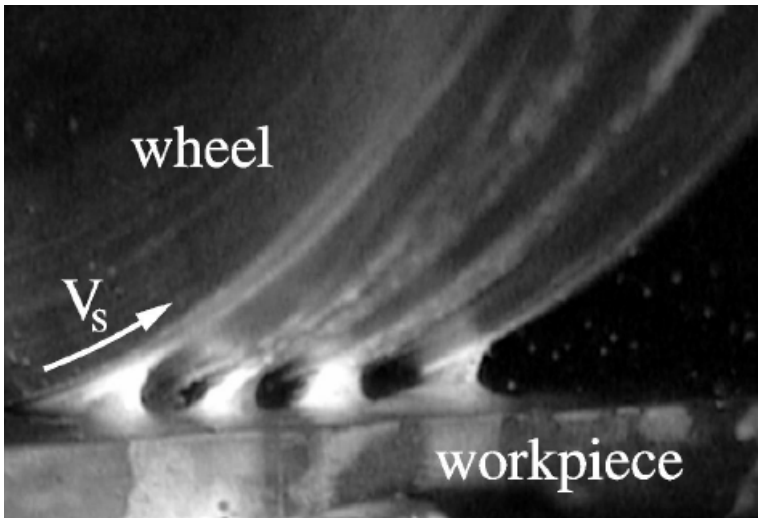



**Figure 2.4:** Coolant Retention Profile on the Grinding Wheel Tooling (Hryniewicz *et al.*, 2000)

Work by Gviniashvili *et al.*, (2004) resulted in the development of a new, numerical model for the coolant within the grinding system. In addition to this numerical model, experimental testing was also undertaken in an attempt to verify the accuracy of the numerical prediction. The reasoning behind developing the new model was that, as it then currently stood, all models representing the grinding process and fluid delivery assumed laminar flow of the coolant. In practice, turbulent flow is seen at the nozzle exit, with vortices often apparent. Two grinding wheels were used; cBN and a knurled aluminium tool. The coolant delivered was a water-based emulsion, whilst the workpiece was carbon. The experimental testing involved altering the mass flow rate of the coolant and wheel speed. Results from the study were significant, with increasing coolant flow rate resulting in an increase in useful coolant flow rate through the grinding zone. However, this relationship was seen to decrease at higher mass flow rates ($\approx$15kg.s$^{-1}$). Additionally, it was also found that an optimum wheel speed of 80m.s$^{-1}$ and nozzle exit velocity of 54.3m.s$^{-1}$ results in an optimal flow rate of the coolant through the system. Although clearly establishing a range of

operating conditions for optimal coolant supply, the study was not conducted on Ti-6Al-4V, so it is still uncertain whether the same coolant delivery process would be optimal for that particular alloy.

Hryniewicz *et al.*, (2001a; 2001b) published two distinct papers on the subject of lubricant application during the grinding process. A numerical method was undertaken via the development of a theoretical model which was subsequently ratified by experimental test data. A non-porous, aluminium grinding wheel was used, which was assumed as perfectly smooth, whilst the coolant volumetric flow rate and wheel speed were varied ($10\text{L.min}^{-1}$ - $11\text{L.min}^{-1}$ and $2.5\text{m.s}^{-1}$ - $30\text{m.s}^{-1}$, respectively). Efforts were made to measure the hydrostatic pressure along the centreline of the workpiece, in addition to the normal force induced on the wheel for a variety of wheel speeds. Part one of the paper concluded that for low Reynolds numbers ($R_e < 300$), Reynolds equation of lubrication (a partial differential expression that describes pressure distributions of viscous fluids) could accurately predict hydrostatic pressures in the system. Part two of the paper was a rework of part one; however, roughness of the grinding wheel was also considered, i.e., a resin bonded diamond wheel was numerically modelled and experimentally tested. Results from the second study indicated that the Reynolds equation was only accurate for a lower Reynolds number than before ($R_e < 100$). Additionally, the roughness model was found to result in a 5% reduction in hydrostatic pressure, despite a 5% increase in flow rate going through the grinding zone. The research also suggested that for $300 < R_e < 1500$, the turbulent model was accurate. Moreover, although a significant contribution to knowledge, the series did not consider either simulation of the grinding process, nor did it conduct research into surface integrity or fatigue life of the ground samples.

Current trends by market suppliers Cool Grind Nozzles Ltd. (2020) reportedly supply several new and innovative nozzle and coolant application methods. Products available include flat and rounded nozzles, rounded (generic) nozzles, specific CFG systems, in addition to the newly developed SpiderGrind system, which automatically relocates the coolant application area to the desired location, taking into account wheel wear.

Gift and Misiolek (2004), conducted research regarding three separate fluid types; a water-based emulsion, a water-based synthetic and an oil fluid. This study assumed a CFG approach of a nickel-based superalloy when all other variables were held constant. A cBN grinding wheel was utilised, whilst an optimised nozzle layout (the initial study had an ≈30° angle aimed at the grinding zone compared to the workpiece centreline) was suggested based on their findings. The grinding wheels were subsequently observed to fail when using water-based emulsions due to increased chip adherence to the wheel which thus caused a severe increase in the cutting forces acting upon the tool. The failed grinding wheels were then compared with the use of a Scanning Electron Microscope (SEM) to determine failure mode. Results displayed signs that the water-based coolant induced greater grinding wheel loading than the oil-based alternative, although it must be noted that no attempt of modelling the grinding zone or the spray distribution of the coolant was considered.

Work has also been extensively covered by several researchers into how cutting fluid is applied to the workpiece being ground, with many suggesting that free-jet nozzles that produce little turbulence and vortices at the nozzle exit are well suited to the process (Brinksmeier *et al.*, 1999; Morgan and Baines-Jones, 2009). This concept has already been accepted by the thermal (oxy-acetylene, oxy-propane, laser and plasma) and non-thermal (abrasive water jet) cutting industries (Valíček *et al.*, 2007; Stanek *et al.*, 2011; Kyas *et al.*, 2011 and Manas *et al.*, 2011).

Research into dry grinding by using graphite as a lubricant has been conducted by Shaji and Radhakrishnan (2002a) and again by Shaji and Radhakrishnan (2003). Their earlier work, Shaji and Radhakrishnan (2002a), considered experimental data obtained through a dry system, a conventional coolant system and a graphite system, where grinding forces, workpiece temperature and surface integrity were the key parameters investigated. Two workpiece materials were employed; a medium carbon steel and bearing steel, whilst the wheel speed and feed rate were held constant at $30\text{m.s}^{-1}$ and $10\text{m.min}^{-1}$ respectively. Results indicated that for all dressing cases the use of graphite as a lubricant resulted in lower cutting forces, lower specific energies and workpiece temperature as shown in Fig 2.5

(a,b and c) (Shaji and Radhakrishnan, 2002a). However, surface roughness quality displayed some variance across the two materials, as well as the wheel wear rate being higher (≈30%) than conventional coolant wheel wear rates at an increased MRR. Further work would have to be undertaken whilst grinding titanium alloys such as Ti-6Al-4V to determine if comparative results are apparent.

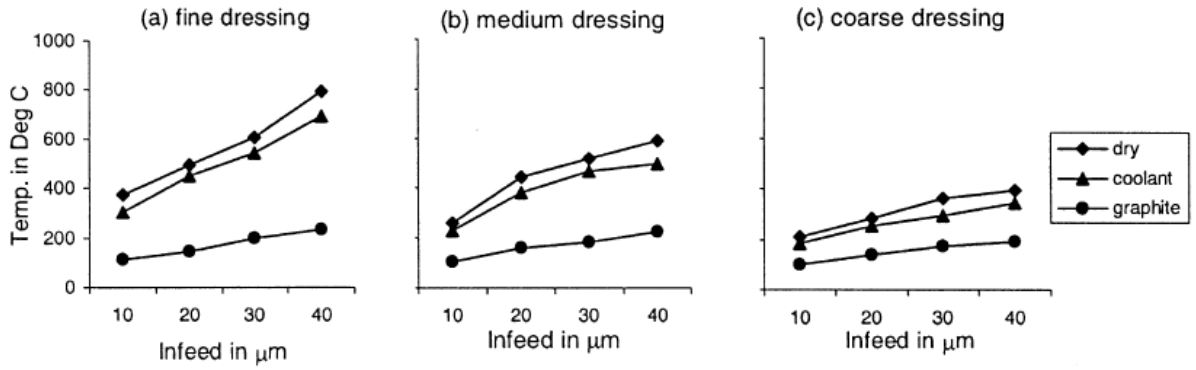



**Figure 2.5:** Workpiece Temperature vs. Dressing Feed Rate (bearing Steel) for fine dressing (a), medium dressing (b) and coarse dressing (c) modes (Shaji and Radhakrishnan, 2002a)

Their later work, Shaji and Radhakrishnan (2003), developed an extensive Taguchi-based Design of Experiments (DoE) test programme to compare graphite and conventional cooling methods. Four factors were chosen as the variables to be analysed (wheel speed, feed rate, in-feed and dressing mode), which were subsequently investigated at three levels within the operating range of the grinding machine. The parameters of interest were $F_T$, $F_N$ and $R_a$. Each of the trials at the three levels were conducted four times to ensure repeatability. The results were then analysed using the normal Taguchi method. Results indicated that for the force components, the in-feed was the most dominant factor, followed by the mode of dressing. For surface roughness, the dressing mode appeared to hold the greatest influence over the response. The comparison between the two coolant approaches also found agreement for the cutting force results; however, the surface roughness varied significantly. Despite a varied study, the research did not consider whether these approaches are suitable when using Ti-6Al-4V or indeed other titanium alloys.

Sadeghi *et al.*, (2009) conducted research into the use of MQL when grinding Ti-6Al-4V, with the primary focus being on the resulting surface quality. An $Al_2O_3$ wheel was used whilst the wheel speed was kept constant at $15m.s^{-1}$. A variety of feed rates were analysed ($20m.min^{-1}$, $30m.min^{-1}$ and $40m.min^{-1}$). Three depths of cut were also compared; 0.002mm, 0.005mm and 0.007mm. Finally, both a synthetic and vegetable oil coolant were altered for the MQL fluid. From the results, an optimal volumetric flow rate ($60mL.hr^{-1}$) and delivery pressure (4bar) were suggested for cutting the Ti-6Al-4V alloy. Also, synthetic oils appeared to offer improved performance over vegetable oils, i.e., lower tangential cutting forces, with the paper's explanation being synthetic oils have good lubricity and film strength and so maintain their integrity at elevated temperatures which reduces friction forces more effectively than vegetable oils. $R_a$ was optimal when using a conventional coolant when compared to synthetic fluids and vegetable oils. Although considering a variety of factors, the study only utilised a single $Al_2O_3$ wheel, and did not comment on cBN or SiC alternatives, for example. Also, as the process was essentially surface grinding (i.e., shallow $a$ values), it remains to be seen if larger SRG processes such as CFG can achieve comparative results when grinding temperatures are higher due to deeper $a$ values being used. Similarly, MQL research has been developed over recent years by the likes of Nadolny *et al.*, (2015), Kalita *et al.*, (2012), Tawakoli *et al.*, (2011), Tawakoli *et al.*, (2010), and Tawakoli and Azarhoushang, (2008).

More recent studies have taken place concerning that of cryogenic cooling; a process whereby liquid nitrogen is used to cool both the tooling and the workpiece (Yildiz and Nalbant, 2008; Manimaran and Kumar, 2013; Reddy and Ghosh, 2014). However, little work has been conducted on its usage when grinding titanium, and, specifically, Ti-6Al-4V. Setti *et al.*, (2014), however, did consider the grinding of the Ti-6Al-4V titanium alloy. Experimental testing was conducted to compare cryogenic cooling against both dry (without coolant) and wet (with coolant) conditions when using a SiC grinding wheel. Normal and tangential forces, surface roughness and surface topography were thus studied. Additionally, regression modelling of the cryogenic process was conducted as it was considered that this method would be the most optimal for the analysis. Results observed a reduction in

tangential and normal cutting forces (12% and 9% respectively) when compared to the other grinding systems studied, with cryogenic grinding being at a minimum on par with wet grinding.

According to Shaji and Radhakrishnan (2002b), historical, conventional fluid lubricants (i.e., water-based emulsions/solutions and oil-based solutions) used during material removal processes are now being reconsidered due to intense environmental and cost effectiveness concerns. Instead, this work determined the effectiveness of using solid lubricants as an alternative. Three distinct options were considered; calcium fluoride ($CaF_2$), barium fluoride ($BaF_2$) and molybdenum trioxide ($MoO_3$). As previously evaluated, studies by the same researchers also considered using graphite as a lubricant (Shaji and Radhakrishnan, 2003). Application of the lubricant was maintained by a pneumatic pump system, whilst the solid powders were altered to become a paste via the addition of both grease and oil. Steel was employed as the workpiece whilst a Carborundum A60L5V10 grinding wheel was used for tooling. Several performance parameters were measured including the grinding forces, workpiece temperature and surface roughness. Additionally, a new design regarding a directly applied solid lubricant was proposed and tested. Results indicated that solid lubricants do have the ability to reduce the surface temperature of the workpiece by between 52.5% and 62.5% when compared against conventional wet grinding when using fine grain sizes. This reduction was observed to lessen, however, as the grain size became coarser. The study also stated that improved results were found from the newly designed grinding wheel despite no empirical data being presented to verify the same temperature reduction observed during their initial study.

De Paiva, de Souza Ruzzi and da Silva (2021) investigated how best to reduce thermal damage when grinding steel, whilst concentrating on the temperature of the coolant used. An $Al_2O_3$ grinding wheel was used for the tooling, with a fixed wheel speed, feed rate and depth of cut of $37 m.s^{-1}$, $3 m.min^{-1}$ and 0.9mm respectively. Four different fluid temperature were assessed; 5°C, 10°C, 15°C and 28°C. The measured parameters post-grinding were $R_a$ via a portable surface roughness tester SJ-201P both parallel and

perpendicular to the grinding direction. The microhardness was also measured up to 300$\mu$m below the ground surface. Finally, the ground sample surface was etched to determine the effect of the fluid temperature upon surface damage. Results indicated that an increase in fluid temperature of 23°C (from 5°C to room temperature of 28°C) resulted in a 40% increase in $R_a$ value. This is to be expected as the cutting fluid temperature is associated with thermal distortions and the underlying material removal mechanism. A lower workpiece temperature reduces the induced distortion which therefore reduces the overall $R_a$ value. Other observations included lowering coolant temperature prevented workpiece burn and lowered the depth of induced microhardness into the workpiece substrate. Again, although an interesting study, it was limited in scope in terms of materials assessed. More research will be required to determine if aerospace grade alloys such as Ti-6Al-4V responds in a similar manner.

### 2.2.4 Importance of Wheel Dressing

As alluded to in section 2.2, dressing of the grinding wheel is important as it has been seen to directly affect the MRR, the cutting forces experienced by the wheel, in addition to the surface quality and integrity of the finished part (Chen, 2002). Dressing also results in a cost-effective approach for regenerating available tooling. Moreover, dressing can be classified into three distinct areas, namely; profiling, sharpening and cleaning. Profiling is the process where the grinding wheel surface is regenerated in both the axial and radial directions; sharpening regenerates the grinding wheel's bond material, and thus re-sharpens the wear-flats induced on the abrasive grits, whilst cleaning involves removing any adhered workpiece and 'used' abrasive wheel material from the cutting surface (Wegener *et al.*, 2011). In addition, the dressing tooling can be either fixed/stationary or rotating in nature. Dressing tools are also usually manufactured from bonded abrasive materials, with bonded diamond being a popular choice. Examples of differing diamond roller-dresser types are electroplated, reverse plated or sintered, with Table 2.3 (Dr. Kaiser, 2012) detailing different diamond profile-roller dresser manufacturing methods, where CVD refers to Chemical Vapour Deposition.

**Table 2.3:** Comparative Manufacturing Methods of Diamond Profile Roller Dressers; (R - Sintered; PG - Reverse Plated; RG - Electroplated) (Dr. Kaiser, 2012)

| **Description** | **Type** | **Manufacturing Process/Bonding** | **Diamond Type Used** | **Edge Protection** | **Application** |
|---|---|---|---|---|---|
| Profile Roller | R | Reverse-sintered with Tungsten bond | Hand Set (H)<br>Random (G)<br>CVD Diamond (C) | Natural Diamond (K)<br>CVD Diamond (C) | Long Tool Life |
| Profile Roller | PG | Reverse-plated with Nickel bond | Hand Set (H)<br>Random (G) | Natural Diamond (K) | Highest Precision/ Fine Profiling |
| Profile Roller | RG | Direct-plated with Nickel bond | Random (G) | CVD Diamond (C) | Pre-Profiling/ Prototyping |

In terms of the grinding of titanium alloys, work conducted during the 1950s by Tarasov (1952) and Yang and Shaw (1955) discovered that the grinding wheel life could be increased, as well an observable improvement in surface finish be achieved, by reducing the grinding wheel speed to one third of the then accepted wheel speed (a reduction to 16.8m.s$^{-1}$). Wegener *et al.*, (2011) discussed the necessity of using a continuous dressing approach during the grinding of alloys such as Ti-6Al-4V. This is due to these alloys being harder to grind, and, as such, wheel wear happens more rapidly, i.e., continuous dressing is more cost effective. The work also concluded that, with the plethora of dressing technologies now available to manufacturers such as traditional mechanical dressing, abrasive water jet and now electric dressing methods such as Electrolytic in-Process Dressing (ELID), ELID dressing appears to offer the best surface roughnesses ($R_a \approx 1n$m), despite its implementation thus far being limited only to high precision grinding applications.

Research by Axinte *et al.*, (2009) studied the dressing of $Al_2O_3$ grinding wheels when using Abrasive Water Jets (AWJs). Two phases of testing were completed; an initial feasibility study as to determine the ability of AWJs to dress $Al_2O_3$ grinding wheels, and a second optimisation study to improve the MRR. The grinding wheel was rotated at a varying angular velocity of between 90rpm and 168rpm. Results indicated a maximum depth of cut up to 10mm could be achieved to manufacture profiled wheels, where each pass had a depth of cut of 0.5mm, and so the study was deemed successful. The optimisation trials utilised an increased depth of cut of 10D (nozzle diameter), which resulted in faster cutting times ($\approx$ x30), and a significant increase in MRR. However, the study did not consider additional wheel materials, such as SiC, for example.

Baseri *et al.*, (2008a) and Baseri *et al.*, (2008b) developed a simulation of the dressing process, as well as an experimental study respectively. An assumed diamond indenter dresser was used for the experimental test when dressing an $Al_2O_3$ wheel, whilst

a subsequent Taguchi based experimental programme was undertaken. The dressing speed ratio ($q$) was varied between 0.1 and 0.95, whilst three depths of cut, $a$, were investigated. Additionally, four different cross feeds ($V_d$) were analysed; 46mm.min$^{-1}$, 96mm.min$^{-1}$, 144mm.min$^{-1}$ and 192mm.min$^{-1}$. Results indicated that at greater speed ratios, there was greater grit fracture. In addition, it was observed that at greater speed ratios, the lower the specific energy. This relationship was similar across all depths of cut studied. Finally, it was determined that the experimental data correlated well with the simulation data (±10%) as shown in Fig 2.6 (Baseri *et al.*, 2008b).

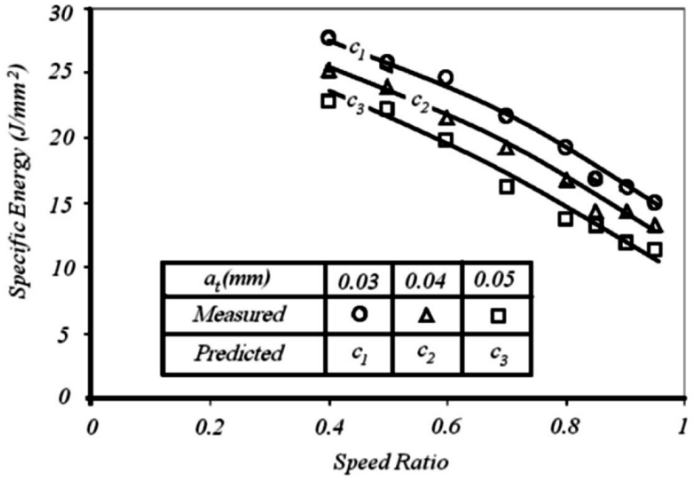



**Figure 2.6:** Specific Energy vs. Speed Ratio Predictions and Test Values (Baseri *et al.*, 2008b)

For more complex geometries like those found in aerospace applications, roller dressers are often used which incorporate random abrasive diamond grits in a metallic bond. Despite this, according to Klocke (2009) and again Klocke *et al.*, (2016), other versions are available where the abrasive diamond grains are more streamlined which display an improvement in dressing performance. Additionally, state-of-the-art dressing methods now exist which utilise lasers (Chen and Feng, 2003) and electrical discharge physics (Curtis *et al.*, 2007).

Linke (2008) developed a numerical prediction of the dressing of a vitrified bonded grinding wheel taking into account the wheel topography as well as the forces and temperature induced whilst dressing occurs. Although useful as a starting point from which to develop more complex visual representations from, the work did not take into consideration the impact energy interaction between the grinding wheel and the dresser unit, and so further work will need to be conducted in this area to further verify the methodology.

A later work by Linke and Klocke (2010) went further by directly measuring temperatures and wheel wear during a dry dressing process on vitrified bonded wheels. Temperature measurement was achieved through the use of a two-colour pyrometer. The heat emissions from within the dressing system were collected via a glass fibre which entered the dresser data logger. The infrared information was then decoded by the pyrometer to yield temperature results within the contact zone. Results from the study indicated that dressing temperatures can reach up to 800°C for dry dressing when using this measurement method and, ergo, it remains clear that lubrication of the dressing process is needed. This was again inferred by the resulting adhesion of the worn grinding wheel and abrasive particulates within the system. Direct temperature measurement using this method for the dressing process was found to be a viable possibility. However, whether the same method can be extended to the material removal process during standard grinding via wear mechanics still remains unanswered.

Rabiey *et al.*, (2012) reported research on the use of lasers for dressing a hybrid cBN grinding wheel which was subsequently compared against dressing with a conventional SiC abrasive. The workpiece chosen was that of hardened steel. For both modes of dressing, the tangential and normal forces were measured. Meanwhile, the wheel speed was held constant at $50\text{m.s}^{-1}$ whilst the cut depth was varied between $10\mu$m and $300\mu$m. The feed rate was also varied between $1\text{m.min}^{-1}$ and $6\text{m.min}^{-1}$. Results from the study concluded that significantly lower specific cutting forces were apparent when using a laser dressing system when compared to a SiC abrasive system across a range of feed rates ($\approx 10\text{N.mm}^{-1}$ for laser assisted dressing versus $\approx 75\text{N.mm}^{-1}$ for conventional methods). Similar trends were also observed for constant material removal rates and constant depths of cut. However, $R_a$ of workpieces ground with laser dressed wheels were within $2.5\% < R_a < 3.5\%$ when compared to conventionally dressed wheels, i.e., $< 0.05\mu$m. Although an interesting technological development, the implementation of the process in industry is not yet viable due to the increased cost of equipment, the research as it currently stands being limited and only a limited range of grinding wheel materials having been analysed using this process.

Maksoud and Wong (2000) developed a method for automatic dressing of a range of grinding wheels, negating the need for an operator to be present. The dressing operation was identical to currently used dressing methods but was guided under a sensory response. The design was based on four key components, namely, a stepper in-feed motor, a mirror

reflective sensor, a dressing motor and a PLC program which was the key controller of the system. Although not theoretically based, the paper was useful when one acknowledges that the down-time of any system does not prove cost effective for industry, so any new, innovative systems which are developed to contrast this are incredibly useful. However, it was not mentioned whether the system was a viable one when grinding notoriously hard to grind materials such as Ti-6Al-4V.

### 2.2.5 Surface Integrity Considerations post-Grinding

In terms of grinding, the biggest factor to affect surface integrity is that of thermal damage (Malkin, 1989; Guo and Malkin, 2000). Thermal damage during grinding occurs when the critical temperature induced in the workpiece is breached. In terms of CFG, Shafto *et al.*, (1975) proposed a critical temperature value of 175°C. Additionally, work regarding thermal damage avoidance whilst grinding has been conducted by Howes (1990). Good surface integrity is vital in terms of other factors such as fatigue strength, fatigue life and corrosion resistance, something originally proposed by Field and Kahles (1964).

Surface integrity in relation to machining processes generally is normally associated with observing the way in which a material alters its properties as a result of the material removal process having taken place. This is a vital consideration that manufacturers must consider whilst performing most manufacturing processes. This is due to the surface integrity having a direct impact on the performance of a component during its in-service lifetime, with the surface finish having a major impact on performance characteristics. The peak-to-valley roughness of the surface, $R_t$, and average surface roughness, $R_a$, for example, can affect the ability for bearings and lubrication to perform at optimal operating conditions, cause wear and ultimately lead to component failure (Ashman, 1987). This area of surface roughness and surface integrity was discussed by Kalpakjian & Schmid (2008), as well as numerous other authors including Childs *et al.*, (2000), Davim (2010), Davim (2011) and Childs, (2013). Additionally, work conducted by Turley (1985), although now somewhat dated, emphasised the importance of maintaining good surface integrity when grinding Ti-6Al-4V workpieces.

Jawahir *et al.*, (2011) delivered a keynote paper in relation to reviewing the current state-of-the-art material removal parameters across the entirety of the machining process industry. The primary emphasis was on how cutting parameters can affect the surface

integrity of the finished workpiece. Several methods for measuring surface integrity were discussed at length, including; diffraction-based methods, micro-magnetic based methods as well as acoustic solutions. A review of the currently available numerical modelling methods were discussed, in addition to a benchmarking programme being undertaken to assess the accuracy of the current state-of-the-art simulation methods. Numerous aerospace materials were considered for the workpiece, including Ti-6Al-4V and nickel-based superalloy Inconel 718. Results from the FE study indicated that modelling of the material removal process under surface integrity criteria is still a misunderstood concept. Current models are oversimplified, resulting in embedded errors often being written into the code, i.e., incorrect assumptions such as boundary conditions, modelling of chip separation and the contact between the workpiece and the tooling. Conclusions from the study also displayed significant variance in stress simulation results for both Ti-6Al-4V and Inconel 718 materials ($\approx$100% and $\approx$170% respectively). Although a comprehensive study involving multiple facets, the effect of changing the wheel material on the subsequent surface integrity of Ti-6Al-4V post-grinding remained unexplored.

More recent work by Yao *et al.*, (2013) considered the affect that different grinding wheels have on the surface integrity of nickel-based superalloy Inconel 718. This study considered both an alumina and cBN grinding tool. Several parameters were measured to assess the performance of each grinding wheel tested, i.e., grinding forces, workpiece temperature and surface roughness. Results indicated that the depth of cut has a direct impact on both the grinding forces (a 65.8% increase for depth of cut increases of 80%) and workpiece temperature (an 81.1% increase for depth of cut increases of 80%). Additionally, the study found that an improved surface roughness can be achieved when using Alumina grinding wheels over that of cBN grinding wheels across a range of wheel speeds, i.e., $R_a$ of 0.38$\mu$m for cBN wheels compared to $R_a$ of 0.25$\mu$m for the alumina wheel. Despite the study considering a variety of parameters, as well as two distinct wheel materials, only one workpiece material was analysed. The study therefore negated to assess whether the same results would be found when evaluating aerospace grade titanium alloy Ti-6Al-4V.

Further studies by Welling (2014) analysed and compared the surface integrity differences between grinding, Electrical Discharge Machining (EDM) and broaching of Inconel 718, which included the surface roughness of the manufactured parts. This particular piece of research was thus conducted under the pretence of turbine blade

manufacturing. The components were then tested via a High Cycle Fatigue (HCF) bending test to determine what affect the surface finish had on performance. SEM inspection of the surface finish indicated that grinding had the smoothest surface with a $R_a$ value of less than $0.2\mu$m. EDM displayed the greatest $R_a$ value of $0.7\mu$m. The maximum bending moment for failure, ($M_b$), was greatest for the ground specimen ($\approx$0.32N.m), whilst the lowest $M_b$ was associated with the EDM specimen ($\approx$0.23N.m). However, the results from all specimens were found to fall within the range of acceptable aerospace industry standards. Limitations of the analysis included only considering a single material for the manufacturing techniques studied. No numerical model was derived for the HCF test, which could have further reinforced the experimentally evaluated data. Interestingly, although somewhat outside the direct scope of this work but related to microstructural changes post-machining, additional research by Koyano *et al.*, (2018) considered temperature measurement during Wire-EDM and surface integrity assessment.

Ulutan and Ozel (2010) reviewed at the length the affect that machining has upon both titanium and nickel superalloys in terms of surface integrity. Several different facets were considered including the type of tooling, material removal process used, current FE trends regarding the material removal process, in addition to what work had previously been conducted via experimental testing. Although not analytical in nature, the paper concluded with the reasoning that issues relating to bad surface integrity when machining aerospace alloys is in part due to the high temperatures experienced during the process, resulting from generally low thermal conductivity of these types of materials, ergo, higher temperatures, ergo, a greater $R_a$ value. Additional conclusions regarding surface integrity resolved that newer tooling resulted in slightly higher $R_a$ values than with slightly blunter tooling. Despite this, the work concluded that as the wear of the tooling become more significant, $R_a$ increases significantly due to the uniformity of the cutting edge. However, this work did not directly consider the grinding process, so a comprehensive review of the current state-of-the-art in this area is needed.

Zeng *et al.*, (2015) considered to what extent the grinding process affects the surface integrity of superalloys. Their work consisted of analysing the iron-nickel GH4169 superalloy which is deemed comparatively new to the market when compared to more common materials such as Ti-6Al-4V or Inconel 718. Experimental tests were conducted on the material with an $Al_2O_3$ grinding wheel, whilst wheel speed, feed rate and the depth

of cut were adjusted at differing levels. Three different measurement parameters were then assessed to determine the surface integrity of the workpiece after grinding, namely; $R_a$, residual stress and microhardness. Surface roughness measurements were achieved via an optical interferometer, residual stresses were determined by X-Ray Diffraction (XRD), whilst the microhardness results were obtained via a microhardness tester. Results concluded that the depth of cut ($a$) and grinding wheel speed ($V_s$) are the overarching parameters which affect the $R_a$ value, i.e., when $a$ was increased by 87.5%, a 68.3% increase was observed for the value of $R_a$. Additionally, external grinding of GH4169 was found to produce advantageous compressive residual stresses in the workpiece, whilst in comparison, conventional grinding of the same alloy resulted in disadvantageous tensile residual stresses. Whilst useful for researchers working in the field of grinding, the work did not consider developing a simulation of the test to determine whether improvements could be made in the experimental testing undertaken. The grinding of this alloy was only conducted with one $Al_2O_3$ grinding wheel and did not consider whether the same results would occur if a cBN alternative was used, for example.

More general work on the surface integrity of Ti-6Al-4V was conducted by Che-Haron and Jawaid (2005) who established to what extent the alloy could be machined when using carbide cutting tooling under dry conditions. Experimental tests were conducted during which a range of feed rates were investigated (45mm.min$^{-1}$, 60mm.min$^{-1}$, 75mm.min$^{-1}$ and 100mm.min$^{-1}$), whilst the depth of cut was held constant at 2mm. Several conclusions were drawn from the research which, although their work did not consider the grinding process, echoed those from previous studies that did consider grinding, i.e., the faster the cutting tool, the greater the surface roughness. This can be explained by the greater magnitude of energy entering the grinding zone, thus causing a vibrational effect between tool and workpiece, or indeed, when using a coarser grain size within the wheel matrix. The $R_a$ values were observed to increase as the tooling neared its end-of-life. Although no research was conducted on the grinding process, the surface integrity response of the Ti-6Al-4V alloy was observed to act in a similar manner as if it were ground. However, more research would have to be conducted to further understand to what extent grinding of Ti-6Al-4V has upon surface finish and burn.

Huang and Ren (1991) conducted studies in an attempt to find the effect that grinding had upon the surface integrity, and hence the fatigue life, of nickel-based superalloy GH33A. The workpiece was firstly machined via rough turning, smooth turning, fine turning

and finally surface ground prior to being tested in both a HCF test and a Low-Cycle Fatigue (LCF) test. The surface roughness from the differing manufacturing processes were recorded, as well as the residual stress and surface hardening response of the workpiece. Results concluded that the grinding of the superalloy resulted in a much lower surface roughness than any other machining method ($0.8\mu\text{m} < R_z < 2\mu\text{m}$), high compressive residual stresses ($550\text{MPa} < \sigma_r < 900\text{MPa}$), and the lowest depth of surface hardening ($35\mu\text{m} < H_m < 65\mu\text{m}$). From the fatigue tests it was subsequently found that an increased surface roughness reduced fatigue life. The paper concluded that grinding of superalloys therefore improves surface roughness and thus fatigue life. Although ahead of their time, the paper's authors did not consider any computational modelling of the fatigue tests or grinding method; neither did they consider the effect of the grinding wheel on the workpiece's $R_a$, or indeed whether a comparative response would be found when grinding Ti-6Al-4V.

Österle *et al.*, (1999) conducted research into what effect surface finish has upon residual stress depths after CFG; in particular, those associated with nickel-based superalloy IN738LC. A factorial experimental programme was conducted with the variables being the wheel material, wheel speed, depth of cut, and with and without coolant supply. Results indicated that for dry coolant systems, high tensile residual stresses (1800MPa) were observed up to $\approx 100\mu\text{m}$ beneath the ground surface when using a Corundum (a crystalline form of $Al_2O_3$) wheel. Other tests whereby coolant was added, high tensile residual stresses were initially shown, before dropping significantly into compressive stress profiles $\approx 5\mu\text{m}$ beneath the surface. Despite the study enabling further data to be gathered in the area of grinding with superalloys, other alloys which are commonly used in the aerospace industry, such as Ti-6Al-4V, were neglected. As such, more research will need to be undertaken to determine whether the findings of the study hold true for other alloys such as Ti-6Al-4V.

Research conducted by Vashista and Paul (2008) analysed the surface integrity when utilising high efficiency, high-speed grinding methodologies. Experimental testing was conducted on a steel workpiece using a cBN grinding wheel. A DoE approach was also used to assess differing independent variables; namely wheel speed, cross feed and feed rate. Results obtained from the research included normal and tangential cutting forces, residual stresses, surface roughness and microhardness. Findings included an increase in feed rate and a reduction in grinding wheel speed lead to an increase in both components of the grinding force, in addition to the specific grinding energy increasing with a reduction in the

maximum depth of cut. However, the work did not consider a range of materials for the workpiece such as Ti-6Al-4V, alternate grinding wheel materials in addition to there being no numerical model proposed.

Puerto *et al.*, (2013) considered the effect that dressing parameters and radial wear of the grinding wheel have upon the surface roughness response post-grinding of steel workpieces. The dressing conditions consisted of two depths of cut, $a$, (0.01mm and 0.02mm), whilst the cross-feeds, $V_d$, studied were 50mm.min$^{-1}$, 100mm.min$^{-1}$, 200mm.min$^{-1}$ and 300mm.min$^{-1}$. The two grinding conditions studied firstly utilised an $a$ value of 0.01mm with a $V_d$ of 10,000mm.min$^{-1}$, whilst the second grinding condition utilised an $a$ value of 0.02mm with a $V_d$ value of 20,000mm.min$^{-1}$. Surface roughness, $R_a$, the grinding forces and radial wear of the grinding wheel were subsequently measured. Results from the study indicated that when utilising less aggressive grinding and dressing conditions, workpiece surface roughness increased as wheel wear increased, whilst more aggressive grinding and dressing conditions observed better surface roughness as wheel wear increased. Despite an interesting study, no mention was made of these claims in terms of titanium alloys, and so additional studies would need to be undertaken to determine the response of Ti-6Al-4V under the same grinding and dressing conditions.

More recent work by Badger, Murphy and O'Donnell (2021) studied the effect that surface grinding of tool steel workpieces with $Al_2O_3$ and cBN wheels had upon the specific energy, wheel wear and surface roughness. The wheel speed, $V_s$, was held constant at 30.2m.s$^{-1}$, the feed rate, $V_w$, was set to 100mm.s$^{-1}$, whilst the depth of cut, $a$, was fixed at 2$\mu$m. Results from the study indicated that better $R_a$ values were achieved when using smaller and sharper abrasive grits than when using bigger and more blunt abrasive grits. Moreover, smaller grits were also observed to produce lower workpiece temperatures, and thus less thermal damage, by up to 30%. Despite an interesting study, the work did not mention whether the same approach would be appropriate in relation to Ti-6Al-4V or additional 'hard to machine' alloys.

Wang and Liu (2020) considered the surface roughness of $\gamma$-titanium aluminide after being milled, with the cutting forces being measured during the machining process. The spindle speeds considered were 60m.min$^{-1}$ and 120m.min$^{-1}$, whilst the feed rates were varied between 0.01mm.tooth$^{-1}$ and 0.025mm.tooth$^{-1}$. The depth of cut was also varied

between 0.1mm and 0.25mm. Results indicated that $V_w$, $V_s$ and $a$ all influence the $R_a$ value of the workpiece. However, the depth of cut was found to be the most statistically relevant parameter affecting $R_a$, resulting in being 45.7% responsible for the total variance. $V_w$ was found to be the second most relevant parameter, resulting in a 32.1% responsibility for the total variance. Although an interesting study, it remains to the seen whether the same relationship would be found when using a Ti-6Al-4V alloy when the grinding operation is applied.

Work by Kekade *et al.*, (2016) considered the effect of delaying quenching on the surface integrity of a Ti-6Al-4V workpiece during face turning. Three delay times were used, namely, 30s, 50s and 70s, whilst $V_w$, $V_s$ and $a$ were held constant at 0.3mm.rev$^{-1}$, 90m.min$^{-1}$ and 1mm respectively. Results from the study found that $R_a$ increased by 22.7% as the delay in quenching time increased. Similarly, the microhardness was found to increase (10.8%) as delay time increased, whilst displaying a 9.5% change in the measured depth below the cutting surface. As such, further work should be undertaken to determine if similar trends are found during grinding.

Ginting and Nouari (2009) explored the surface integrity of dry machined titanium alloys. A dry-milling operation was considered, with the parameters of interest being $R_a$, microhardness and microstructure changes subsequent to the machining process. Two carbide inserts were used; an uncoated and a CVD coated alternative. The tool speed was then varied between 100m.min$^{-1}$ and 125m.min$^{-1}$, whilst the feed rate was varied between 0.15mm.tooth$^{-1}$ and 0.2mm.tooth$^{-1}$. The axial depth of cut was varied between 1.5mm and 2.5mm, whilst the radial depth of cut was held constant at 8.8mm. Results indicated that the CVD coated insert induced a slightly improved $R_a$ value than the uncoated tooling (0.55$\mu$m and 0.65$\mu$m respectively). The measured microhardness trend observed an initial increase below the cutting surface before reaching a maximum, before gradually reducing to the bulk microhardness of the material at 350$\mu$m. This trend was observed for both tools used, and across all feed rates tested. These microstructural changes were observed below the machining surface due to high levels of plastic deformation from the milling process. Again, despite a significant study, further research would need to be undertaken to determine the effect that the grinding process has upon the surface integrity of titanium workpieces such as the Ti-6Al-4V alloy.

More recently, Mathohol *et al.*, (2018) considered the effect of altering process parameters on both the microhardness and material microstructure when dry and flood milling the Ti-6Al-4V alloy. Tool speed, $V_s$, was varied at 120rev.min$^{-1}$, 150rev.min$^{-1}$ and 180rev.min$^{-1}$, whilst the depth of cut, $a$, was varied at 1mm, 1.5mm and 2mm. The feed rate, $V_w$, was held constant across all tests at 4.6mm.min$^{-1}$. Results from the study indicated a clear trend whereby increasing the cutting speed (33.3%) increased the microhardness of the sample (5.6% for dry-milling and 3.8% for flood-milling). The microhardness was observed to reduce as the depth of cut increased whilst dry-milling (2.9%) yet increase with larger depths of cut when flood-milling (3.6%). As such, similar work should be undertaken when assessing the grinding operation to determine changes in microhardness and other surface integrity parameters such as $R_a$, residual stresses and fatigue life.

Additional work was presented by Moussaoui *et al.*, (2013). Their work considered how the milling operation affects the microhardness and microstructure of Ti-6Al-4V workpieces. A Physical Vapour Deposition (PVD) coated carbide tool was used, whilst the cutting speed, $V_s$, was varied between 54m.min$^{-1}$ and 78m.min$^{-1}$. Three depths of cut were used; two 'roughing' cuts of 1.65mm and 2.35mm, and one 'finishing' cut of 0.15mm. Results from the study concluded that microhardness measurement techniques are inadequate when assessing a dual phase $\alpha + \beta$ alloy such as Ti-6Al-4V, and nanohardness measurements should be the excepted standard. This assessment was based on the inconsistency found in the microhardness vs. depth profiles across the range of parameters tested. Nanohardness measurements on ground Ti-6Al-4V samples would prove an interesting study to add to the literature in regards to grinding.

Although considering a nickel-based superalloy (IC10), Zhang *et al.*, (2021) investigated how CFG affects the surface integrity and fatigue life of given workpieces. A white and pink fused $Al_2O_3$ wheel were utilised as the tooling for the grinding tests. Both the cutting forces and grinding temperatures were measured with a dynamometer and semi-artificial thermocouples respectively. The wheel speed was then varied between 10m.s$^{-1}$ and 30m.s$^{-1}$ whilst the feed rate was varied between 100mm.min$^{-1}$ and 300mm.min$^{-1}$. Additionally, the depth of cut was varied between 0.3mm and 0.7mm. Results indicated that $R_a$ increased with feed rate and depth of cut (50.7% and 40% respectively), whilst wheel speed displayed a more varying response. The induced maximum microhardness depth appeared to generally decrease from the ground surface into the workpiece material for

increases in wheel speed and depth of cut. However, varying the feed rate indicated a more inconsistent response. Slower wheel speeds appeared to result in a higher microhardness value than faster wheel speeds, in addition to deeper depths of cut indicating the same trend. The fatigue life of the specimens also indicated to be inversely proportional to $R_a$ and directly proportional to microhardness depth. Although considering a state-of-the-art, high temperature resistant alloy, no reference was made to titanium alloys, and as such no critique of how the Ti-6Al-4V alloy would react under the same grinding parameters was made. This work has been reinforced by the earlier work of Maroju and Jin (2017), who conducted research into how vibration assisted grinding affects the residual stresses induced in the Ti-6Al-4V alloy. Similar later works include Ding *et al.*, (2020) who evaluated the effect of phase transition on residual stress when microgrinding and Li *et al.*, (2015) who considered the effect of the depth of cut on residual stresses when milling the thin-walled, aluminium alloy AL2024-T3 which is commonly used for aerospace applications.

Contrasting work has also been conducted by Naskar, Choundhary and Paul (2020) regarding SEM after grinding Ti-6Al-4V. Here, the surface integrity in relation to surface redeposition of the wheel's abrasive grits post grinding were evaluated. The experimental test programme consisted of two electroplated cBN grinding wheels which were tested at 20m.s$^{-1}$, 30m.s$^{-1}$ and 60m.s$^{-1}$. The feed rate of the workpiece was kept constant at 4m.min$^{-1}$. Different cooling methods including MQL (neat oil and emulsion water), MQL (soluble oil and emulsion water) and flood cooling were tested. The flow rate for the coolants were 5L.min$^{-1}$. Images were taken at two positions for each wheel. A total area of 12mm$^2$ for each wheel surface were then subsequently evaluated. Results indicated that surface redeposition was more prevalent in both flood and MQL (soluble oil and emulsion water) cooling modes than during MQL (neat oil and emulsion water). Although an interesting study, no usage of SEM was undertaken to assess subsurface damage of the ground Ti-6Al-4V workpieces. Studies undertaken by de Mello *et al.*, (2015) assessed Ti-6Al-4V when using varying coolant methods. A white $Al_2O_3$ wheel was utilised, whilst the feed rate, wheel speed and depth of cut were kept constant (6.8m.min$^{-1}$, 35m.s$^{-1}$ and 10$\mu$m respectively). Both a flooded approach and a MQL approach were thus evaluated via SEM. Results indicated that for both cooling modes, microcracks could be observed parallel to the grinding direction. It should also be noted that this same phenomenon could also be observed to propagate perpendicular to the grinding direction. This was claimed to be due to combined thermal, mechanical and chemical factors resulting from the process, i.e.,

higher workpiece temperatures result in greater levels of plastic deformation. Additional observations included adhered blunted grinding wheel grains upon the ground surface. The authors claimed that this was a result of higher grinding forces being apparent.

Xi *et al.*, (2021) assessed the performance of CFG of $\gamma$-TiAl when using diamond and cBN tooling. Here, the workpiece was tested using feed rates of 150mm.min$^{-1}$, 300mm.min$^{-1}$ and 600mm.min$^{-1}$, whilst the depth of cut was varied at 0.9mm, 1mm and 1.2mm. The wheel speed was kept constant at 30m.s$^{-1}$. Grinding forces were measured using a piezoelectric dynamometer, whilst the subsequent surface integrity was also evaluated using SEM. Results from the study indicated that the ground surface had a mixture of grinding striations, both even and some uneven portions and microcracking as previously reported by de Mello *et al.*, (2015). When assessing the metallographic structure of the workpieces, the recrystallized layer, white layer and severe plastic deformations were observed, in some cases forming up to approximately 10$\mu$m into the samples before reaching a maximum depth of 2010$\mu$m. Despite being a highly interesting study, no direct comparison could be drawn between the plastic deformation which occurs during grinding and the associated grinding temperature. Further research should therefore be considered within this area in future.

### 2.2.6 Grinding Operations

There are many varying methods and iterations in which the grinding process can manifest itself. Some examples include the finishing process, such as surface grinding, whereby the depth of cut, $a$, is low and the feed rate, $V_w$, is fast, and larger stock removal processes such as CFG where depths of cut are high but feed rates are slower. Further examples and a more detailed description of some of these grinding operations are discussed below.

#### 2.2.6.1 Creep Feed Grinding

Creep Feed grinding (CFG) is categorised by slow feed rates which thus allows for deep depths of cut to be made (Rowe, 2009). According to Andrew *et al.*, (1985) CFG is regarded as SRG, and has ultimately materialised to combine both the conventional machining operation and the grinding operation into one. In terms feed rate values, a $V_w$ range of between 150mm.min$^{-1}$ and 600mm.min$^{-1}$ are typical, whilst depths of cut, $a$, range from 1mm to 10mm.

In terms of superalloys, Sunarto (2001) conducted research into CFG of nickel-based superalloy nimonic 80A when using a variety of cBN grinding wheels. The depth of cut was held constant at 2mm, whilst the grinding wheel speed was fixed at 2600m.min$^{-1}$. The feed rate was then varied between 15mm.min$^{-1}$ and 30mm.min$^{-1}$. Results from the study indicated a clear relationship between an increase in cutting forces with an increase in feed rate; a rise of 46.6% for $F_T$ and 87.5% for $F_N$. Despite a state-of-the-art grinding wheel being experimentally tested, the authors were unable to replicate their findings via a numerical model representation.

Ding *et al.*, (2010) conducted research into the possibility of using brazed cBN grinding wheels when CFG the nickel-based superalloy K424, commonly utilised for turbine blades. The workpiece was subsequently experimentally tested using wheel speeds varying between 15.5m.s$^{-1}$ and 25m.s$^{-1}$, whilst the feed rate was varied between 100mm.min$^{-1}$ and 400mm.min$^{-1}$. The depth of cut was also altered between the limits of 0.08mm and 0.2mm. The grinding wheel was dressed using a diamond tipped dresser prior to testing. The normal and tangential forces acting on the tooling, as well as the surface temperature and microhardness of the workpiece were then measured and assessed. It was found that although the specific grinding energy can reach values of between 200J.mm$^{-1}$ and 300J.mm$^{-1}$, the actual surface temperature within the grinding zone remained at approximately 100°C. Both $F_N$ and $F_T$ were observed to increase with an increase in feed rate yet decrease with an increase in wheel speed. Additionally, the compressive residual stress induced in the workpiece was found to decrease as a function of the depth of cut, altering from a highest residual compressive stress of -300MPa ($x$ direction) for a 0.08mm depth of cut, to a lowest residual stress of -40MPa ($x$ direction) for a 0.2mm depth of cut; a change of 86.6%. This study was a useful contribution to the open literature; however, the paper did not discuss whether other aerospace materials such as Ti-6Al-4V would behave in the same manner.

Bhaduri *et al.*, (2012) experimentally tested the use of Ultrasonic Assisted (UA) grinding of Inconel 718 with an $Al_2O_3$ grinding wheel. Wheel speed, $V_s$, feed rate, $V_w$, and both an UA and none-UA grinding method were thus compared. Findings from the study indicated that the use of UA grinding resulted in a reduction in cutting forces (≈18%) and an improved $G$-ratio (7% < $G$-ratio < 45%). Despite the study indicating that UA grinding results in improvements, only one alloy was analysed with no reference made to Ti-6Al-4V. Additionally, no predictive model was developed for more efficient assessments of

alterations in input parameters such as workpiece material. Further work by Bhaduri *et al.*, (2013) conducted additional research regarding UA-CFG using Inconel 718. Experimental testing via a full factorial DoE approach was conducted which included comparing the tests with and without UA. An alumina grinding wheel was used, whilst the wheel speed and feed rate were fixed at 30m.s$^{-1}$ and 600mm.min$^{-1}$ respectively. Results from the study elucidated that both the normal grinding force ($F_N$) and tangential grinding force ($F_T$) were significantly lower when using UA; 28% and 37% respectively. Additionally, a lower $G$-ratio of between 30% and 60% was also observed. An increase in the UA amplitude reduced both $F_N$ and $F_T$ by 30% and 43% respectively, although a 24% increase in $R_a$ was subsequently observed. Despite the work being novel, no numerical model was alluded to in the study, with the author believing a further vibrational analysis of the experimental tests would help to determine the accuracy of the results presented. Moreover, additional work by Bhaduri *et al.*, (2017) investigated UA grinding of gamma-titanium aluminide, Nik *et al.* (2012), considered UA of Ti-6Al-4V, whilst Paknejad *et al.*, (2017) assessed workpiece temperature distribution during UA-CFG.

More recently, Tooling and Production (2014) published an industrial online article relating to the current resurgence of Continuous Dress Creep Feed Grinding (CDCF), especially for turbine blade applications. This renaissance has thus been a result of increased power deliverable to the spindle, with current models located in the range of 50kW up to 112kW.

#### 2.2.6.2 Speed Stroke Grinding

Speed Stroke Grinding (SSG) is typified by high grinding wheel speeds (≈160m.s$^{-1}$) and feed rates (≈200m.min$^{-1}$), in addition to shallow depths of cut. SSG also involves a shorter arc contact length than other grinding modes available (Klocke *et al.*, 2016).

Recent advances regarding SSG research has been conducted by Zeppenfield (2006) who concentrated on the SSG of $\gamma$-titanium aluminide. Numerical models were developed in relation to tool wear, mechanical and thermal energies in the grinding zone, in addition to crack propagation predictions. For comparison, experimental tests were undertaken to assess the numerical metonyms. The study utilised a vitrified diamond grinding wheel, whilst a water-based emulsion was used for the coolant. Results from the study indicated that a reduction in the depth of cut, at the same time as increasing the feed rate, resulted

in a decrease in grinding wheel wear. Above what they deemed the 'critical feed rate' ($V_w$ $\approx$ 120m.min$^{-1}$), the opposite effect was observed, i.e., tool wear was observed to increase. Ultimately, the study was found to achieve a good comparison between both the analytical and experimental data. Additionally, compressive residual stresses were found to be induced in the workpiece as a result of faster feed rates e.g. $\sigma_{comp}$ = -630MPa at the maximum $V_w$ of 200m.min$^{-1}$. However, the study only developed a numerical model of the process, and no visualised representation was presented.

Linke *et al.*, (2011) considered the effect that SSG has on sustainable manufacturing. Experimental tests were carried out on hardened steel, whilst a cBN grinding wheel was used for the tooling. A dynamometer was used to measure the tangential and normal forces, with the feed rate, $V_w$, and the wheel speed, $V_s$, being varied (12m.min$^{-1}$ < $V_w$ < 180m.min$^{-1}$ and 80m.s$^{-1}$ < $V_s$ < 160m.s$^{-1}$, respectively). The specific material removal rate, Q'$_w$, was held constant at 40mm$^2$.s$^{-1}$. Results from the study inferred that a reduction in production time can be easily achieved through an improved 'right first time' approach via FE methods, in addition to improved process sustainability. Also, by combining SSG and an additional high-speed machining method, there was a decrease in grinding power, grinding energy and tool wear. Lastly, the study found acceptable results of the finished component surface integrity (residual stress and surface roughness), with a reduction in the amount of coolant used, i.e., a direct impact on the improved sustainability of the grinding process. Although an interesting study, there was no mention if production times could be shortened when using aerospace grade alloys such as Ti-6Al-4V under the same operating conditions, as the work only considered steel as the workpiece material.

#### 2.2.6.3 High Efficiency Deep Grinding

High Efficiency Deep Grinding (HEDG) is the natural successor to CFG, using much faster grinding wheel speeds (80m.s$^{-1}$ – 250m.s$^{-1}$) and feed rates (0.5m.min$^{-1}$ – 10m.min$^{-1}$) (Rowe, 2009). HEDG also has additional benefits over CFG and SSG as the specific material removal rate, Q'$_w$, is extremely high ($\approx$1200mm$^2$.s$^{-1}$). HEDG displays lower specific energies when compared to other grinding processes; a distinct difference as grinding normally embodies high specific energies in the range of 30J.mm$^{-1}$ to 90J.mm$^{-1}$ (Ghosh *et al.*, 2008). Lower specific energy values result in lower surface temperatures within the grinding zone, partly due to more heat being removed by thicker chip thicknesses (Jin *et al.*,

2002). Despite these improvements, HEDG has significant requirements to operate at full efficiency, i.e., high coolant flow rates and supply pressures to ensure a clean grinding surface is maintained, increased power delivery to the machine to maintain a vast MRR, as well as designing a stiff enough system to diminish high vibrational amplitudes when grinding at significant wheel speeds ($\approx$160m.s$^{-1}$).

This was alluded to by Tawakoli *et al.*, (2012). Their work consisted of studying both the static and dynamic responses of the grinding wheel during HEDG. Two cBN grinding wheels were used with the central hub of the wheel was altered (1 steel, 1 CFRP), to determine differences in vibrational performance whilst subsequent experimental tests were undertaken. Results indicated that for the same depth of cut ($a$ = 0.1mm), the steel hub induced a much lower $R_a$ value ($\approx$1$\mu$m) than the CFRP hub value ($\approx$4.5$\mu$m). Whilst the feed rate ($V_w$) and depth of cut ($a$) were held constant, the CFRP hub induced a lower normal force ($F_N$) than the steel alternative ($\approx$100N less). Despite interesting and state-of-the-art research, no indication of a numerical model was alluded to, as well as there being no mention of whether the same results would be achieved when grinding either Ti-6Al-4V or advanced titanium alternatives.

Liu *et al.*, (2007a) conducted research into the cost viability of HEDG of a steel and nickel-based superalloy workpiece when using $Al_2O_3$, cBN superabrasive and diamond grinding wheels. Specifically, the work conducted a multi-optimisation approach when using performance indices, e.g., $R_a$ and $G$-ratio for both roughing and finishing grinding operations. An overall performance index also included relevant 'weighting' coefficients for both processes. Their rationale was that this could then easily be applied to the grinding of turbine blades as both processes are used during their manufacture. An experimental investigation was also undertaken to compare CFG and HEDG of the workpieces using the same grinding wheel materials assessed numerically. The grinding wheel speed was varied up to a maximum of 60m.s$^{-1}$, whilst the depth of cut and feed rate were varied between 0.01mm and 2.5mm, and 500mm.min$^{-1}$ and 2000mm.min$^{-1}$, respectively. Several factors were then analysed such as $G$-ratio, the grinding forces and the workpiece surface temperature of the different systems. Workpiece surface temperature measurements were observed to vary considerably between the differing wheels that were analysed, with cBN wheels causing a 600°C surface temperature, compared to over 1000°C for an $Al_2O_3$ system. Results also indicated that water-based coolants were unsuitable when using cBN wheels

for grinding nickel-based superalloys, yet are suitable for usage with $Al_2O_3$ and diamond grinding wheels. Other observations included diamond having advantages over other wheels in terms of performance-to-cost ratio. Moreover, this research was furthered by their later work, Liu *et al.*, (2007b), Liu, Chen and Gindy (2008) and Liu *et al.*, (2008).

## 2.3 Grinding Ti-6Al-4V

Teicher *et al.*, (2006) conducted experimental testing on the grinding of Ti-6Al-4V when using superabrasive wheels exclusively, whilst Teicher *et al.*, (2008), conducted experimental testing on the grinding of Ti-6Al-4V when comparing both diamond and cBN wheels. The earlier study considered the performance of the coolant which was monitored with an evaluation of the grinding forces induced on the tooling, chip formation and tool wear being undertaken. Wheel speed, feed rate and the depth of cut were kept constant ($16\text{m.s}^{-1}$, $2\text{m.min}^{-1}$ and $10\mu\text{m}$ respectively) whilst several coolant systems were investigated (dry, liquid nitrogen, emulsion and oil). The study found that the use of liquid nitrogen, (i.e., cryogenic cooling) was not as optimal as the use of the traditional emulsion based coolant, with the chips formed being observed to adhere to the grinding wheel. There was also a limited reduction in cutting force magnitude when compared to dry grinding conditions ($\approx$12.5%). Additionally, it was found that cryogenic cooling cannot replicate the same levels of lubrication between the grinding wheel and the workpiece that conventional coolants can, and thus higher cutting forces of $\approx$33.3% were observed. This is contradictory to the results presented by Setti *et al.*, (2014), who demonstrated that the tangential cutting force reduced by 26.5% when using cryogenic cooling over that of other cooling modes tested (dry and soluble oil). It was surmised that this finding was due to the cooling mist surrounding the wheel's surface, which provided improved slippage between the wheel and the workpiece.

Work conducted by Ohkubo *et al.*, (2000) considered the machinability of commercially pure titanium, ASTM grade 2, Ti-6Al-4V, a gold (Au) alloy and a cobalt chromium (CoCr) alloy. Experimental tests regarding surface microgrinding were conducted using wheel speeds of 15000rpm and 30000rpm applied to two rotary burrs of 2mm in diameter. Results

of the Vickers hardness tests conducted on the workpieces were then analysed with SEM images also taken of the chips formed from each machining process. Results from the study indicated that for both titanium alloys, a significantly higher microhardness was observable post-machining than from the other materials investigated. This is due to Ti-6Al-4V work hardening at low temperatures in the region of <500°C as quoted by Teicher *et al.*, (2008). Additionally, the chip formation from Ti-6Al-4V appeared less pronounced than those from the ASTM grade 2. Readings also confirmed other well-established results such as faster cutting speeds resulted in a quicker MRR and higher cutting forces. However, no numerical data was presented for each alloy tested in terms of the induced grinding forces.

Wang *et al.*, (2014) analysed the effect that UA operations have when grinding titanium alloys. The experimental work considered what effect the UA process had upon the MRR, surface topography and roughness, in addition to the associated cutting forces. Wheel speed, vibrational frequency and depth of cut were amongst the variables altered. Results indicated that increasing vibrational frequency of the grinding wheel led to lower cutting forces across the same range of depths of cut and feed rates. Related further work on UA grinding has been conducted by Brehl and Dow (2008) and Nik *et al.*, (2012), and in more recent years; Zhou *et al.*, (2020), Zhu *et al.*, (2020) and Wen *et al.*, (2019).

## 2.4 Grinding other Titanium Alloys

Other work also considered the grinding of $\gamma$-titanium aluminide alloys such as those by Bentley *et al.*, (1999) and Bentley *et al.*, (2001). The later research detailed the changes in cutting force when altering grit size, depth of cut, wheel grade and wheel porosity. The effect of machining $\gamma$-titanium aluminide in terms of fatigue strength post-grinding was also considered. The samples were subsequently surface-ground using a standard SiC grinding wheel. Results included an observable relationship between the depth of cut and cutting force. Additionally, no microstructural changes were noticed when grinding $\gamma$-titanium alloys. The study also concluded that there could be a potential reduction in the fatigue life of the ground part despite there being no microstructural changes present. Similar to other works, no mention of numerical predictions to support the experimental findings were made.

Stone and Kurfess (2007) compared experimental data results with theoretical modelling results for titanium aluminide subsurface damage after grinding. Mathematical models relating to the workpiece temperature induced within the grinding zone and subsurface damage models were derived. Experimental work was undertaken and compared against the results pertaining to the predicted models. The theoretical and experimental data proved viably close to assume a positive response from this methodology. However, only one material was used in the study, so it is still unclear whether this approach would suit other titanium alloys such as Ti-6Al-4V.

Testing of advanced titanium alloys has been available throughout the literature for decades, as is demonstrable through such works by Hood *et al.*, (2007a). Experimental work was undertaken to determine to what extent altering grinding wheel material, wheel speed, depth of cut and feed rate had upon $\gamma$-titanium aluminide. Results indicated that softer grinding wheels produced the lowest $G$-ratios and more porous wheels decreased the likelihood of surface burn due to an improved coolant delivery; a finding which was in accordance with the work by Irani *et al.*, (2005). However, no numerical modelling of the experimental tests were presented. An additional work in the same year by Hood (Hood *et al.*, 2007b) detailed the differences between $\gamma$-titanium aluminide and burn-resistant titanium. Again, experimental testing was undertaken altering wheel speed, (15m.s$^{-1}$ - 35m.s$^{-1}$), feed rate, (150mm.min$^{-1}$ - 600mm.min$^{-1}$) and depth of cut (1.25mm - 5mm). Results suggested that at lower operating parameters, crack-free components could be achieved. Other results indicated that the $\gamma$-titanium aluminide alloy was easier to grind than the burn-resistant titanium grade with higher $G$-ratios of x10, 28% lower tangential cutting forces in addition to on average a 15% lower surface roughness value being induced.

Beranoagirre and Lopez de Lacelle (2013) also considered the grinding of titanium aluminide alloys. A review of the principles of grinding, as well as the variety of abrasive materials available, were also presented. An experimental test programme was also undertaken to determine how surface roughness after grinding varied with feed rate for three different workpiece materials; a molybdenum copper silicon alloy (MoCuSi), Ti-6Al-4V and a TNB alloy. The grinding tests also utilised three corundum $Al_2O_3$ grinding wheels at varying coarseness. Results inferred that surface finish varied with changes in feed rate. Secondly, a finer grain size resulted in an improved surface roughness response. Despite the experimental data, no data relating to numerical modelling from which to

draw a comparison were discussed. Moreover, these findings can be explored further when contrasting the two different material properties. $\gamma$-titanium is observed to have a higher $\lambda$ value ($\approx$22W.m$^{-1}$.K$^{-1}$) against Ti-6Al-4V ($\approx$6.9W.m$^{-1}$.K$^{-1}$). This is in addition to the room temperature ductility of $\gamma$-titanium being $\approx$2% against Ti-6Al-4V being $\approx$20% thus resulting in Ti-6Al-4V being more difficult to grind (Hood, 2010; Chestnut, 1992).

## 2.5 Grinding Modelling Methods

Two different approaches for modelling the grinding process are discussed. The methods as entitled in this thesis are i) Classical Numerical Solutions (CNS), and ii) Dimensional Analysis (DA). The CNS approaches detailed in section 2.5.1 are classical, equation-based solutions for workpiece temperature and cutting force prediction, whilst section 2.5.2 details DA solutions gleaned through assessing the grinding process from a base unit quantity approach.

### 2.5.1 Classical Numerical Solutions

Two earlier works by Tönshoff *et al.*, (1992) and Mackerle (1999) discussed and compared the many different numerical modelling approaches relating to the grinding process. Modelling of differing outputs discussed included topography, chip thickness, cutting forces and energy predictions amongst others. However, the research was solely analytical, and no experimental data was supplied for verification.

Later work by Durgumahanti *et al.*, (2010) developed an improved theoretical model for determining normal and tangential cutting forces whilst grinding. The model also incorporated the often neglected ploughing force to improve overall accuracy of the predicted result. This was discovered to increase the cutting force response by 15%-17% on average. An experimental test programme was also undertaken to ensure that a comparison could be drawn between the predicted and physical data. The study found good agreement between the two data sets as demonstrated in Fig 2.7 (a,b, c and d), with a 10.28% error in average normal cutting force per unit width, and a 7.87% error in average tangential cutting

force per unit width. This was attributed to the fact that the model incorporated a varying coefficient of friction value as the wheel speed and feed rate were varied; something which had previously been modelled as constant.

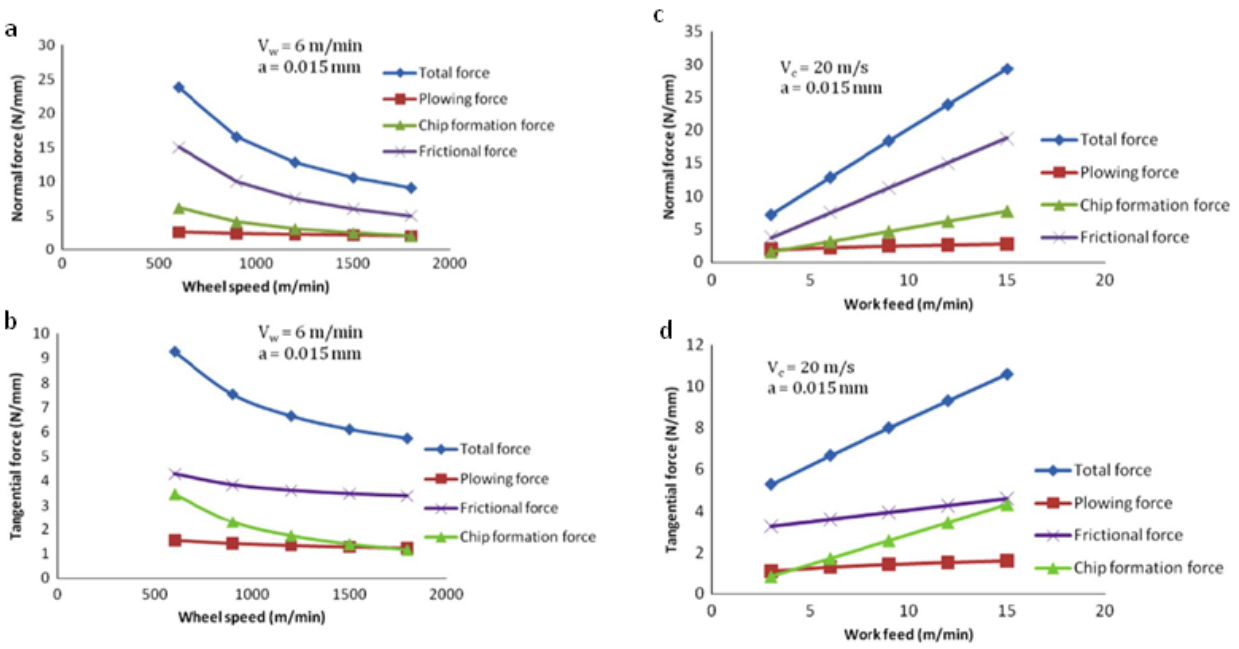



**Figure 2.7:** Numerical and Experimental Normal (a, c) and Tangential (b, d) Cutting Force Model with Ploughing Force Component (Durgumahanti *et al.*, 2010)

Hou and Komanduri (2004a) published a detailed work regarding a thermal analysis of the grinding process. Three separate model types were discussed and analysed; namely the local, the global and finally a combination of the two approaches. Results from the comprehensive study concluded that the percentage of actual cutting grains engaged with the workpiece to be between 5%-10%, and that the thermal properties of the grinding wheel had a fundamental influence on the temperature partition to the workpiece. Despite the data being compared against other published works on the subject, and were in good agreement, this paper did not experimentally test the claims independently of the results published in the literature for additional validation.

The final part of their study, (Hou and Komanduri, 2004b), specifically concerned the heat transfer to the cutting chip during grinding. Again, a numerical prediction was developed which took into consideration the real area of contact between the abrasive grains within the grinding wheel and the workpiece, i.e., the true grinding zone area which was something not considered by previous research. Experimental tests were conducted on a standard steel workpiece using two resin-bonded wheels which had different grain sizes. Measured parameters included cutting forces and the $G$-ratio. Special attention was given to the predicted number of abrasive grains in contact with the workpiece. The results from the experimental tests were then compared with theoretical model predictions. Results were found to be in accordance with the theoretical models, and so thus their approach to modelling the contact of the abrasive grain-workpiece interface as a heat source was deemed a viable option.

Esnault and Roux (2013) developed a 3D numerical prediction of the grinding process. Although based on conventional and well-established models as discussed previously, they developed an interesting micro-scale procedure for modelling granular structures for cement applications. Sub-assemblies of spherical geometries with a given diameter were applied a Hertz-Mindlin contact elasticity and a Coulomb friction coefficient to simulate abrasive breakage. Although not directly linked to grinding of metallic workpieces, it remains to be seen whether the same method can be applied in terms of metal workpiece simulations, or for grinding wheel wear predictions.

Liu, Chen and Gindy (2008) developed a numerical method for modelling the grinding of superalloys, in addition to undertaking an experimental test programme to assess a range of grinding parameters and grinding wheels. An advanced superalloy, CMSX4, and Inconel 718 were chosen as the investigated workpiece materials. Performance indices were subsequently used to determine the effect of the parameters tested, including those for grinding forces, workpiece temperature, surface roughness and $G$-ratio. Both a conventional $Al_2O_3$ and superabrasive cBN wheel were assessed, with $a$ values varying between 0.01mm and 2.5mm, $V_s$ values varying between 30m.s$^{-1}$ - 55m.s$^{-1}$ and $V_w$ values of 500mm.min$^{-1}$

and 2000mm.min$^{-1}$. A sample of the results are provided in Fig 2.8 (a, b). The study indicated that superabrasive systems produced higher $R_a$ values and cutting force responses than conventional abrasives; that when using superabrasive grinding wheels there was a negligible change in $R_a$ value as $V_w$ was increased, in addition to their being an ≈87.1% increase in $F_T$ value when comparing up and down grinding modes when using superabrasive wheels. Subsequent regression analysis was conducted on the process, which was thus deemed acceptable. However, no actual figure was placed on the result. Additionally, no visual representation of grinding with nickel-based superalloy CMSX4 was presented.

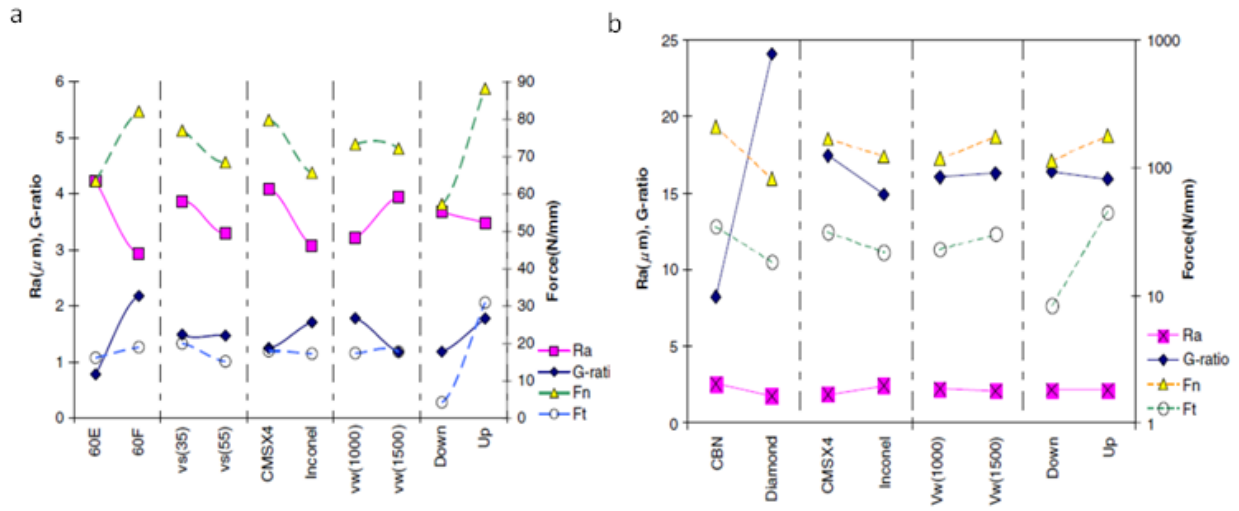



**Figure 2.8:** Conventional (a) and Superabrasive (b) wheel response optimisations during rough grinding (Liu, Chen and Gindy, 2008)

Wang and Chen (2002) investigated using numerical predictions for the workpiece temperature during grinding. What was unique about the research was that it established the temperature distribution in three dimensions. This contrasts with other researchers who often only consider the 2-D temperature distribution (Shen and Xiao, 2011). The research considered two approaches for the prediction, including that of the direct and inverse approach. Several test cases were assessed, and temperature distributions were found to be in accordance with previous data collected. However, no alteration of workpiece material was mentioned, in addition to there being no reference to alteration of grinding wheel and what affect that would have on the peak workpiece temperature.

Rowe (2001) developed on the work by Jaeger (1942) which involved the moving heat source model. For HEDG applications, this numerical approach was observed to overestimate (≈25%) the heat conducted to the workpiece, and thus a more accurate representation was suggested using a moving heat source that is inclined to the surface. our individual studies were conducted, namely; surface grinding at 1$\mu$m depth of cut, CFG at 1mm depth of cut, CFG at 20mm depth of cut, and HEDG at 0.002mm $< a <$ 8.2mm. Rowe stated that the inclined heat source model improved accuracy across the range of case studies assessed. However, even with this improvement, HEDG still poses a challenge for prediction of heat entering the workpiece, and so more research is still needed in this area. Additionally, the study did not determine the effect of film boiling of the coolant occurring in the grinding zone. Jin *et al.*, (2003) developed a thermal and hydrostatic numerical prediction of the heat transfer coefficient within the grinding zone when HEDG, after they theorised that it would be significantly greater than which was previously believed. The results from the numerical prediction were then assessed against experimental data available in other peer reviewed papers. Despite an interesting mathematical exercise whose results were found to be comparable with the available experimental data, the researchers did not collate their own experimental data sets and thus questions must remain over the validity of the comparison.

Tang *et al.*, (2009) developed a new, easy to manipulate model for predicting the cutting forces acting on the grinding wheel during service. Both experimental and theoretical data sets were compared, with findings indicating that the theoretical $F_T$ value was 13.6% lower than the physical test data, whilst the theoretical $F_N$ value was 20% lower. Despite an adequate correlation between the experimental and theoretical results, no mention of simulated data was referred to in the work. The research was built upon other works by Malkin and Cook (1971a) who considered the relationship between cutting forces and the development of wear flats on the abrasive grains within the grinding wheel. Results from that work suggested that the cutting force increased in a linear manner with an increase in wear flat area. Additionally, Li *et al.*, (1980) also influenced Tang *et al.*, (2009), by deriving an improved theoretical model for predicting the cutting forces whilst grinding, comprising of both the friction force components and the chip formation force

components. An experimental test programme was also undertaken to assess the physical performance. When the data sets were compared, the theoretical model was found to be in good agreement with the physical tests with an ≈5% deviation in results regarding $F_T$ vs. $a$ value and ≈10% deviation in results regarding $F_T$ vs. $V_w$ value.

### 2.5.2 Dimensional Analysis

Dimensional Analysis (DA) is a well-respected and credible procedure for data evaluation across varying engineering and physical science disciplines that can be applied. The DA procedure can be thought of as reducing the number of variables within a given physical system to a number of dimensionless groups. This then allows experimental relationships to be analysed with improved efficiency using the smallest allowable number of variables (Sterrett, 2009). DA is also founded on the concept of 'Base Quantities' from which all other quantities can be subsequently derived and expressed in terms of a Standard Index (SI) unitary system. The SI units are detailed as; Length, (m), Mass, (kg), Time, (s), Electric Current, (A), Thermodynamic Temperature, (°C), Amount of Substance, (kg.mol$^{-1}$), and Luminous Intensity ($C_d$). Additionally, when wishing to analyse a given system, the following universal expression can be applied as indicated by Eqn. 2.20;

$$dimQ = L^a M^b T_1^c I^d \theta_1^e N^f J^g \qquad \text{(Eqn. 2.20)}$$

where $L$ is the base quantity related to length, $M$ is the base quantity related to Mass, $T_1$ is the base quantity related to Time, $I$ is the base quantity related to Electric Current, $\theta_1$ is the base quantity related to Temperature, $N$ is the base quantity related to the Molar Mass and $J$ is the base quantity related to Luminous Intensity. Additionally, the superscripts $a$, $b$, $c$, $d$, $e$, $f$ and $g$ are dimensional indices. Once the analysis has been conducted the variables are arranged into Buckingham-$\pi$ groups for application and assessment of the system. Although DA has most commonly been applied for Computational Fluid Dynamic

(CFD) problems previously (Abdolahi *et al.*, 2018; Seco-Nicolás *et al.*, 2018; Mihic *et al.*, 2013; Dillon *et al.*, 2010 and Alhama and Madrid, 2007), it can and has been applied for machining-based systems (Nigm *et al.*, 1977). However, little to no work using the approach has been conducted on the grinding process.

Nigm *et al.*, (1977) was further influenced by the earlier work of Drucker and Ekstein (1950), who published research on applying DA to metal cutting; specifically focusing on deriving dimensionless groups for predicting chip formation. An additional source where DA has been applied to machining of orthogonal cutting tools was the work by Bisacre and Bisacre (1947). Their research concentrated on predicting the tool life and wear rate of carbide-tipped turning tools. The workpiece considered was medium-carbon steel, whilst the tooling was designated as tungsten-carbide. The system was assumed to be dry, with no coolant being applied. Results were then compared against experimental work conducted earlier by Judkins and Uecker (1933), with the DA prediction being observed to replicate the experimental data. Additional work was reported by Shaw (1994), where DA was applied for predicting workpiece temperatures when wishing to evaluate surface integrity and tool life. Further extensive evaluation of the use of DA was also proposed by Shaw (1985) and again by Singh and Khamba (2009), who reviewed how DA had been applied to the general machining field in regard to titanium specifically. More recently, Oraon and Sharma (2022) applied DA to the Single Point Incremental Forming (SPIF) process when evaluating average surface roughness, $R_a$, whilst Du *et al.,* (2022) also applied DA for predicting surface roughness for the additive manufacturing process.

Dimensional Analysis has a historical place within science and engineering. Early works which considered this method across a variety of disciplines can be observed via Sedov (1959), with examples of the approach used when considering gaseous flow, viscosity of fluids and within astrophysics. Further DA has been extensively studied by established researchers in the field of elastohydrodyanamic lubrication (EHL) theory and tribology such as Dowson and Higginson (1959), which proposed a numerical solution of EHL, followed by Dowson and Higginson (1960) and a more complete text on the field (Dowson and Higginson,

1966). In regards to the machining sector, previous works by Shaw and Oxford (1957) and Kronenberg (1966) are two examples which have utilised the DA method previously. Moving towards more recent years, some work has been conducted regarding the grinding process. One such example was the work by Zhang *et al.*, (1993). Their work considered how DA can be applied to model the $E$ value of grinding wheels and the cutting forces acting on the wheel during service. Initially, they postulated that the $E$ value was a function of twelve variables; temperature, specific weight, hardness grade, grit concentration, grain grade, total apparent volume, volume of grain, volume of bond material, volume of pores, type of grain, type of bond material and the mean diameter of the grains. However, this was further simplified with the number of variables, m, being reduced to five when considering a singular class of wheel material, i.e., temperature, specific weight, mean diameter of the grains, volume of grain and volume of bond material. Using the Buckingham-$\pi$ theorem, the number of primary dimensions, n, equalled three (M, L and T), thus the number of Buckingham-$\pi$ groups resolved to two. The models were then evaluated against experimental work conducted by Umino *et al.*, (1972), Umino *et al.*, (1972a) and Umino *et al.*, (1972b). Fig 2.9 details the predicted non-dimensional $E$ value ($\bar{E}$) from the DA method when compared against the findings from Umino *et al.*, (1972), Umino *et al.*, (1972a) and Umino *et al.*, (1972b). The $X_1$ variable plotted on the $x$-axis refers to the first dimensional group derived. This was a function of $V_g$ and $V_b$ (the volumetric percentages of grain and bond material, respectively), $d_{g_{av}}$ (the grain mean diameter) and $d_{100}$, the diameter of a grain of wheel grade 100. Findings suggested an excellent correlation between the theoretical DA predictions for the $\bar{E}$ value and the experimental data. Additionally, it was found that the $\bar{E}$ value for any given class of grinding wheel was a function of the dimensionless temperature and the predicted Buckingham-$\pi$ group I. These findings suggest that using the DA approach in conjunction with the Buckingham-$\pi$ method for prediction of workpiece temperatures with such accuracy could be applied with confidence within grinding based research.

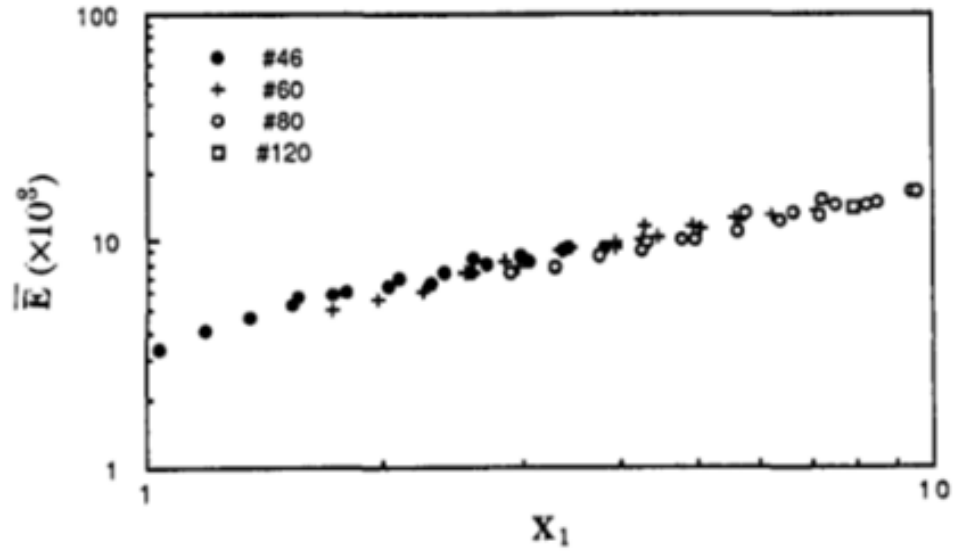



**Figure 2.9:** Predicted Values from DA vs Test Data from Umino *et al.*, (1972), Umino *et al.*, (1972a) and Umino *et al.*, (1972b) as presented by Zhang *et al.*, (1993)

Work by Rowe *et al.*, (2009) presented temperature derivation predictions using DA for workpiece temperature resulting in a dimensionless temperature expression described in Eqn. 2.21;

$$T = \frac{2\alpha P_w}{\pi k V_w b_c l_c}.\bar{T} \qquad \text{(Eqn. 2.21)}$$

where T is the actual workpiece temperature, k is the thermal conductivity, $\alpha$ is the thermal diffusivity, $l_c$ is the contact length, $b_c$ is the wheel thickness, $P_w$ is the power delivered to the workpiece from the grinding wheel and $\bar{T}$ is the dimensionless temperature.

Although not directly related to grinding, additional examples of where the DA approach and the Buckingham-$\pi$ method has been applied to the broader manufacturing industry was proposed by Rane and Date (2021), who used DA to predict solvent de-binding steps for metal injection moulded components.

Osorio *et al.*, (2019) investigated the effect of differing fluid viscosities on the breakage parameters during a wet grinding process. This was achieved by deriving Buckingham-$\pi$ groups via DA to determine if fluid viscosity had a key influence on the specific breakage rate of minerals. Although somewhat outside of the scope of 'pure' machining of metallic workpieces, the approach was found to provide highly indicative predictions when compared with physical test data, and again provides further evidence that the DA method has and continues to be a widely adopted tool for accurate numerical analysis.

Kaelani and Syaifudin (2021) analysed wear volumes due to the sliding speed when grinding via the Buckingham-$\pi$ method. Three Buckingham-$\pi$ groups were derived before physical testing was undertaken so the data sets could be compared. Three workpiece materials were investigated; an Ultra High Molecular Weight Poly Ethylene (UHMWPE), Poly Tetra Flouro Ethylene (PTFE) and Nitrile Rubber (NBR). Three wheel speeds were tested (80rpm, 90rpm and 100rpm), whilst the sliding speeds were 0.173m.s$^{-1}$, 0.181m.s$^{-1}$ and 0.192m.s$^{-1}$ respectively. Results detailed reliable comparisons between the DA predictions and the experimental trials as presented in Fig 2.10 (a and b). Such findings provide further credence for DA to be applied to the grinding process, and, specifically, accurate theoretical predictions for both workpiece temperatures and cutting forces.

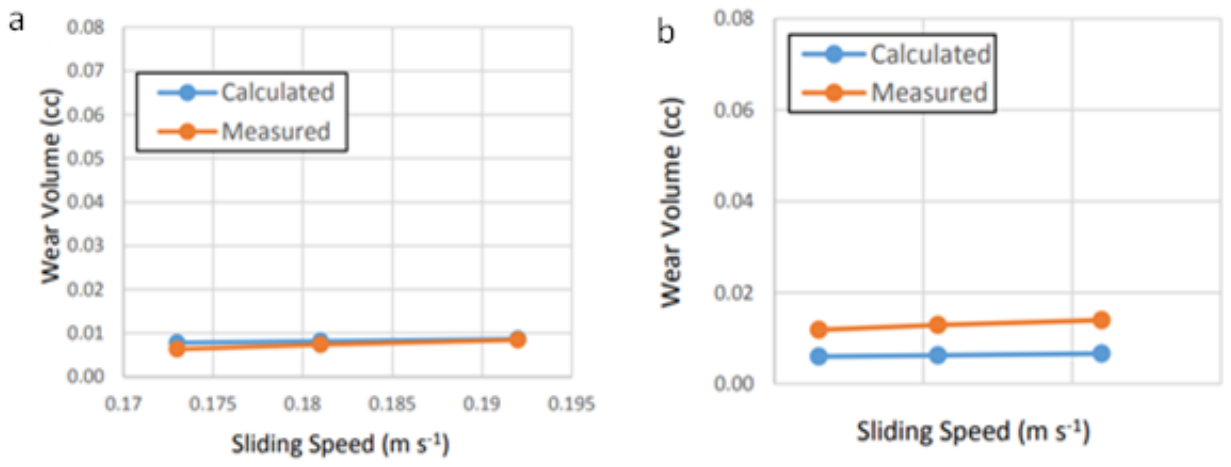



**Figure 2.10:** Wear Volume vs. Sliding Speed (Test Data and DA Comparison) for UHMWPE (a) and NBR (b) (Kaelani and Syaifudin, 2021)

Kamble, Rajiv and Jadhav (2021) utilised a DA approach whilst undertaking experimental investigations when drilling aluminium to determine the parameters which most influenced an increase in heat generation. The effect on the workpiece temperature by altering tool speed, feed rate and the associated torque were assessed. The tooling used for the drilling process was HSS. The experimental data was then analysed using the Buckingham-$\pi$ theorem. From the six parameters required to produce friction drilling, DA reduced these variables to three ($M$, $L$ and $T_1$), thus meaning three Buckingham-$\pi$ groups. Results proved highly credible with almost comparable trends across all parameters considered. Additionally, Phate and Toney (2019) utilised the DA method to reduce the number of variables involved (pulse on time, pulse off time, wire feed rate, current, voltage, thermal conductivity of the workpiece material, coefficient of thermal expansion, density and the wire tension) when wishing to predict the MRR and $R_a$ of an WEDM aluminium/SiC Metal Matrix Composite (MMC) workpiece. The DA approach was subsequently compared against an Artificial Neural Network (ANN) method. From the twelve variables associated with WEDM, the DA method reduced these down to five ($M$, $L$, $T_1$, $I$, $\theta_1$), thus resulting in six Buckingham-$\pi$ groups. When compared against the experimental data, the DA indicated a maximum difference of 14.2%, and at best a difference of 1%. The subsequent ANN approach indicated more favourable results than from DA, however, both were deemed capable approaches for predicting the experimental data. Fig 2.11 and Fig 2.12 detail the sample DA data against the experimentally derived results for surface roughness and the MRR respectively.

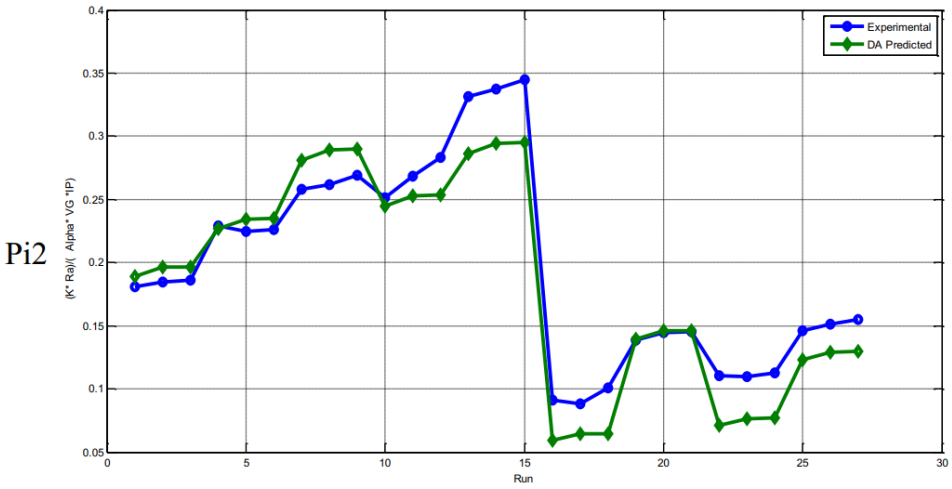



**Figure 2.11:** Dimensional Analysis Data for Surface Roughness (Phate and Toney, 2019)

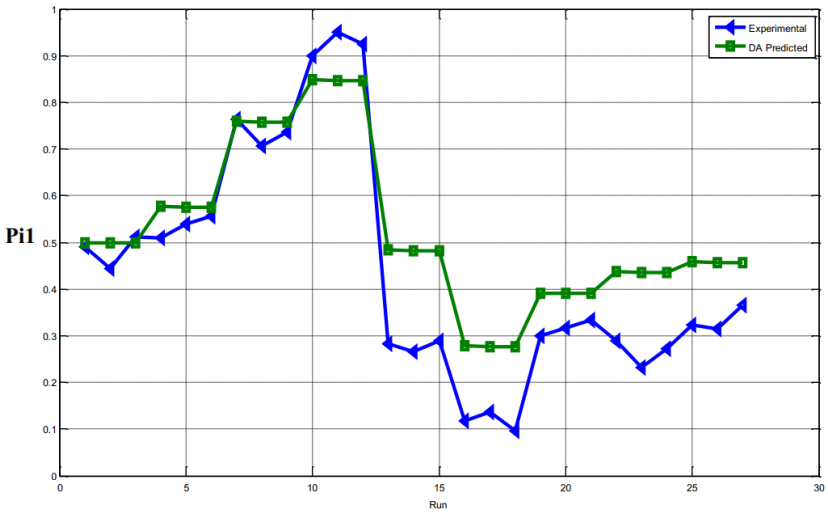



**Figure 2.12:** Dimensional Analysis Data for MRR (Phate and Toney, 2019)

Alauddin and Zhang (2007) considered modelling the grinding forces via the DA approach when surface grinding a steel workpiece. Their model considered the variables of spindle speed, work speed, depth of cut, engagement width and workpiece tensile strength. An $Al_2O_3$ wheel was used for the tooling with the feed rate being varied between 5.6m.min$^{-1}$ $< V_w <$ 7.6m.min$^{-1}$, the depth of cut being varied between 6.5$\mu$m $< a <$ 10$\mu$m, whilst the engagement width and wheel speed were held constant at 25mm and 25m.s$^{-1}$ respectively. A subsequent Response Surface Methodology (RSM) was also employed to determine how applying both approaches could improve the predicted response. Similarly to previous works, the six variables were reduced to three after the DA was conducted ($M$, $L$ and $T_1$), thus resulting in six Buckingham-$\pi$ groups. Again, after data from the DA was compared against the experimental test findings, an excellent correlation was found, with the conclusion drawn that the DA approach is a perfectly viable method for predicting grinding force responses. However, no mention of whether DA could be applied for workpiece temperature prediction was referred to, and so further work would be needed in this area for this assessment to be undertaken. Examples of their findings when compared to experimental data for predicted cutting force is given in Fig 2.13.

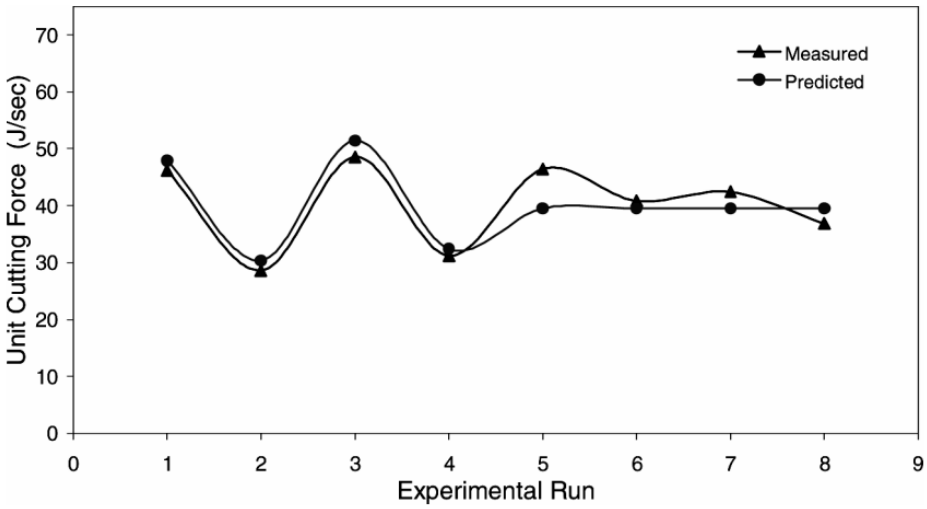



**Figure 2.13:** Dimensional Analysis Data for Cutting Force (Alauddin and Zhang, 2007)

Kumar and Kamba (2010) investigated the UA grinding of pure titanium when considering the MRR. A Taguchi based DoE approach was employed for the experimental testing, whilst a DA method was utilised for developing predictive models for the MRR. Three different wheel materials were chosen (SiC, $Al_2O_3$ and cBN), whilst the depth of cut and vibrational frequency were both held constant at 2mm and 21kHz respectively. The DA results were subsequently assessed against the experimental findings for validation. An example of their predicted data via DA versus experimentally gathered data is presented in Fig 2.14. When analysing the MRR through DA, the number of variables was reduced from four to three ($M$, $L$ and $T_1$) resulting in two Buckingham-$\pi$ groups. Findings from the study proved satisfactory, with the DA model predicting comparable results to the experimental tests for MRR for all tool materials investigated. Conclusions suggested that the DA approach could be used for assessing additional parameters pertaining to the grinding process. Work utilising the DA approach in regards to grinding mechanisms during ball end milling using Alumina powder was conducted by Giraud *et al.*, (2021). Although not a direct cutting study, the research was within the scope of abrasive wear and so it can be stated that DA methods have been utilised for frictional wear applications previously.

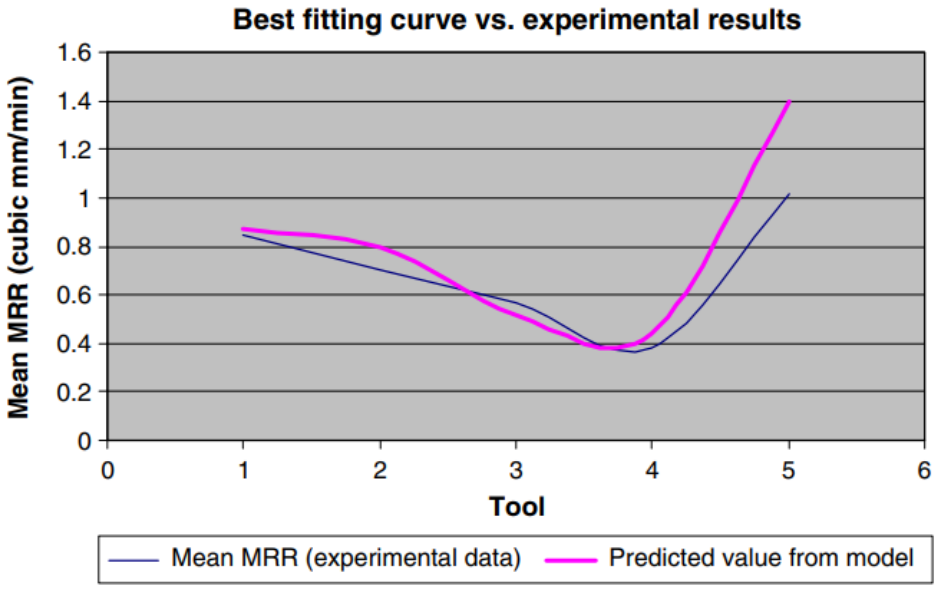



**Figure 2.14:** Dimensional Analysis Data for MRR (Kumar and Kamba, 2010)

Further examples of where DA has been applied to analyse the grinding process include the works by Sisodiya, Viswanathan and Dinakaran (2016), who derived Buckingham-$\pi$ groupings for predicting grinding wheel wear, El Wakil and Azab (2010) who applied DA to the grinding of composite materials and Zhang (1999) who conducted research into the modelling of the polishing and grinding process through both DA and FE methods. Results from that study proved that modelling of the grinding process was still clearly problematic due to the inherent complexity of the tooling-to-workpiece friction model and abrasive wear modelling limitations. Finally, the earlier work of Walsh and Torrence (1999) investigated the influence of temperature on the form of ground workpieces via a DA approach. This was then subsequently compared against a thermal FE model. Results from the study suggested that a DA approach for predicting workpiece temperature was suitable when applied to an analysis of plunge-die grinding and the angle-grinding process. However, it still remains to be seen whether the Dimensional Analysis method via the Buckingham-$\pi$ theorem would hold true for the CFG of current aerospace grade materials such as Ti-6Al-4V.

## 2.6 Temperature Measurement during Grinding

Temperature measurement within the workpiece can be particularly complex, depending on whereabouts one wishes to analyse within the system. By far the most common approach for measuring workpiece temperature is via using a thermocouple arrangement. Thermocouples work by using two dissimilar metals which are joined at their two ends. If one end of the thermocouple is placed on something hot (known as the 'hot junction') and the other end on something cold (known as the 'cold junction'), a current is induced. This current causes a voltage (potential difference) drop across the two junctions. This induced voltage can then be measured by placing a voltmeter across the two junctions. The phenomenon is called the Seebeck effect, named after Thomas Johnson Seebeck who noticed the occurrence in 1821 and whom after which the governmental equations are named (Davies *et al.*, 2007). Nonetheless, it must be noted that these equations only suffice for temperature fields in one dimension. Two-dimensional or three-dimensional temperature fields are not considered.

However, the usage of thermocouples during machining does have its limitations. Due to the distinct difference between what is largely considered a 'tight' abrasive material

removal process such as grinding, and 'loose' abrasive material removal processes such as ploughing and rubbing, temperature measurement becomes more difficult to achieve. To date, little work has been conducted by previous researchers regarding temperature data acquisition within these two areas. Some additional studies regarding epoxy-based fixation methods for thermocouples embedded in the workpiece material have been suggested by Shen *et al.*, (2008). Experimental testing was conducted in addition to a theoretical heat transfer model to determine the energy partitions within the system assuming shallow depth of cut values ($<25\mu$m) during MQL scenarios. When compared against conventional coolant delivery systems, MQL methods were found to only observe limited temperature reductions of 24% when using a conventional thermocouple temperature measurement system. Meanwhile, later work by Ding *et al.*, (2018) conducted similar research when cylindrical grinding.

Grimmert, Pachnek and Wiederkehr (2023) undertook experimental testing and developed simulation models of the CFG process. Again, this suggests that obtaining experimental data and numerical predictions is a key foundation for engineering research. An $Al_2O_3$ wheel was used for the tooling, whilst Inconel 718 was used for the workpiece. Temperature of the workpiece and cutting forces were the desired outputs, with temperature being measured via a k-type thermocouple arrangement. The cutting forces measured via a Kistler dynamometer. The stand off distance of the thermocouple from the cutting surface was 4mm, the depth of cut was varied between 0.05mm and 3mm, the feed rate was varied between 100mm.min$^{-1}$ and 1000 mm.min$^{-1}$ while the wheel speed was varied between 10m.s$^{-1}$ and 30 m.s$^{-1}$. The FEA simulation was developed in the heat transfer module of COMSOL Multiphysics, with the boundary conditions being based off the work previously discussed in this thesis of Carslaw and Jaeger (1959). The cutting force model was derived from first principles. Results from the thermal simulation study indicated significant differences between the up-grinding model and the down-grinding model. It was suggested that this was due to the application and position of the coolant within the grinding zone. Due to the average temperature distribution being used for comparison against the test data, it was found that the resulting plot deviated from the physical test data by 16.3%.

Although the study was an interesting addition to the literature, only Inconel was assessed, and so further work would need to be conducted on titanium workpieces to determine if the modelling method is suitable for those alloys.

Batako *et al.*, (2005) presented a review of the current trends in terms of temperature measurement during grinding. Optional temperature measurement techniques addressed were non-contact methods such as fibre-optics, and the more conventional, direct-contact method of thermocouples. The thermocouple technique was compared and analysed in terms of the validity and accuracy differences between both the direct insertion into the workpiece material and direct insertion into the grinding wheel methods. Experimental testing was conducted using HEDG to assess the different grinding temperature measurement methods. The response time of the thermocouples tested was ≈8ms, the wheel speed, $V_s$, was set at 35m.s$^{-1}$, the feed rate, $V_w$, was 0.3m.s$^{-1}$ and the depth of cut, $a$, was varied between 0.006mm and 0.05mm. The study found that the peak workpiece temperature observed was 500°C. The investigation concluded that the embedded workpiece thermocouple method was the simplest and most accurate approach available and was therefore recommended. Comparatively, later researchers such as Nedić and Erić (2014), made the same observations regarding embedded thermocouple accuracy and reliability via temperature measurement during turning and drilling machining operations. Example results are detailed in Fig 2.15 (a and b). During this study, the peak workpiece temperature during drilling was found to be 330°C, whilst turning observed lower workpiece temperatures of approximately 160°C.

Investigations conducted by Xu and Malkin (2001) experimentally tested embedded thermocouple configurations for workpiece temperature measurement which were then compared with infrared temperature measurement systems. Although thermocouples were observed to be the simpler solution for generating accurate workpiece temperature data, both direct-contact and non-contact temperature acquisition systems were deemed to be comparable in terms of accuracy when compared against numerical energy partition predictions.

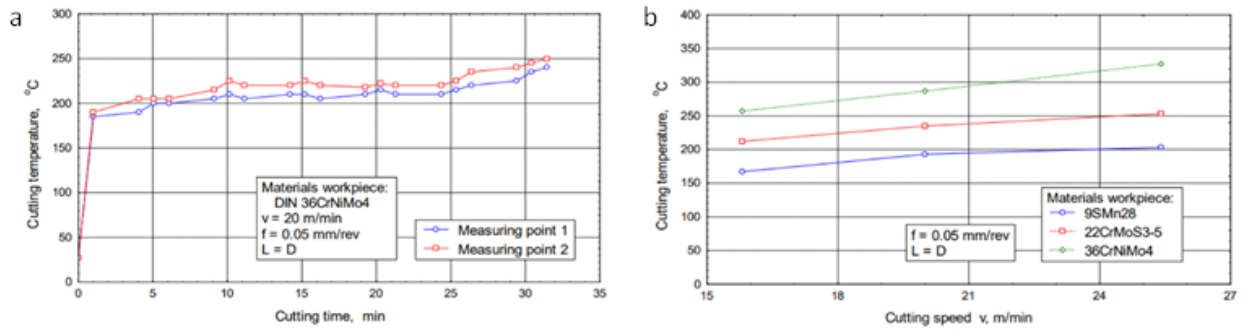



**Figure 2.15:** Workpiece Temperature v Cutting Time for steel alloy DN 36CrNiMo4 (a) and Workpiece Temperature vs. Cutting Speed for steel alloys DIN 9SMn28, DIN 22CrMoS3-5 and DIN 36CrNiMo4 (b) via a Thermocouple Arrangement during Drilling (Nedić and Erić, 2014)

More recently, Liu *et al.*, (2016) assessed the viability of using infrared techniques for measuring workpiece temperatures during HEDG of martensitic stainless steel. An infrared pyrometer and infrared thermometer were thus tested and compared. Results from the study indicated that infrared pyrometers perform better where grinding conditions are more aggressive, i.e., deeper $a$ and greater $V_s$ and $V_w$ values. However, no comparison was made of the two optic techniques studied against traditional thermocouple placements, and so no conclusive arguments could be drawn. The work by Urgoiti *et al.*, (2018) developed a new estimation for workpiece temperatures during grinding via the use of a combined pyrometer, a non-contact temperature measurement system and a subsequent passing of the data through a derived analytical thermal model. This novel approach appeared to offer significant error for estimations at positions closer to the grinding surface than for estimations at greater stand off distances from the grinding plane. It can be surmised that this newly derived method performs in an inverse fashion to thermocouples which are found to measure temperature gradients more accurately towards the grinding surface. Moreover, Anderson *et al.*, (2008a) and Anderson *et al.*, (2008b) also considered temperature measurement and prediction whilst grinding using infrared techniques.

In recent years, several innovative temperature measurement solutions have been proposed including thermal imaging, the application of Thermal History Paints (THPs) and the newly emerging Thermal History Coatings (THCs). Together, these non-contact measurement techniques are referred to as TIP (Thermal Image Processing) and are now

available in addition to the traditionally used thermocouple configuration. A discussion of these methods are expanded upon herein. Although thermal imaging has been successful across many sectors, i.e., the biomedical and aerospace professions, TIP has proven to be of little value for the machining sector, with issues including errors regarding camera calibration and high magnification requirements (Whitenton, 2012), and overall uncertainty in the system (Lane *et al.*, 2013). These results are further consolidated when one considers their application to grinding. This is primarily due to the vast volume of fluid applied to both the workpiece and the grinding wheel to reduce surface temperature and therefore surface burn and damage. This is in addition to wishing to keep the grinding wheel cool and removing as much chip material from the wheel surface as possible to improve wheel life and performance. Table 2.4 provides an overview of the differing workpiece temperature measurement methods available for use when machining Ti-6Al-4V as compared by Conradie *et al.*, (2012).

**Table 2.4:** Comparative Performances of a Range of Workpiece Temperature Measurement Techniques (Conradie *et al.*, 2012)

| **Measurement Method** | **Cost** | **Accuracy** | **Liquid Cooling Compatible** | **Ease of Calibration** | **Transient Response** | **Simplicity** |
|---|---|---|---|---|---|---|
| Thermal History Paints | Good | Bad | Bad | Good | Average | Good |
| Metallographic Methods | Average | Good | Good | Bad | N/A | Average |
| Thermocouples | Excellent | Good | Bad | Good | Bad | Good |
| Embedded Thermocouples | Excellent | Good | Good | Good | Bad | Good |
| Tool-Workpiece Thermocouples | Average | Average | Bad | Bad | Bad | Good |
| Single Wire Thermocouples | Excellent | Average | Bad | Good | Bad | Good |
| Transverse Wire Thermocouples | N/A | Good | Bad | Bad | Average | Bad |
| PVD Coatings | N/A | Good | Bad | Good | Average | Good |
| Thermochemical Powders | N/A | Good | Bad | Excellent | Average | Excellent |
| Optical Thermocouples | Average | Good | Bad | Bad | Excellent | Good |
| Infrared Cameras | Average | Good | Bad | Bad | Excellent | Good |
| Optical Fibre Pyrometry | Average | Good | Bad | Bad | Excellent | Good |

THPs are specialised temperature sensors which can be applied to a workpiece via a conventional spray mechanism to determine surface temperature. The technology works by utilising the naturally occurring luminescence of ceramic material for the sensor, whilst the sensor coating utilises phosphorescence phenomenon. When the surface is subjected to Ultra-Violet (UV) light, the optically compliant elements within the coating absorb the energy, which thus causes electron excitation to higher energy shells within the atom. Due to the instability of these higher excitation states, the electrons eventually drop back to their ground state, resulting in the emission of visible light of differing wavelengths. When subject to specialist camera technologies, these wavelengths can be detected, and a surface profile of temperature distributions can be observed. Advantages of utilising this technique include the ability to monitor the surface temperature remotely without the need for any internal measurement equipment, with the only limitation being on the camera equipment used for the analysis, in addition to it being a NDT method unlike thermocouple embodiment. Moreover, a wide range of temperatures can be determined (300°C $< T <$ 900°C), with accuracies in the range of $\pm$ 5°C - 10°C.

THCs are similar to THPs. However, they are deemed more robust than their THP counterparts due to their adherence to the surface of the workpiece via more secure and substantial means. Additionally, they have the ability to withstand harsher and more demanding environments than THPs. Again, THCs utilise the luminescence of the material coating, which records the peak temperature of the surface after the manufacturing operation has been completed. In comparison to THPs, the temperature recording window is greatly increased i.e., 300°C $< T <$ 1700°C. Similarly to THPs, the isotherms induced on the workpiece are also processed through an optical equipment setup. Unfortunately to date, very little research has been conducted into implementing THPs and THCs for measuring workpiece temperature during abrasive removal processes such as grinding (Davies *et al.*, 2007).

## 2.7 Cutting Force Measurement during Grinding

Dynamometers are the most commonly used approach for measuring cutting forces during machining operations, having been available since their invention in the nineteenth century. However, the invention of the piezoelectric dynamometer has since allowed for more accurate

and stable readings to be made. Piezoelectric dynamometers operate by containing three quartz sensors that measure the three force components: $F_x$, $F_y$ and $F_z$. When loaded, this causes a charge to form proportional to the effective force. The relevant moments can then be calculated from the force measurements if needed.

There are two methodologies that can be utilised when wishing to measure the cutting forces acting on a grinding wheel; namely, the direct and indirect approach. Indirect approaches are deemed less accurate and reliable - examples include using a servo drive motor to provide the output signal. This method has been criticised due to the resulting signals from indirect approaches containing undesirable noise due to the change in friction as a result of the reciprocating table, i.e., a continuous relevant sign change (Kim *et al.*, 1999). Further analysis of indirect approaches include the work by Stein and Huh (2002), who proposed a numerical model prediction of cutting forces based on motor current and speed. Conversely, direct approaches are deemed to be more accurate and reliable and are deemed the better method of the two; an example being the use of piezoelectric dynamometers which are known for their high resonant frequency and stiff system architecture (Assarzadeh and Ghoreishi, 2013). However, direct approaches have also been scrutinised due to their high cost and layout limitations.

## 2.8 Experimental Design Methods

The use of the Design of Experiments (DoE) approach is a scientific and highly utilised method for being able to determine interactions between the variables wishing to be analysed at the levels at which they are being tested within a given process. For the case described in this thesis, that process would be grinding. DoE has been used extensively across industrial manufacturing processes more generally within the last twenty-five years (Durakovic, 2017), which has ultimately seen an increased improvement in component quality and reliability (Telford, 2007). Fig 2.16 details a schematic outlining the general DoE method for assessing the grinding process. However, before beginning to discuss the extent to which DoE has been applied to the grinding process, a brief discussion on how DoE is conducted is provided.

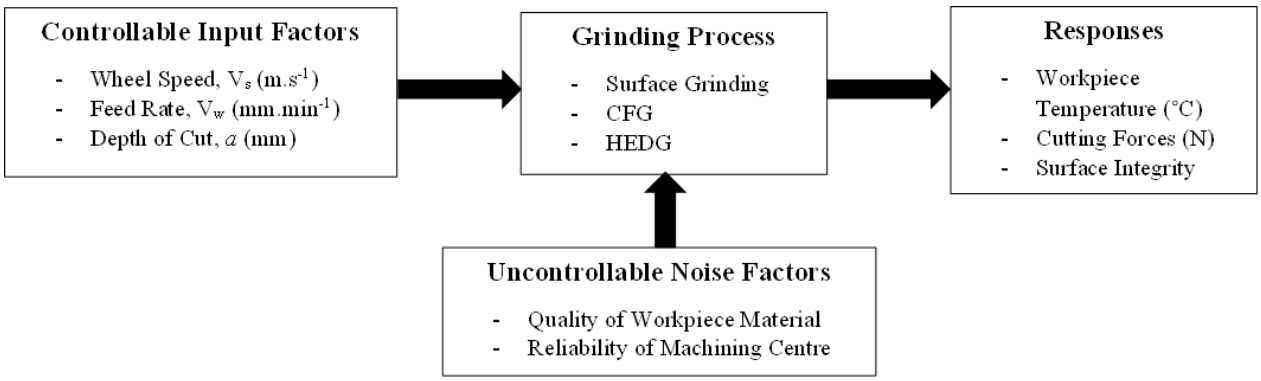



**Figure 2.16:** Experimental Design Flowchart regarding the Grinding Process

### 2.8.1 Components of Experimental Design

#### 2.8.1.1 Factors, Levels and Responses

A factor is considered the input into the process and can be deemed either controllable or uncontrollable. In terms of this thesis, the controllable input variables for the grinding process are the wheel speed, $V_s$, feed rate, $V_w$ and the depth of cut, $a$. However, this range of input variables could be expanded, i.e., wheel material, workpiece material, coolant type or the delivery method utilised, etc. Examples of uncontrollable factors include the reliability of the machining centre upon which tests are conducted or the temperature of the workpiece prior to being machined. There are specific forms of uncontrollable factors referred to as Noise Factors; a factor that causes variability under normal operation conditions, but which can be controlled via a process of Blocking and Randomisation (Durivage, 2016). The levels are the settings at which the previously discussed factors are tested. In terms of grinding, these levels will vary depending on the application of the process being undertaken, with the value of the wheel speed, feed rate and depth of cut being altered accordingly. Finally, when discussing the responses from a given DoE for assessing grinding, the key outputs are primarily workpiece temperature, cutting forces, $G$-ratio and the subsequent surface integrity of the workpiece, i.e., surface roughness, microhardness, residual stresses and microstructural changes.

#### 2.8.1.2 Unexplained Variation, Noise Factors, Correlation/Causation and Interactions

When undertaking DoE, several potential issues can arise. Firstly, there can be "Unexplained Variation" which is beyond the limit of the experiment designer to control. Secondly, there are "Noise Factors". However, if these can be identified prior to designing an experimental test programme, they can be built into the design to minimize their effect on the response of the experiment. Thirdly, both "Causation" vs. "Correlation" must be considered, i.e., it is possible for two factors to vary together (Correlation) but it may not be directly due to one other (Causation). In situations such as this, they may be caused by a third factor. Finally, the interactions between factors should also be considered. An example would be where a given factor has both a positive and negative effect once a certain level is reached (Montgomery, 2013).

### 2.8.2 Types of Design of Experiments and Applications to Machining

DoE can be considered either Full Factorial, or Fractional-Factorial in nature. Both of these approaches have their positive and weaker attributes. In general, Full-Factorial experiments consider a combination of all number of factors at all possible levels (Anthony, 2014). Here, the number of experiments to be investigated for a given number of variables, k, would be 2k. Full-Factorial DoE is often utilised during the early phases of research programmes when the number of factors to be investigated is typically low (generally $< 4$). As such, Full-Factorial experimental design has the benefit of giving a detailed and comprehensive representation of all possible outcomes from the given test factors and levels. However, this approach does place a greater demand on both time and resources available.

Conversely, it is also possible to conduct a Fractional-Factorial design. As the name suggests, here only a fraction of the total number of parameters are assessed, allowing for quicker and more time-effective conclusions to be drawn. Fractional-Factorial designs are more often used when wishing to assess the most critical factors which affect the given response of the system. In the case of grinding, these would be wheel speed, feed rate and depth of cut. One example of this approach is the work by Alagumurthi, Palaniradja and Soundararajan (2006) who considered optimising the cylindrical grinding process via the use of the DoE Fractional-Factorial method. Wheel speed, feed rate and the depth of cut were identified as the three key factors for assessment, with the levels being varied at

1750rpm and 2000rpm, 140rpm and 300rpm and 0.01mm and 0.02mm for the speeds, feeds and depths of cut respectively. An $Al_2O_3$ wheel was utilised for the tooling. Mild steel was the workpiece material investigated, with the surface roughness being the key response that was considered. Results indicated the feed rate had the biggest influence on the surface roughness response post grinding, with a 24.7% increase when the feed rate was increased from level 1 to level 2. Additionally, the Taguchi DoE approach has also been reported when analysing machining processes previously. Examples of where this method has been applied and been successful include Yang and Tarng (1998) who optimised the turning process, Dhavlikar *et al.*, (2003) who utilised Taguchi arrays for analysing the centreless grinding operation, Ghani *et al.*, (2004) who investigated the end milling process, Kwak (2005) who considered surface grinding and Nalbant *et al.*, (2007) who optimised the surface roughness post turning.

## 2.9 Conclusions from the Literature

This literature review has identified and critically evaluated a wealth of appropriate academic and industrial sources that concern the grinding process. Critical emphasis was taken to assess the peak workpiece temperature, cutting forces and associated surface integrity when grinding "hard to grind" materials, including the Ti-6Al-4V alloy. Additionally, both the historical and state-of-the-art experimental and DA modelling procedures for predicting these abrasive cutting system outputs were also assessed. From the critical review, the author has drawn the following conclusions:

- Grinding is a highly complex abrasive machining process. This is partially due to the inherent nature of the grinding wheel tooling material matrix which constitutes of bond material and different shaped abrasive particles. This complexity is heightened further with the abrasive being held at different orientations and angularities within the matrix. During the grinding process, the tool is deemed to self-sharpen as old, wear flat grits are torn from the material matrix revealing new and sharpened grit materials, with grain fracture, bond fracture and attritious wear being the three wear mechanisms pertaining

to grinding wheels. This, in conjunction with difficulties in fully understanding precisely what is occurring in the grinding contact zone is a significant problem for academic and industrial development. Moreover, there is now the increasing need to grind "hard to machine" materials such as the Ti-6Al-4V alloy which is problematic due to its low thermal conductivity and relatively high ductility. Additionally, vitrified bonded SiC grinding wheels are recommended for grinding titanium alloys due to their increased hardness, with typical CFG parameters for grinding titanium including slow $V_w$ values of $60\text{mm.min}^{-1} < V_w < 1000\text{mm.min}^{-1}$ and moderate $V_s$ values of $15\text{m.s}^{-1} < V_s < 30\text{m.s}^{-1}$.

- Furthermore, the need to improve the accuracy and availability of grinding performance measurements such as workpiece temperature and cutting forces has increased with the development of new, innovative grinding processes such as Very Impressive Performance Extreme Removal (VIPER) methods and the expanding use of advanced aerospace grade materials. Such materials are often used in temperature and pressure critical applications where surface integrity is of vital importance. With the workpiece temperature having a direct impact on the surface integrity of all metallic materials, when considering Ti-6Al-4V, the need to measure and additionally predict workpiece temperature values induced is crucial for ensuring component surface integrity (and therefore safety) requirements are met. Issues which can arise when workpiece temperatures are too high include unwanted high residual tensile stresses and subsurface metallurgical damage, whilst surface topography changes include surface burn and microcracking. Further substantial time savings would be made if predictive grinding temperature models could be developed.

- Experimental temperature measurement during grinding is limited within the academic literature, with much scope available for future research and publication opportunities. This contrasts with other machining processes which have seen significant research conducted in this regard. The more traditionally observed method used to date has

been that of a direct-contact, embedded K-type thermocouple configuration. This has been limited to a single thermocouple being used to obtain workpiece temperature measurements. This clearly does not suffice when wishing to measure temperatures at multiple locations throughout the grinding pass, and so multiple thermocouples should be used to verify where the peak workpiece temperature is located. Whilst newer, innovative, non-contact methods regarding temperature measurement have been tested with success such as those by pyrometer infrared methods, embedded thermocouples have been found to offer the simplest and comparably accurate solution when compared to the more expensive and complex non-contact methods. For cutting force measurement, piezoelectric dynamometers appear to be ubiquitous in this regard, with errors in this type of system setup being negligible.

- Post-grinding surface integrity assessment should be conducted on the workpieces tested. This is due to the influence that workpiece temperature and the associated cutting forces have on the in-service life of ground components. Surface integrity tests to be conducted include ascertaining magnitudes for surface roughness, microstructural changes, microhardness and residual stresses; all of which have influence over fatigue life, for example.

- As physical testing of any system can be costly in terms of finances and time, DoE methods via either a Full-Factorial or Fractional-Factorial approach appear to offer a suitable alternative for assessing interactions between parameters of interest. In terms of grinding, the process parameters of concern are wheel speed, $V_s$, feed rate, $V_w$, depth of cut, $a$, wheel material and workpiece material. As this thesis is concerned with Ti-6Al-4V for the workpiece and SiC for the wheel material exclusively, only $V_s$, $V_w$ and $a$ should be considered as these are the key process parameters applicable when undertaking grinding. DoE methods should therefore be used when conducting either theoretical or experimental tests throughout this thesis.

- Dimensional Analysis appears to offer a sound and credible approach for modelling different process parameters across a range of different engineering systems. To date, some work has been investigated with its application to machining such as with WEDM and drilling. However, little to no work has been conducted with its application to the grinding process. If the Buckingham-$\pi$ method could be applied to grinding, and, in particular, the grinding temperatures and cutting forces associated with the process, good predictive models using this analytical approach could be derived.

- Moreover, the literature appears to indicate that obtaining both experimental test data and predictive models is the most reliable scientific method to employ when wishing to determine both workpiece temperature and cutting force responses when analysing the grinding process. This can be determined via undertaking physical trials to obtain test data, with predictive models being developed by contemporary FEA software or more established numerical methods such as DA. The author proposes that this approach of obtaining two independent data sets which can be directly compared be utilised throughout the thesis for analysis and so subsequent conclusions can be drawn.

- Finally, this literature review clarifies the scarce lack of research regarding experimentally evaluating workpiece temperature outputs via physical testing within the area of grinding research. As such, any data obtained pertaining to grinding temperature via physical trials would add significantly to the scientific literature and is the foundation of the novelty of the presented thesis.

# Chapter 3

# Methodology

This section outlines the methodology employed throughout the course of this thesis. Firstly, a detailed account of the experimental grinding programme is outlined, including workpiece preparation and the data acquisition methods for collecting workpiece temperature, cutting forces, $G$-ratio and subsequent surface integrity performances. Secondly, an explanation of the approach for modelling both workpiece temperature and cutting force performance via applying dimensional analysis and the Buckingham-$\pi$ theorem are presented.

## 3.1 Phase 1: Experimental Grinding Tests

### 3.1.1 Machine Tool and Cutting Fluid

For the grinding tests conducted, the project utilised the Bridgeport FGC 1000 3-axis grinding centre [*Hardinge, St. Gallen, Germany*], which has a maximum spindle speed of up to 6000rpm, in addition to delivering a maximum power of 28kW. The SiC grinding wheel was held using MST BT40 FMSB32-60 tool holders, with associated blotters and flanges. The grinding centre also had a maximum travel and feed rate capability along the $x$, $y$ and $z$ axis of 1020mm, 560mm and 600mm respectively; and 43m.min$^{-1}$, 43m.min$^{-1}$ and 30m.min$^{-1}$ respectively. TRIM C270 coolant fluid was delivered to the workpiece and grinding wheel (of which a maximum diameter of 220mm for both conventional and superabrasive tools can be used) via coherent-jet coolant nozzles (Webster, 2007). The coolant had a concentration of $\approx$ 7%-10%. The nozzles had a rectangular outlet cross-section of 2mm x 20mm width and which were capable of laminar flow criteria of between 1L.min$^{-1}$

and 140L.min$^{-1}$ at a pressure of up to 84bar. The used operating conditions for grinding were 90L.min$^{-1}$ at 84bar. For wheel cleaning, a volumetric flow rate of 25L.m$^{-1}$ was supplied at a pressure of 70bar, with the nozzle having a 0.5mm x 20mm wide rectangular outlet cross-section. The Bridgeport also utilised an integrated Wendt Mk IV Cantilever dressing roller spindle supplied by 3M to dress the wheel prior to and in between testing.

#### 3.1.1.1 Data Acquisition

After close analysis of the available solutions for workpiece temperature data collection during grinding gleaned from the literature presented in Chapter 2, the author decided on utilising a thermocouple configuration. This was decided on for several reasons; namely, ease of application, ease of availability and level of accuracy (Inasaki and Tönshoff, 2001). For the purpose of measuring all workpiece temperature responses experimentally during the project, six OMEGA XC-24-K-60 thermocouples were embedded in the workpiece (i.e., two lines of three thermocouples) resulting in three thermocouples being used per test. The thermocouples were of the k-type variety, which were additionally coated in a ceramic fibre insulated sheath to achieve a 1200°C rating. The response time for this thermocouple model (the time taken for the thermal voltage (output) to reach 63% of the maximum for the step change in temperature) was experimentally tested and calculated to be 0.22s via a boiling water plunge test; the results of which are detailed in Fig C1 and Fig C3 in Appendix C. The thermocouples were then connected to the OMEGA DAQ USB 2400 data logger via a bespoke designed extraction plate which allowed the instrumentation to be threaded out of the machining bay. The data logger was capable of housing a maximum of sixteen OMEGA XC-24-K-60 thermocouples per pass, however, this would have compromised the response time and thus accuracy of the reading. The maximum response time of the data logger unit was 1000 samples.s$^{-1}$. The data logger was subsequently connected to a Windows operating system PC. The associated DAQ Central software was used to manipulate and log the data before being exported to Microsoft Excel for post processing. All the cutting force data gathered from the experimental testing was recorded via the Kistler 9257A three-component piezoelectric platform dynamometer. This was then in turn connected to three Kistler 5011

charge amplifiers highlighting the $x$, $y$ and $z$ directions respectively. Finally, the charge amplifiers were attached to the same Windows PC running Kistler Dynoware software for the cutting force data collection.

#### 3.1.1.2 Workpiece Preparation

The material used throughout the entirety of this test programme was that of annealed Ti-6Al-4V alloy. This particular alloy was chosen due to it being considered a 'hard to grind' material with a low thermal conductivity and relatively high ductility. It has an associated Vickers Hardness of approximately 396HV. Additionally, the influence the machining parameters have on secondary surface integrity performances such as microhardness and surface roughness are actively sought after. Although Ti-6Al-4V has been studied more broadly, temperature measurements taken whilst grinding this alloy are scarce, so results gained via conducting any form of test programme would add greatly to the academic literature. Table 3.1 details the chemical composition of the annealed alloy. This is important to consider as the chemical formulation has a significant effect on the material properties and the subsequent grindability of the workpiece. Prior to the workpiece preparation, the workpiece material was initially available to the author in the dimensions of 485mm x 360mm. The thickness for the blank was 19.05mm.

**Table 3.1:** Chemical Composition of Ti-6Al-4V

| **Titanium** | **Aluminium** | **Vanadium** | **Iron** | **Oxygen** |
|---|---|---|---|---|
| 89.5% | 6% | 3.5% | <0.4% | <0.2% |
| **Carbon** | **Nitrogen** | **Hydrogen** | **Other (trace)** | ⟍ |
| <0.08% | <0.03% | < 0.015% | 0.275% | ⟍ |

To ensure that the final workpieces could be mounted onto the Kistler dynamometer platform on the grinding centre, the initial blanks had to go through several steps of preparation. These processes are summarised here.

**i. Water Jet Cutting**

This was undertaken at the School of Physics and Astronomy at the University of Birmingham due to limitations of cutting availability for larger plate sizes within the School of Mechanical Engineering. The larger plates were cut to ≈200mm x 200mm. This initial preparation stage was deemed necessary to ensure that further preparation could be done within the School of Mechanical Engineering. Cutting parameters consisted of a constant mass flow rate, $\dot{m}$, of 10g.s$^{-1}$ supplied at a pressure of 170MPa with a stand off distance of 2.5mm.

**ii. Wire EDM of the Final Workpiece Size**

The smaller blanks were then cut into the final sized workpiece samples (75mm x 70mm) via the Agie-Charmilles FI240 Wire EDM Machine *[Biel, Switzerland]* capable of a maximum MRR of 500mm$^3$.min$^{-1}$ and a maximum workpiece allowance of 1000mm x 550mm x 220mm located within the Machining Research Group. Six samples were achieved from the blank, before being split along the centreline to achieve a final batch of twelve possible samples.

**iii. Surface Grinding of the Samples**

The twelve samples were subsequently mounted onto the Jones and Shipman 540AP surface grinder machine *[Butterworth, Leicestershire, UK]* via a magnetic plate and vice, before being ground both sides using a 180mm diameter vitrified bonded SiC wheel. This was undertaken to ensure a flush surface on both the mounting and grinding faces. A feed rate and complimentary cross feed of 7m.min$^{-1}$ and 1m.min$^{-1}$ were used respectively, whilst a depth of cut of 0.01mm was used across both surfaces. The final workpiece thickness was 9mm.

**iv. Drilling of Dynamometer Mounting and Thermocouple Holes**

Once the four mounting point through-holes at the corner of each sample had been manufactured via Wire-EDM (each with an associated diameter of 6.5mm), the samples were mounted onto the Matsuura FX-5 Vertical Machining Centre *[Coalville, Leicestershire, UK]*. The six holes that housed the thermocouples were then drilled via solid carbide drill

bits with an associated diameter of 0.6mm to a depth of 8.5mm. A distance of 20mm was left between each thermocouple hole to avoid interference between thermocouple readings. Additionally, six relief holes of 6mm diameter were drilled to a depth of 3mm to house an end bead attached to the thermocouple node and provide relief for the thermal cement. Fig 3.1 shows a CAD model of the finally prepared workpieces used with a fully dimensioned engineering drawing presented in Fig D.3.

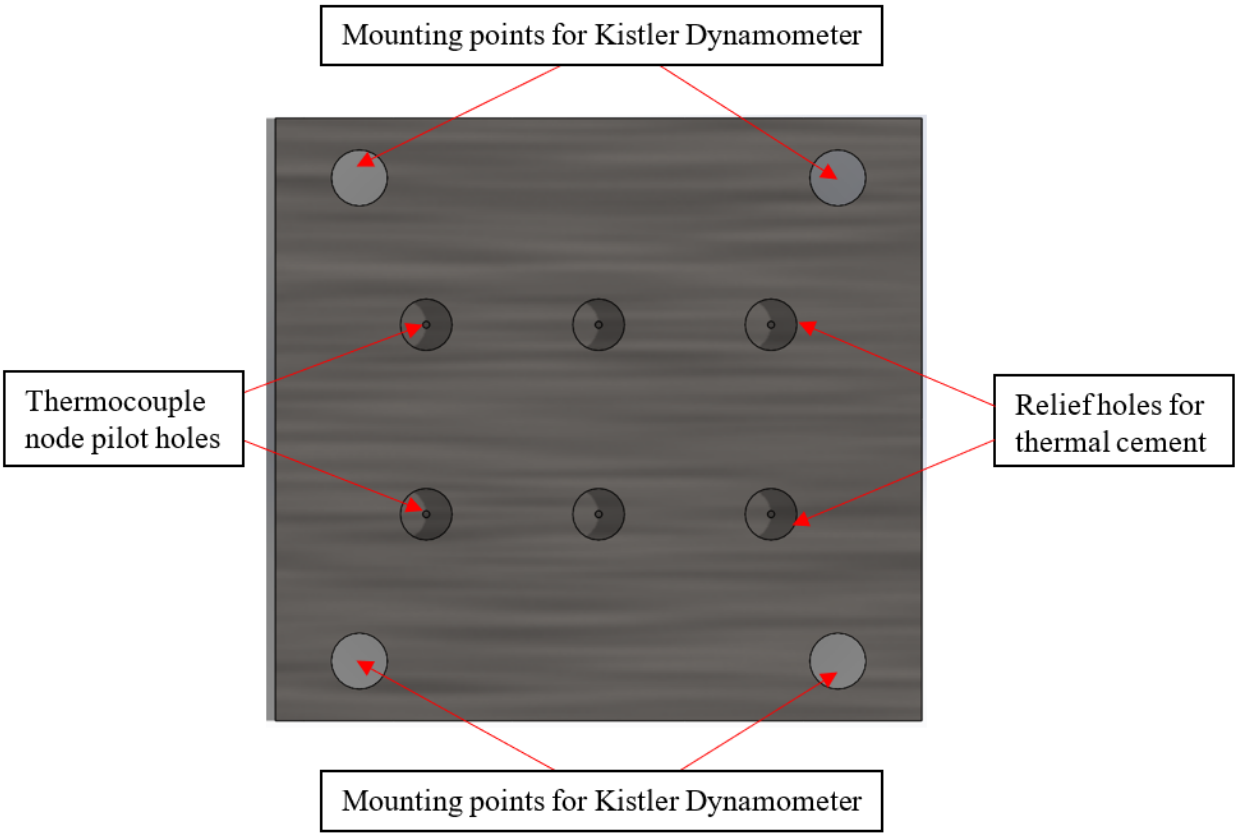



**Figure 3.1:** Thermocouple Placement CAD Model

### v. Thermocouple Implantation

The six thermocouples were subsequently embedded in the workpieces. This was achieved via cementing the thermocouples into the drilled holes using the OMEGA CC High Temperature thermal cement mixture of 3/4 powder to 1/4 water by weight, and then left to cure for at least twenty-four hours at room temperature. From each thermocouple arrangement, one slot was ground resulting in two ground slots per workpiece being possible. Fig 3.2 details the implanted thermocouple arrangement within the workpiece.

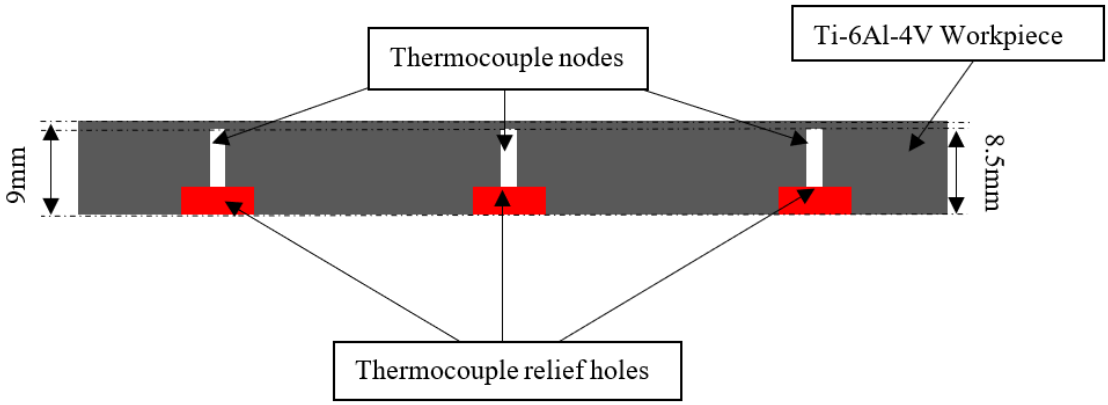



**Figure 3.2:** Thermocouple Embedded Depth Schematic

### vi. Workpiece Sample Mounting

The final process was to mount the workpiece with the embedded thermocouples onto the thermocouple extraction plate and dynamometer platform on the Bridgeport Grinding Centre. Fig 3.3 details the experimental setup. Once the sample had been mounted onto the Bridgeport FGC 1000, the thermocouple wirings were threaded out of the machining centre before being connected to the OMEGA DAQ-USB-2401 unit. The subsequent grinding setup is shown in Fig 3.4 (a, b and c). The temperature data was collected via the DAQ Central software, whilst the force profiles were collected by the Kistler DynoWare software.

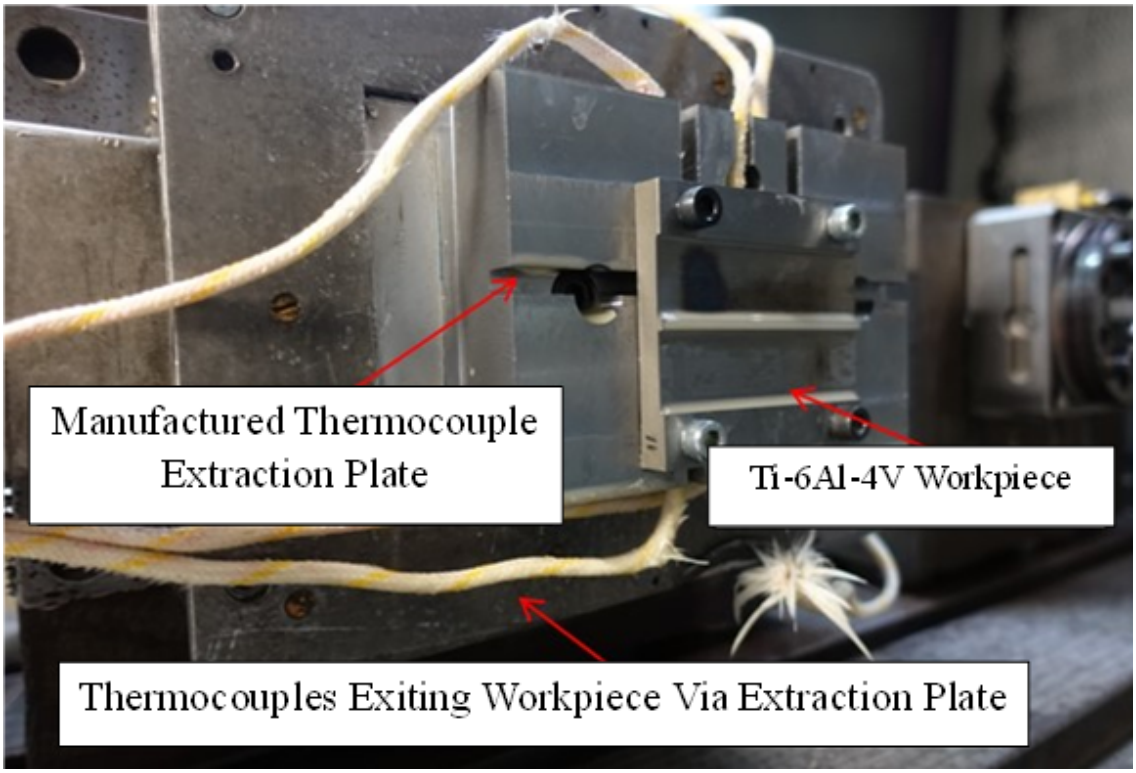



**Figure 3.3:** Embedded Thermocouple Extraction Method

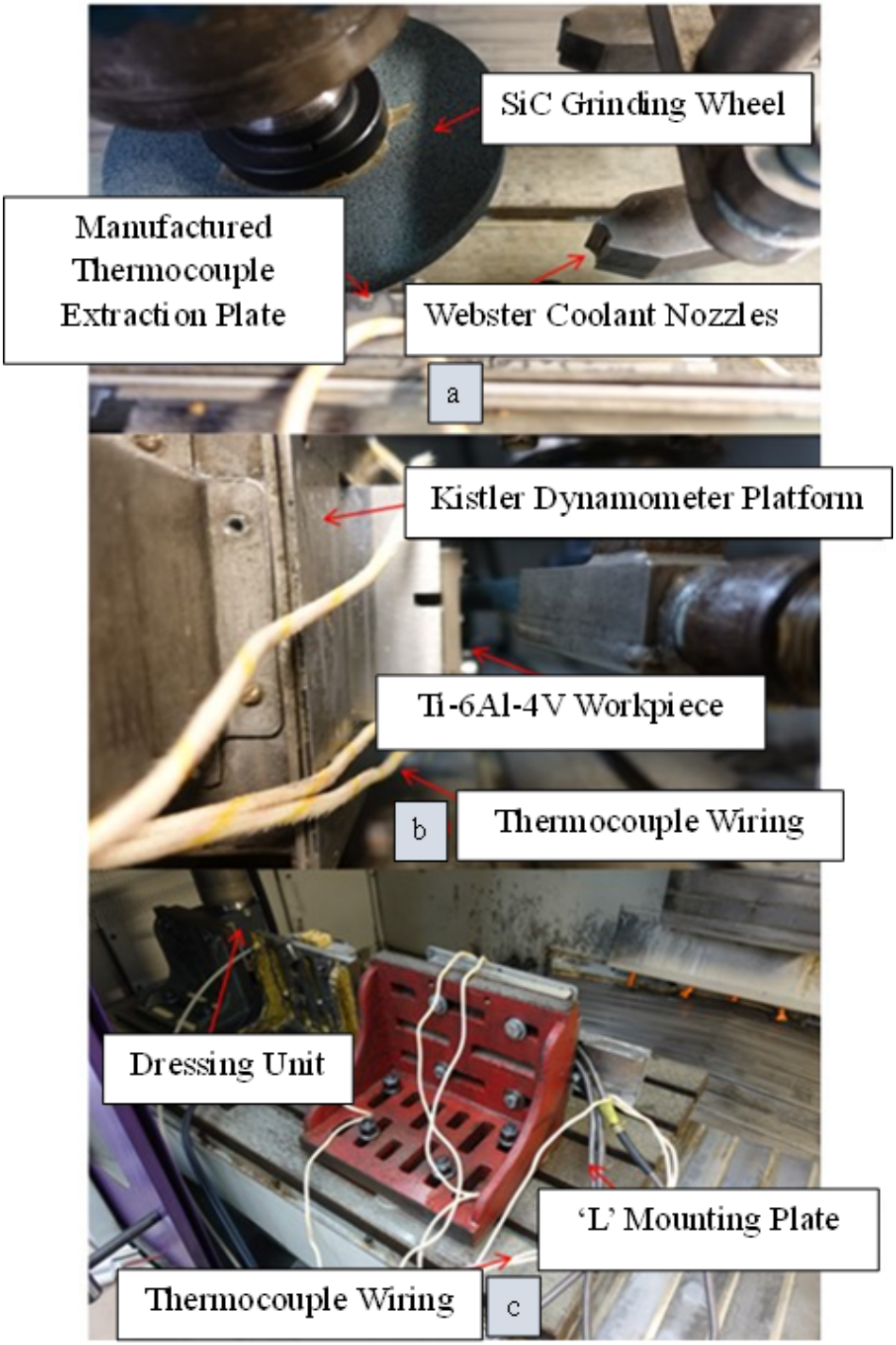



**Figure 3.4:** Complete Experimental Test Setup detailing grinding wheel (a), mounted workpiece and dynamometer platform (b) and mounting plate and dressing unit (c)

#### 3.1.1.3 Experimental Test Programme Array

Table 3.2 details the experimental test programme conducted, including the process variables and their corresponding levels. The experimental programme was proposed as an experimental array, with the variables chosen for this test programme being depth of cut, $a$, feed rate, $V_w$, and wheel speed, $V_s$, whilst the wheel material and workpiece material were kept constant as SiC and Ti-6Al-4V respectively.

Firstly, an initial stability test programme to assess workpiece temperature changes and the effect on cutting force magnitudes due to coolant delivery where no grinding occurred was conducted. This monitoring study therefore considered the effect of high pressure (84bar) and low pressure (70bar) coolant supply via the coherent jet nozzle configuration assigned to the Bridgeport had on workpiece temperature and cutting force responses. Once the stability test programme had been conducted, the test programme as presented in Table 3.2 was investigated. The wheel was intermittently dressed between passes to ensure a true a wheel as possible via a Wendt Mk IV Cantilever Dressing unit. During the dressing process, the grinding wheel speed was 20m.s$^{-1}$ and the dressing tool speed, $V_{ds}$, was 16m.s$^{-1}$ resulting in a dresser/wheel ratio of 0.8. These and further dressing parameters (wheel diameter, $\phi_s$, and dressing tool diameter, $\phi_d$), prior to the first dress are tabulated in Table 3.3. The grinding wheel used was a Saint Gobain GC 601 J 62 VKRNN SiC with 60 grit size, 43.7% grit material, 5.9% porosity and 50.5% bond. A SiC wheel was chosen as they offer a simple tooling to integrate onto conventional spindles and are cost effective for grinding materials such as Ti-6Al-4V which have low thermal conductivities and higher ductilities.

**Table 3.2:** Experimental Test Programme Process Parameters

| **Exp.** | **Wheel Speed, $V_s$ (m.s$^{-1}$)** | **Depth of Cut, $a$ (mm)** | **Feed Rate, $V_w$ (mm.min$^{-1}$)** |
|---|---|---|---|
| Test [1] | 20 | 0.3 | 150 |
| Test [2] | 20 | 1 | 150 |
| Test [3] | 20 | 1 | 150 |
| Test [4] | 30 | 1 | 150 |
| Test [5] | 20 | 1 | 150 |
| Test [6] | 30 | 0.3 | 150 |
| Test [7] | 20 | 1 | 300 |
| Test [8] | 20 | 2 | 150 |
| Test [9] | 30 | 2 | 150 |
| Test [10] | 30 | 2 | 300 |

In terms of test criteria outcomes, $G$-ratio, peak workpiece temperature and cutting forces were the desired responses, in addition to post-grinding surface integrity measurements of the workpieces pertaining to surface roughness, microhardness, residual stress and microstructural changes. The reasoning for why the variables and levels at which they were chosen and tested are briefly discussed, with each being grouped within their own variable, i.e., depth of cut, $a$, feed rate, $V_w$ and wheel speed, $V_s$;

i) The initial depth of cut analysed was 0.3mm. This parameter was chosen at this level due to it being highly indicative of the finishing grinding process (Rowe, 2009). The finishing process is a vitally important process for many thermally and mechanically sensitive components (such as turbine blades) which require this high precision process.

ii) The secondary depth of cut analysed was 1mm. This level of cut depth was chosen as a mid-point between that of finishing and large roughing machining processes.

iii) The final depth of cut assessed was 2mm. This clearly falls into the roughing machining process group and is often used for larger stock removal applications early on in the component's manufacturing cycle (Ghosh *et al.*, 2008).

iv) Slower feed rates of 150mm.min$^{-1}$ were used to approximate those feeds associated with the CFG process, whilst faster feeds of 300mm.min$^{-1}$ were chosen to represent the finishing process (Andrew *et al.*, 1985).

v) Two wheel speeds of 20m.s$^{-1}$ and 30m.s$^{-1}$ were chosen as both were applicable for either process (Donovan, Murray and Torrance, 2006; Godino *et al.*, 2018).

vi) Three thermocouples were chosen as most work from the literature only concentrate on a single thermocouple arrangement in the centre of the workpiece (Spina and Cavalcante, 2020). The positioning of the thermocouples were equi-spaced along the full length of the workpiece to ensure a diverse range of the induced workpiece temperatures along the entire grinding pass could be evaluated, i.e., at the point of entry, the middle of the workpiece and at the point of exit. The peak workpiece temperature was expected to be located at the middle point of the workpiece within the ground slot. The equi-spaced distance of 20mm between thermocouples also ensured minimal error in terms of temperature readings between each thermocouple in the series. This additionally allowed for subsequent surface integrity analysis to be determined at three different positions along the pass and at differing depths from the ground surface at those three positions.

vii) Multiple grinding passes were also undertaken to determine the temperature gradient induced in the workpiece as the thermocouples became closer to the machined surface. Further understanding of this grinding response has applications for rough-grinding, where the key passes are close to the workpiece surface.

viii) Finally, this range of parameters allowed for both roughing and finishing grinding processes to be tested, as well as a mix between the two most extreme case scenarios.

**Table 3.3:** Experimental Dressing Parameters

| **Grinding Wheel Diameter** $\Phi_s$ (mm) | **Dressing Tool Diameter** $\Phi_d$ (mm) | **Grinding Wheel Speed** $V_s$ ($m.s^{-1}$) | **Dressing Tool Speed** $V_d$ ($m.s^{-1}$) | **Dresser/ Wheel Ratio** |
|---|---|---|---|---|
| 214.1 | 105 | 20 | 16 | 0.8 |

### 3.1.2 Surface Integrity and Optical Microscopy Analysis

Once the grinding tests had been completed, the workpiece samples were cut via wire EDM into six further samples, each detailing the location of the embedded thermocouples as detailed in Fig 3.5 (a and b). The order in which the surface integrity tests were conducted followed the procedure as outlined in Field and Kahles (1964). This is based on the concept of conducting None-Destructive Test (NDT) prior to Destructive Testing (DT) to ensure that the output was not affected by the latter being conducted first. The initial surface

integrity testing then considered the surface roughness of the ground workpiece surfaces. This was achieved via the portable Mitutoyo Surftest 310-SJ surface roughness device *[Coventry, Warwickshire, UK]*. The testing probe's diamond tipped stylus was then drawn across the ground surface evaluation length of 5mm with a cut-off length of 0.8mm, whilst 2D readings detailing the $R_a$ surface profile were the requested output. This was completed for both the parallel direction and the perpendicular direction to the grinding pass. Three measurements of each were taken so an average could be calculated to reduce overall error.

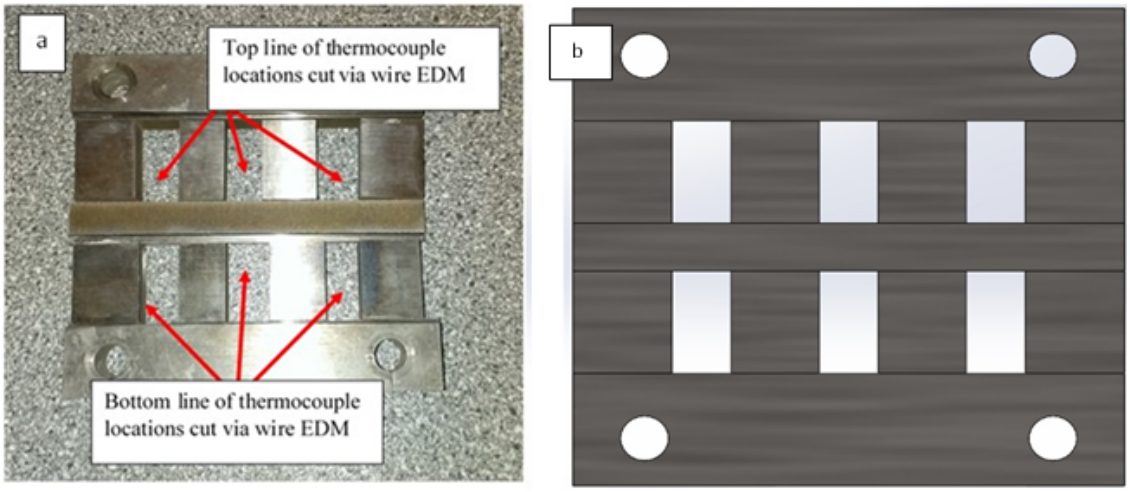



**Figure 3.5:** Surface Integrity Wire EDM Prepared Sample; Physical (a) and CAD Model (b)

After the surface roughness testing had been completed, the wire cut EDM samples were mounted in edge retentive Bakelite powder, with the cross-sectional surface being the visible face. The mounting was achieved via the Buehler-Simplimet 2 mounting press. Subsequently, grinding and polishing of the mounted samples via the Buehler Alpha-2 speed grinder/polisher was undertaken.

Table 3.4 details the operating conditions implemented for the sample grinding/polishing method as per the standard Buehler operating procedural manual. Three SiC grinding papers were used for the grinding portion of the process (240$\mu$m, 600$\mu$m and 1200$\mu$m respectively) for two minutes with a standard water coolant. The final polishing process utilised three polishing cloths for a total of four minutes each, with a decreasing diamond and colloidal silica suspension per cloth (9$\mu$m, 3$\mu$m and 0.05$\mu$m).

**Table 3.4:** Buehler Alpha-2 Speed Grinder Polisher Operating Parameters

| **Grinding** | | | | |
|---|---|---|---|---|
| **SiC Paper (Grit Size - $\mu$m)** | **Force (N)** | **Time (mins)** | **Water (On/Off)** | **Speed (rpm) Rotating Direction** |
| 240 | 25 | 2 x 1 | On | 120/complimentary* |
| 600 | 25 | 2 x 1 | On | 120/complimentary* |
| 1200 | 25 | 2 x 1 | On | 120/complimentary* |
| **Polishing** | | | | |
| **Polishing Cloth** | **Force (N)** | **Time (mins)** | **Liquid Suspension** | **Speed (rpm) Rotating Direction** |
| Trident Cloth | 25 | 4 | 9$\mu$m MetaDi Supreme Diamond | 120/complimentary* |
| Trident Cloth | 25 | 4 | 3$\mu$m MetaDi Supreme Diamond | 120/complimentary* |
| MicroCloth | 25 | 4 | 0.05$\mu$m Mastermet Colloidal Silica | 120/complimentary* |
| ***Complementary: Workpiece specimen holder/grinder disc rotating in the same direction** ****Contrary: Workpiece specimen holder/grinder disc rotating in opposite directions** | | | | |

Once the samples had been mounted, polished and achieved a mirror surface finish, microhardness testing of the mounted samples was undertaken. This analysis was conducted via the Mitutoyo microhardness tester HM 124 *[Coventry, Warwickshire, UK]* fitted with a Knoop Hardness diamond tipped indenter for the tooling equipment. The measurement method utilised an applied load of 50g for a dwell time of fifteen seconds. Three readings per depth were taken across a range of depths (10$\mu$m - 500$\mu$m) to establish a HK vs. Indentation Depth curve. Average microhardness values at each thermocouple location were also calculated to establish potential trends in microhardness values across the length of the grinding pass.

After the microhardness tests had concluded, the mounted samples underwent a chemical etching procedure. The etching of the sample surfaces was conducted via an amended Kroll's reagent solution consisting of 7%HF, 10% $HNO_3$ with balanced water for approximately thirty seconds to enable the duplex $\alpha$ and $\beta$ microstructure of Ti-6Al-4V to be scrutinized. This was deemed as a sensible and next logical analysis to undertake as images of the cross-sectional depth surface would yield possible features not discernible via visual inspection; something important to inspect for making links between the surface

roughness ($R_a$) values, microhardness values and subsurface damage that was also to be experimentally measured. The optical microscopy analysis was conducted via the Leica DMLM microscope and integrated Pixelink camera for image acquisition. The captured images were subsequently analysed via the Omnimet 8.7 digital image software installed on an attached PC. The associated resolution for the microscopy analysis was 1280x1024, whilst the lens position was 50x, resulting in a resolution rate of 0.4312$\mu$m/pix. Once the etched samples were returned, the microscopy analysis was conducted on the cross-section using the setup and parameters as described above using four different magnifications; 2.5x, 5x, 20x and 50x. Additionally, the Wire-EDM subsurface microstructure was also scrutinized using the same magnifications as used previously.

A small number of samples were sent out to Stresscraft Ltd. *[Leicestershire, UK]* for residual stress measurements to be gathered. This was achieved by first bonding one EA-06-031RE-120 strain gauge rosette [*Vishay Measurements Group Ltd., UK]* to the surface of the sample. Fig 3.6 details the prepared strain gauge rosette for the Test [2]a sample. This was subsequently connected to a strain indicator. A hole was then orbitally drilled through the rosette into the sample using an inverted cone T/C cutter. Fig 3.7 (a and b), details the setup for the incremental drilling and measurement process for the Test [2]a sample. Measurements depths were assigned progressively from 16$\mu$m to 704$\mu$m. The relaxed residual stresses thus causes a change in strain gauge response at the hole boundary. The strain responses were finally processed through a patented software logarithm to calculate the relaxed residual stresses in the sample. Results from the surface integrity assessments are detailed in section 6.1.

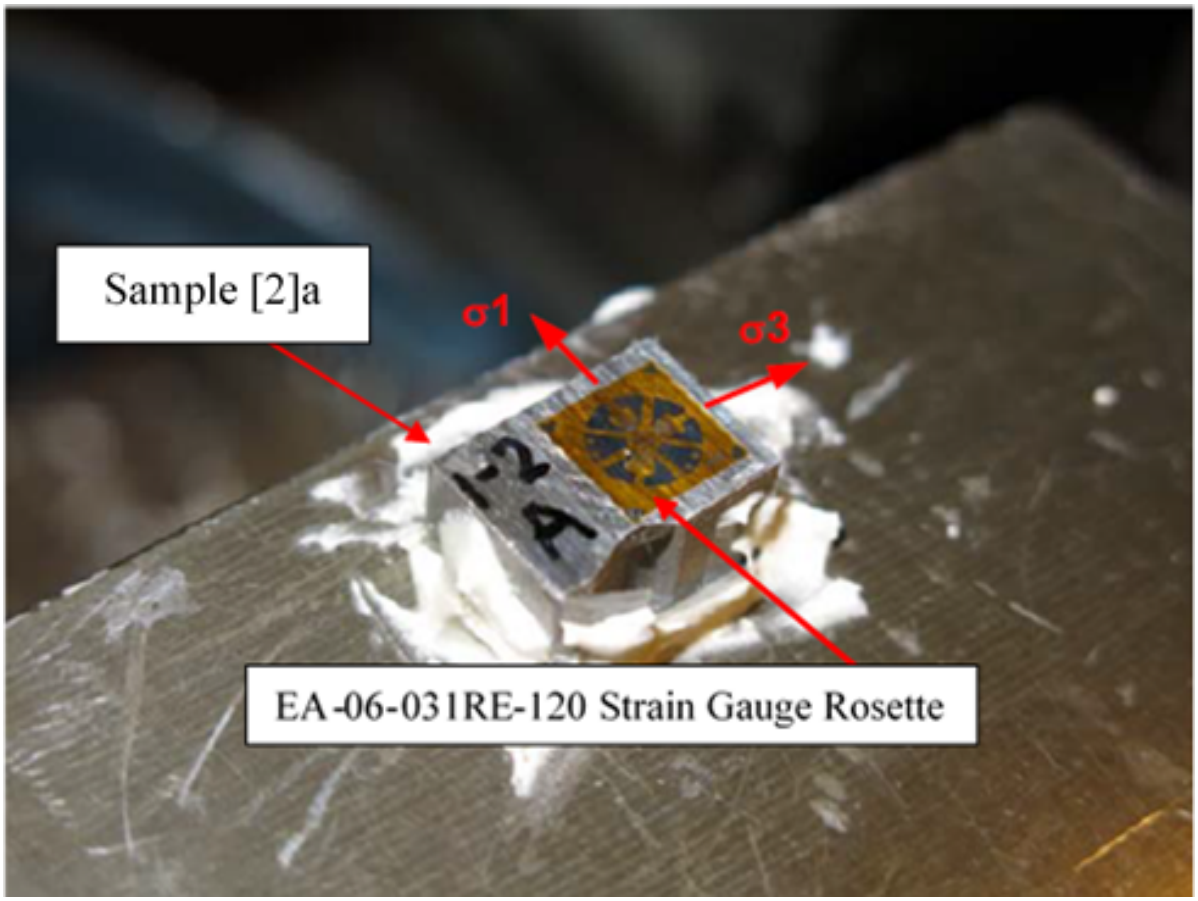



**Figure 3.6:** Residual Stress Strain Gauge Setup Example

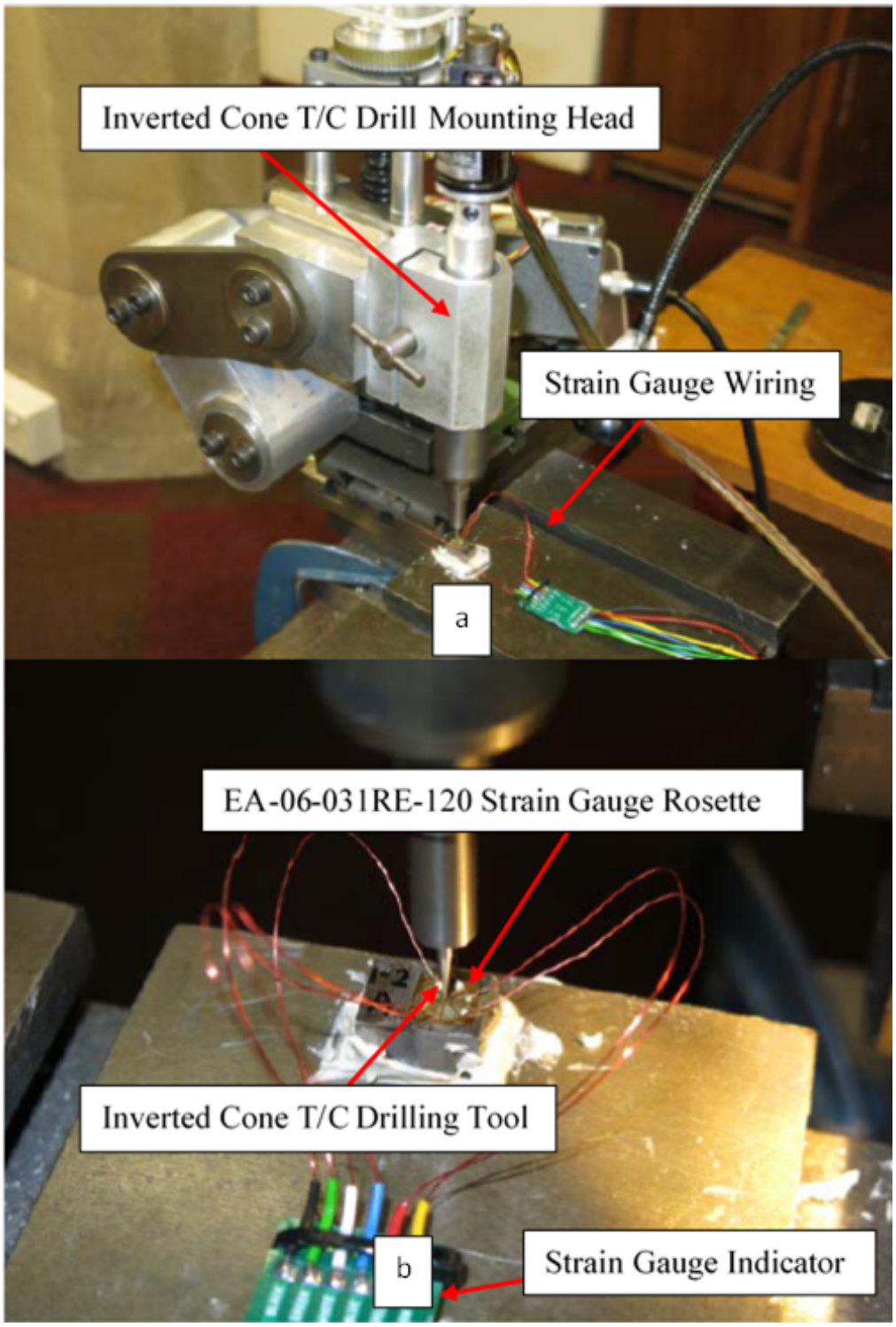



**Figure 3.7:** Incremental Drilling Setup (a) and Process (b) for Test [2]a Sample

After the standard microscopy evaluations of the samples had been completed, a SEM analysis was undertaken to investigate whether any additional microstructure alterations could be ascertained that couldn't be detected by conventional investigations. One hundred SEM images were captured detailing all ten experimental tests conducted. This was initiated to assess the complete range of grinding parameters evaluated. Due to the extensive nature of this final study, only a sample of the total SEM captures are presented in section 6.1.2.3 as the study involved taking SEM images at x200, x500, x1000 and x1500 magnifications for both the cross-section of the ground sample to evaluate subsurface damage, in addition to the ground faces to determine changes at the grinding wheel/workpiece surface interface. For completeness, the surface due to sample manufacture via Wire EDM was also evaluated. As discussed, section 6.1.2.2 details samples for Test [1] ($V_s$ = 20m.s$^{-1}$, $a$ = 0.3mm and $V_w$ = 150mm.min$^{-1}$), Test [6] ($V_s$ = 30m.s$^{-1}$, $a$ = 0.3mm and $V_w$ = 150mm.min$^{-1}$), Test [9] ($V_s$ = 30m.s$^{-1}$, $a$ = 2mm and $V_w$ = 150mm.min$^{-1}$) and Test [10] ($V_s$ = 30m.s$^{-1}$, $a$ = 2mm and $V_w$ = 300mm.min$^{-1}$). As a final study, cross-sectional images were obtained via a standard camera for comparison with the SEM images regarding Test [9] and Test [10].

### 3.1.3 *G*-ratio Analysis

Further data calculated included the *G*-ratio for the grinding tests conducted. Since it is well established that the wear of the grinding wheel along its diameter is caused by the failure of both the abrasive grain and the bond material, resulting in sharper defined cutting edges to replace blunter grains, higher workpiece temperatures are subsequently observed (Rodriguez *et al.*, 2019). If the wheel wear could then be measured it would allow for the grinding process efficiency, i.e., the *G*-ratio, to be evaluated (Ribeiro *et al.*, 2020). To ensure that the *G*-ratio could be calculated, the diameter of SiC grinding wheel used throughout the test programme was subsequently measured between each pass and after each subsequent dress via the Mitutoyo CMM *[Coventry, Warwickshire, UK]*. Six points were taken around the cutting face of the wheel, before an average diameter was calculated (mm). Additionally, the roundness profile of the wheel was also noted. The change in wheel diameter (i.e., the level of wheel wear between tests/passes) could then be determined. This process was undertaken after being measured prior to both the initial dress and the initial Stability Check 4 test. Knowing the depth of cut used for each test/pass and the thickness of the grinding wheel, the volume of Ti-6Al-4V material removed from the test/pass could be calculated. Once both

the wheel wear and the volume of material removed were known, the subsequent $G$-ratio could be evaluated using Eqn. 2.1.

## 3.2 Phase 2: Dimensional Analysis Numerical Models

Once the experimental test programme had been concluded and analysed, a subsequent DA of the same grinding test programme outlined in Table 3.2 was also undertaken in an attempt to analytically predict the test findings. In terms of the approach applied, with both the workpiece temperature and cutting force upon the tool being the required output, the six Buckingham-$\pi$ groups were derived using the Exponent Method for both outputs, with the base quantities in relation to the analysis of grinding temperature and cutting forces being Mass, $(M)$, Length, $(L)$, Time, $(T_1)$ and Temperature $(\theta_1)$. The variables considered when deriving the workpiece temperature and cutting force Buckingham-$\pi$ groups were feed rate, $(\mathrm{V}_w)$, depth of cut, $(a)$, wheel speed, $(\mathrm{V}_s)$, the specific heat capacity of the workpiece, $(c_w)$, the thermal conductivity of the workpiece, $(\lambda_w)$, the shear strength of the workpiece, $(\tau_w)$, the specific heat capacity of the wheel, $(c_s)$, the shear strength of the wheel, $(\tau_s)$, and the thermal conductivity of the wheel, $(\lambda_s)$. Once the DA had been undertaken, a basic power-law evaluation was conducted, before a regression analysis on the data was subsequently assessed. This then allowed for trends to be plotted comparing the predicted DA data for both peak workpiece temperature and cutting forces when observing changes in feed rate, wheel speed and depth of cut against that of the experimental data pertaining to the same variables.

# Chapter 4

# System Stability Tests

## 4.1 Results

Fig 4.1 details the stability check temperature traces for TC1, TC2 and TC3 respectively, where no grinding or coolant delivery were apparent. Some variance between the thermocouples are visible, but these were deemed negligible and within engineering error when considering the expected temperature magnitudes when material removal began.

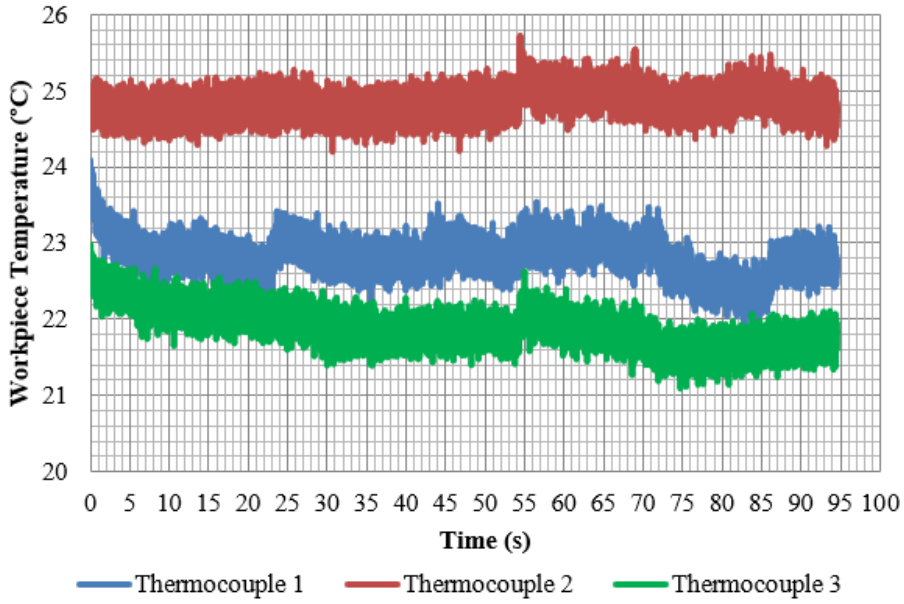



**Figure 4.1:** Thermocouple Temperature Measurement System Stability Check 1 - No Grind; No Coolant

Fig 4.2 details the stability check cutting force traces for $F_x$, $F_y$ and $F_z$ respectively, where no grinding or coolant delivery were apparent. Again, some drift is noticed; however, this was deemed negligible in terms of the expected cutting forces predicted by the literature (Tang, Du and Shen, 2009).

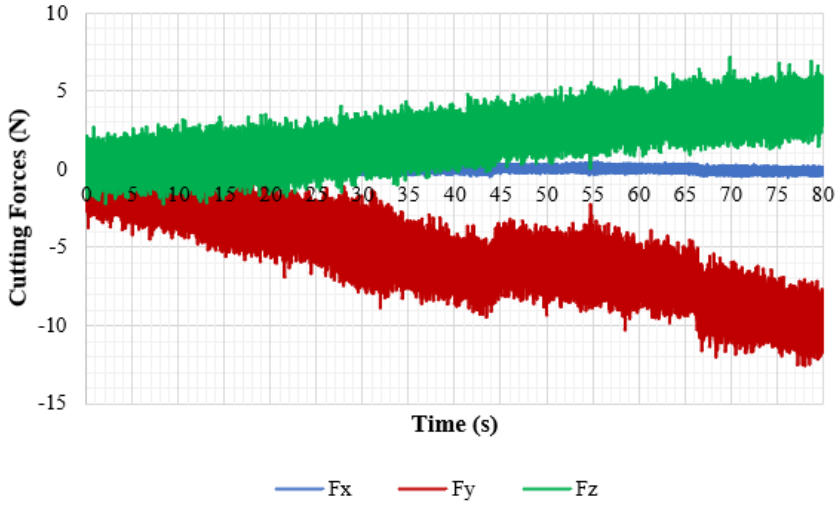



**Figure 4.2:** Cutting Force Measurement System Stability Check 1 - No Grind; No Coolant

Fig 4.3 details the stability check temperature traces where no grinding and low pressure coolant delivery were apparent. The temperature response for TC2 is somewhat unexpected, potentially resulting from issues regarding the thermal cement fixation at that location.

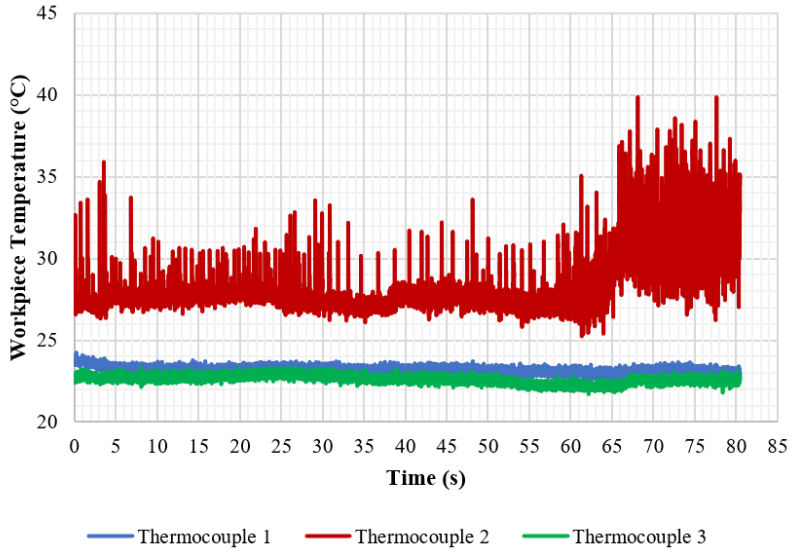



**Figure 4.3:** Thermocouple Temperature Measurement System Stability Check 2 - No Grind; Low Pressure Coolant

Fig 4.4 details the stability check cutting force traces where no grinding and low-pressure coolant delivery were apparent. The inclusion of the low pressure coolant demonstrates a minimal effect on the cutting force responses of +25N to -42N for the $F_z$ and $F_y$ components respectively.

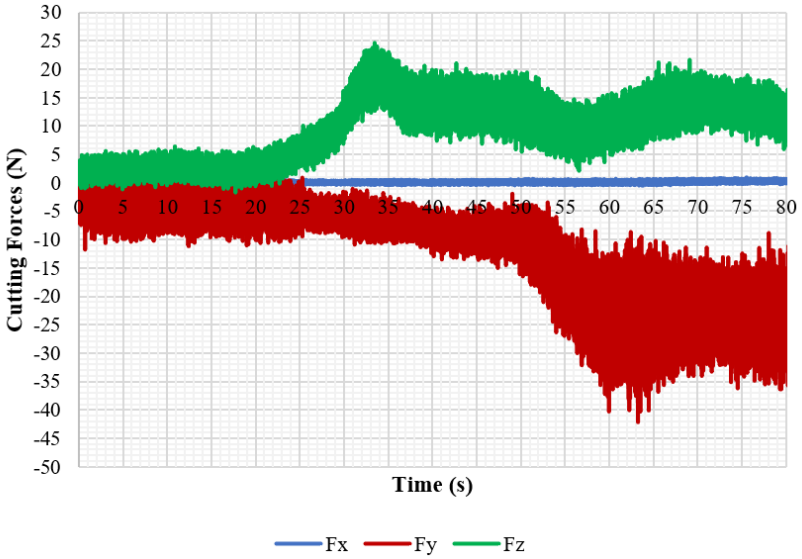



**Figure 4.4:** Cutting Force Measurement System Stability Check 2 - No Grind; Low Pressure Coolant

Fig 4.5 details the stability check temperature traces where no grinding and high pressure coolant delivery were apparent. Again, TC2 demonstrates an unexpected response, possibly caused by the implantation mode used for fixation.

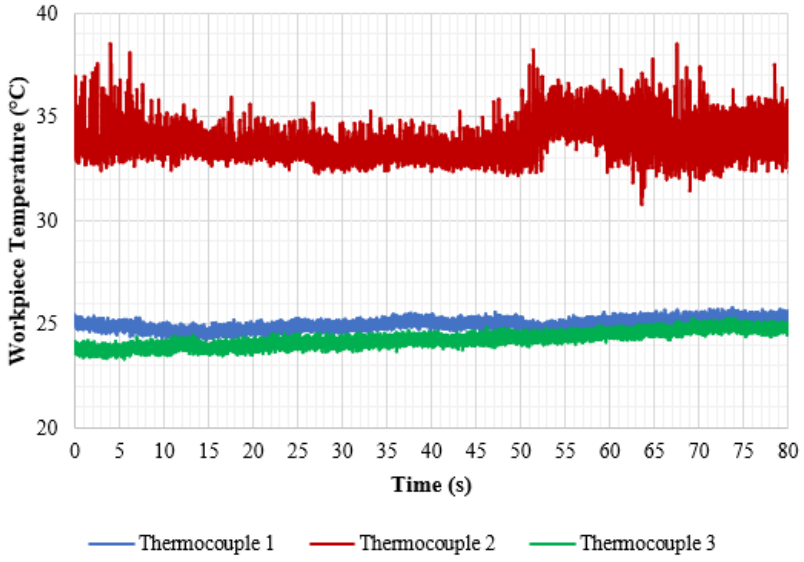



**Figure 4.5:** Thermocouple Temperature Measurement System Stability Check 3 - No Grind; High Pressure Coolant

Fig 4.6 details the stability check cutting force traces where no grinding and high pressure coolant delivery were apparent. Here, the application of the coolant significantly increased the associated cutting forces, resulting in +200N to -180N on the $F_z$ and $F_y$ components respectively.

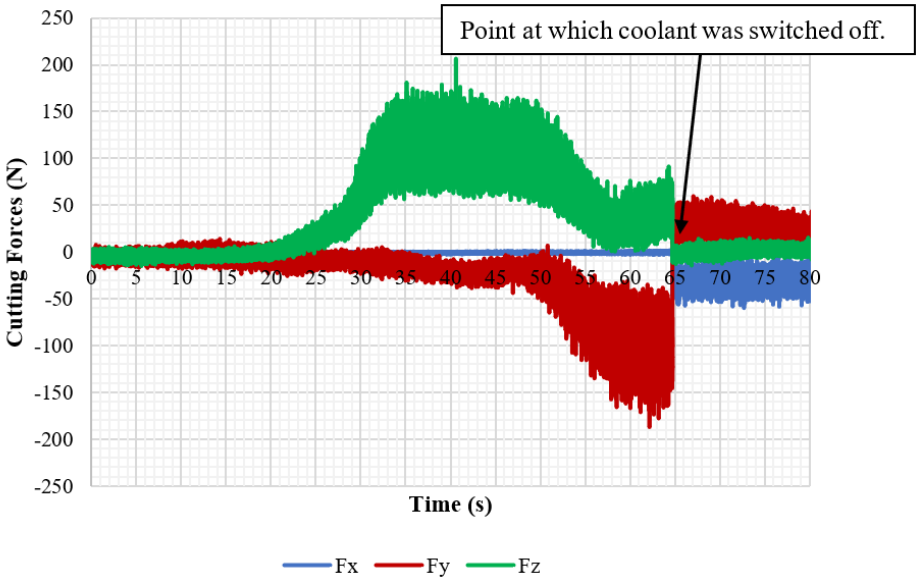



**Figure 4.6:** Cutting Force Measurement System Stability Check 3 - No Grind; High Pressure Coolant

Fig 4.7 details the stability check temperature traces where an initial grinding cut and high pressure coolant delivery were apparent. A clear trend of increasing workpiece temperature as the grinding wheel traversed the workpiece is evident, increasing linearly through TC1, TC2 and TC3.

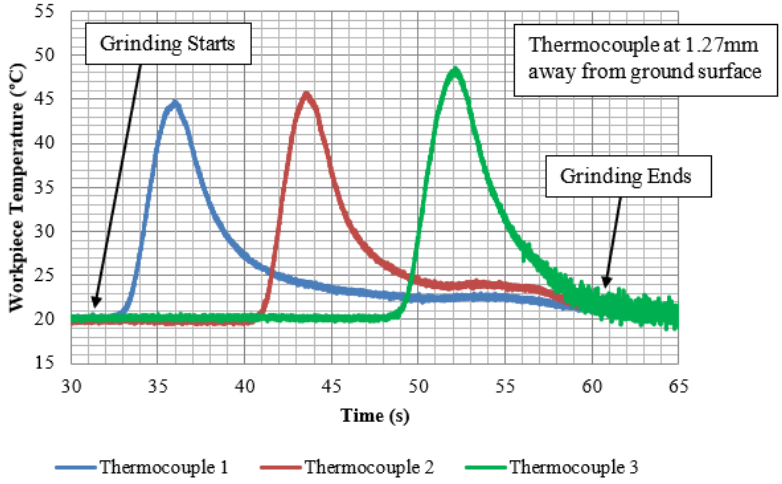



**Figure 4.7:** Stability Test 4: Workpiece Temperature Thermocouple Response - With Grind; High Pressure Coolant

Fig 4.8 details the stability check cutting force traces where an initial grinding cut and high pressure coolant delivery were apparent. A clear relationship regarding $F_y$ and $F_z$ is demonstrated, with $F_z > F_y$. This is to be expected as $F_z$ is the tangential cutting force and is therefore the component of the total cutting force which results in the shearing of the workpiece (Shaw, 1996a).

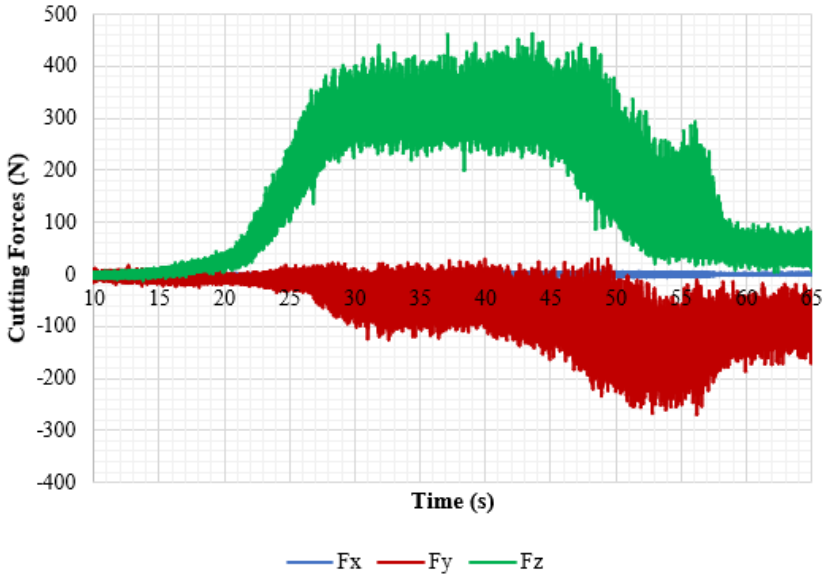



**Figure 4.8:** Stability Test 4: Cutting Force Response - With Grind; High Pressure Coolant

## 4.2 Discussion

Prior to commencing the workpiece temperature and cutting force testing, an initial stability check for the 1 x 3 thermocouple configuration detailed in Fig D.3 was conducted. As the nature of the experimental work was completely unique, with almost no research undertaken when using multiple thermocouples in series, a baseline stability check regarding workpiece temperature changes and the affect on cutting force magnitudes due to coolant delivery where no grinding occurred was deemed an appropriate study. This monitoring investigation therefore considered the effect of high pressure (84bar) and low pressure (70bar) coolant supply via the Webster nozzle configuration assigned to the Bridgeport. This was representative of grinding and wheel cleaning coolant delivery parameters respectively. The workpiece was thus mounted onto the dynamometer force platform and thermocouple extraction plate configuration which was positioned at 90° to the machining bed, and 100mm away from the grinding tooling. For Stability Check 1 through to Stability Check 3 (Fig 4.1 - Fig 4.6), no grinding was apparent, and so only the supply pressure was altered. For Test Stability Test 4 (Fig 4.7 – Fig 4.8), a grinding pass was made. This grinding pass utilised the same process parameters as Test [1] which are detailed in Table 4.1. In terms of the experimental data collected, $F_N$, $F_T$ and $F_{CrossFeed}$ are detailed as the $z$, $y$ and $x$ components of the cutting force respectively.

**Stability Check 1 – No Grind; No Coolant**

Fig 4.1 presents the response of the thermocouple arrangement whilst operating without any external factor influence. As can be seen, there is a very slight variance in the thermocouple response, with thermocouple 2 responding approximately 12% above thermocouple 3 and 8% above thermocouple 1. Possible causes for this phenomena include thermocouple 2 being slightly closer to the grinding plane than either thermocouple 1 or thermocouple 3, or possibly thermocouple embodiment error in relation to the thermal cement Shen *et al.*, (2008). An increased workpiece temperature reading such as that suggested by thermocouple 2 would indicate that an increased voltage difference between the hot and cold junctions was occurring. This also reinforces the underlying physics of how thermocouples create a temperature gradient via a change in voltage due to the two dissimilar metals within the thermocouple (chromium and aluminium for this k-type) having different thermal conductivities; 69.1W.m$^{-1}$ and 250W.m$^{-1}$, respectively. This also suggests that a change in thermocouple type, i.e., a change in the metal wirings used, might affect the temperature

readings gathered. This variance was deemed sufficiently low in error for the required temperature ranges wishing to be predicted, and so the thermocouple placement method and configuration was deemed successful.

Fig 4.2 indicates the baseline cutting force readings acquired from the Kistler dynamometer instruments. There is also clearly some degree of drift occurring within the cutting force responses, as can be seen by the system's $F_y$ and $F_z$ plot (approximately 13N for $F_y$ and 4N for $F_z$). This could potentially be due to the inherent current leakage of the Metal Oxide Semiconductor Field Effect Transistor (MOSFET)/Junction Field Effect Transistor (JFET) which piezoelectric dynamometers and the connected charge amplifiers consist of, or possibly due to the internal resistance being too low as $\tau_{tc} = \mathrm{R}_t.\mathrm{C}_t$, thus resulting in an increase in voltage and thus increased drift. Here, $\tau_{tc}$ is the time constant, $\mathrm{R}_t$ is the resistance and $\mathrm{C}_t$ is the capacitance. However, as long as the input insulation resistance is sufficiently high, the drift observed should be relatively slow towards the positive/negative limit, thus resulting in minimal error. Again, in a similar manner to the baseline thermocouple temperature responses, this was deemed to be sufficiently within acceptable error due to the generated cutting forces generally being up to 2.5kN. Again, it should also be noted that some degree of drift is to be expected within any system when one considers electronic inaccuracies. As such, these drift patterns are often observed unless upgrading the relevant hardware.

**Stability Check 2 – No Grind; Low Pressure Coolant**

From Fig 4.3, an apparent increase in workpiece temperature is observed sixty-five seconds into the data acquisition. This contradicts the usually expected temperature response when using coolants, i.e., coolants reduce workpiece temperatures within a machining context. The author surmises that potential manufacturing abnormalities within the thermocouple cement locations have resulted in a relative movement between the thermocouple node and the grinding surface, thus causing the thermocouple node to be moving in the workpiece, i.e., friction between the node and the cavity limit resulting in an increase in workpiece temperature reading. Another possible explanation could be the coolant being at a different initial temperature during the course of the testing time frame. It should also be suggested that the manufacturing of the embedded thermocouples within the workpiece via thermal cement will need to be highly accurate to reduce potential errors from any temperature data

gathered.

The cutting force results from Stability Check 2, which are presented in Fig 4.4, show an interesting response at twenty seconds into the pass. A further significant increase of 80% in cutting force result is observed peaking at thirty-three seconds into the pass. The author surmises that despite the low pressure coolant being used, this additional load on the workpiece increased the overall cutting forces experienced, in addition to the observation being associated with the nozzle angle and stand off distance from the workpiece. Despite this peak, the cutting force response was observed to then reduce again to a steady response of ≈58% of the original value from forty seconds into the pass until the termination of the data acquisition. Similarly, the $F_y$ trace observed a similar peak at fifty seconds into the data acquisition, whereby a 62.5% spike was observed. This increased magnitude in load was then observed until the end of the data acquisition. Additional observations include the $F_y$ response undergoing an overall larger level of signal variation than $F_z$, as well as the unexpected trend of $F_z$ (Tangential Direction) indicating higher cutting forces than $F_x$ (Normal Direction).

**Stability Check 3 – No Grind; High Pressure Coolant**

Fig 4.5 displays an interesting result in terms of workpiece temperature response. When utilising the high pressure coolant supply, a similar magnitude of temperature is observed as when using the low pressure coolant supply. A similar trend in the workpiece temperature traces is seen until approximately ninety seconds into the pass, when a more sustained increase can be noted. Thermocouple 2 is observed to indicate a higher temperature reading than both thermocouple 1 and thermocouple 2 by ≈25.6%. Again, this could indicate thermocouple 2 being slightly closer to the grinding plane than both thermocouple 1 and thermocouple 3. The author suggests similar explanations to those expressed for the increase in temperature as proposed for the low pressure coolant stability test.

Fig 4.6 displays the cutting force response when the high pressure coolant supply was introduced into the system. From twenty seconds into the data acquisition, a gradual rise in $F_z$ response is observed, reaching an average peak of 170N. This trace then clearly gradually reduces until fifty-six seconds, before a short second rise, which then flat lines. A similar trend is observed with the $F_y$ trace, again, gradually rising until approximately

sixty seconds into the acquisition, whereby a peak cutting force of -170N was indicated. It is clear from sixty-five seconds into the pass the point at which the coolant delivery system was switched off, as can be determined from the quick fall in cutting force response. The higher pressure coolant increases the overall cutting force within the system by a significant margin ($\Delta$81.9% in magnitude of $F_{Total}$ between the two differing coolant pressure stability tests), and is an important observation to make reference to for future experimental tests when grinding with high pressure coolant supplies. This result has also been observed in the literature by the likes of Sai *et al.*, (2015).

**Stability Test 4 – With Grind; High Pressure Coolant**

Stability Test 4 was the first point during the experimental test programme that any material removal was undertaken. The workpiece temperature results from Stability Test 4 are presented in Fig 4.7. Again, as mentioned, little work has been published in relation to workpiece temperature measurement whilst grinding, with what little work that has been conducted concentrating on single thermocouples for temperature data acquisition. This work goes much further by using a multiple, in-series, thermocouple configuration. As can be clearly ascertained from Fig 4.7, the peak workpiece temperature is observed to increase as the grinding wheel continued along its path through the workpiece, i.e., thermocouple 1 observed an initial workpiece temperature of 36°C, thermocouple 2 observed a workpiece temperature of 37°C whilst thermocouple 3 experienced a peak workpiece temperature of 43°C. This result suggests that a single point thermocouple placement method within the workpiece is insufficient by 13.9% for experimentally testing Ti-6Al-4V workpiece temperature responses whilst grinding. However, as can be demonstrated by the temperature readings collected via the stability checks, some variation in the responses is apparent. To ensure a more accurate and consistent temperature reading a more appropriate fixation method should be used for future testing.

As presented in Fig 4.8, the grinding force responses are detailed with the expected trends evident, i.e., a gradual increase in $F_z$ at twenty seconds into the pass, peaking at 400N in magnitude which is in reference to the initial phase of the grinding wheel entering the workpiece. A secondary cutting stage follows, with chatter of $\pm$150N, until the $F_z$ trace decreases at forty-five seconds into the pass before becoming negligible at eighty seconds into the pass. Again, as is to be expected, a similar trend is observed in the $F_y$ trace, but

in the opposite direction to $F_z$. Finally, the $F_x$ response is negligible throughout, as this is the cross-feed force in the experimental test set-up, and whose response is also to be expected.

When assessing the effect of both the low pressure and high-pressure coolant on the cutting forces acting on the tooling, an increased load was observed when using the high-pressure coolant. This added ± 170N to the response. Clearly this would have a greater impact on the measured data when cutting forces are lower such as when testing less aggressive grinding parameters as detailed, for example, in Test 1 ($a$=0.3mm, $V_w$=150mm.min$^{-1}$, $V_s$=20m.s$^{-1}$). Here the cutting forces reached a maximum of +700N and -300N for $F_z$ and $F_y$, respectively indicating that the effect of the high-pressure coolant should be considered a factor when analysing the data set. What is also interesting to note is that both $F_z$ and $F_y$ appeared to respond with similar levels of chatter of around ± 170N during the system stability checks, indicating some variance without any metal cutting taking place.

In summary from the baseline stability checks, it can be inferred that for all future testing presented herein, the use of low pressure coolant alone for wheel cleaning would add approximately 25N to any cutting force reading. When the high-pressure coolant is used for grinding, it would add approximately 170N-180N to any cutting force measurement.

# Chapter 5

# Experimental Test Programme

## 5.1 Results

### 5.1.1 *G*-ratio

Fig 5.1 details the change in *G*-ratio when the depth of cut was increased from 0.3mm through to 2mm. A 77.8% decrease in *G*-ratio can be observed when assessing this relationship.

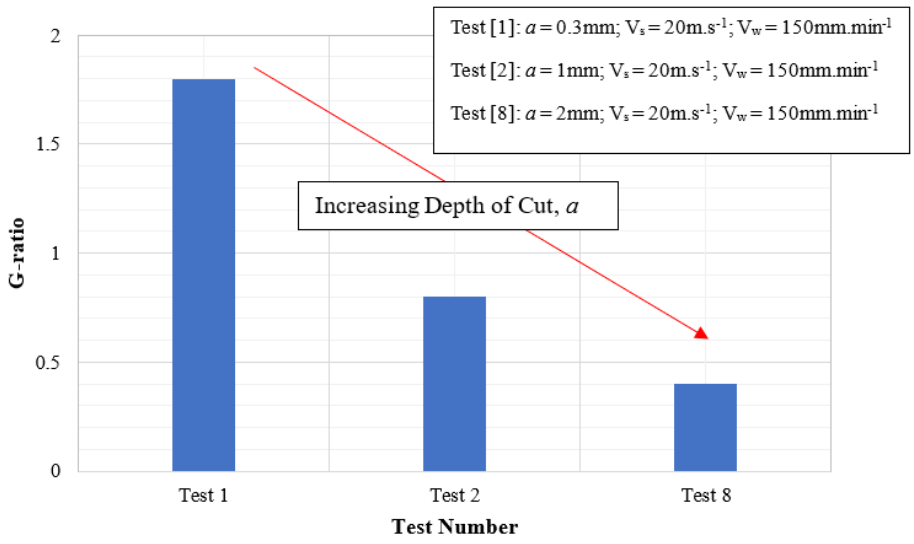



**Figure 5.1:** *G*-ratios for changes in Depth of Cut for Test [1], Test [2] and Test [8]

Fig 5.2 presents the change in $G$-ratio when the wheel speed was increased from 20m.s$^{-1}$ to 30m.s$^{-1}$. An increase in $G$-ratio of 37% can be determined when altering this grinding variable.

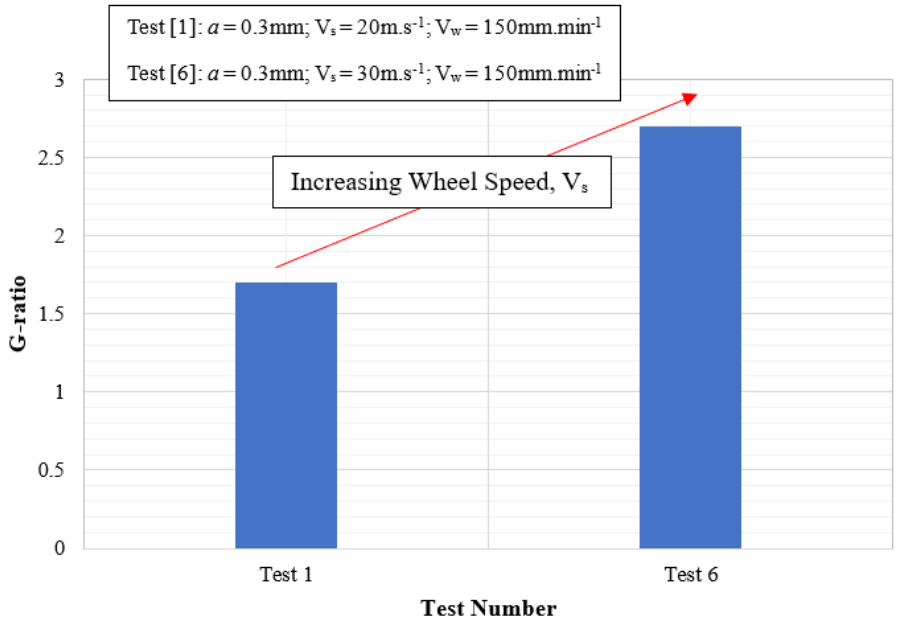



**Figure 5.2:** $G$-ratios for changes in Wheel Speed for Test [1] and Test [6]

Fig 5.3 details the change in $G$-ratio when increasing the feed rate from 150mm.min$^{-1}$ to 300mm.min$^{-1}$. A 16% increase can be evaluated when altering this grinding variable.

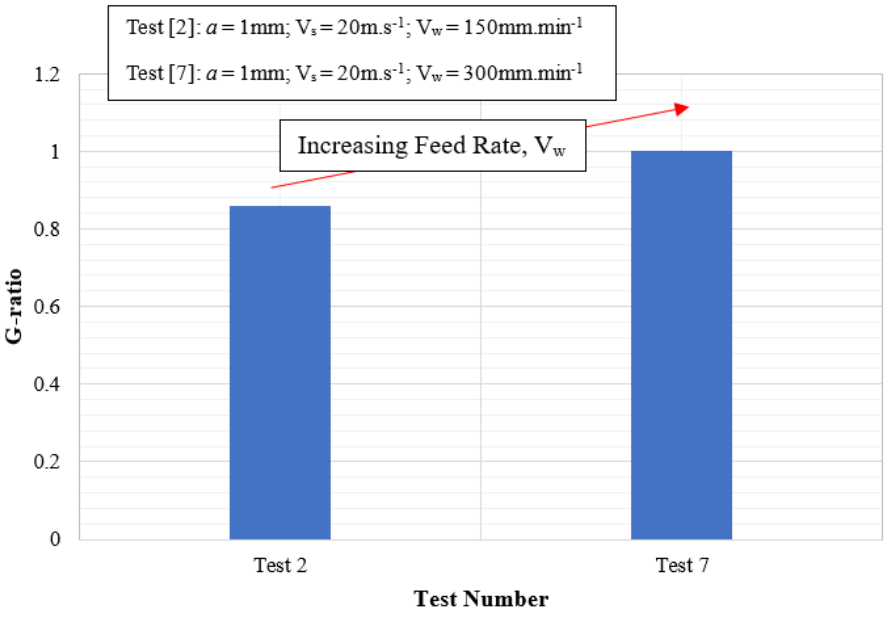



**Figure 5.3:** $G$-ratios for changes in Feed Rate for Test [2] and Test [7]

Here, as presented in Fig 5.4, the $G$-ratio is plotted against the volume of material removed for the Test [1] data sets acquired. This figure indicates signs of an attritious wear mechanic occurring even when low level grinding conditions are implemented.

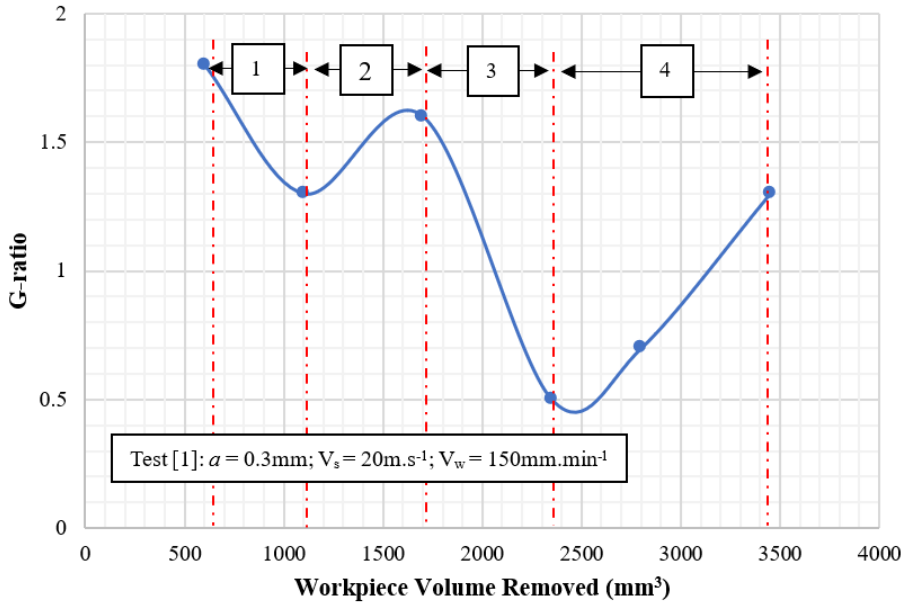



**Figure 5.4:** $G$-ratio vs. Volume of Workpiece Removed - Test [1] across five passes

As demonstrated in Fig 5.5, the $G$-ratio is plotted against the volume of material removed for the Test [6] data sets acquired. Interestingly, the wear profile indicates that constant wear, attritious wear, grain fracture and bond fracture are all apparent, and are discussed in more detail in section 5.2.1.

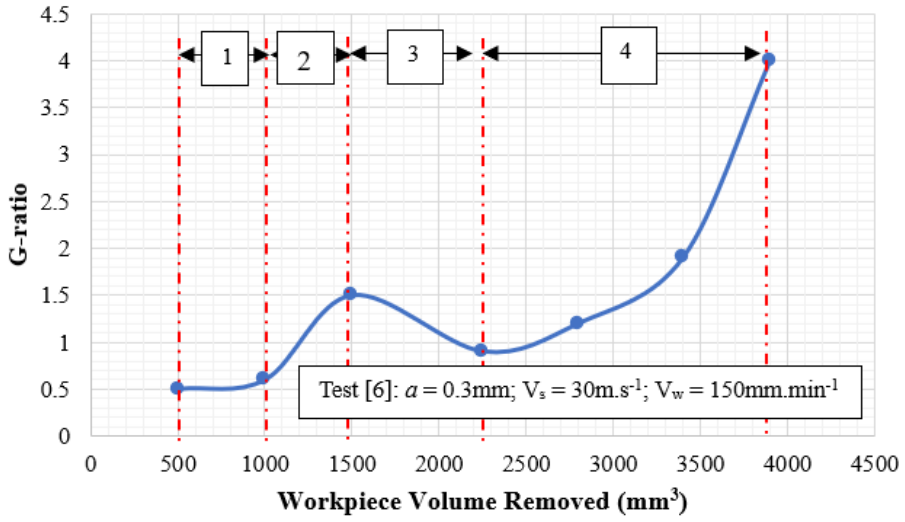



**Figure 5.5:** $G$-ratio vs. Volume of Workpiece Removed - Test [6] across seven passes

### 5.1.2 Workpiece Temperature

Fig 5.6 details the thermocouple responses for pass one of Test [1]. A similar trend can be determined as was presented in Fig 4.7. The workpiece temperature clearly increases along the grinding pass from point of tool entry to point of tool exit, with the location of TC3 indicating the peak workpiece during the cut.

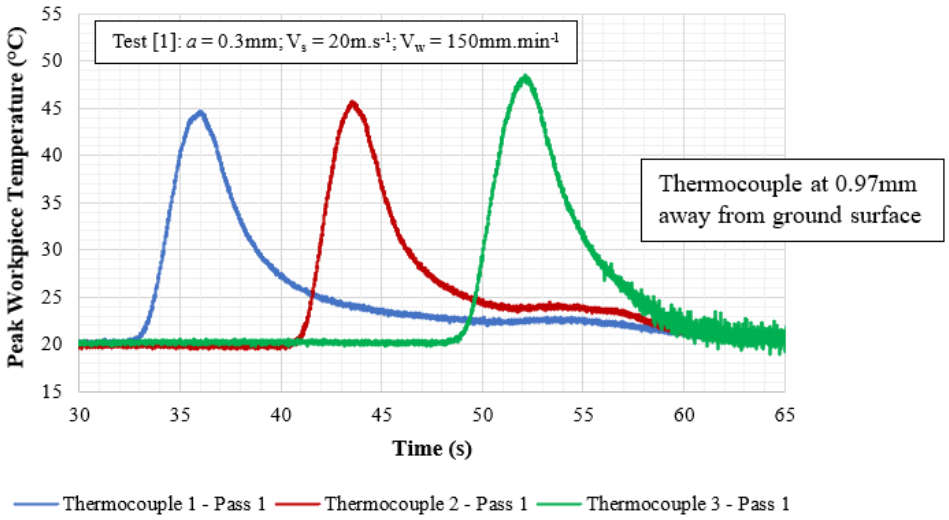



**Figure 5.6:** Test [1] – 0.97mm Stand Off Distance Workpiece Temperature Measurement (Pass 1)

Fig 5.7 details the thermocouple responses for pass two of Test [1]. An increase in peak workpiece temperature of 17.2% was observed when the thermocouples were 0.3mm closer to the grinding surface. Again, this was located at the position of TC3.

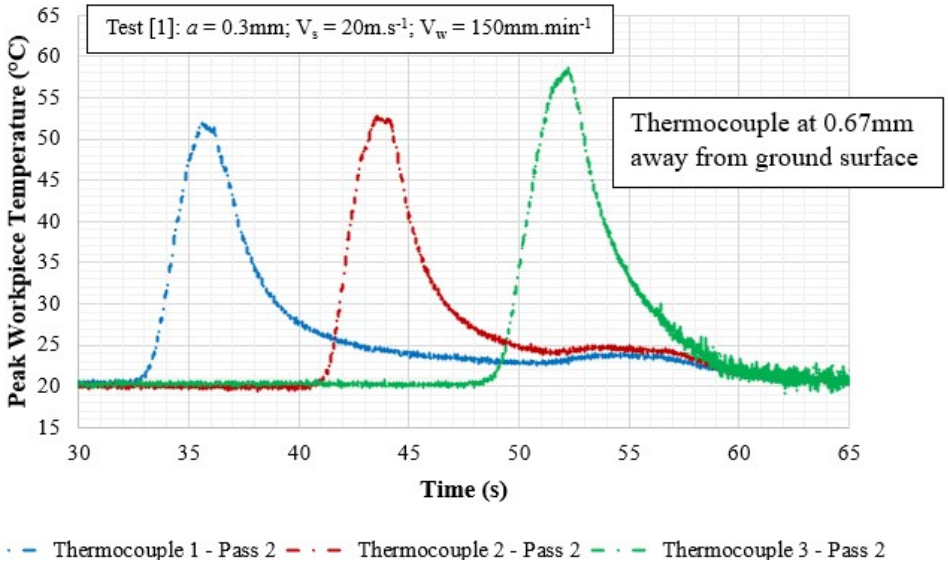



**Figure 5.7:** Test [1] – 0.67mm Stand Off Distance Workpiece Temperature Measurement (Pass 2)

Fig 5.8 details the thermocouple responses for pass three of Test [1]. Again, a further, albeit smaller, increase in peak workpiece temperature can be determined of 3.3% against the previous pass. This was similarly located at the position of TC3.

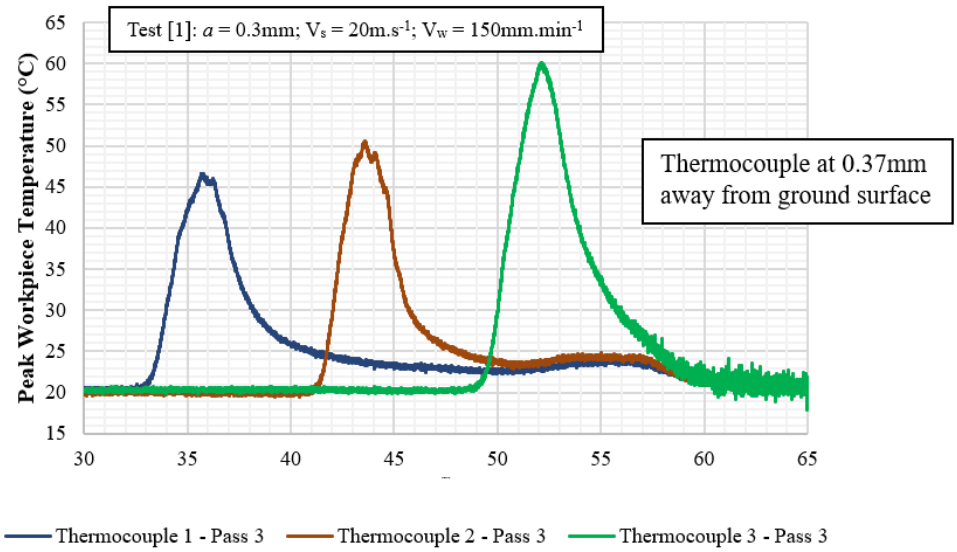



**Figure 5.8:** Test [1] – 0.37mm Stand Off Distance Workpiece Temperature Measurement (Pass 3)

Fig 5.9 details the thermocouple responses for pass four of Test [1]. The increase in workpiece temperature is evident; however, the response of TC2 displays some evidence of irregularity with peaks and troughs replacing the smooth plots determined from previous passes.

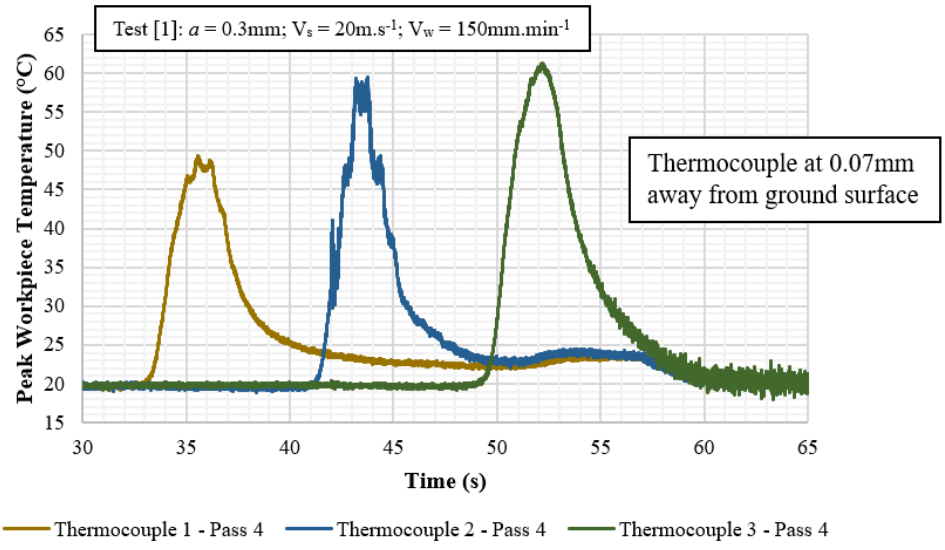



**Figure 5.9:** Test [1] – 0.07mm Stand Off Distance Workpiece Temperature Measurement (Pass 4)

Fig 5.10 details the thermocouple responses for pass five of Test [1]. It is clear from the plot that TC2 has become compromised, and therefore TC2 destruction is occurring. However, both TC1 and TC3 still appear to be functional demonstrated by the linear trend between them being clearly discernible.

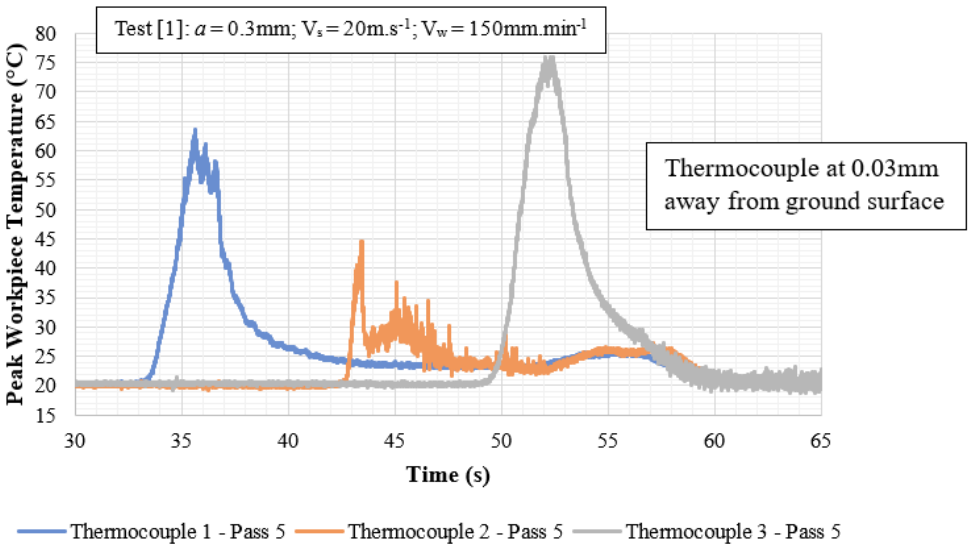



**Figure 5.10:** Test [1] – Thermocouple Destruction Workpiece Temperature Measurement (Pass 5)

Fig 5.11 details the thermocouple responses for all passes for Test [1]. The plot clearly displays that the peak workpiece temperature increased across all subsequent passes, something to be expected with the thermocouples becoming increasingly closer to the grinding surface.

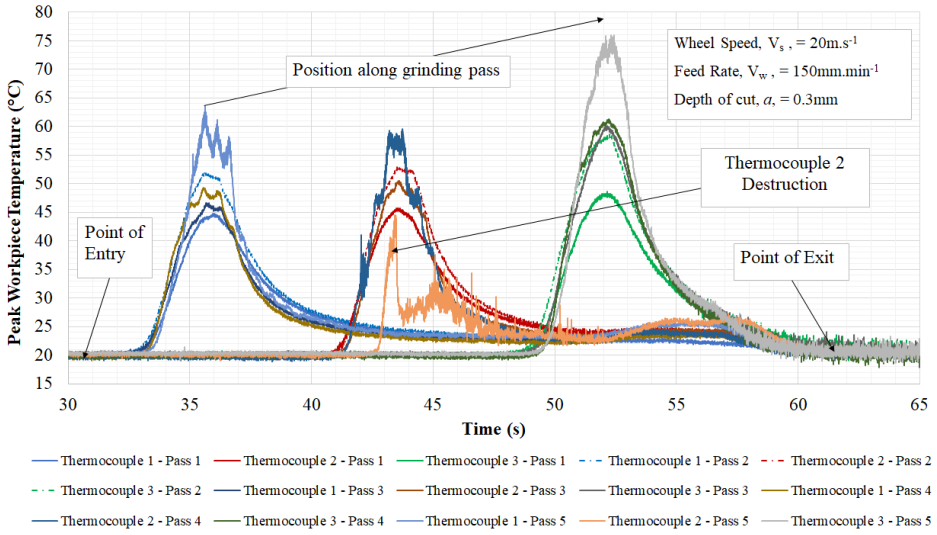



**Figure 5.11:** Workpiece Temperature at all Thermocouple Locations vs. Time for all Grinding Passes (Test 1)

Fig 5.12 presents microscope images of thermocouples used throughout Test [1]. The TC cement is visible, alongside the thermocouple nodes. Additionally, the image for TC1 clearly indicates that the thermal cement had been compromised via the visible lack of the cement in the nodal cavity.

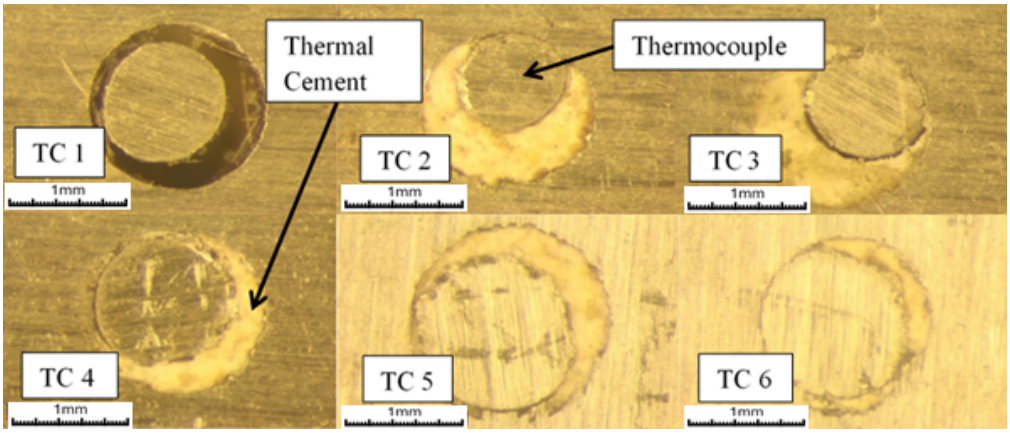



**Figure 5.12:** Microscope Images of Destroyed Thermocouple Nodes

Fig 5.13 presents the thermocouple responses at the stand off distances from the ground surface for the five grinding passes made during Test [1]. There is a clear increase in workpiece temperature during the passes made, and reinforces the data presented in Fig 5.11.

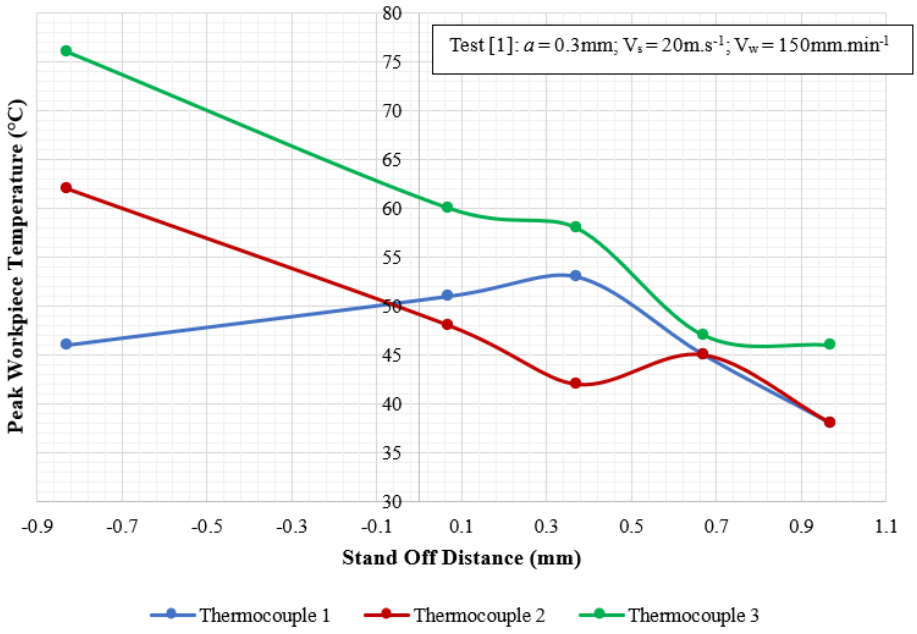



**Figure 5.13:** Test [1] - Workpiece Temperature vs. Thermocouple Stand Off Distance

Fig 5.14 presents the temperature traces for pass one of Test [2]. Similarly to the profiles regarding Test [1], an increasing temperature response along the grinding path can be noted. A significant increase in workpiece temperature at the location of TC3 is also presented; something attributable to the increase in $a$ value between the two tests conducted.

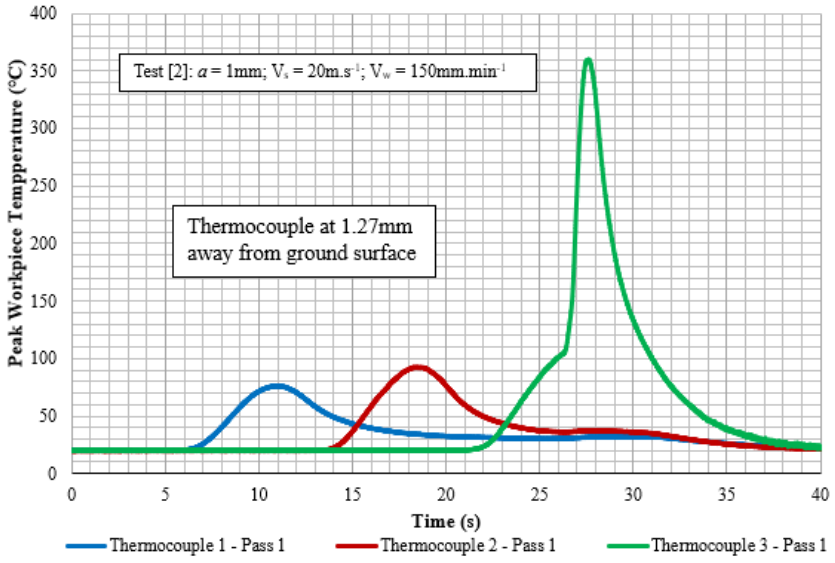



**Figure 5.14:** Test [2] - 1.27mm Stand Off Distance Workpiece Temperature Measurement (Pass 1)

Again, Fig 5.15 details a second increase in all workpiece temperature values during pass two of Test [2] at all TC locations, with TC3 displaying the largest rise.

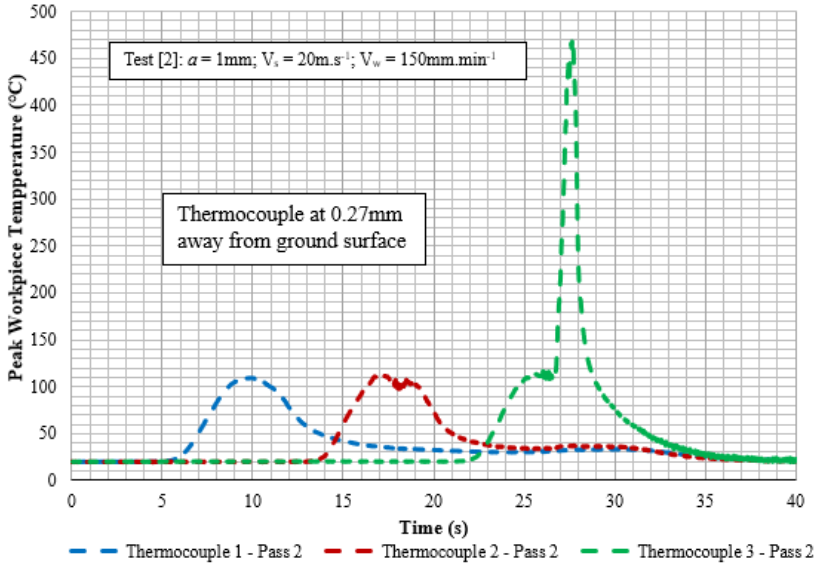



**Figure 5.15:** Test [2] - 0.27mm Stand Off Distance Workpiece Temperature Measurement (Pass 2)

Fig 5.16 details the thermocouple temperature traces for both passes of Test [2]. A similar trend is apparent from Test [1] as presented in Fig 5.11. The temperature responses clearly become more pronounced with subsequent passes due to the decreasing stand off distance between the grinding surface and the thermocouple depth position.

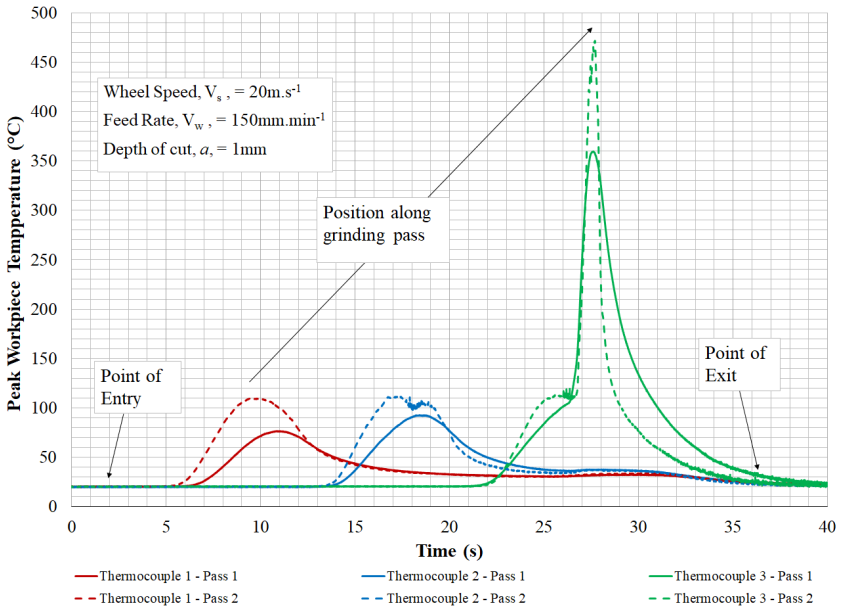



**Figure 5.16:** Peak Workpiece Temperature at all Thermocouple Locations vs. Time for all Grinding Passes (Test 2)

Fig 5.17 reinforces the data presented in Fig 5.16, i.e., TC3 presents higher temperature magnitudes than TC1 and TC2 across the grinding path and at all stand off positions.

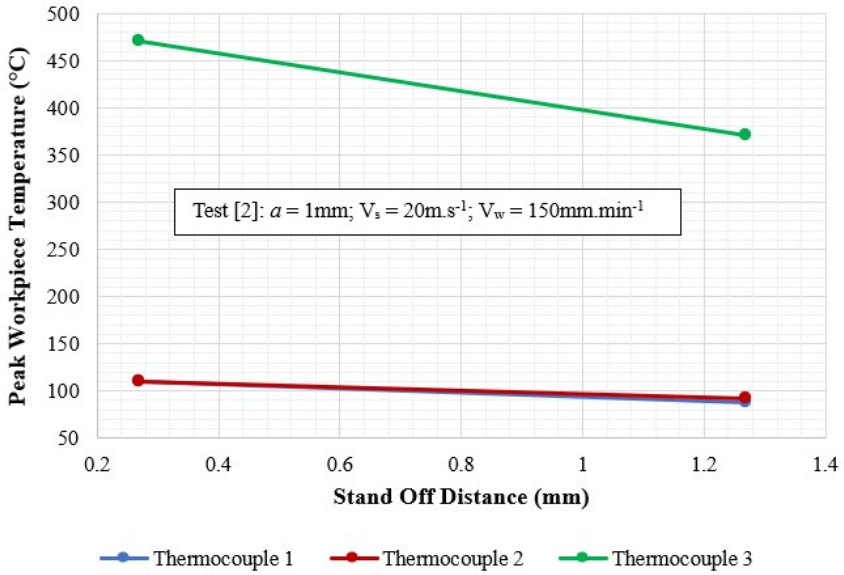



**Figure 5.17:** Test [2] - Workpiece Temperature vs. Thermocouple Stand Off Distance

Fig 5.18 was a repeat trial of Test [3]. An identical trend is observed for all three thermocouples utilised. TC3 is again observed to experience the most significant temperature rise; something observed during previous experimental test cases.

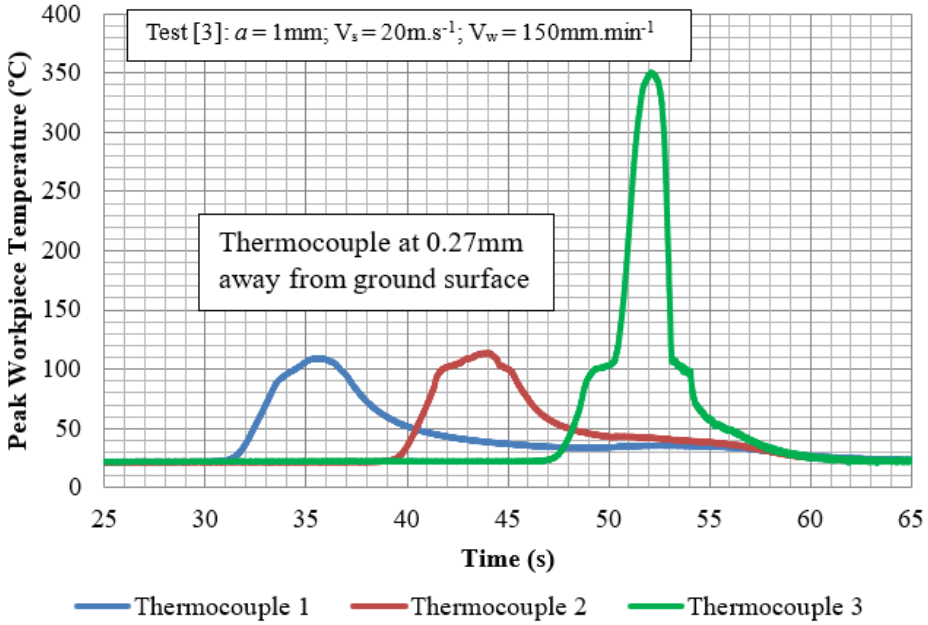



**Figure 5.18:** Test [3] - Repeatability Test for Peak Workpiece Temperature Response

Fig 5.19 outlines the radial temperature reading of the thermocouples during Test [4]. Despite being 22mm radially apart, a temperature response was still captured by the TC data-logging equipment.

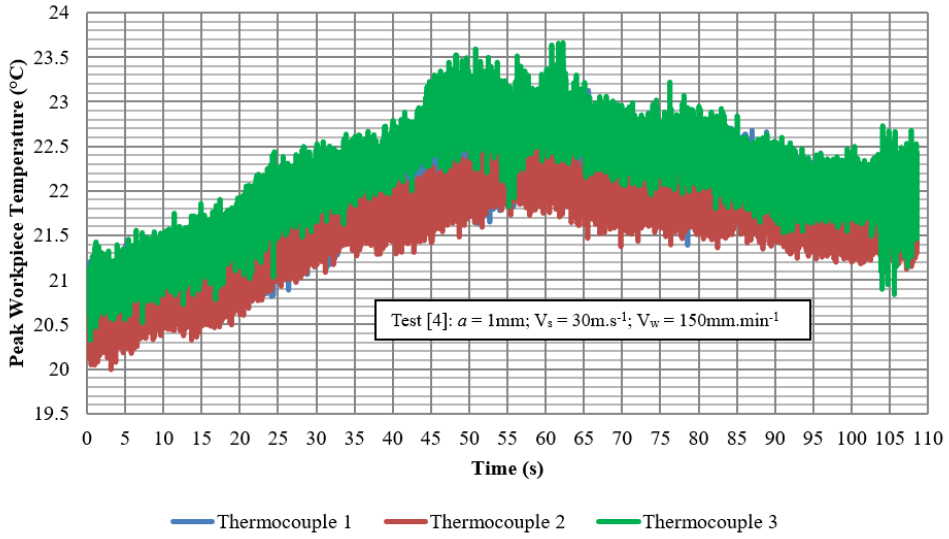



**Figure 5.19:** Test [4] - Pass 1 Radial Workpiece Temperature Readings (TC1 plot not shown as trace variance does not go beyond TC2 and TC3 limits)

Fig 5.20 compares the TC temperature retention time for Test [3] and Test [4]. It is clear that when increasing $V_s$ values, the heat within the workpiece is retained for a longer time period. A more detailed analysis of this observation is discussed in section 5.2.2.

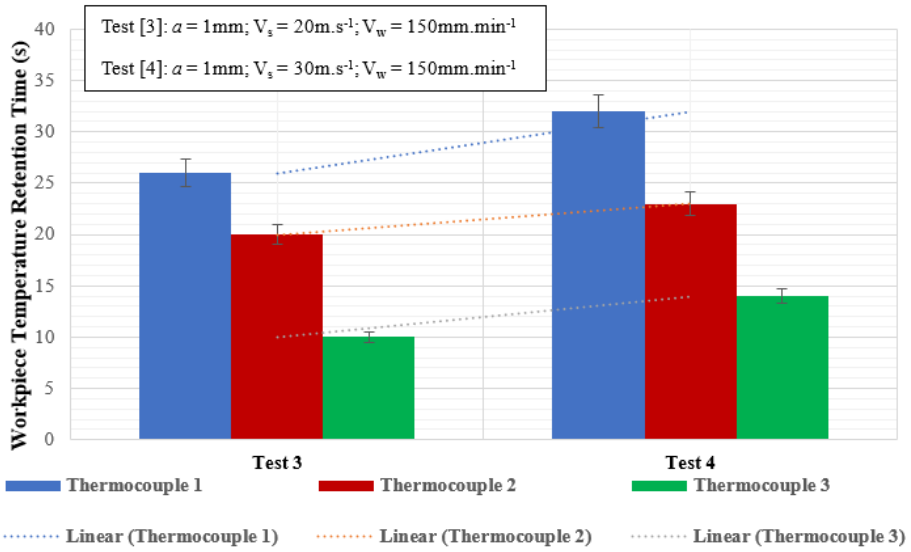



**Figure 5.20:** Example Workpiece Temperature Retention Time Comparison for TC1, TC2 and TC3 for Test [3] and Test [4]

Fig 5.21 presents the thermocouple responses for the second pass of Test [4]. TC3 once again observes the greatest workpiece temperature value of the three thermocouples within the test piece, mirroring other results from earlier trials.

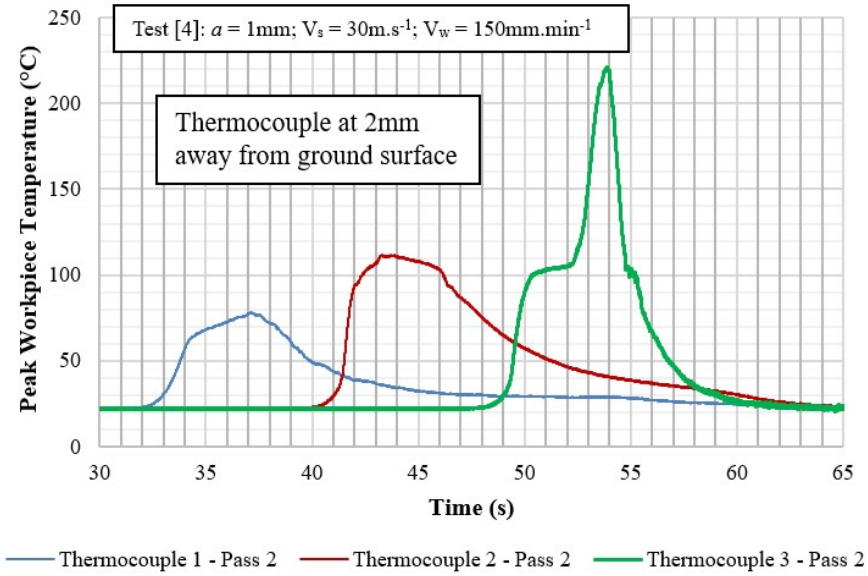



**Figure 5.21:** Test [4] – 2mm Stand Off Distance Workpiece Temperature Measurement (Pass 2)

Fig 5.22 presents the TC temperature traces for pass three of Test [4]. A strange anomaly can be determined at the location of TC3, although similar responses are also observed at the position of TC1 and TC2. Relative movement of the TC nodes within the cavity are possible explanations for these temperature profiles and are further discussed in section 5.2.2.

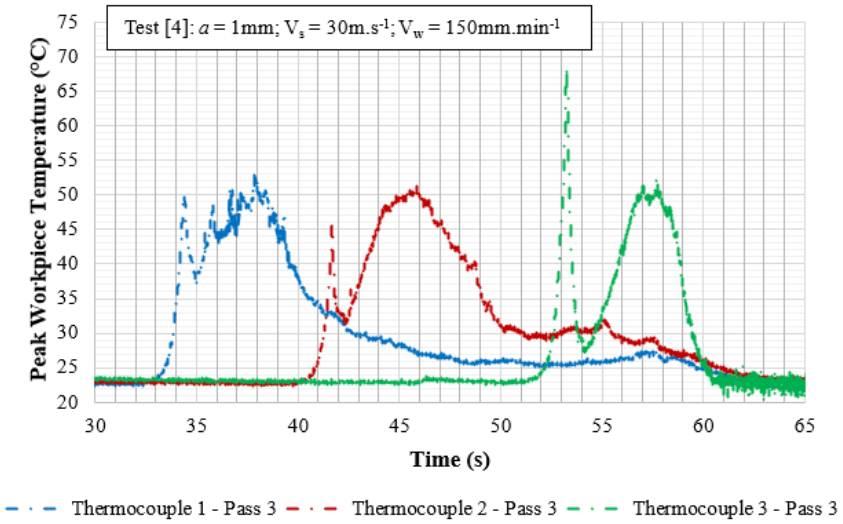



**Figure 5.22:** Test [4] - Thermocouple Destruction Workpiece Temperature Measurement (Pass 3)

Fig 5.23 details the amalgamated TC temperature traces for the two passes of Test [4]. Although the second pass gave inconclusive results, the initial pass suggested that a single thermocouple configuration is unsuitable for measuring the actual peak workpiece temperature as demonstrated by TC3's response.

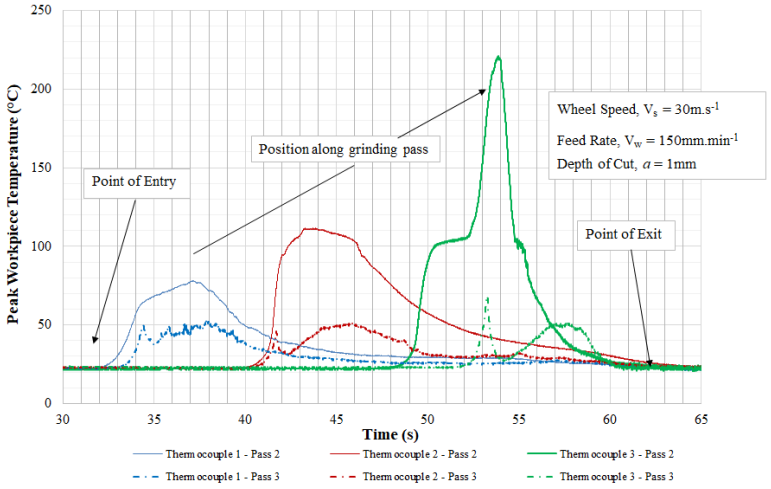



**Figure 5.23:** Peak Workpiece Temperature at all Thermocouple Locations vs. Time for all Grinding Passes (Test 4)

Fig 5.24 outlines the temperature traces relating to pass one of Test [5]. The pass demonstrates the same, linearly increasing TC magnitudes as expressed in previous trials. This adds increased confidence to the thermocouple configuration used, as these trace profiles have been observed across numerous tests with varying grinding parameters evaluated within this thesis.

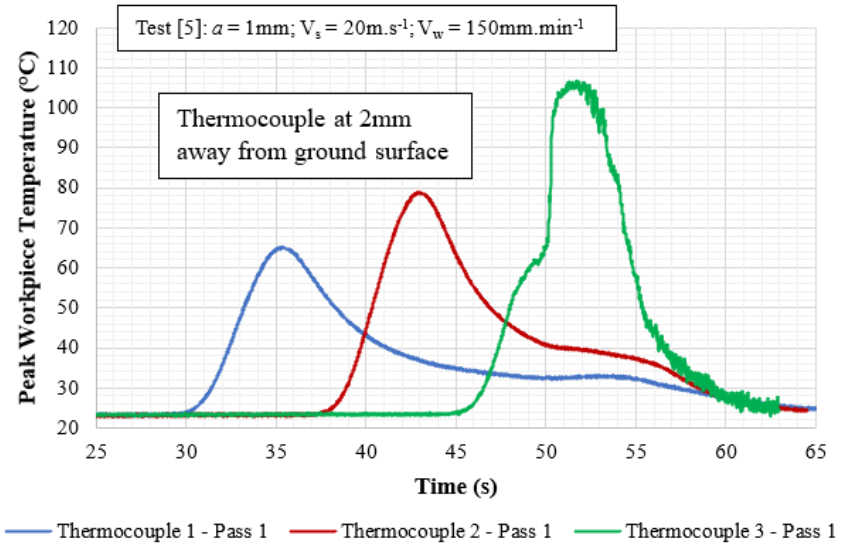



**Figure 5.24:** Test [5] - 2mm Stand Off Distance Workpiece Temperature Measurement (Pass 1)

Fig 5.25 presents the TC traces for the second pass of Test [5]. Again, all temperature traces per thermocouple location increased when compared against the initial pass, indicating that the thermocouples were becoming increasingly closer to the cutting plane.

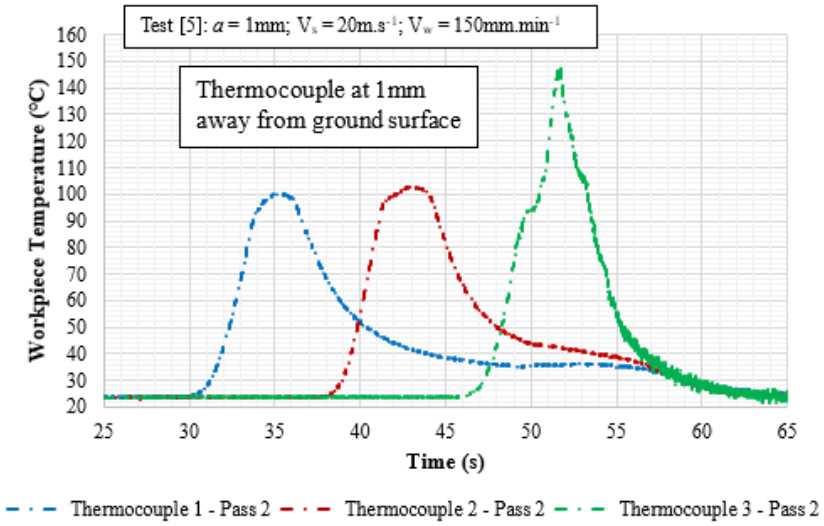



**Figure 5.25:** Test [5] – 1mm Stand Off Distance Workpiece Temperature Measurement (Pass 2)

Fig 5.26 details the amalgamated temperature profiles for the two passes undertaken for Test [5]. The traces provide a clear example of how the workpiece temperature increased linearly across the grinding path at the location of TC1, TC2 and TC3 respectively. The grinding temperature is also evident to increase as the thermocouples become closer to the grinding surface via subsequent volumes of material being removed during successive passes.

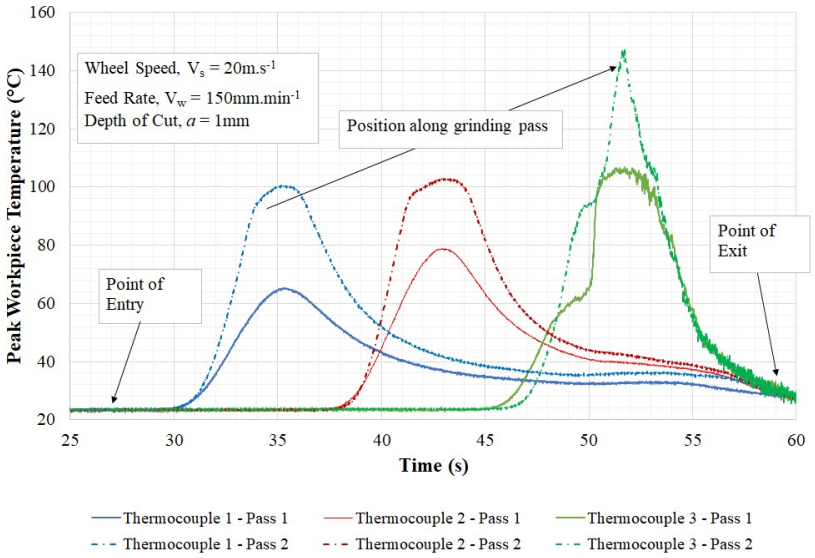



**Figure 5.26:** Peak Workpiece Temperature at all Thermocouple Locations for all Grinding Passes (Test 5)

Fig 5.27 further ratifies the findings presented in Fig 5.26; the temperature measurement becomes more accurate the closer to the grinding plane the thermocouples become.

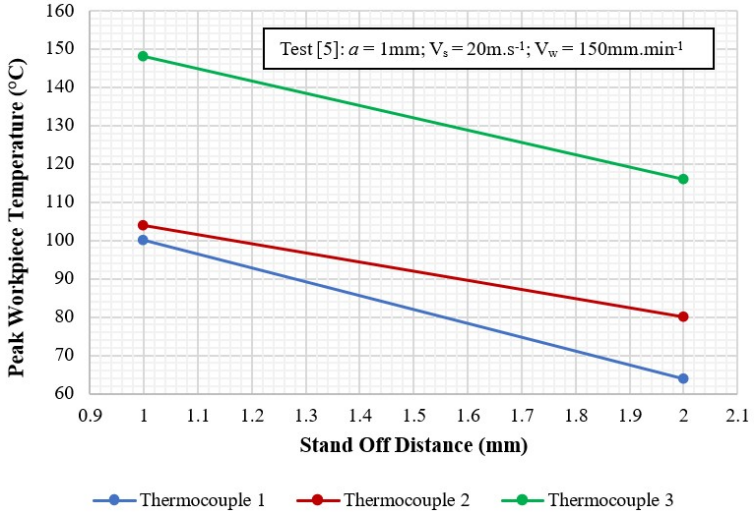



**Figure 5.27:** Test [5] - Workpiece Temperature vs. Thermocouple Stand Off Distance

Fig 5.28 outlines the temperature traces gathered from the initial pass of Test [6]. A clear increase in thermocouple temperature can be noted the further along the grinding wheel pass, with TC3 registering the peak temperature reading which is expected.

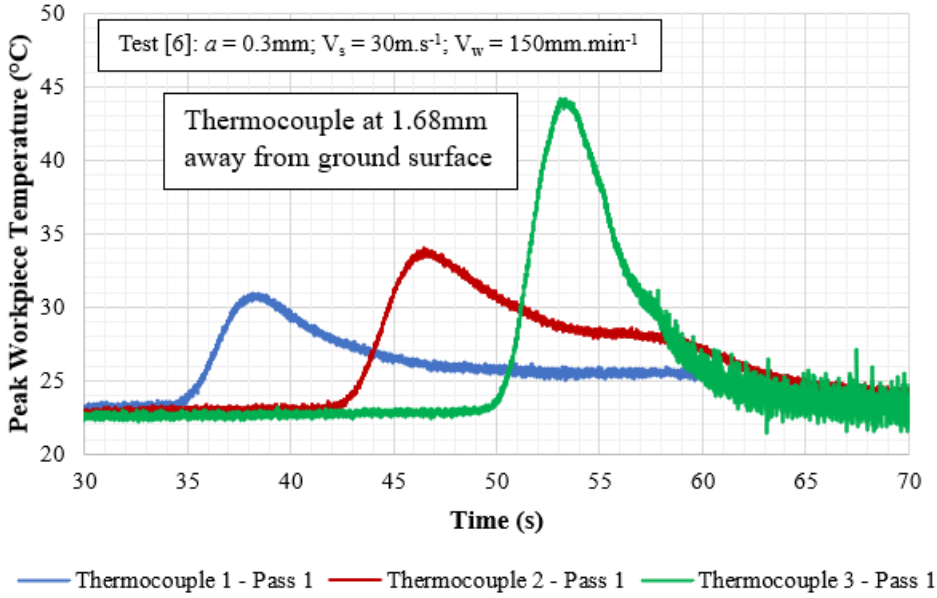



**Figure 5.28:** Test [6] – 1.68mm Stand Off Distance Workpiece Temperature Measurement (Pass 1)

Fig 5.29 indicates a similar response between TC1 and TC3 during pass two; however, TC2 appears to indicate a lower temperature than TC1, although the reading was still higher than the previous pass. Further explanation is detailed in section 5.2.2

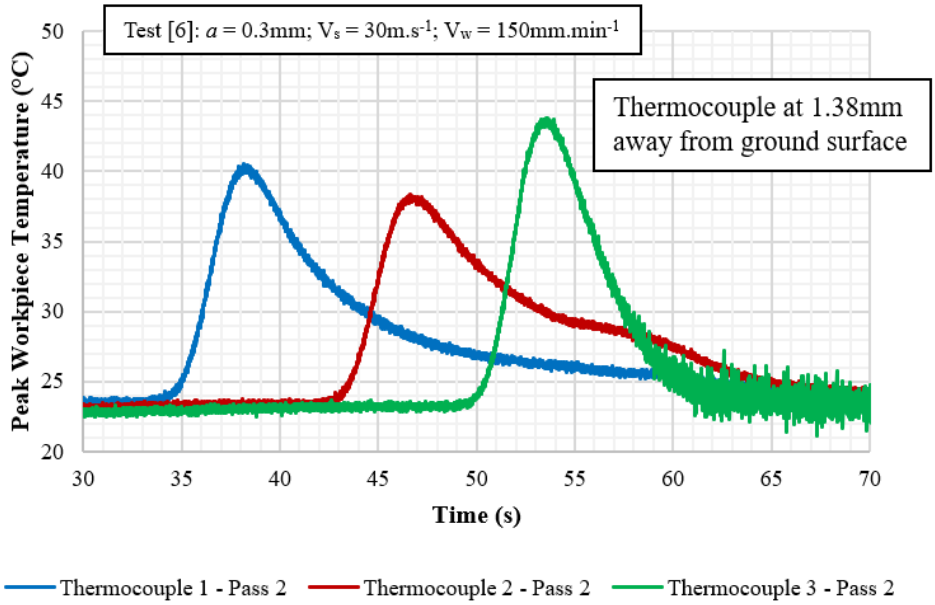



**Figure 5.29:** Test [6] – 1.38mm Stand Off Distance Workpiece Temperature Measurement (Pass 2)

Fig 5.30 provides a surprising result for the thermocouple temperature responses during pass three of Test [6]. TC1 appears to register a greater workpiece temperature than both TC2 and TC3. The location of the thermocouple node within the cavity hole is one possible explanation for this result; possibly caused by the thermal cement becoming compromised.

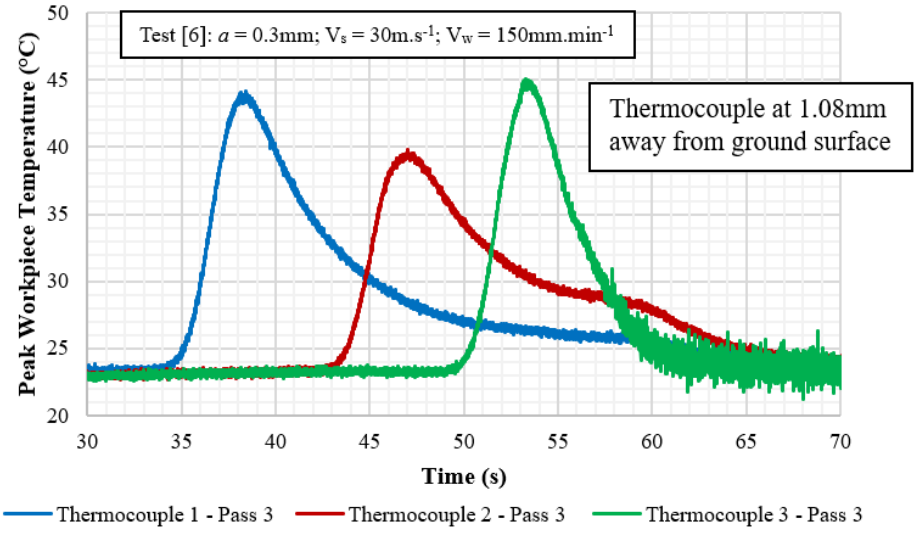



**Figure 5.30:** Test [6] – 1.08mm Stand Off Distance Workpiece Temperature Measurement (Pass 3)

Likewise, Fig 5.31 again details a similar trend to the fourth pass of Test [6]. However, it should be noted that all thermocouple readings are increasing with each subsequent pass which mirrors the relationship presented during previous trials.

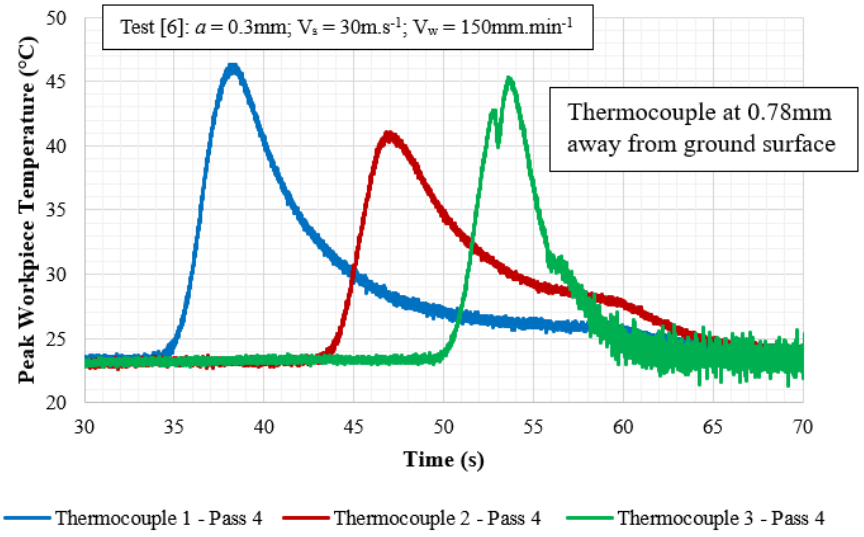



**Figure 5.31:** Test [6] – 0.78mm Stand Off Distance Workpiece Temperature Measurement (Pass 4)

It is apparent from Fig 5.32 that a more familiar temperature trend returned across TC1 and TC3 during the fifth pass of Test [6]. Conclusions can be drawn that some irregularity was occurring during this particular test case when compared to earlier test cases studied, and further investigation should be conducted to determine the source of this phenomenon.

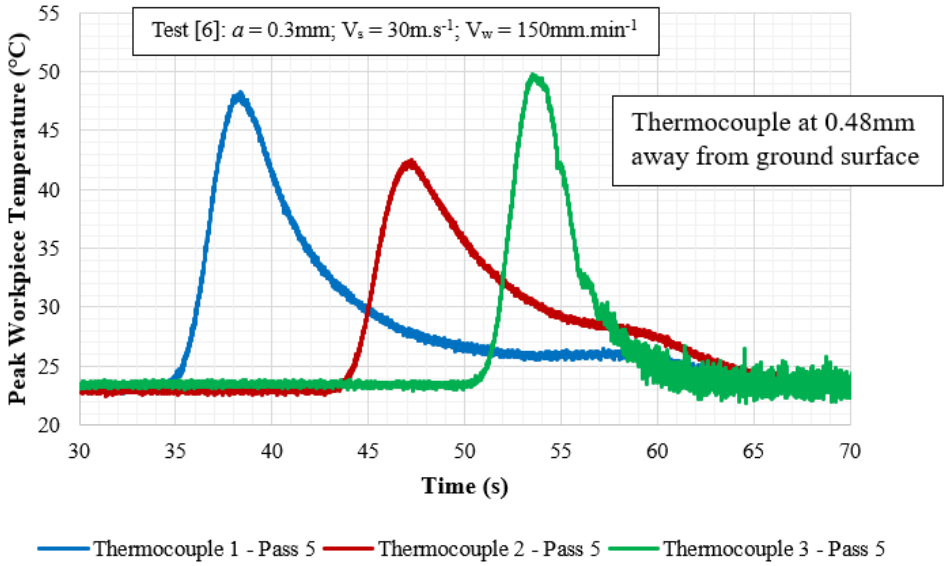



**Figure 5.32:** Test [6] – 0.48mm Stand Off Distance Workpiece Temperature Measurement (Pass 5)

The fundamental point of interest from Fig 5.33 is that the sixth pass of Test [6] indicated that TC3 had started to become compromised as can be determined from the thermocouple's irregular response at fifty-eight seconds into the pass.

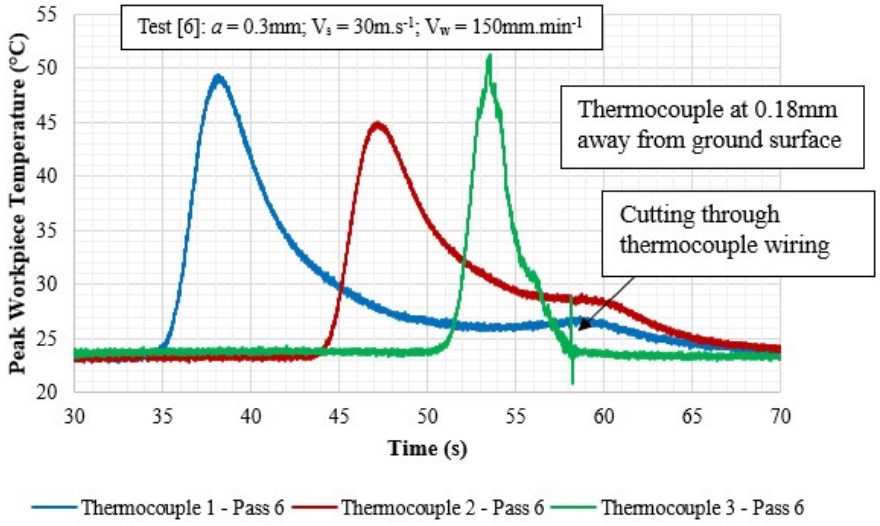



**Figure 5.33:** Test [6] – 0.18mm Stand Off Distance Workpiece Temperature Measurement (Pass 6)

Fig 5.34 details the final pass for Test [6]. TC3 has clearly been destroyed during the previous pass, as indicated by the temperature trace being independent of the time period of the pass.

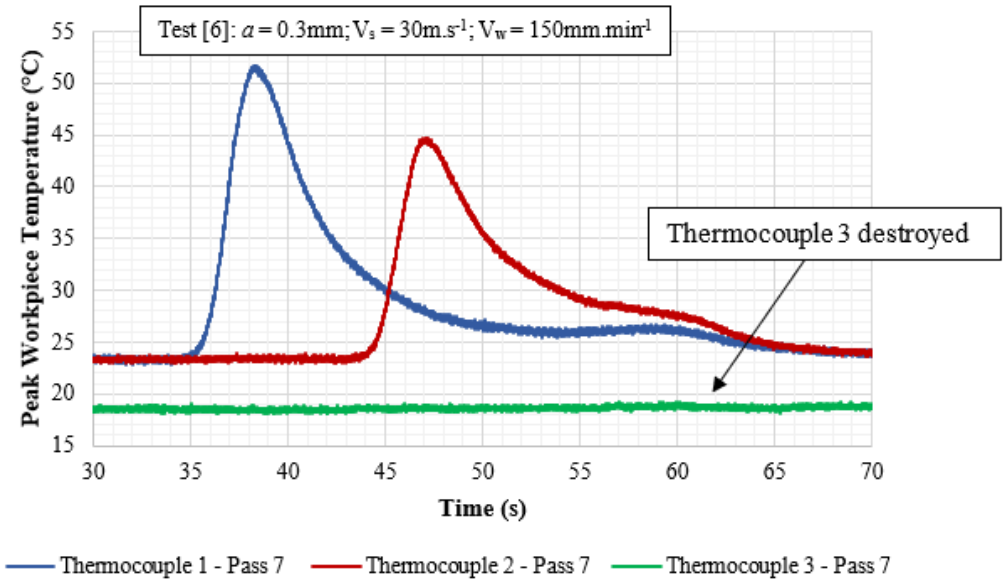



**Figure 5.34:** Test [6] – Final Pass/Thermocouple Destruction Workpiece Temperature (Pass 7)

Fig 5.35 provides a combined temperature trace plot for all seven passes made during Test [6]. Although some discrepancies were noted during the test, the stand off distance responses for the thermocouples were as expected.

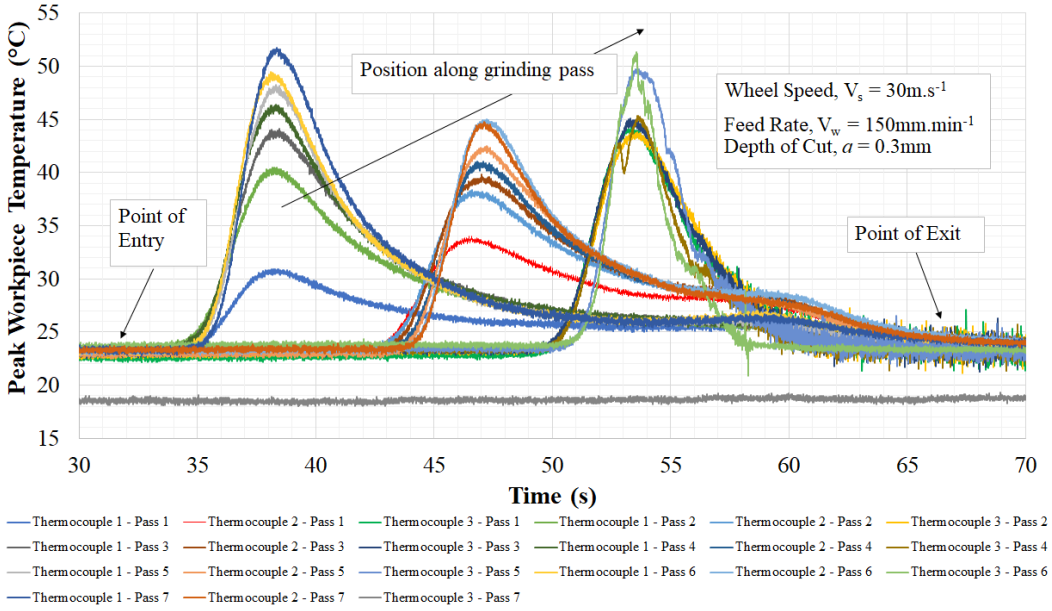



**Figure 5.35:** Peak Workpiece Temperature at all Thermocouple Locations for all Grinding Passes (Test 6)

Fig 5.36 outlines the stand off distance temperature responses for the seven passes made during Test [6]. Again, a noticeable increase in thermocouple temperature is evident as the stand off distance decreased across the multiple grinding passes made.

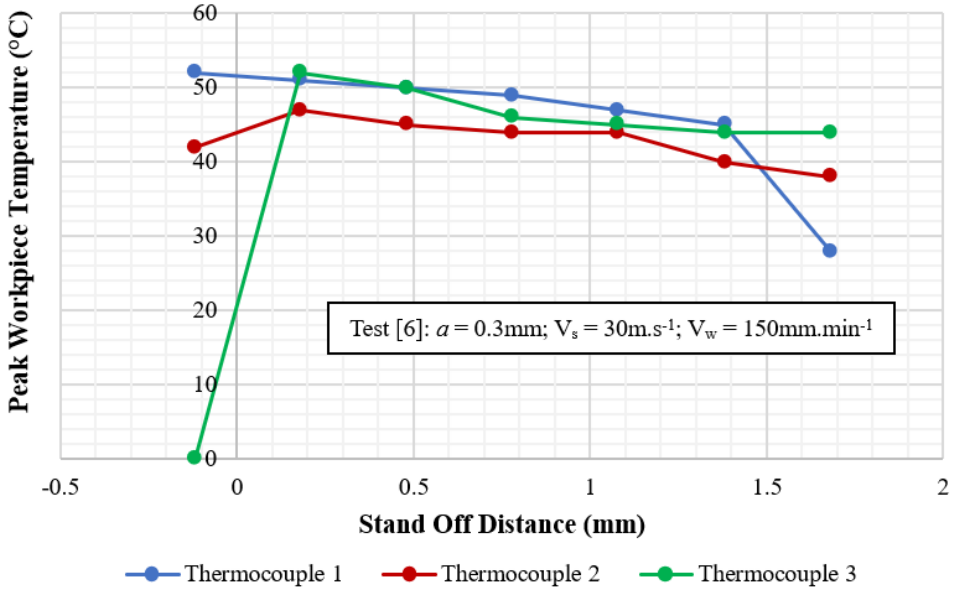



**Figure 5.36:** Test [6] - Workpiece Temperature vs. Thermocouple Stand Off Distance

Fig 5.37 provides an exemplar thermocouple temperature response gleaned from the initial pass made during Test [7]. A significant increase in workpiece temperature at the location of TC3 is evident, resulting from a combination of high $a$ and $V_w$ variables evaluated.

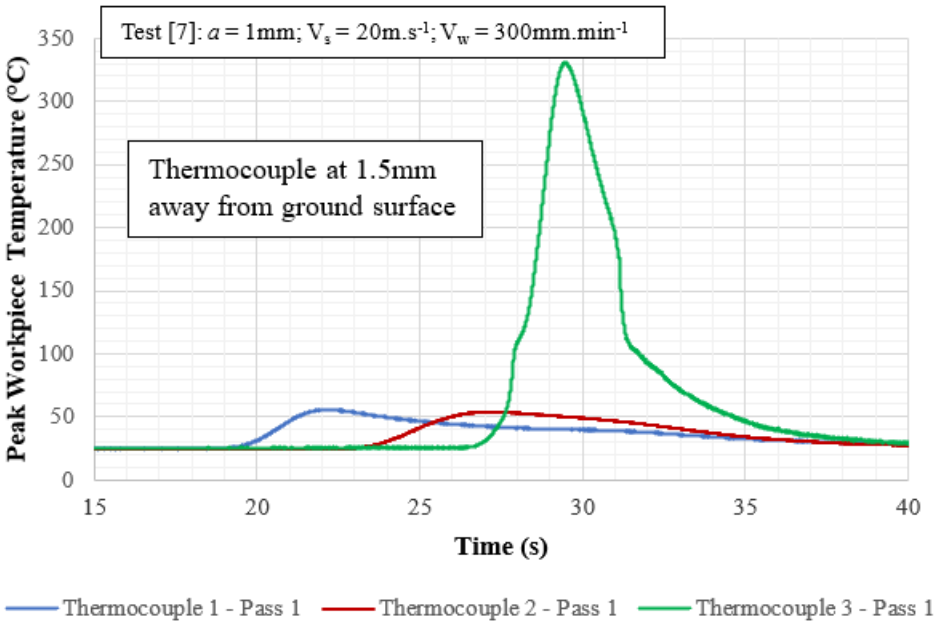



**Figure 5.37:** Test [7] – 1.5mm Stand Off Distance Workpiece Temperature Measurement (Pass 1)

Fig 5.38 again indicates a clear increase in workpiece temperature across the length of the second grinding pass made during Test [7]. TC3 registers a significantly higher temperature response than either TC1 or TC2; something demonstrable via numerous plots presented previously.

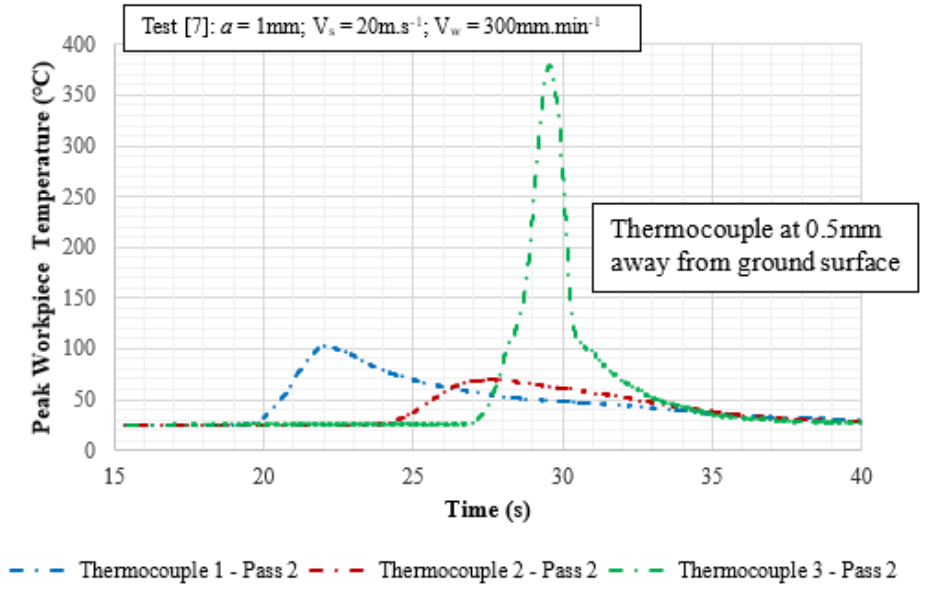



**Figure 5.38:** Test [7] – 0.5mm Stand Off Distance Workpiece Temperature Measurement (Pass 2)

Fig 5.39 is an amalgamated temperature plot for the two passes made during Test [7]. Clear increases in workpiece temperatures are observed across the individual grinding passes, with the peak workpiece temperature in both passes occurring at the location of TC3.

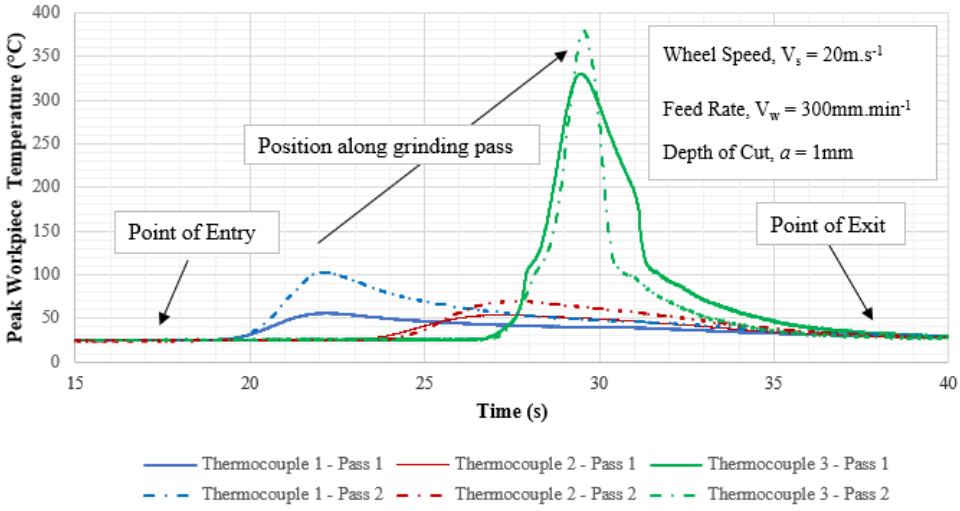



**Figure 5.39:** Peak Workpiece Temperature at all Thermocouple Locations for all Grinding Passes (Test 7)

Fig 5.40 presents the stand off distance temperature plots for the three thermocouples used during Test [7]. Again, TC1 and TC3 detail obvious temperatures increases over subsequent passes, whilst TC2 indicates a less sensitive response to a reduced stand off position.

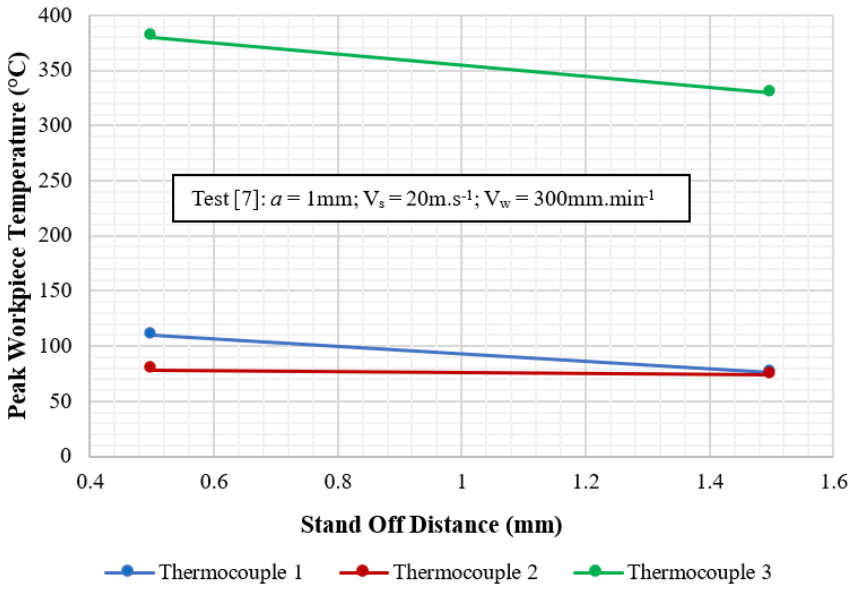



**Figure 5.40:** Test [7] - Workpiece Temperature vs. Thermocouple Stand Off Distance

The temperature traces relating to pass one of Test [8] are outlined in Fig 5.41. The plot displays the same relationship as was presented in Fig 5.8 and Fig 5.14. Further confidence can therefore be associated with the three thermocouple configuration methodology used throughout the experimental trials.

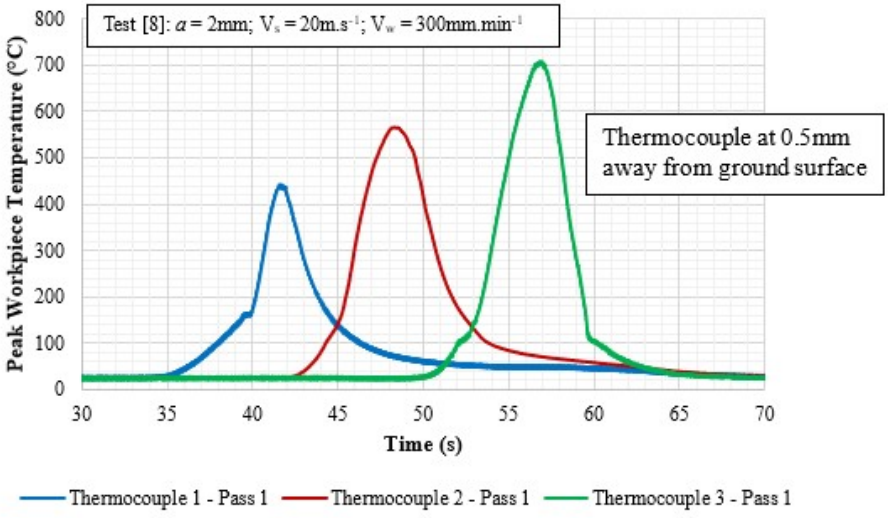



**Figure 5.41:** Test [8] – 0.5mm Stand Off Distance Workpiece Temperature Measurement (Pass 1)

Fig 5.42 outlines the only pass associated with Test [9]. Here, TC1 and TC3 appear to register similar workpiece temperature values, whilst TC2 registered a lower peak temperature. A comparative result was presented in Fig 5.30 and could be attributed to fixation issues regarding the thermal cement used for the TC embodiment within the workpiece.

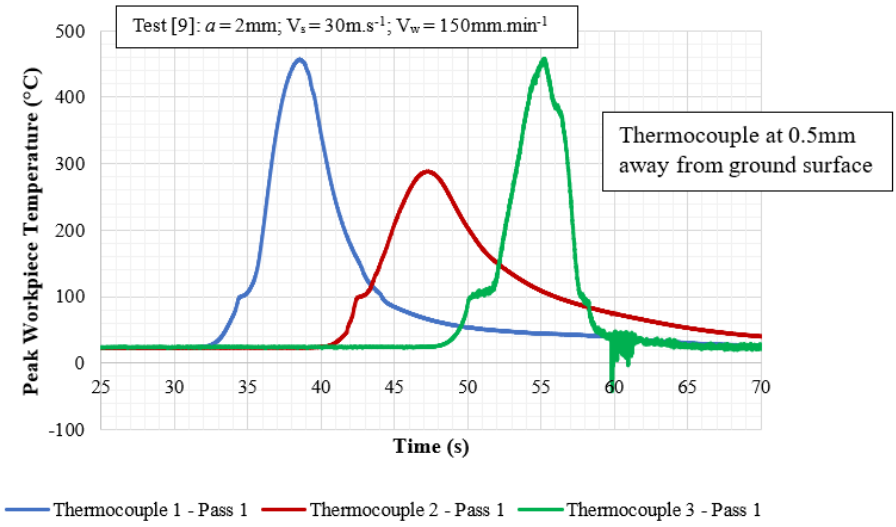



**Figure 5.42:** Test [9] – 0.5mm Stand Off Distance Workpiece Temperature Measurement (Pass 1)

Fig 5.43 presents the singular pass made during Test [10]. For this final temperature measurement trial, a linear response of increasing workpiece temperature as the grinding pass was made is evident. TC3 also experienced the highest workpiece temperature measurement found during the test programme; something to be expected due to the combination of aggressive grinding parameters evaluated, i.e., high $a$, $V_s$ and $V_w$ magnitudes.

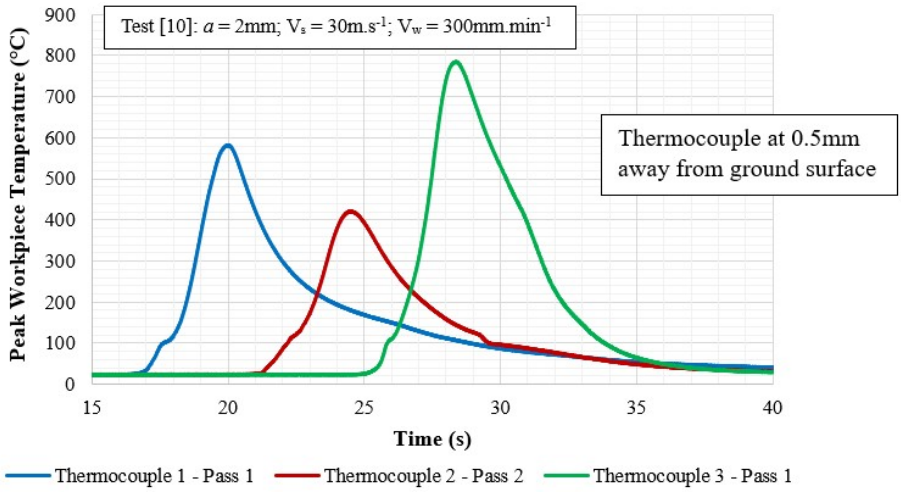



**Figure 5.43:** Test [10] – 0.5mm Stand Off Distance Workpiece Temperature Measurement (Pass 1)

A summary of the workpiece temperature data is presented in Table 5.1 which details each thermocouple temperature response during each pass for each test case conducted.

**Table 5.1:** Summary of Experimental Workpiece Temperature Data

| **Test Number/Parameters** | **Pass Number** | **Thermocouple 1 Temperature (°C)** | **Thermocouple 2 Temperature (°C)** | **Thermocouple 3 Temperature (°C)** |
|---|---|---|---|---|
| Test [1] | 1 | 40 | 38 | 43 |
| $a$ = 0.3mm | 2 | 44 | 44 | 48 |
| $V_s$ = 20m.s$^{-1}$ | 3 | 52 | 54 | 60 |
| $V_w$ = 150mm.min$^{-1}$ | 4 | 47 | 50 | 60 |
| | 5 | 64 | 46 | 76 |
| Test [2] | 1 | 70 | 95 | 360 |
| $a$= 1mm | 2 | 110 | 115 | 475 |
| $V_s$ = 20m.s$^{-1}$ | | | | |
| $V_w$ = 150mm.min$^{-1}$ | | | | |
| Test [3] | 1 | 110 | 110 | 350 |
| $a$ = 1mm | | | | |
| $V_s$ = 20m.s$^{-1}$ | | | | |
| $V_w$ = 150mm.min$^{-1}$ | | | | |
| Test [4] | 1 | VOID | VOID | VOID |
| $a$= 1mm | 2 | 60 | 110 | 220 |
| $V_s$ = 30m.s$^{-1}$ | 3 | 53 | 50 | 69 |
| $V_w$ = 150mm.min$^{-1}$ | | | | |
| Test [5] | 1 | 64 | 76 | 108 |
| $a$ = 1mm | 2 | 100 | 104 | 148 |
| $V_s$ = 20m.s$^{-1}$ | | | | |
| $V_w$ = 150mm.min$^{-1}$ | | | | |
| Test [6] | 1 | 28 | 32 | 44 |
| $a$ = 0.3mm | 2 | 40 | 38 | 44 |
| $V_s$ = 30m.s$^{-1}$ | 3 | 45 | 40 | 46 |
| $V_w$ = 150mm.min$^{-1}$ | 4 | 46 | 41 | 45 |
| | 5 | 48 | 42 | 50 |
| | 6 | 50 | 44 | 52 |
| | 7 | 52 | 44 | 0 |
| Test [7] | 1 | 55 | 53 | 330 |
| $a$ = 1mm | 2 | 105 | 60 | 380 |
| $V_s$ = 20m.s$^{-1}$ | | | | |
| $V_w$ = 300mm.min$^{-1}$ | | | | |
| Test [8] | 1 | 440 | 520 | 710 |
| $a$ = 2mm | | | | |
| $V_s$ = 20m.s$^{-1}$ | | | | |
| $V_w$ = 150mm.min$^{-1}$ | | | | |
| Test [9] | 1 | 430 | 290 | 430 |
| $a$ = 2mm | | | | |
| $V_s$ = 30m.s$^{-1}$ | | | | |
| $V_w$ = 150mm.min$^{-1}$ | | | | |
| Test [10] | 1 | 590 | 400 | 790 |
| $a$ = 2mm | | | | |
| $V_s$ = 30m.s$^{-1}$ | | | | |
| $V_w$ = 300mm.min$^{-1}$ | | | | |

### 5.1.3 Cutting Forces

Fig 5.44 outlines the cutting force profiles relating to pass one of Test [1]. Three noticeable regions are apparent; a clear lead-in section at the entry of the workpiece, the grinding cutting region and a clear lead-out region towards the exit from the workpiece. Some chatter within the system is also present and is something which is further discussed in section 5.2.3.

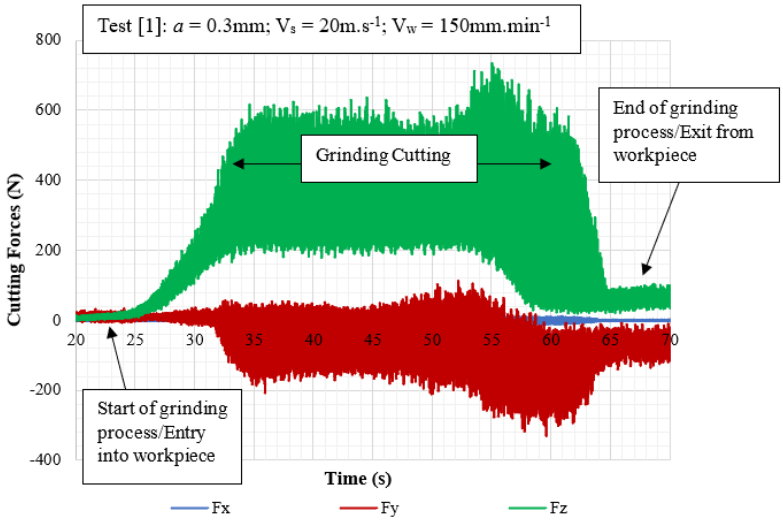



**Figure 5.44:** Test [1] – Cutting Forces vs. Time (Pass 1)

Fig 5.45 details the cutting forces obtained for pass two of Test [2]. An increase in all force component values is observed; something attributable to the increase in the depth of cut evaluated.

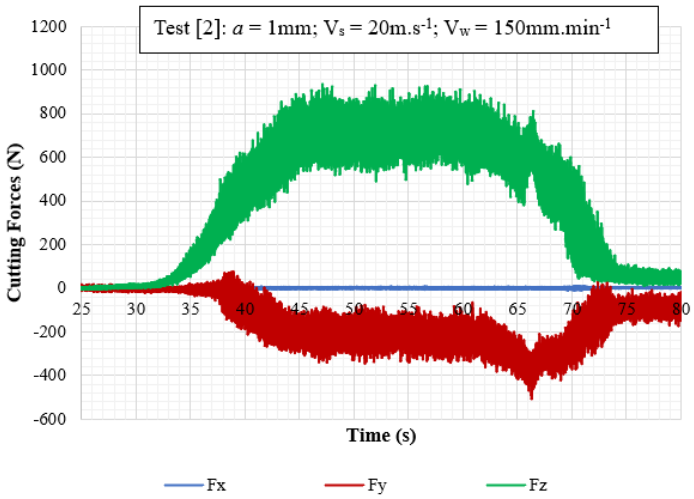



**Figure 5.45:** Test [2] – Cutting Forces vs. Time (Pass 2)

Fig 5.46 presents the cutting force profiles for Test [3] which was a repeat of Test [2]. Similar force magnitudes can be observed indicating that increased $a$ values results in increased cutting force values acting on the grinding tooling.

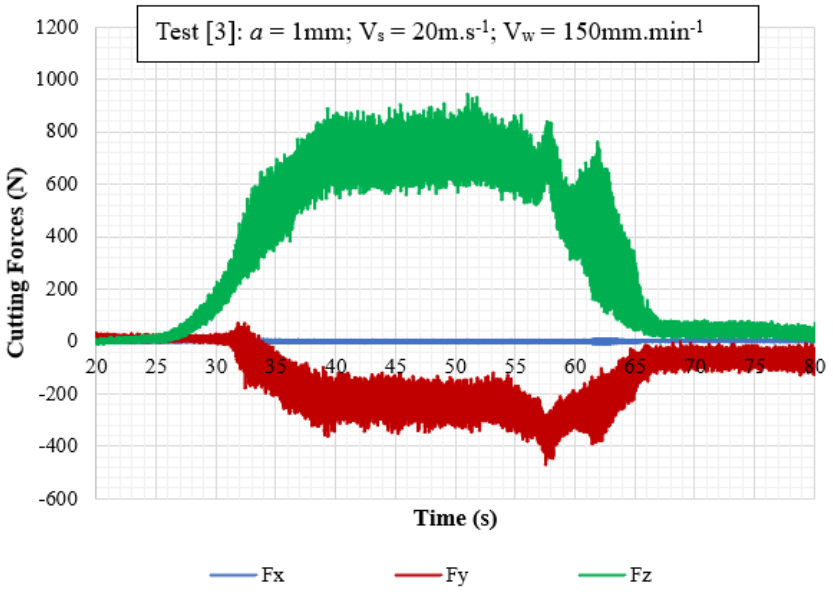



**Figure 5.46:** Test [3] - Repeatability Test for Peak Cutting Force Response

Fig 5.47 details the cutting force traces for pass three of Test [4]. A severe chatter effect can be noted between fifty-three and sixty-three seconds into the pass which could be attributable to an increase in $V_s$ value tested.

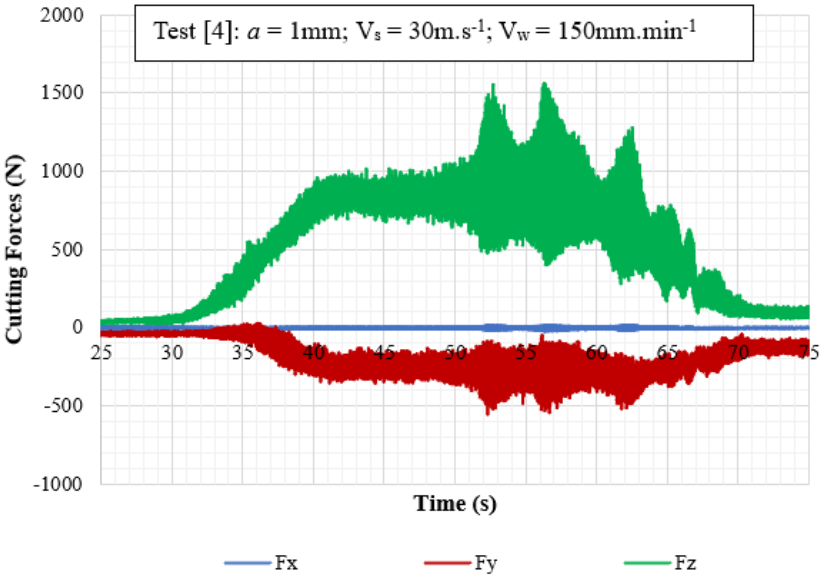



**Figure 5.47:** Test [4] - Cutting Force vs. Time (Pass 3)

Fig 5.48 outlines the cutting force traces obtained from pass two of Test [5]. A clear lead-in profile can be determined for the $F_z$ plot, whereas a less obvious lead-in trace can be observed in relation to the $F_y$ profile. Conversely, both traces observe a severe chatter response at sixty-five seconds into the pass during the lead-out region.

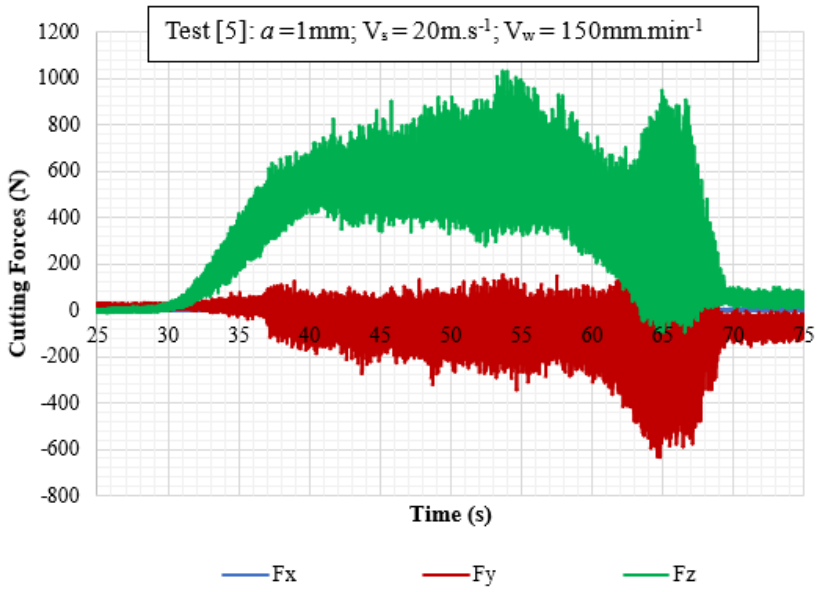



**Figure 5.48:** Test [5] - Cutting Force vs. Time (Pass 2)

Fig 5.49 provides the cutting forces obtained from pass seven of Test [6]. Again, a clear lead-in profile is noticeable for the $F_z$ trace; something not obvious with the $F_y$ trace.

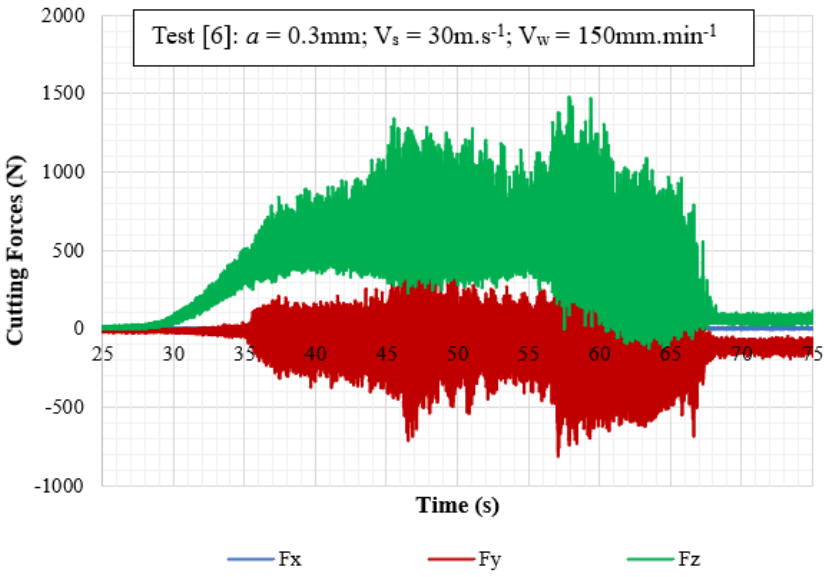



**Figure 5.49:** Test [6] - Cutting Force vs. Time (Pass 7)

Fig 5.50 details the cutting force profiles for pass two of Test [7]. Both the $F_z$ and $F_y$ traces are clearly distinct, with both indicating the three individual regions relating to grinding tool lead-in, grinding period and lead-out region as previously observed in preceding trials.

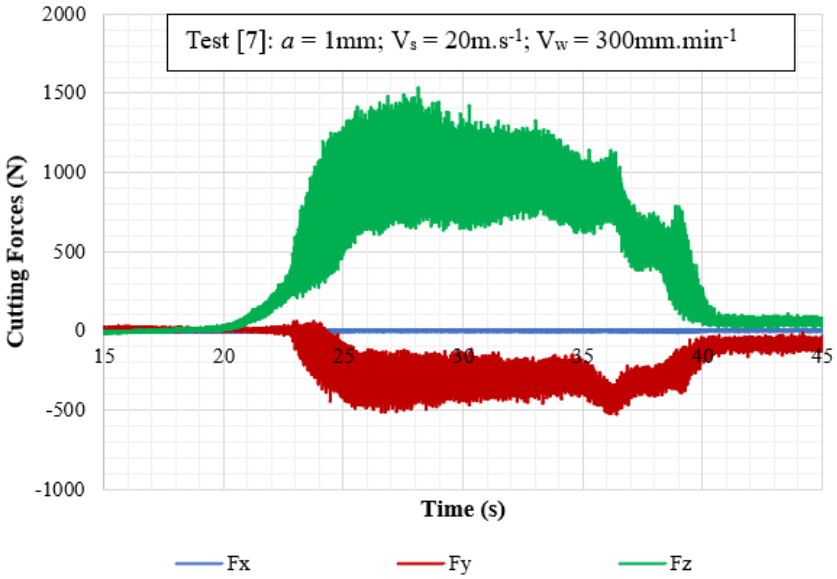



**Figure 5.50:** Test [7] - Cutting Force vs. Time (Pass 2)

Fig 5.51 presents the cutting force profiles for the pass associated with Test [8]. It is interesting to note that more stable and distinguishable cutting force traces become apparent when utilising more aggressive grinding variable magnitudes.

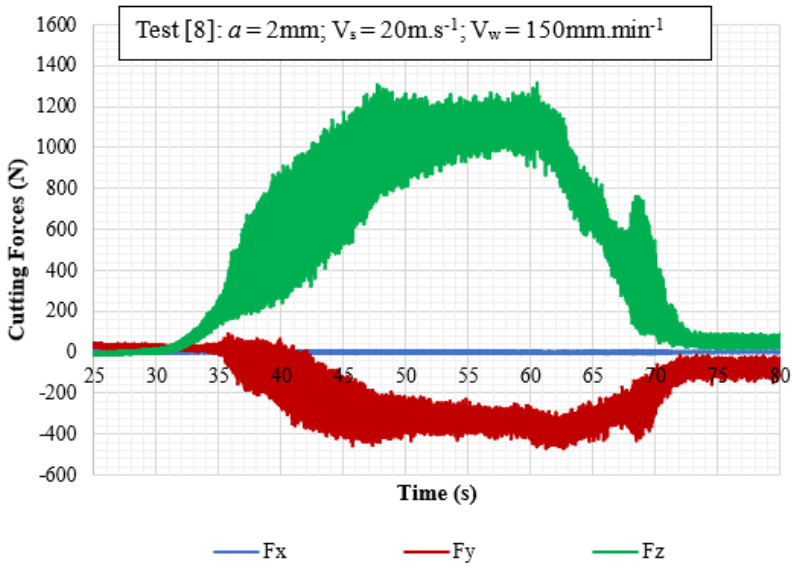



**Figure 5.51:** Test [8] - Cutting Force vs. Time (Pass 1)

Fig 5.52 details the singular pass associated with Test [9]. A decrease in $F_z$ is noted when compared with Test [8] when the wheel speed was increased by 33%.

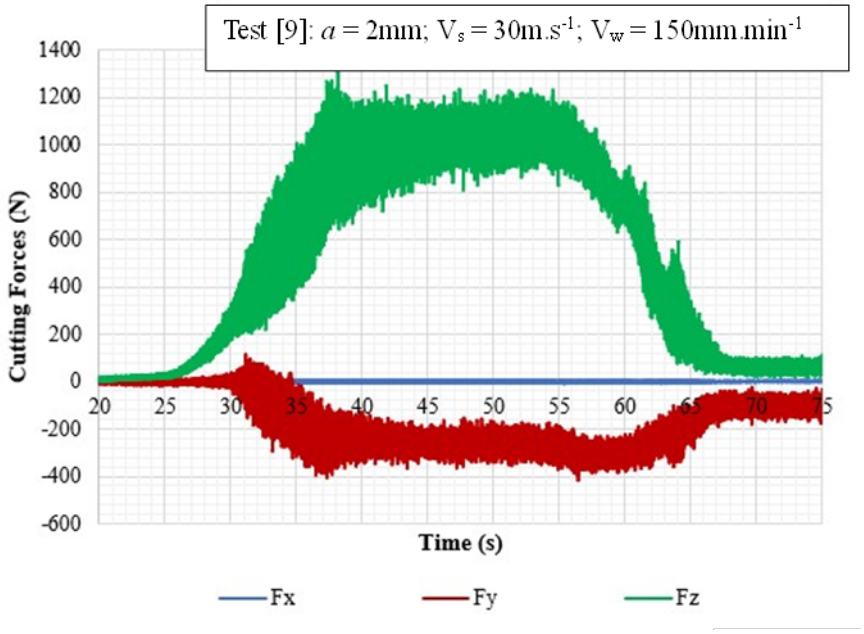



**Figure 5.52:** Test [9] - Cutting Force vs. Time (Pass 1)

Fig 5.53 presents the singular pass associated with Test [10]. Significant cutting force magnitudes can be observed, something attributable to the combined aggressive grinding variables tested, and is something also demonstrated for the workpiece temperature responses for the same test outlined in Fig 5.43.

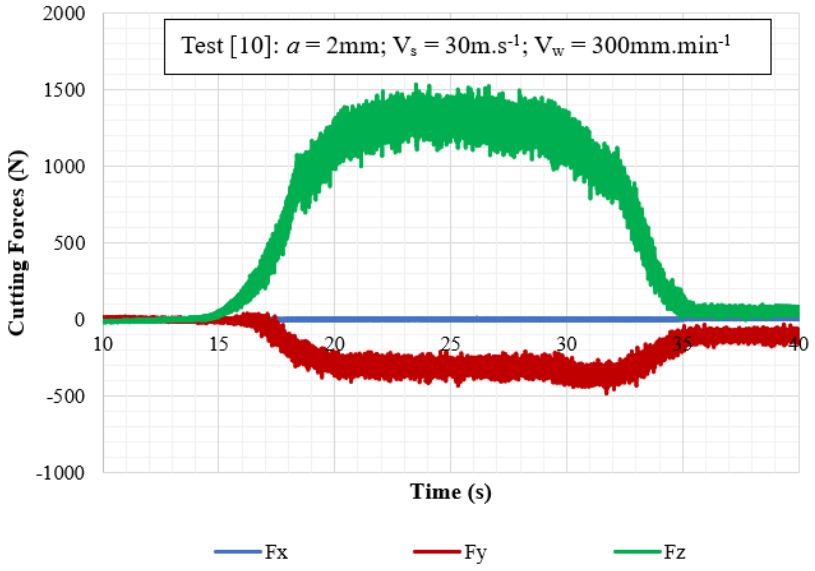



**Figure 5.53:** Test [10] - Cutting Force vs. Time (Pass 1)

A summary of the cutting force data per test, per pass, is presented in Table 5.2, whilst a summary of the workpiece temperature and cutting force data for each test, per pass, are detailed in Table 5.3 for completeness.

**Table 5.2:** Summary of Experimental Cutting Force Data

| **Test Number** | **Pass Number** | $F_x$**(N)** | $F_y$**(N)** | $F_z$**(N)** |
|---|---|---|---|---|
| Test [1] | 1 | 40 | 290 | 620 |
| | 2 | 40 | -390 | 1040 |
| | 3 | -120 | 100 | 580 |
| | 4 | 20 | -600 | 840 |
| | 5 | 40 | -600 | 840 |
| Test [2] | 1 | 30 | -600 | 960 |
| | 2 | 30 | -500 | 900 |
| Test [3] | 1 | 30 | -540 | 940 |
| Test [4] | 1 | 30 | -480 | 960 |
| | 2 | 40 | -550 | 1400 |
| | 3 | 20 | -600 | 1550 |
| Test [5] | 1 | 20 | -550 | 1480 |
| | 2 | 30 | -440 | 840 |
| Test [6] | 1 | 30 | -640 | 1000 |
| | 2 | 30 | -440 | 1200 |
| | 3 | 40 | -640 | 1180 |
| | 4 | 40 | -700 | 1200 |
| | 5 | 40 | -500 | 1700 |
| | 6 | 40 | -700 | 1450 |
| | 7 | 40 | -700 | 1400 |
| Test [7] | 1 | 40 | -700 | 1500 |
| | 2 | 20 | -520 | 1020 |
| Test [8] | 1 | 20 | -600 | 1500 |
| Test [9] | 1 | 20 | -500 | 1300 |
| Test [10] | 1 | 20 | -440 | 1300 |

**Table 5.3:** Summary of Experimental Workpiece Temperature and Cutting Force Data

| **Test Number** | **Pass** | **TC 1 Temperature** (°C) | **TC 2 Temperature** (°C) | **TC 3 Temperature** (°C) | $F_x$ (N) | $F_y$ (N) | $F_z$ (N) |
|---|---|---|---|---|---|---|---|
| Test [1] | 1 | 40 | 38 | 43 | 40 | 290 | 620 |
| $a$ = 0.3mm | 2 | 44 | 44 | 48 | 40 | -390 | 1040 |
| $V_s$ = 20m.s$^{-1}$ | 3 | 52 | 54 | 60 | -120 | 100 | 580 |
| $V_w$ = 150mm.min$^{-1}$ | 4 | 47 | 50 | 60 | 20 | -600 | 840 |
| | 5 | 64 | 46 | 76 | 40 | -600 | 840 |
| Test [2] | 1 | 70 | 95 | 360 | 30 | -600 | 960 |
| $a$ = 1mm | 2 | 110 | 115 | 475 | 30 | -500 | 900 |
| $V_s$ = 20m.s$^{-1}$ | | | | | | | |
| $V_w$ = 150mm.min$^{-1}$ | | | | | | | |
| Test [3] | 1 | 110 | 110 | 350 | 30 | -540 | 940 |
| $a$ = 1mm | | | | | | | |
| $V_s$ = 20m.s$^{-1}$ | | | | | | | |
| $V_w$ = 150mm.min$^{-1}$ | | | | | | | |
| Test [4] | 1 | VOID | VOID | VOID | 30 | -480 | 960 |
| $a$ = 1mm | 2 | 60 | 110 | 220 | 40 | -550 | 1400 |
| $V_s$ = 30m.s$^{-1}$ | 3 | 53 | 50 | 69 | 20 | -600 | 1550 |
| $V_w$ = 150mm.min$^{-1}$ | | | | | | | |
| Test [5] | 1 | 64 | 76 | 108 | 20 | -550 | 1480 |
| $a$ = 1mm | 2 | 100 | 104 | 148 | 30 | -440 | 840 |
| $V_s$ = 20m.s$^{-1}$ | | | | | | | |
| $V_w$ = 150mm.min$^{-1}$ | | | | | | | |
| Test [6] | 1 | 28 | 32 | 44 | 30 | -640 | 1000 |
| $a$ = 0.3mm | 2 | 40 | 38 | 44 | 30 | -440 | 1200 |
| $V_s$ = 30m.s$^{-1}$ | 3 | 45 | 40 | 46 | 40 | -640 | 1180 |
| $V_w$ = 150mm.min$^{-1}$ | 4 | 46 | 41 | 45 | 40 | -700 | 1200 |
| | 5 | 48 | 42 | 50 | 40 | -500 | 1700 |
| | 6 | 50 | 44 | 52 | 40 | -700 | 1450 |
| | 7 | 52 | 44 | 0 | 40 | -700 | 1400 |
| Test [7] | 1 | 55 | 53 | 330 | 40 | -700 | 1500 |
| $a$= 1mm | 2 | 105 | 60 | 380 | 20 | -520 | 1020 |
| $V_s$ = 20m.s$^{-1}$ | | | | | | | |
| $V_w$ = 300mm.min$^{-1}$ | | | | | | | |
| Test [8] | 1 | 440 | 520 | 710 | 20 | -600 | 1500 |
| $a$ = 2mm | | | | | | | |
| $V_s$ = 20m.s$^{-1}$ | | | | | | | |
| $V_w$ = 150mm.min$^{-1}$ | | | | | | | |
| Test [9] | 1 | 430 | 290 | 430 | 20 | -500 | 1300 |
| $a$ = 2mm | | | | | | | |
| $V_s$ = 30m.s$^{-1}$ | | | | | | | |
| $V_w$ = 150mm.min$^{-1}$ | | | | | | | |
| Test [10] | 1 | 590 | 400 | 790 | 20 | -440 | 1300 |
| $a$ = 2mm | | | | | | | |
| $V_s$ = 30m.s$^{-1}$ | | | | | | | |
| $V_w$ = 300mm.min$^{-1}$ | | | | | | | |

### 5.1.4 Workpiece Temperature and Cutting Force Comparison

Fig 5.54 demonstrates that when comparing Test [1] and Test [2], both workpiece temperature and the associated cutting forces increase significantly as a result of the depth of cut being increased.

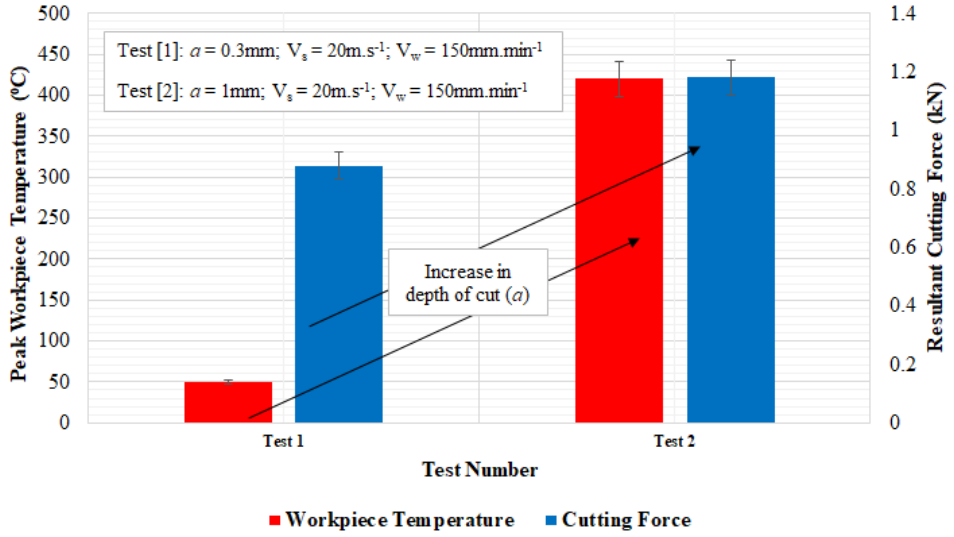



**Figure 5.54:** Peak Workpiece Temperature and Cutting Force Comparison for Test [1] and Test [2] ($\Delta a$)

Similarly, Fig 5.55 demonstrates increases in both workpiece temperature and the associated cutting forces when increasing workpiece feed rate magnitudes, i.e., when comparing Test [5] and Test [7].

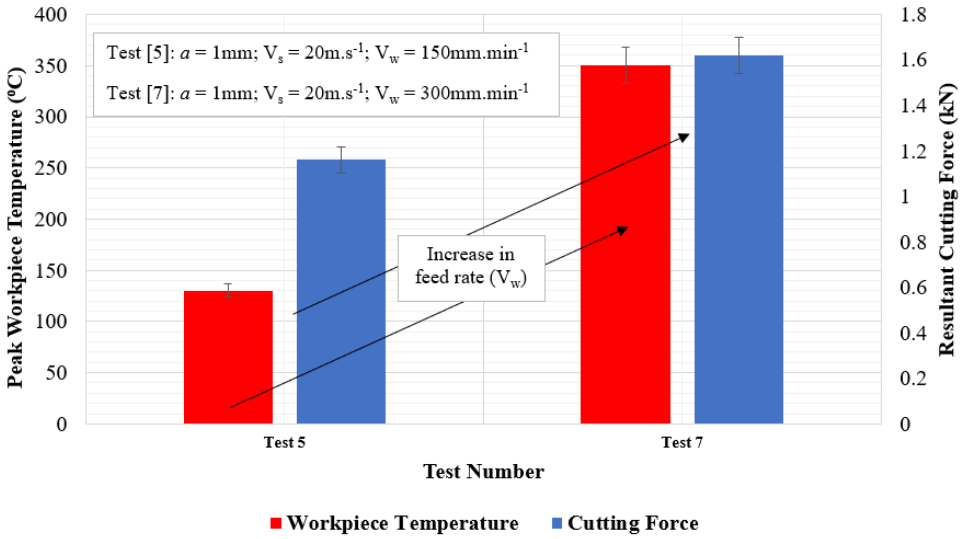



**Figure 5.55:** Peak Workpiece Temperature and Cutting Force Comparison for Test [5] and Test [7] ($\Delta V_w$)

Fig 5.56 indicates a dissimilar response when directly comparing an increase in wheel speed. The workpiece temperature is clearly observed to decrease with an increase in wheel speed, whilst the cutting force magnitude clearly increases with an increase in wheel speed. This inverse relationship is further explored in section 5.2.4.

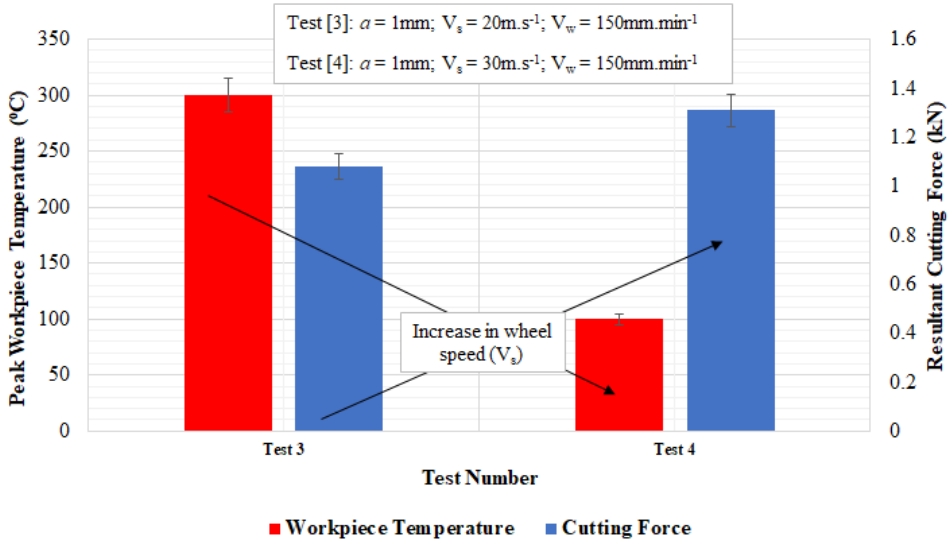



**Figure 5.56:** Peak Workpiece Temperature and Cutting Force Comparison for Test [3] and Test [4] ($\Delta V_s$)

For completeness, Fig 5.57 provides an amalgamated plot comparing both workpiece temperature and cutting forces for each experimental test case conducted. Key points to note are that, in general, workpiece temperatures and cutting forces were higher when using greater depths of cut and feed rates, whilst an inverse relationship when comparing these two output parameters was discovered when increasing the grinding wheel speed.

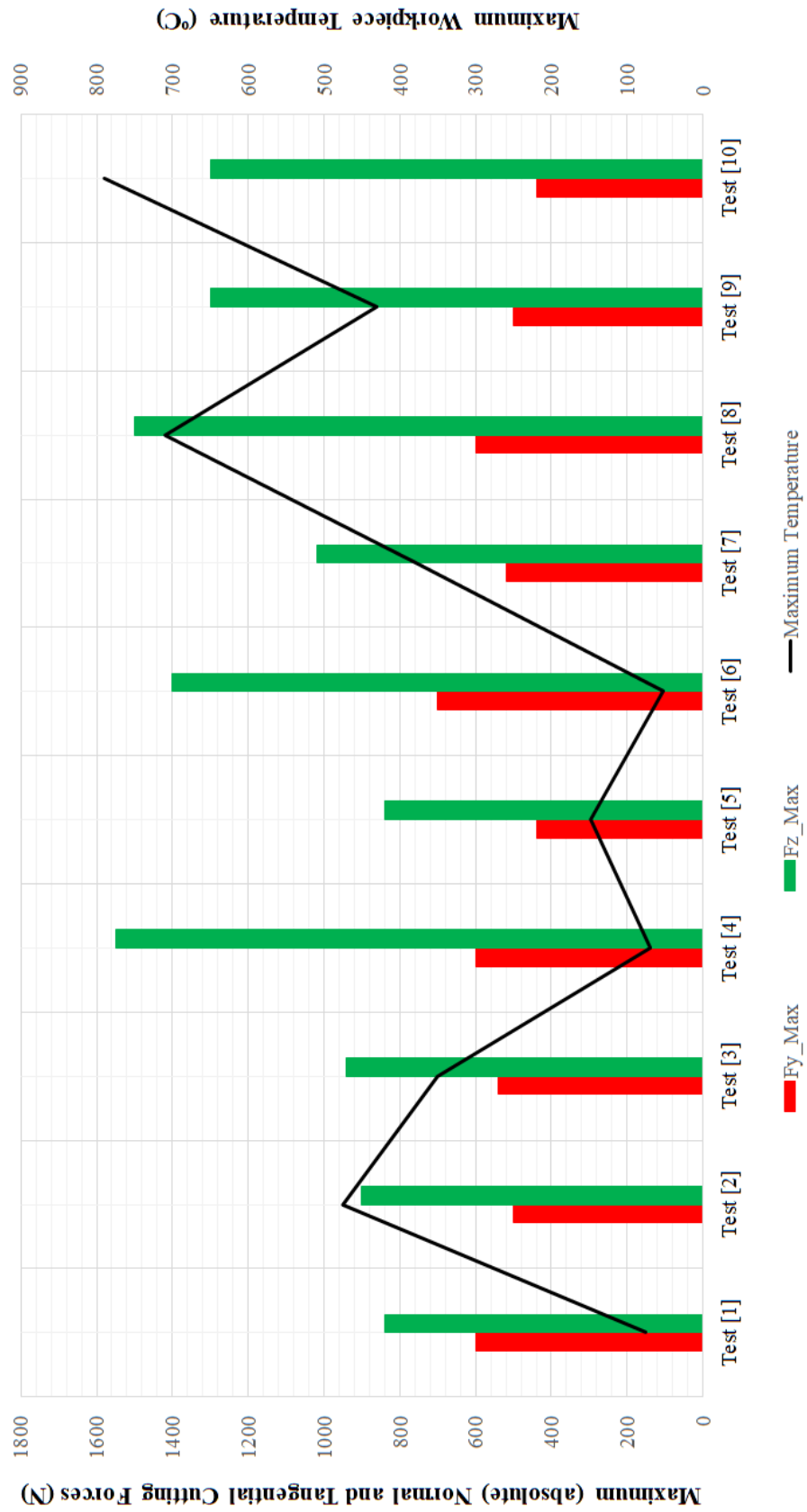



**Figure 5.57:** Cutting Forces and Workpiece Temperature for all Tests

## 5.2 Discussion

Once the initial stability testing had been conducted, a further series of tests were undertaken which considered the workpiece temperature and cutting forces acting on the grinding wheel when grinding a Ti-6Al-4V workpiece. The wheel was intermittently dressed between passes to ensure a true a wheel as possible, with the dressing parameters used being detailed in Table 3.3. The wheel wear was also measured between passes and dressings and is presented in terms of the $G$-ratio in section 4.1.2.1. The experimental programme was proposed as an experimental array. Table 4.1 displays a full summary of these variables and their levels, in addition to the number of passes conducted per sample, and the stand off distance for each successive pass.

### 5.2.1 $G$-ratio

The $G$-ratio is an important aspect to consider when grinding, and in particular when grinding more difficult to machine materials such as Ti-6Al-4V. The $G$-ratio can be expressed as the ratio of the volume of workpiece material removed ($mm^3$) to volume of grinding wheel wear ($mm^3$). During the experimental testing, the total wheel wear was measured with the Mitutoyo CMM, allowing for the $G$-ratio to be calculated. A sample plot of the $G$-ratio is presented in Fig 5.1 for Test [1], Test [2] and Test [8]. It can be determined that as the depth of cut increased from 0.3mm through to 2mm, the $G$-ratio decreased from 1.82 to 0.4 (78%), indicating that the SiC wheel used during the tests was grinding a much harder material in Ti-6Al-4V with a HV of 396, and therefore demonstrated an extremely low $G$-ratio (i.e., $G < 1$) value. As the MRR rate increases due to an increase in the $a$ value, the wheel wear also increases due to the inherent workpiece material properties such as its hardness which causes the work to be less malleable. This is in addition to the low thermal conductivity which can induce thermal softening of the workpiece resulting in an increase in tool wear because of an increase in chatter (Altintas and Weck, 2004). Additionally, subsequent passes results in continually increasing wheel wear (i.e., a measured decrease in wheel diameter). A higher wheel wear rate thus results in a lower $G$-ratio; however, due to the high friability index

of SiC, this suggests that the abrasive grits should re-generate their sharp rake angle after dulling through numerous passes and attritious wear (Malkin and Cook, 1971a). Sharper edges result in a more efficient cutting mechanic, thus resulting in a higher $G$-ratio when compared to a lower friability wheel. Chemical reactions occurring within the grinding zone must also be considered as a possible reason for the decrease in $G$-ratio, with interactions between the metal-working fluid and the workpiece chips adhering to the wheel at localised temperatures and pressures. This results in the wheel being additionally loaded, thus resulting in faster wheel wear (Vinay and Rao, 2013; Rascalha *et al.*, 2017).

From Fig 5.2, it can be determined that the $G$-ratio increased for an increase in wheel speed, $V_s$. Rowe (2009) discussed this at significant length whereby the relationship between the wheel wear was strongly dependent on wheel speed and feed rate, especially at a higher workpiece MRR. In this case, as the wheel speed increased from $20 m.s^{-1}$ in Test [1] to $30 m.s^{-1}$ in Test [6], the average $G$-ratio increased from 1.82 to 2.76, i.e., 34.1%. Smaller chip thicknesses are observed when using more aggressive grinding parameters such as higher wheel speeds, which leads to a reduction in the associated cutting forces acting on the wheel where the MRR is held constant (Kopac and Krajnik, 2006). This reduction in the magnitude of the cutting forces results in much lower radial wheel wear, and therefore a subsequently higher $G$-ratio. However, when chip thicknesses are held constant, the wheel wear is found to remain constant with increases in wheel speed. This phenomena has been observed previously during HEDG, whereby higher $G$-ratios are observed when the wheel speed, $V_s$, is increased to compensate for increased overloading of the wheel due to increased $V_w$ values (Batako *et al.*, 2012).

This increase in $G$-ratio when increasing the feed rate, $V_w$, as expressed by Rowe (2009) can be observed from the analysis of Test [2] and Test [7] as presented in Fig 5.3, whereby the feed rate was doubled from $150 mm.min^{-1}$ to $300 mm.min^{-1}$. A 16% increase can be evaluated from this relationship and is clearly an important result to present in regards to the effect of feed rate on the $G$-ratio resulting from increased wheel wear. It appears that from the variables considered here, the feed rate has a secondary influence over

the increase in $G$-ratio when compared to increases in wheel speed within the range that was tested. This response has also been reported previously for nickel superalloys such as the work by Guo *et al.*, (2007) and Batako *et al.*, (2012). Conversely, when grinding hard to machine materials such as Ti-6Al-4V, slow wheel wear is not always a desirable outcome. When this occurs, the grinding wheel can become glazed, resulting in much higher cutting forces acting on the tooling. Such an outcome often results in poor quality surface finish, i.e., an increase in $R_a$ value, increased vibrational responses within the cutting system and lowered workpiece holding quality. This ultimately is a result from high attritious wear of the tooling. In Fig 5.4 for example, between pass 2 and pass 3, a decrease in $G$-ratio is observed, inferring a lowering of the grinding efficiency and a decrease of its service life. Finally, Fig 5.1, Fig 5.2 and Fig 5.3 highlights the importance of wheel dressing between passes to ensure a sharp a cutting edge as possible to alleviate the outcomes of wheel wear through grain fracture, attritious wear and bond fracture (Malkin and Cook, 1971a; Malkin and Cook, 1971b).

An improved $G$-ratio can be explained by the undeformed chip thickness ($h_m$) equation presented in Eqn. 4.1;

$$h_m = \sqrt{a}.\frac{V_s}{V_w} \qquad \text{(Eqn. 4.1)}$$

Comparable results by Rowe (2009) found that at increased wheel speeds, undeformed chip thicknesses were observed to reduce by up to a third, with the conclusion being that a threshold exists where rapid wear, grain fracture and grain pull-out of the tooling is experienced. This therefore indicates that if grinding below this threshold by using faster wheel speeds and feed rates, then lower grinding forces will be induced on the tooling for reduced wheel wear.

When analysing the $G$-ratio vs. volume of workpiece material removed plot as outlined in Fig 5.4 which relates to Test [1], it appears that wheel wear appears to be increasing over subsequent passes. However, some interesting phases occur across this trend. Phase 1 appears to indicate initially low levels of grinding wheel wear between first dress and Pass 1, before an increase in wheel wear occurs during Phase 2. Again, a decrease in wheel wear is observed between Pass 2 and Pass 3 (Phase 3), before the tooling appeared to be undergoing attritious wear between the final two passes (Phase 4). This is an interesting result to highlight when considering that Test [1] utilised the least aggressive grinding parameters tested and was indicative of a surface grinding/finishing process. This data indicates that when using surface grinding parameters for machining Ti-6Al-4V workpieces with SiC grinding wheels, a minimum of three passes is required before a steady-state wear condition of the wheel can be expected. This has implications for surface integrity being potentially worse during initial passes where grinding wheel wear may not necessarily be uniform, which can influence surface roughness or waviness, for example. Additionally, despite no additional passes being completed after Pass 5 one can surmise that a levelling off of the wheel wear rate would be expected after the steady-state condition had ended.

However, when analysing the $G$-ratio for Test [6], a very different wear rate profile can be determined as presented in Fig 5.5, with the test being split into four distinct phases. During Phase 1, the grinding wheel appears to offer a constant rate of wear i.e., a $G$-ratio of $<1$ which implies an equal amount of material was removed from the wheel and the workpiece with a 'contra' grinding operation occurring), after which rapid attritious wheel wear appears to occur. This phenomenon has also been previously reported on by Kumar (1990) who also studied grinding Ti-6Al-4V workpieces when using SiC tooling. Attritious wear (i.e., the dulling of the sharpened abrasive grains and development of wear flats) causes little wear of the wheel material; however, the attritious wear rate is the primary cause of the tooling being considered spent via wheel glazing (Fathima *et al.*, 2003), and is possibly what is occurring during Phase 1. When considering Phase 2, a more steady-state wear response is observed. Phase 3 indicates a reduction of wheel wear over these subsequent passes, before Phase 4 suggests an increasing wear rate over the final three passes. It can be

inferred that during the final three passes, all three wear mechanisms were occurring, i.e., attritious wear, grain fracture and bond erosion. This is an interesting finding, as when this wear rate profile is compared against that presented in Fig 5.4, whereby the only change in variable was wheel speed, a significant increase in the overall $G$-ratio can be determined. This suggests a decrease in wheel wear rates where wheel speeds are higher, and an increase in wheel wear rates where wheel speeds are slower.

### 5.2.2 Workpiece Temperature

Temperature readings for Test [1] are detailed in Fig 5.6, Fig 5.7, Fig 5.8, Fig 5.9 and Fig 5.10. These plots relate to the five passes made after the initial stability test temperature findings detailed in Fig 4.7. Pass 1 occurred when the thermocouples were 0.97mm away from the cutting surface, whilst the subsequent passes saw 0.3mm depths of cut removed from the workpiece surface. As in Fig 4.7, the same relationship can be observed in Fig 5.6 in relation to the gradual increase in thermocouple response across the length of the grinding pass, i.e., thermocouple 3 indicates a higher temperature than that of thermocouple 1 and thermocouple 2. It can also be noted that the peak workpiece temperature magnitude increased between that of the initial pass (1.27mm away from the cutting surface), when compared to the pass when the thermocouples were located 0.97mm away from the grinding surface (2.4%). This increase in peak workpiece temperature was observed to be 46°C for thermocouple 3, whilst thermocouple 1 and 2 observed smaller individual increases (5°C for thermocouple 1 and 3°C for thermocouple 2). The author surmises that workpiece manufacturing inconsistencies could be the reason for this slight variation in result between thermocouple responses per pass.

The same trend is observed in Fig 5.7, whereby the peak workpiece temperature change between thermocouple 1 and thermocouple 3 is 2°C, whilst the increase in peak workpiece temperature as the thermocouples were now located closer to the cutting surface

(0.67mm) was 10.4%. Moreover, the trend upward was still observed between these two passes and is what should be expected.

Pass 3 of Test [1] indicated an increase in workpiece temperature of 15.3% for thermocouple 1, 13.2% for thermocouple 2, whilst thermocouple 3 observed a negligible increase as presented in Fig 5.8. This indicates that as the volume of material removed from the grinding surface was increased, thermocouple 3 became less sensitive to the stand off distance when compared to thermocouples 1 and 2.

Interestingly, Fig 5.9 indicates that thermocouple 3 observed a 3.3% workpiece temperature increase from pass 3, whilst thermocouple 1 and thermocouple 2's temperature reading observed a reduction. As such, the author is confident that the OMEGABOND cement had certainly started to be compromised by this point due to the high pressure coolant having a substantial loading on the system as was gleaned and presented earlier in this chapter in Fig 4.6. This is an important result and should be taken into consideration for future testing as clearly high pressure coolant can potentially result in thermal cement failure used in thermocouple fixation, and so only up to three grinding passes can be deemed accurate for workpiece temperature measurement purposes. However, another possible explanation is that part of the thermocouple hole had been ground 'open', and fluid was able to enter from the ground surface side instead of from the thermocouple implantation surface.

As presented in Fig 5.10, the final pass for Test [1] resulted in the full destruction of thermocouple 2, whilst thermocouple 1 and thermocouple 3 remained active. The general trend in terms of gradually increasing peak workpiece temperature was still observed, with this final pass resulting in the greatest peak workpiece magnitude of Test [1]; i.e., 76°C. It can therefore be stated that a total change in thermocouple stand off distance from the cutting surface of 100% results in an increased workpiece temperature reading of 43.3%. Additionally, with the peak workpiece temperature observed to be 76°C for Test [1], this is evidently not significant enough in magnitude to induce workpiece damage or indeed

microstructural changes at a given depth into the workpiece due to it being significantly lower than the $\alpha + \beta \rightarrow \beta$ phase transition temperature of $\approx$ 840°C - 990°C (Wang *et al.,* 2020).

Fig 5.11 details the peak workpiece temperature at all thermocouple locations vs. time traces pertaining to all five passes regarding Test 1. As can be perceived from the figure, the peak temperature increases progressively from thermocouple 1 through to thermocouple 3 and can be expected due to the reduction in coolant within the grinding zone at the position of thermocouple 3 (Rowe, 2009). Moreover, it can also be ascertained that as progressive passes were made, the thermocouple temperature reading at each position increased, and again can be expected due to the thermocouple node becoming increasingly closer to the cutting plane, and thus a higher temperature reading being registered. This is true until pass five, whereby thermocouple 2 becomes inactive due to the grinding wheel destroying the thermocouple node.

Additionally, as indicated by Fig 5.12, the microscope images of the thermocouples taken after the final pass of Test [1] clearly display the exposed thermocouple nodes. An interesting point to note is the difference in surface damage to the nodes, with thermocouples 1, 2 and 3 on the top row displaying clear, straight friction marks, whilst thermocouples 1, 2 and 3 on the bottom row display more uneven and random damage. The image which details thermocouple 1 (top row) is also interesting in relation to the aforementioned issues regarding thermocouple fixation using the OMEGABOND thermal cement; here it is clearly visible that the thermal cement has completely failed when compared to the other thermocouples in the workpiece, thus leaving a totally free and exposed thermocouple junction.

It can and should be noted from the Test [1] data that as the grinding wheel was observed to pass progressively over thermocouples 1, 2 and 3 respectively, the temperature response of the thermocouples increased with a linear trend. Again, this is to be expected as thermocouple 1 experiences an initial temperature response as the grinding

wheel passes over it before reducing just before the second thermocouple takes its reading. This second thermocouple does not, however, only read what itself is experiencing, but also the residual heat the workpiece has retained from the path of the cut already made. As such, thermocouple 2 indicates a higher temperature reading than thermocouple 1. Similarly, thermocouple 3 experiences its own temperature reading as well as measuring the higher residual heat in the workpiece than either thermocouple 1 or thermocouple 2 were registering. It can be seen that the thermocouple closest to the point of grinding wheel exit from the workpiece indicates the highest workpiece temperature response in almost all cases and is something that been demonstrated by Farahani (2019) during milling previously. This gradual build-up of residual heat within the workpiece therefore results in higher workpiece temperatures which can have a negative effect on the *in situ* performance of the final component due to higher residual tensile stresses forming on the grinding surface via thermal expansion and contraction, phase transformation (such as $\alpha$ and $\beta$ phases in Ti-6Al-4V) and high plastic deformations (Fergani *et al.*, 2014). Additionally, based on the findings from the previous workpiece temperature results presented, subsequent surface integrity performances should be conducted at locations towards the exit of the workpiece where workpiece temperatures are highest. This would allow tribologists a 'worst case scenario' for assessment of component performance, knowing that surface integrity is worst at locations which undergo the highest grinding temperature.

It is also clear from the thermocouple temperature gradient plot in Fig 5.13, that the predicted workpiece temperature increases as the thermocouple becomes closer to the cutting plane. This trend is to be expected due to the inherent natural physical phenomena on which thermocouples operate. This is obviously a correct assertion to make, as is proposed by the Seebeck effect on which thermocouple functionality is based, i.e., the initial cold junction temperature is known and is a function of the material properties, whilst an electromotive force generates a current due to the temperature differential between the cold and hot junction. The temperature differential becomes increased as the hot junction becomes closer in proximity to the grinding zone. This relationship has been published in the literature by the likes of Shen *et al.*, (2008) experimentally, as well as by Madopothula

*et al.*, (2017) via finite volume analysis. In the case of Test [1], the peak temperature differential between the closest and remotest thermocouple in proximity to the cutting face can be observed to be 40.7%, based on a thermocouple 3 reading of 76°C and a thermocouple 1 reading of 38°C. It is also interesting how a purely linear response was observed between 0.1mm and -0.8mm stand off distances, i.e., when further away from the cutting plane, the relationship appears to offer more irregularities. This result therefore indicates to the author that as close as is feasibly possible to the grinding surface is the highly recommended position for future grinding workpiece temperature measurements when using thermocouples due to steep temperature gradients. In practical terms, this would mean a single pass per workpiece temperature measurement to get the most accurate result at the expense of thermocouple destruction. However, this approach would prevent multiple passes being made and therefore limit a temperature gradient plot being realised. The negative values of the stand off distance also indicates that the thermocouples were further away from the cutting plane than expected, despite using a depth gauge to check the thermocouple cavity depth prior to cementing the nodes in the workpiece. More material located between the cutting surface and the thermocouple position would infer a lower temperature reading response from the thermocouple, meaning the grinding temperature may actually have been higher than those presented. A repeat of this trial would prove useful for clarifying this result. The irregularity of thermocouple 1's response as it became closer to the cutting plane could be a result of the actual depth being slightly inconsistent due to tool wear on the Matsuura FX-5 Vertical Machining Centre used for machining the thermocouple holes.

Test [2] utilised a wheel speed, $V_s$, of 20m.s$^{-1}$, a feed rate, $V_w$, of 150mm.min$^{-1}$, and a depth of cut value, $a$, of 1mm. Two passes were made, thus removing 2mm of material from the workpiece. The obvious result of note from Test [2] is the very high workpiece temperature of 350°C experienced by thermocouple 3 as presented in Fig 5.14. Whilst a gradual trend is observed between thermocouple 1 and thermocouple 2, the temperature spike at thermocouple 3 noted a significantly higher magnitude than either of the previous thermocouple responses. This increase in peak workpiece temperature is 71.4% higher in thermocouple 3 than in thermocouple 1 and is a significant result to highlight.

Thermocouple 3's temperature profile can be observed to steadily increase with a similar trend to thermocouple 1 and thermocouple 2 until ≈100°C before rising sharply. It can be surmised that a build-up of latent heat in the workpiece could be occurring, as well as the level of coolant entering the grinding zone being significantly reduced by the time the contact zone was above thermocouple 3. This phenomena, known as *film boiling*, occurs when the heat generated in the grinding zone exceeds the specific heat capacity of the coolant fluid being delivered, thus causing the coolant to evaporate (Marinescu *et al.*, 2006). Fig 5.58 (Alagan *et al.*, 2020) details the thermal-mechanics occurring during the process which therefore results in significant spikes in workpiece temperature being observed as demonstrated by Fig 5.14. It should also be noted the workpiece temperature observed by thermocouple 3 is extremely high despite being 1mm away from the cutting surface; a result which clearly has negative consequences for surface integrity performance.

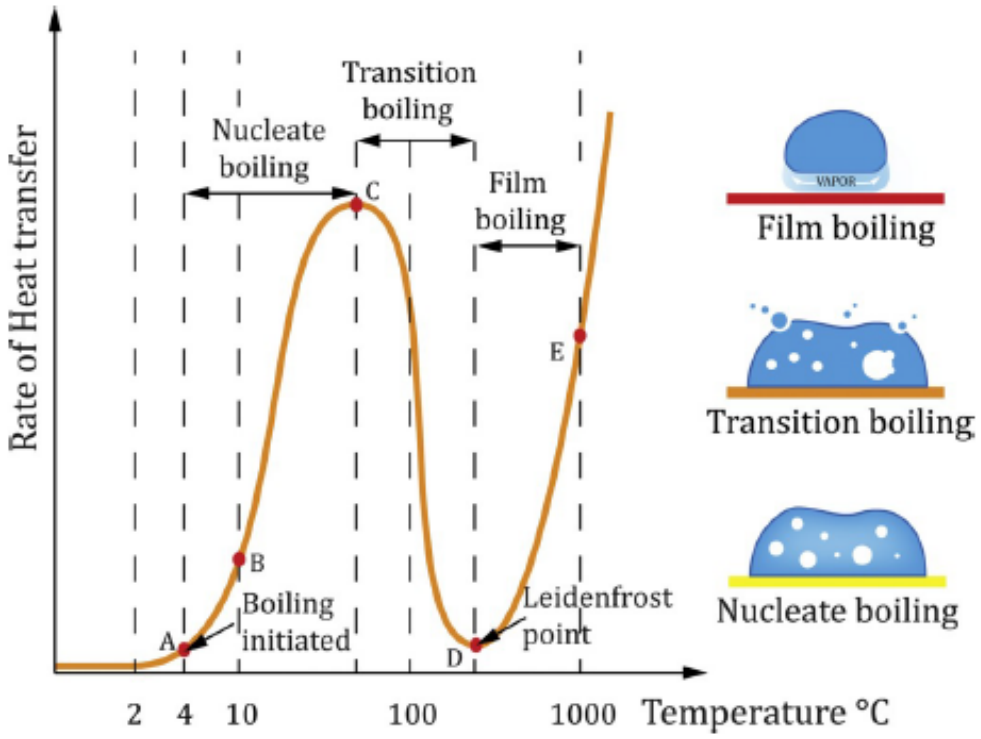



**Figure 5.58:** Typical Boiling Curve for Water at 1bar (Alagan *et al.*, 2020)

The expected impact on the peak workpiece temperature observed within Fig 5.15 is clearly apparent. There is a significant increase in the workpiece temperature value between that determined from pass 1 and that from pass 2. This trend is to be expected and was presented to the reader from the previous pass via Fig 5.14. An interesting result was found within thermocouple 3 at fifty-eight seconds into the pass. Here, the workpiece temperature appears stable at 110°C, before increasing significantly to 460°C. From the first set of 1 x 3 in-series thermocouple configuration, it can be easily observed that workpiece temperature responses increase when the thermocouple location within the workpiece is closer to the grinding plane; something freely accessible from the literature (Amritkar *et al.*, 2012). A total of $\Delta$24.2% increase in workpiece temperature can be observed between thermocouple 3 being 1.27mm away from the grinding surface (pass 1) than from being 0.27mm away from the grinding surface (pass 2). The argument can be made that thermocouple 3 is in a far better position than either thermocouple 1 or thermocouple 2 for accurately capturing workpiece temperature during grinding due it being further along the grinding path. This also has implications for capturing more accurate surface integrity responses. Conversely, if the workpiece temperature had been measured only in the middle of the grinding path, these aspects would not have been recorded, and key aspects pertaining to workpiece temperature and surface integrity assessment would have been missed.

Fig 5.16 details the peak workpiece temperature at each thermocouple location in relation to Test 2. Between pass 1 and pass 2, thermocouple 1 experienced a 36.3% increase in measured workpiece temperature, whilst thermocouple 2 and thermocouple 3 experienced a 18.1% and 23.4% increase respectively. Although thermocouple 3 indicated a significant spike in absolute temperature of 110°C, it is noteworthy that thermocouple 1 detailed the maximum temperature differential between subsequent passes. The figure also clearly details that subsequent passes resulted in increased thermocouple temperature readings, something which was mirrored in Fig 5.11, and is also something that has been reported in the literature by the likes of Batako, Rowe and Morgan (2005) and more recently by Grimmert, Pachnek and Wiederkehr (2023) who undertook experimental research on CFG of Inconel 718 workpieces. The workpiece temperature rise in the vicinity of thermocouple

3 is consistent with the film boiling hypothesis proposed. As the coolant was a water-based emulsion, and the boiling temperature of water being 100℃ at one bar of pressure, it can be expected to boil at this temperature, thus resulting in little to no coolant being present in the grinding zone, thus causing an increase in friction between the tooling and the workpiece, and therefore increasing the workpiece temperature significantly. The increase in workpiece temperature due to the film boiling effect would also produce a worsened surface integrity condition in terms of surface roughness and unwanted tensile residual stresses, for example (Batako, Rowe and Morgan, 2005).

Fig 5.17 details the thermocouple temperature gradient results acquired via the subsequent passes of the grinding wheel during Test [2]. As is evident from the figure, there is an obvious negative correlation between passes, with a maximum 24.2% increase in workpiece temperature between pass 1 and pass 2. Thermocouple 3's temperature trace also details a higher temperature than either thermocouple 1 or thermocouple 2 by 80% at the closest stand off distance. The response is again expected due to thermocouple 3 experiencing the highest temperature during the test. It can also be noted that there is a negligible difference between the response of thermocouple 2 and thermocouple 1, indicating that there was an optimal level of coolant within the grinding zone to keep workpiece temperature consistent, before rapid film boiling of the coolant away from the grinding zone occurred at thermocouple 3's position during the pass.

Continuing, the author was interested in discovering the likelihood of the occurrence of the high workpiece temperature peak observed via thermocouple 3's response and so decided to repeat Test [2]. As can be clearly determined from Fig 5.18 and Fig 5.15, the high temperature response is apparent in both, proving that it is an actual physical effect on the system and not an anomalous result. The peak workpiece temperature is again observed in thermocouple 3, with a maximum reading of 350°C which is comparable with Test [2]. It is also interesting to note the response of thermocouple 3 which appears to plateau for a short duration, before rising rapidly. The author surmises that thermocouple embodiment

irregularities were at play (Shen *et al.*, 2008). However, the peak workpiece temperatures observed in thermocouple 1 and thermocouple 2 were concurrent with the previous test.

During Test [4], there was a data acquisition error in relation to the thermocouple data logger. This meant that the second row of 1 x 3 thermocouples were active instead of the required first row. This meant the first grinding pass temperature measurements were taken by the second row at a radial distance from the cutting path. As can be observed from Fig 5.19 despite thermocouples 1, 2 and 3 being 22mm radially apart from the desired first row, they still delivered a reading on the first pass. This $\Delta$T is 3.5°C, or 14.89% of the reading that the second row of thermocouples would have read due to the linear, first order response of the thermocouple; an interesting result if wishing to assess the sensitivity of the thermocouples used throughout this study.

Test results for Test [4], pass 2 displayed a longer temperature retention time for thermocouples 1 and 2 of approximately fifteen seconds when compared to Test [3]. A direct comparison of the workpiece temperature retention data between these two tests are detailed in Fig 5.20. This is unlike earlier tests whereby the thermocouples retained their temperature for approximately twelve seconds as in Fig 5.6.

It can also be determined from Fig 5.21 that using higher wheel speeds at the same depth of cut resulted in a lower workpiece temperature by 34.2% for SiC wheels. However, this finding from the experimental test program is contradictory to Mahamani and Jawahar (2018) who found higher workpiece temperatures at higher wheel speeds.

The final pass for Test [4] resulted in thermocouple destruction as presented in Fig 5.22. As can be clearly ascertained from the plot, thermocouple 1 observed a peak workpiece temperature of 52°C before experiencing thermocouple failure; thermocouple 2 displayed a similar trace, at fifty seconds into the pass, whilst thermocouple 3 indicates a peak workpiece temperature spike of 68°C at fifty-six seconds. It is also evident from the plot that the response from thermocouple 3 is obscure, with one possible explanation being

a possible cutting of the thermocouple wiring. It is also clear that these temperatures are significantly lower than those presented in Fig 5.21 and should be apparent upon destruction of the thermocouple node. Moreover, the failure of the thermocouple could be due to the increased mechanical loading from previous passes resulting in over stressing of the thermal cement, thus dislodging the thermocouple node out of *situ*. Finally, unlike previous test cases, the thermocouple vs. stand off distance plot for Test [4] yielded inconclusive results as the second pass observed thermocouple destruction before reaching peak temperature, and so subsequently has been omitted from this thesis.

Fig 5.23 details the merged temperature traces for Test 4. Again, two passes were made, with the thermocouples reading an increasingly higher temperature throughout the first pass. This is again in accordance with the differing temperature readings at the location of thermocouple 1, 2 and 3, respectively. This adds increasing confidence to the conclusion that a single thermocouple configuration is unfit for purpose when assessing workpiece temperatures whilst machining and is a key novel finding to be drawn from this thesis. Interestingly, the horizontal portion of thermocouple 3 after fifty seconds into the first pass before rising sharply thereafter indicates that some coolant was still present in the grinding zone before the film boiling effect occurred, after which the sudden rise in workpiece temperature is apparent, something predicted by Singleton (2014).

As Test [5] was a repeat of Test [3], it is evident that some variation in the peak workpiece temperature reading via thermocouple 3 would be observed. The workpiece temperature results pertaining to Test [5] are presented in Fig 5.24, whilst the workpiece temperature results pertaining to Test [3] was shown in Fig 5.18. When comparing these figures, the same trend is apparent whereby a significant spike in thermocouple 3 can be determined; this is certainly a key point to note and one which is novel in its application for this and future research. This result would not have been discovered if the author had not settled upon assessing three thermocouples positioned in series as little, if any work, has been conducted whilst applying this approach. Clearly, single point thermocouples are inadequate when wishing to ascertain a correct reading for workpiece temperatures in

grinding, and, more broadly, for any machining approach used. Moreover, the most critical aspect of interest of this approach is monitoring the lead-out point of the workpiece where the temperatures are at a maximum, before a high reduction in the MRR is observed. During Test [5], pass 1, there is a significant 40.7% difference in workpiece temperature reading when using a single thermocouple when compared to a multiple thermocouple configuration. The author believes that potentially film boiling of the coolant away from the grinding zone is occurring as the pass is completed and is why such significant peaks in workpiece temperature are observed. A typical boiling curve for water at 1bar is presented in Fig 5.58 detailing this physical phenomenon (Alagan *et al.*, 2020). This lack of available coolant in the grinding zone allows for the peak workpiece temperature to increase, as the energy partitions within the system are ineffective at keeping other related temperatures at normal levels. Clearly this is an undesirable outcome regarding component manufacture and is therefore a result of importance that should be considered for future machining applications.

The temperature increase observed during the second pass when compared to the first pass for Test [5] is considerable, i.e., $\Delta$T of 20% within the Workpiece Temperature vs. Time plot being presented in Fig 5.25. This is of course in line with the notion that the closer the thermocouple is to the cutting surface, then the higher and more accurate the temperature reading will be when compared to thermocouples which are further away from the cutting surface.

Two key points of interest are thermocouple 3's response at fifty seconds into the pass, i.e., the thermocouple temperature appears to rise as expected, before a small kink in the trace becomes noticeable. The temperature response is again then observed to increase further until the peak temperature reading of 148°C. Additionally, the temperature trace of thermocouple 1 appears to indicate a steady state before reducing at sixty seconds into the pass. This is explained via thermocouple 1 retaining the temperature of the workpiece for the longest duration of the pass (entry into the workpiece to exit), and also why thermocouple 3, despite observing the highest peak workpiece temperature, observes a swift drop off as the wheel exits shortly after passing over this final thermocouple in the

arrangement. Additionally, the temperature traces from thermocouple 1 and thermocouple 2 are identical to previous tests whereby a steady increase in thermocouple temperature reading is obtained across the face of the pass and which has now become the expected response.

Fig 5.26 summarises the two passes relating to Test 5. As Test 5 was a repeat of Test 2 and Test 3, similar results should be expected. Whilst the temperature traces were highly similar, dissimilar magnitudes were found. However, near perfect trends were found as the grinding wheel traversed through the workpiece, with a linear increasing magnitude through the positions of thermocouple 1, 2 and 3. This indicates that coolant was still present in the grinding zone, or, perhaps, a lower MRR was actually being removed from the workpiece, i.e., a lower $a$ value was actually being used due to more prominent wheel wear. However, appropriate steps were made to minimise this source of error through measuring the tooling after each pass and undergoing a dressing process to calculate $G$-ratios as presented in subsection 5.1.1.

Finally, Fig 5.27 displays the thermocouple temperature gradient for the peak workpiece temperatures obtained from the trial. Clearly, a negative correlation can be determined. This gradient profile can also be expected with the higher temperature responses being obtained when the stand off distance from the thermocouple node was at a minimum, and the lowest workpiece temperatures observed when the stand off distance was at a maximum. In the case of Test [5], a 22.4% increase in thermocouple temperature was observed between the two thermocouple stand off distances tested, and so reinforces the conclusion that the optimal accuracy workpiece temperature readings are obtained when thermocouples are placed as close to the grinding plane was possible. The individual thermocouple responses across the passes are also validated in the figure, whereby each thermocouple experienced an increase in workpiece temperature than the preceding one due to the build-up of latent heat in the workpiece and subsequent film boiling away of the coolant from the grinding zone. Also, when compared against Test [8], where the only

change in parameter was a doubling of the depth of cut, a significant increase in maximum workpiece temperature is recorded; something that is expected due to the higher MRR.

As Test [6] utilised the smallest depth of cut, ($a$), value of 0.3mm within the experimental test programme, seven passes were made which allowed for multiple workpiece temperature and associated cutting force data to be obtained. Fig 5.28 details similar thermocouple traces from previous tests, where steady increases are observed from thermocouple 1 in the configuration, through to thermocouple 3 in the series. In terms of the accumulation of temperature across the face of the workpiece, a $\Delta$T of 41.9% between thermocouple 1 and thermocouple 3 is observed. Clearly, from tests conducted throughout this thesis, the final thermocouple in the series has been demonstrated to yield the highest workpiece temperature value of the grinding pass due to the accumulation of heat and is thus also apparent in Test [6]. During the initial pass of Test [6], the workpiece temperature retention phenomena as similarly detailed for Test [5], pass 2 in Fig 5.25 is also apparent. For Test [6], pass 1, this retention rate is even more evident for thermocouple 1 and 2 than in previous tests, displaying an obvious increase across the thermocouple configuration; an extremely interesting result. As mentioned, the question of ensuring a consistent and accurate thermocouple node/thermal cement interface which in turn is in contact with the workpiece material is incredibly hard to predict. Several possible solutions could be implemented in future such as the use of a higher operating temperature cement; the development of an automatic or direction injection nozzle to locate the cement directly into the thermocouple hole; reducing the thermocouple hole size to the smallest allowable diameter without reducing cement adherence to negate temperature field effects, and limiting more aggressive grinding parameter tests where grinding temperatures are higher.

The workpiece temperature results for Test [6], pass 2 as displayed in Fig 5.29 indicated some variation from the initial trial as was previously presented in Fig 5.28. Thermocouple 1 acknowledged a higher workpiece temperature response than thermocouple 2. The author surmises that this is to do with an issue with regards to the sample's thermocouple embodiment process, i.e., thermocouple 2 is actually further away from the

grinding surface than thermocouple 1, an observation made by Shen *et al.*, (2008). The apparent long workpiece temperature retention time is also an interesting note to emphasize which has been highlighted by the author during previous tests, i.e., it is evident again that temperature accumulation is occurring within the workpiece. Even with the slightly anomalous result of thermocouple 2 (with one assuming that thermocouple 1 would have indicated the lowest temperature reading due to it not having any residual heat from which to draw from the workpiece as has been demonstrated via previous observations), the $\Delta$T change from the lowest temperature response (assumed in this case to be thermocouple 1) and the highest temperature response (thermocouple 3) is 6.9%.

A similar workpiece temperature response to the first and second passes is presented for the third pass in Fig 5.30. However, there appears only a negligible difference between the three passes analysed, with marginal workpiece temperature increases observed for thermocouple 1 and thermocouple 2. It is apparent that thermocouple 3 appears to remain largely thermally static throughout. This is somewhat surprising considering previous passes presented throughout this section which indicate increases in workpiece temperature with subsequent passes. However, it should be noted that this marginal increase in the third thermocouple in the series was apparent during the five passes conducted during Test [1], and therefore it can be determined that more research would need to be conducted to establish why that occurrence has been detected twice in this study when assessing shallow depths of cut.

Fig 5.31 details the workpiece temperature responses obtained from Test [6] pass 4. Again, only a negligible 5°C increase in the overall temperature profile of the thermocouples were observed. This is to be expected as only small depths of cut were being used. An additional point of note is the apparent workpiece temperature retention within thermocouple 2, whilst thermocouple 1 appears to indicate limited retention during this pass. The trend whereby thermocouple 3 always registers the highest temperature response now saw thermocouple 1 indicating the peak response. Again, the author surmises this is due to issues regarding the thermocouple implantation procedure.

Fig 5.32 details the negligible workpiece temperature response changes observed during pass 5. Here, the trend of thermocouple 3 indicating the peak temperature response returned during this pass. Peak temperatures were observed to reach 50°C in the final thermocouple in the series, whilst the thermocouple retention time trend was observed in thermocouple 1, reaching 24°C and lasting twelve seconds before returning to a linear response, and thermocouple 2 reaching 28°C and lasting eight seconds before returning to a linear response. Again, this response was observed in previous passes such as those detailed in Fig 5.28, Fig 5.29, Fig 5.30 and Fig 5.31.

Fig 5.33 presents the workpiece temperature profiles for pass 6 of Test [6]. Only a marginal temperature response increase from the thermocouple configuration was observed. There did appear, however, to be some sort of noise occurring in the system at fifty-nine seconds, with thermocouple 3 appearing to drop below its baseline temperature before rising again almost instantaneously. This is in contrast to the previous pass which noted a clear general trend as shown in Fig 5.32. The author surmises this must have been the destruction of thermocouple 3 and the reading thus indicated an inactive thermocouple. This hypothesis was logical, as, by the completion of pass 6, a total of 1.8mm of material had been removed from the surface of the material, and the grinding wheel would thus be cutting behind the thermocouple implantation depth and thus causing thermocouple destruction.

The final thermocouple temperature responses for pass 7 presented in Fig 5.34 vindicated the author's suspicions prior to undertaking the final pass; that pass 6 had fully destroyed thermocouple 3. This can be determined from the completely linear response data series for thermocouple 3 as shown in the figure. In terms of the other thermocouples in the configuration, there appeared only small temperature response increases with thermocouple 1 (approximately 2°C), and negligible temperature changes for thermocouple 2.

Fig 5.35 details the seven passes in relation to Test 6. Some discrepancies are apparent from these trials, with only minimal changes in the peak workpiece temperature at the position of thermocouple 1, 2 and 3. The errors associated with the test were found to

increase as further passes were made, with the initial four passes resulting in the expected trend of increasing workpiece temperature the further along the pass as presented by previous trial data. Possible errors that could have occurred include wearing of the carbide drill bits when manufacturing the thermocouple housing cavities resulting in inconsistent depths of cut causing differing stand off distances from the ground surface. Upon further analysis, Test 6 could be evaluated through a second round of trials with additional passes as a way to ensure the reduction in the random error potential of the associated workpiece temperature when using the grinding parameters being assessed.

Fig 5.36 details the thermocouple temperature gradient across all passes conducted for Test [6]. When compared against other temperature gradients presented herein, the response across the stand off distance is clearly not linear. It appears that for stand off distances significantly away from the grinding surface, the temperature response only marginally increases. It is also clearly noticeable from the figure that at stand off distances $<$ 1mm, a more linear trend is observed. This again vindicates previous results regarding workpiece temperature vs. stand off distance, i.e., that the closer the thermocouple is to the grinding surface, the higher and more accurate the temperature reading. The author proposes that an optimal operating distance is reached at a stand off distance of 0.5mm, whereby thermocouple temperature responses appear to be independent of distance from the grinding surface. This is an important observation and could result in several passes being made for depth of cut, $a$, values of 0.5mm or less, thus enabling repeatable passes to be made of experiments for validation purposes with little to no additional cost to the production budget or testing timeframe. It can also be noted that thermocouple 2 appears to indicate a lower temperature than thermocouple 1 which goes against previous results. This indicates that thermocouple 1 could be closer to the cutting surface than thermocouple 2. Again, this could be due to tool wear of the drill bit used on the Matsuura FX-5 Vertical Machining Centre. If this is the case, it would infer than thermocouple 2's response is lower than the actual grinding temperature at the position of the thermocouple 2, and so additional tests should be established to verify this data point. Thermocouple 3 is also observed to reduce to 0°C, which corroborates Fig 5.34 and the destruction of the instrumentation during pass 7.

Fig 5.37 details the workpiece temperature responses from the initial pass of Test [7]. Again, there is an observable spike in temperature at thirty seconds into the grinding action as the grinding wheel passes over thermocouple 3. Thermocouple 1 and thermocouple 2 peak at 60°C and display a significant temperature retention decay curve. Thermocouple 3 displays a peak workpiece temperature of 330°C, with a $\Delta$T between both thermocouple 1 and thermocouple 2 of 270°C (81.8%). Interestingly, when a direct comparison is made against Test [3], whereby the feed rate, $V_w$, is doubled and all other parameters are held constant, the workpiece temperature is observed to reduce by 5.7%. As stated by the literature (Mahamani and Jawahar, 2018), increases in $V_w$ should result in an increase in workpiece temperature. As the $\Delta$T response between the two passes from the two separate tests was $\approx$6%, the author deemed this within engineering error, and believes that if a more suitable and accurate thermocouple embedding method could be implemented, such discrepancies would prove unfounded.

Fig 5.38 presents the workpiece temperature results from pass 2 of Test [7]. A workpiece temperature rise of 50°C can be observed between pass 1 and pass 2. This relates to a percentage increase of 13.2%. Again, the same spike in the data is observable in thermocouple 3 when compared to thermocouple 1 and thermocouple 2. This peak workpiece temperature result is greater in magnitude than during pass 1 and should be considered a significant result. During pass 2, the temperature response in thermocouple 1 is far more pronounced than during pass 1. Thermocouple 1 also observes a temperature increase of 50°C, whilst thermocouple 2 only indicates a temperature rise of approximately 15°C. This can be accounted for by possible issues relating to the actual location of the thermocouple bead in the drilled hole. As mentioned previously, without the use of a direct injection device for applying the thermal cement securely into the thermocouple cavity, it can be difficult to achieve 100% accuracy in thermocouple placement.

Fig 5.39 presents the two passes assessed for Test 7. Here, the peak workpiece temperature occurs at the position of thermocouple 3; something observed during previous trials. Interestingly, the temperature traces for all three thermocouples are similar in nature

to Test 2 as detailed in Fig 5.16, where the first two thermocouples in the configuration were observed to register a similar level of magnitude, before a severe spike in workpiece temperature at the location of thermocouple 3 was observed. A key observation between these two tests were that all grinding parameters were kept constant, except for a change in the feed rate, $V_w$, from 150mm.min$^{-1}$ to 300mm.min$^{-1}$. This is an interesting observation inferring that an increase in feed rate results in a decrease in workpiece temperature and is something that has been repeatedly published in the scientific literature most recently by Pratap *et al.*, (2023) and Yan *et al.*, (2023) and can be explained due to shorter exposer time and dominant transient heat transfer within the grinding zone.

Fig 5.40 presents the thermocouple temperature gradient response for the two passes conducted during Test [7]. As expected, decreasing the stand off distance from 1.5mm to 0.5mm results in an improved thermocouple temperature response of 13.1%. The same trend was demonstrated in Fig 5.13, Fig 5.17, Fig 5.27 and Fig 5.36. Once more, it can be stated that thermocouple placement has a significant impact on the consistency of the workpiece temperature reading and so should be carefully considered before manufacturing of workpiece housing cavities for the instrumentation is undertaken. Thermocouple 3 again indicates the highest temperature reading than either thermocouple 1 or thermocouple 2 as observed during previous trials, although there is some discrepancy between the temperature reading when comparing thermocouple 1 and 2; the former indicating a higher temperature than the latter. This would indicate thermocouple 1 being somewhat closer to the grinding surface than thermocouple 2. Another possible explanation is that the workpiece material had some subsurface damage during the manufacturing of the thermocouple cavity holes or during initial raw production resulting in the heat generated by the grinding process not being uniformly distributed through the workpiece in that vicinity of the cutting path.

Fig 5.41 presents the workpiece temperature readings for pass 1 of Test [8]. As can be ascertained from the plot, the thermocouple temperature response of the pass displayed a clear and structured trend precisely mirroring those from earlier tests. The peak temperature occurring in thermocouple 3 was the highest temperature recorded by

the thermocouple system developed, described and discussed within this thesis. A key finding from this test is that the temperature spike that was observed was less pronounced, with a 40% change in temperature results between thermocouple 1 and thermocouple 3. It is evident that the trend of increasing thermocouple temperature response as the grinding wheel moves through the workpiece is more consistent when one gets closer to the thermocouples. Despite not destroying the thermocouples as hoped, the author surmises the accuracy and consistency of the trend lines are twofold; firstly, the thermocouples are all consistently the same distance away from the grinding surface, and secondly, the grinding pass got very close to the thermocouple, without actually leading to thermocouple destruction. With the recorded workpiece thickness for Test [8] having been measured to be 9.02mm, the expected thermocouple depth to ensure destruction during the grinding pass would have to have been 7.02mm into the workpiece.

Fig 5.42 presents the thermocouple responses for Test [9]. An interesting trend can be determined. Both thermocouple 1 and thermocouple 3 appear to be reaching the same peak temperature of 460°C, whilst thermocouple 2 only reaches a peak temperature of 290°C. This is likely due to thermocouple 2 not being fully embedded in the workpiece, possibly in an air pocket in the thermal cement. It can be observed that thermocouple 3 is fully destroyed during the pass due to the vertical drop-off in the thermocouple response at sixty seconds into the data acquisition. The trace is then observed to flat line for the remainder of the pass. This is in the same manner as Test [6]. However, the same cannot be said for thermocouple 1 and thermocouple 2, as it can be determined that thermocouple 3 was slightly closer to the grinding surface than either thermocouple 1 or thermocouple 2. When Test [9] is compared to Test [8], with the only difference being $V_s$, it is demonstrable that the workpiece temperature was lower for higher wheel speeds. A percentage reduction in peak workpiece temperatures when moving from a 20m.s$^{-1}$ wheel speed to a 30m.s$^{-1}$ wheel speed was observed to be 34.2%.

Fig 5.43 presents the workpiece temperature responses gathered from Test [10]. The final test indicated some interesting results in-keeping with similar tests from earlier in this study; namely, the trend of the thermocouple responses along the path of the grinding wheel observing a gradual increase in temperature. Despite thermocouple 2 not following this general trend, the clear observation from the lead in thermocouple 1 against the lead out thermocouple 3 does show a linear trend of this nature. Between thermocouple 1 and thermocouple 3 a $\Delta$T of 25.6% can be determined. Clearly, a percentage difference of this nature is an extremely important phenomenon that manufacturers should be sentient of to ensure that when grinding safety critical components, operators are actually grinding at the temperature they believe to be, and not at a temperature, in actuality, which is 25.6% above it. This could result in unwanted thermal damage, higher surface roughness or residual tensile stresses within the component, and thus incur additional issues with component accuracy and production stoppages before the problem can be isolated.

When one compares Test [10] against Test [9], where all parameters are kept constant except the feed rate, $V_w$, it can easily be observed that the workpiece temperature increases with $V_w$. In this instance, a $\Delta$T between the two peak temperatures reached is 40%; not an insignificant margin. Moreover, the temperature result from Test [10] would be of extremely high interest to manufacturers of temperature critical components such as jet engines as the peak workpiece temperature is of vital importance for determining surface integrity and subsequent fatigue performance. Finally, Table 4.2 details a summary of the workpiece temperature at each thermocouple location per pass, per test.

When considering the temperature effects presented herein, it should be noted that Tawakoli (1990) postulated that the observable surface temperature changes during grinding were a result of *contact layer theory*, otherwise referred to as the grinding or contact zone. The size of this layer also has a direct impact on the cutting forces experienced by the grinding tool. It is known that during grinding, almost all the generated energy is expressed as heat. This is attributed to the large plastic deformations and shearing of the workpiece involved when metal cutting. Additionally, high temperatures resulting from film boiling

occur in tests where grinding parameters are more aggressive with the cooling effect from the coolant, i.e., the energy partition of the thermal energy within the grinding zone, being ineffective. Film boiling results when the fluid begins to boil and creates an insulated micro layer of air between the contact zone and cutting fluid, inhibiting the flow of heat away from the cutting zone (Singleton, 2014). This is clearly more pronounced in Test 10 resulting in an unwanted increase in $R_a$ value as well as an increase in microhardness depth. Test 8 also indicated unwanted levels of tensile residual stresses which can again be attributed to the increased workpiece temperature from the increased depth of cut of 2mm and slow feed rate of 150mm.min$^{-1}$ and is therefore indicative of CFG (Marinescu, *et al.*, 2013). As has been previously presented, the depth of cut and feed rate are the primary attributing process parameters for increased workpiece temperature (Mahamani and Jawahar, 2018), something that been previously alluded to in the literature, and it also something proposed herein. Increased wheel speeds are also found to induce lower workpiece temperatures; a finding presented here and within previous research (Singleton, 2014).

Whilst assessing the temperature responses measured throughout this thesis, it could be argued that a repeat of the testing would prove useful as some uncertainty remains when utilising thermocouples for temperature measurement. For instance, this was found during the initial stability testing as presented in section 4.1, Fig 4.3. When utilising low-pressure coolant, the workpiece temperature appeared lower than when using higher pressure coolant. This would appear counter-intuitive whereby coolant application should reduce workpiece temperature (Yang *et al.*, 2022). However, it can be observed that this phenomenon only appears in association with thermocouple 2 in the configuration, with the change in both thermocouple 1 and thermocouple 3 (both relatively stable at approximately 25°C) response being negligible. Possible explanations for this could be incorrect placement of the thermocouple node in its cavity and was therefore a result of human error, something reported on by Demichela, Barresi and Baldissone (2018) during the freeze-drying process. Being as such, the limitations of using the manufacturing technique to produce the thermocouples becoming embedded within the workpiece using thermal cement, some uncertainty remains as to whether a more reliable and resilient process

should be used during further research. However, it could also be argued that this matters most only when workpiece temperatures are lower, i.e., when grinding with less aggressive parameters than when grinding with more aggressive parameters. This is due to the significant workpiece temperature difference between test cases such as when comparing the workpiece temperature in Test 1 to the workpiece temperature during Test 10. During Test 1, the workpiece temperature was 75°C, whilst during Test 10, the workpiece temperature was 780°C. When considering thermocouple temperature measurement, given readings are subject to some questionability which was discussed by Nee and Tay (1981). What readout thermocouples provide is the experimental grinding temperature. This is due to there being a period before the thermocouple can reach a steady-state value and thus provide a magnitude for the measured temperature. This ultimately leads to an underestimation of the actual grinding temperature, which in practice means the data provided herein could be the minimum workpiece temperature that should be considered when designing for manufacture. This is to be expected due to this added thermal inertia from the thermocouple system. It should also be noted that this phenomenon of a corrected temperature only holds for higher feed rates and wheel speeds, something that was further alluded to by Outwater and Shaw (1952) and appears to have little influence when feed rates and wheel speeds are slower such as those evaluated within this thesis. Further discussion regarding calculating the time constant, $\tau$, to correct this experimental issue are given in Appendix C.

### 5.2.3 Cutting Forces

When wishing to analyse a machining process such as grinding, it is common practice for the cutting forces to be measured. This is undertaken for several reasons which include evaluating the machinability of the material, the vibrations within the system and monitoring tool wear. Moreover, the measurement of the associated cutting forces is straightforward whereas workpiece temperature measurement during machining is not.

Table 4.3 details a summary of the cutting forces associated with each test conducted. From the data presented, a clear trend can be seen in that the cutting forces were higher

when using more aggressive grinding parameters (indicative of a HEDG process) and were lower when using less aggressive grinding parameters (indicative of a surface grinding process). This is to be expected during machining processes and has been reported in the literature previously (Seker, Kurt and Ciftci, 2004). This can be determined from Fig 5.44 which details Test [1] (a less aggressive system), whereby the cutting forces reach a maximum of 620N and Test [10] in Fig 5.53 (a highly aggressive system) where the cutting forces were 1300N.

Taking Fig 5.44 as a typical Cutting Force vs. Time plot for the grinding process, it can determined for both the $F_z$ and $F_y$ traces that a clear lead-in section of each occurs (consistent with the grinding wheel entering the workpiece material), before reaching an approximate stabilisation point. This general stable cutting force relationship remains for the most part during the pass (with some observable chatter), before a final lead-out section of the plot is observed towards the end of the grinding pass where the cutting force responses reduce. In the case of these tests, the $F_z$ and $F_y$ traces are represented as the normal and tangential force components respectively, with $F_z$ being always greater than $F_y$ (Shaw, 1985). Again, this is to be expected as the normal force undertakes the majority of the cutting load. The $F_x$ trace for all the cutting force plots appears negligible and is also to be expected as this represents the cross-feed force across the face of the grinding tooling which can be shown numerically to be insignificant in terms of providing any material removal (Shaw, 1996a).

The chatter phenomenon observed during the cutting force plots can be distinguished between forced and regenerative chatter, with the former being associated with eccentricity between the grinding wheel and the workpiece, whilst the latter being deemed the most dangerous and yet most common form of chatter. This phenomenon is associated with the class of 'self-excited' vibration, an area of research which has been considered by Inaski, Karpuschewski and Lee (2001), Altintas and Weck (2004), Quintana and Ciurana (2011) and Alexandre *et al.*, (2018).

Similarly, as Fig 5.44 suggests, the cutting force results from Test [1], pass 1 also indicated an increase in magnitude when compared directly against those obtained from Stability Test 4 which utilised the same parameters. This is firstly apparent when comparing the $F_y$ responses of the two tests; i.e., a $\Delta F_y$ of 42.8%. It can also be stated that the level of chatter experienced during the cutting stage of the process when compared against the previous test is increased (±200N for pass 1, whilst Stability Test 4 observed ±100N). This chatter phenomenon is common during CFG when feed rates are slower (Toth, 2020). This is because chatter is dependent on the frictional conditions between the tool and the workpiece (Jalili *et al.*, 2017). Another point of interest is the secondary spike and swift drop-off occurring at sixty seconds into the pass which could indicate abrasive grain breakage in the wheel matrix.

As can be determined from Fig 5.45, (Test [2]; pass 2) the $F_z$ cutting force response increases to approximately 950N when compared to pass 1 which indicated a maximum $F_z$ value of 900N. Again, this trend in the data is to be expected. During pass 2, there appears to be more chatter representative in the system when compared with pass 1, i.e., ±400N for pass 1, whilst pass 2 indicates ±540N.

When considering the cutting force response from Test [3] as outlined in Fig 5.46, a similar trace and magnitude to those presented in Fig 5.45 for Test [2] is observed. One point to note from Fig 5.46 is the slight fall in $F_z$ value at sixty seconds into the pass before rising sharply again at sixty-four seconds into the pass. This response was not observed during Fig 5.45, so clearly some variance in cutting force response for the same test is noticeable.

Test [4] looked at increasing the wheel speed, $V_s$, to 30m.s$^{-1}$ whist keeping all other parameters the same. One ineffective pass was made initially, whilst on the second and third attempts, a positive outcome was recorded. As presented in Fig 5.47, the cutting force responses for Test [4], pass 3 are as expected. However, as with the workpiece temperature responses from the thermocouples outlined in Fig 5.22, at fifty seconds and fifty-six seconds

into the pass, two spikes of 1550N are observed for the $F_z$ trace. This is a 35.4% increase from the steady state cutting response observed from twenty seconds into the pass. At this exact point during the cutting action, thermocouple 2 and thermocouple 3 were observed to fail. Interestingly, the $F_y$ trace did not observe the same phenomena. It can be surmised that the failure of the thermocouple system could not have been the cause for the significant increase in the cutting force measured, as the subsequent hole within the workpiece would have resulted in a decrease in cutting force magnitude. This is an interesting note to mention when comparing the workpiece temperature and cutting force profiles simultaneously and could be an area for additional research.

The cutting force response for Test [5], pass 2 as presented in Fig 5.48 clearly indicates a significant step change from previous tests conducted. The usual response can be observed until fifty seconds into the pass whereby a small spike then becomes prominent, with $F_z$ displaying a 1000N response. However, a brief fall in the trace is then observed until sixty seconds into the pass where a substantial level of chatter is apparent, i.e., $\pm$1000N. The same response was observed within the $F_y$ trace of the cutting force output. At sixty seconds into the pass, a peak is observed of -620N, up from -300N during the steady state cutting region. This chatter is then sustained until the end of the pass when the grinding wheel exits the workpiece. This chatter level resulted in significant pitting of the grinding surface upon visual inspection of the workpiece post-testing and therefore had a negative impact on the surface integrity of the sample.

Finally, Fig 5.49 details the cutting forces associated with the final pass of Test [6]. Unlike previous passes, the $F_z$ response appeared to be significantly reduced to 1300N, despite a noticeable peak still being observed at sixty seconds into the pass. At this point during the cut, the author can only surmise again that some manufacturing issue in relation to the thermocouple implantation method or in-service wheel sharpening being responsible for the cutting force responses. Another comparison can be made for the cutting force profiles for Test [6] when they are compared against Test [4], where all parameters were kept constant except the depth of cut. Test [4] used a depth of cut of 1mm and overall

observed a greater magnitude of cutting force (≈1600N) than Test [6] which observed a lower magnitude of cutting force (≈1500N). Drawing conclusions from Test [6], it can be stated that shallower depths of cut result in a lower cutting force response. Conversely, it can also be determined that Test [4] had very low levels of chatter when compared to Test [6] where chatter was extremely high, i.e., deeper depth of cut, $a$, values are more likely to decrease chatter marks and thus make for more favourable surface integrity performances when grinding Ti-6Al-4V workpieces when holding other operating conditions constant. However, the author also proposes that machine vibration and/or the workpiece not being fully supported on the dynamometer as a possible explanation for this result.

Fig 5.50 displays the cutting force results for pass 2 of Test [7]. $F_z$ increased significantly between pass 1 and pass 2, where peak grinding forces reached a maximum at 1550N for the $F_z$ component, whilst in pass 1, they were 1100N; $\Delta$F of 450N or 29%. For the $F_y$ component, the magnitude was observed to increase slightly by 4% which can be deemed negligible in this instance. However, the chatter within the force results for pass 2 is significantly more pronounced than the chatter that is observable during pass 1; i.e., the chatter did not exceed more than 200N for the initial pass, whilst in pass 2, the chatter in the system was 750N; a change of 73.3%. Clearly, it can be stated that increasing the feed rate significantly affects the level of chatter in the grinding process when all other variables are held constant, something reported by Quintana and Ciurana (2011).

The cutting force responses for Test [8] are outlined in Fig 5.51 and from which some interesting results are detailed. It can be determined that the $F_z$ force trace reached a significant magnitude of 1300N, whilst the $F_y$ profile detected a -480N peak. As with Test [7] which utilised the deepest depth of cut, ($a$), value considered in this test programme (2mm), the cutting force profile appeared more stable than those which utilised the shallowest depth of cut value of 0.3mm. This is an interesting result, which indicates to the author that, despite the resulting cutting forces being larger in magnitude at increased values of process parameters such as $V_s$ and $V_w$, the stability of the force profiles appears significantly improved during these test cases.

Whilst considering the cutting force responses of Test [9] as presented in Fig 5.52, and when subsequently compared against Test [8] where the only process parameter changing being an increase in $V_s$ from 20m.s$^{-1}$ to 30m.s$^{-1}$, the $F_z$ component was found to reduce by 7.69%.

Fig 5.53 presents the cutting force data for Test [10]. It can be established that the final cutting force experimental data yielded some positive results. A standard cutting force response resulting in a consistent lead-in and lead-out profile, with some low level chatter during the actual cutting action, can be observed and is something also described by Li *et al.*, (2017). The peak cutting force magnitude for the $F_z$ component was observed to reach 1500N; a value that is largely regarded as commonplace for this significant depth of cut (Kalpakjian and Schmid, 2008). When compared to the cutting profile of Test [9], it was observed that the ΔF peak is 13.3% greater for Test [10]. This is unsurprising with Test [10] evaluating all three variables at their 'high' level, i.e., all at a maximum in magnitude. Higher wheel speeds also should result in lower maximum uncut chip thickness due to less mechanical loading being exerted on each grain within the grinding tool. The maximum uncut chip formation phenomenon has also been alluded to by Zhang, Kang and Tang (2020) who evaluated surface integrity post-grinding, and Vinay and Rao (2003), who reported on the expression for maximum undeformed chip thickness presented in Eqn. 2.4.

### 5.2.4 Workpiece Temperature and Cutting Force Comparison

Once the workpiece temperature and cutting forces had been analysed, further analysis to compare them directly was undertaken. As can be determined from Fig 5.54, it is clear that as the workpiece temperature increases, so does the cutting force response when the depth of cut, $a$, is increased from 0.3mm to 1mm, i.e., a 70% increase in the depth of cut results in an 86.2% increase in workpiece temperature and a 17.4% increase in cutting force. This indicates that the workpiece temperature response of Ti-6Al-4V samples is more sensitive

to depth of cut increases than the induced cutting forces are. This relationship is again expected as proposed by Rowe (2009).

In Fig 5.55, the workpiece temperature can be observed to increase with cutting force as the feed rate, $V_w$, is increased. Here, when the feed rate was doubled from 150mm.min$^{-1}$ to 300mm.min$^{-1}$, the workpiece temperature was observed to increase by 99.7%, whilst the resultant cutting force increased by 27.9%. Again, the increase in feed rate displays a positive linear correlation between workpiece temperature and cutting force and is certainly a key point of interest to note from the experimental studies conducted. In addition, the increase in cutting force with an increase in feed rate was determined from the experimental study as presented in section 4.1.2.2 and has also been reported in the literature (Mahamani and Jawahar, 2018).

Fig 5.56 indicates that the workpiece temperature appears to decrease as the cutting force increased when the wheel speed, $V_s$, increased, i.e., a 72.4% decrease in workpiece temperature and 16.8% increase in cutting force with a 33.3% increase in $V_s$. Again, the decrease in workpiece temperature with an increase in wheel speed was found during the experimental test programme as presented within section 4.1.2.1 and so this relationship has discernible validation. This correlation can also be expected due to higher wheel speeds resulting in less time for the workpiece to absorb heat, thus resulting in lower workpiece temperatures (Wu *et al.*, 2017). Fig 5.57 also details both the normal and tangential cutting forces in addition to the associated workpiece temperatures for each test. When comparing Test [2] and Test [3] which was a repeated test, it is apparent that the cutting forces were close in magnitude (<5% for Fz and <7% for Fy). This lies within the level of acceptable error and is due to be expected. This result indicates that cutting force measurement during grinding is consistent and can be relied upon for accuracy. Conversely, when comparing the temperature measurement for the same two tests, a change of 26.3% difference is observed. This indicates some discrepancy between the tests. Again, this could be due to movement of the thermocouples within their pilot holes via the fixation procedure as reported by Shen *et al.*, (2008), or an issue regarding drilling the holes in the workpiece

prior to being cemented *in situ*.

Test [4] displayed a significant decrease in workpiece temperature when compared to both Test [2] and Test [3]. This is expected as the only difference in variable was an increase in wheel speed from $20 m.s^{-1}$ to $30 m.s^{-1}$. Increases in wheel speed result in decreases in workpiece temperature when grinding titanium alloys as has been published by Shi *et al.*, (2020). Interestingly, when comparing the Fz component of the cutting force, a significant increase is observed when increasing the wheel speed. This contrasts with work published by Baksa *et al.*, (2018), who suggested that cutting forces decrease with wheel speed when the MRR is held constant. Whilst comparing Test [9] and Test [10] where the feed rate was doubled, an increase in workpiece temperature was observed; an observation provided by Mahamani and Jawahir (2018).

When machining alloys such as Ti-6Al-4V, high workpiece temperatures are observed in the grinding zone. This due to the alloy's low thermal conductivity. This observation is heightened when more aggressive grinding parameters are utilised such as during Test 8, Test 9 and Test 10. This response can be explained by only a small proportion of the generated heat being removed from the system via chip formation. A significantly larger proportion of the generated heat is removed via the energy partition to the tool and coolant respectively, something reported by Klocke (2009) and Malkin and Guo (2007). Also, reducing the contact time between the wheel and the workpiece and increasing the contact length of the grinding zone has been shown to reduce workpiece temperature and heat penetration depth, thus resulting in less subsequent subsurface damage, something that has been previously confirmed via experimental test data (Novikov *et al.*, 2019). These findings clearly have implications when grinding hard to machine materials such as Ti-6Al-4V to improve surface finish and in-service lifespan due to the thermomechanical stresses being lower, thus decreasing surface roughness, for example. It should also be noted that the porosity of the grinding wheel affects the workpiece temperature induced, with highly porous tools resulting in reduced workpiece temperatures due to a reduction in the co-efficient of friction acting between the tooling and workpiece. This would also lead to

lower thermomechanical stresses. Within this thesis, a low porosity tooling was utilised (SiC with a 5.9% porosity) which therefore could potentially result in higher workpiece temperatures and thus have a negative effect on surface integrity. This was further reported upon by both Lebedev *et al.*, (2021) and Novikov *et al.*, (2022).

As can be determined from Fig 5.6, during Test 1, where the grinding parameters were the least aggressive ($a$ = 0.3mm, $V_w$ = 150mm.min$^{-1}$, $V_s$ = 20m.s$^{-1}$), workpiece temperatures were observed to be 43°C whilst the cutting force components for $F_y$ and $F_z$ were 600N and 840N respectively. Firstly, it can be established that $F_z$ was greater in magnitude than $F_y$, thus confirming that $F_z$ was the primary cutting force during the test. An interesting discussion point here is that the peak cutting force occurs at the same position as thermocouple 3, i.e., at the position of peak workpiece temperature. This indicates a clear relationship between workpiece temperature and cutting force, something which has been reported on previously when turning pure iron (Yang *et al.*, 2022). The inverse appears to be accurate whereby thermocouple 1 offers the lowest temperature and cutting force response. It can also be established that the level of chatter increases with an increase in temperature. This can be explained via chatter being a direct result of varying cutting force, which itself affects the distribution of the workpiece's temperature field which adjusts the temperature flux (Sun *et al.*, 2018). This chatter phenomenon (due to it being a result of workpiece temperature) also then has a direct impact on the ground workpiece's surface integrity post grinding; microhardness, transformation of the sub/surface microstructure, surface roughness and residual stresses, and thus the ultimate in-service lifespan of the component being manufactured (Inasaki, Karpushchewski and Lee, 2001). This chatter trend is discernible again in Test 4, Test 5 and Test 8.

The chatter displayed during grinding is a result of uneven wheel wear (or grit dullness) around the circumference of the grinding wheel, which thus causes an increase in specific grinding energy. This therefore infers that dull grits induce a higher specific energy, whilst shaper grains induce lower specific energies and is something that has been repeatedly presented in the literature (Toth, 2020). In terms of the higher chatter magnitudes displayed

in Test 4, Test 5 and Test 8, it can be surmised that those three tests observed higher off-centre wheel wear as a result. It is, however, incredibly difficult to say with total certainty that this is the only reason, as not all the specific energy goes into chip formation, with certain specific energies being attributed to the rubbing and ploughing process as referred to in chapter 2.

# Chapter 6

# Surface Integrity and Optical Microscopy Tests

## 6.1 Results

### 6.1.1 Surface Roughness

Fig 6.1 outlines the average surface roughness measurements taken parallel to the grinding path for Test [1] through to Test [6]. An unsurprising range of $R_a$ values can be determined, despite an obvious anomalous result occurring at position six during Test [1].

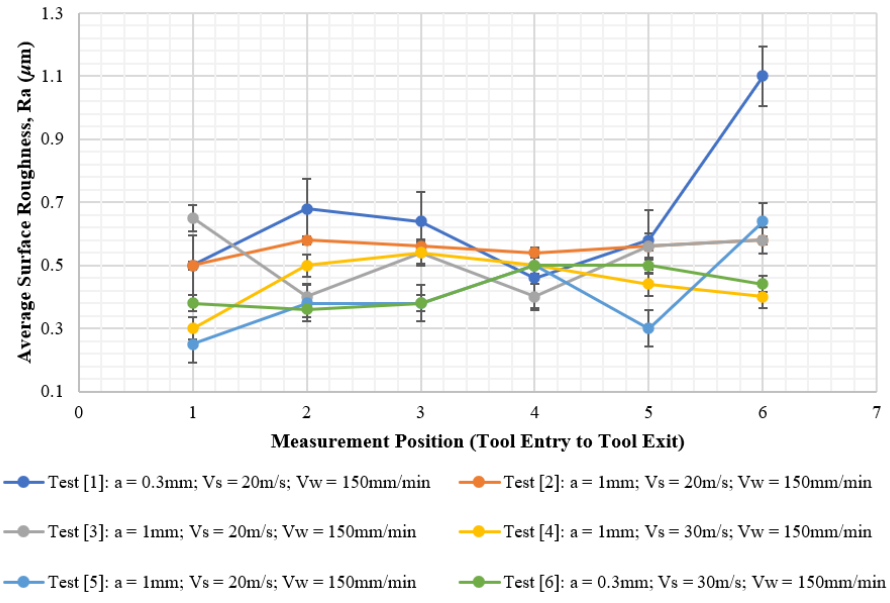



**Figure 6.1:** Average Surface Roughness vs. Position for Grinding Tests Conducted (Parallel)

Fig 6.2 presents the average surface roughness measurements taken parallel to the grinding path for Test [7] through to Test [10]. Again, a similar range of magnitudes are observed as in Fig 6.1, with a further, somewhat anomalous, result occurring at position three of Test [7].

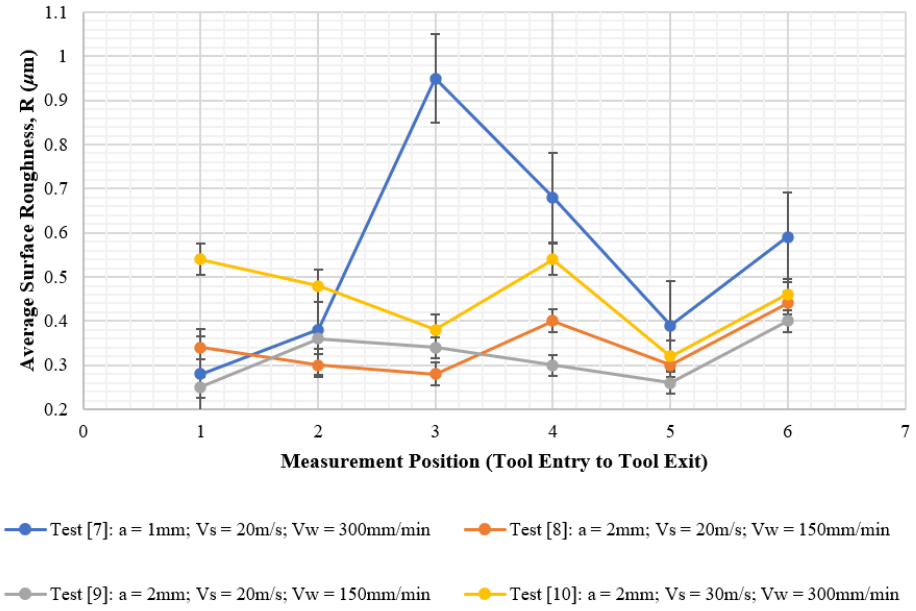



**Figure 6.2:** Average Surface Roughness vs. Position for Grinding Tests Conducted (Parallel)

A summary plot is given in Fig 6.3 which details all average parallel surface roughness values for each experimental test undertaken. A range of magnitudes were evaluated, all of which fall within the range expected of the grinding process (Badger, Murphy and O'Donnell, 2021).




**Figure 6.3:** Average Surface Roughness Values across all Grinding Test Cases (Parallel)

Fig 6.4 provides the average surface roughness data perpendicular to the grinding path for Test [1] through to Test [6]. Greater $R_a$ values for the perpendicular measurements when compared to the parallel tests evaluated are apparent, in addition to a broader variance across the positions tested.

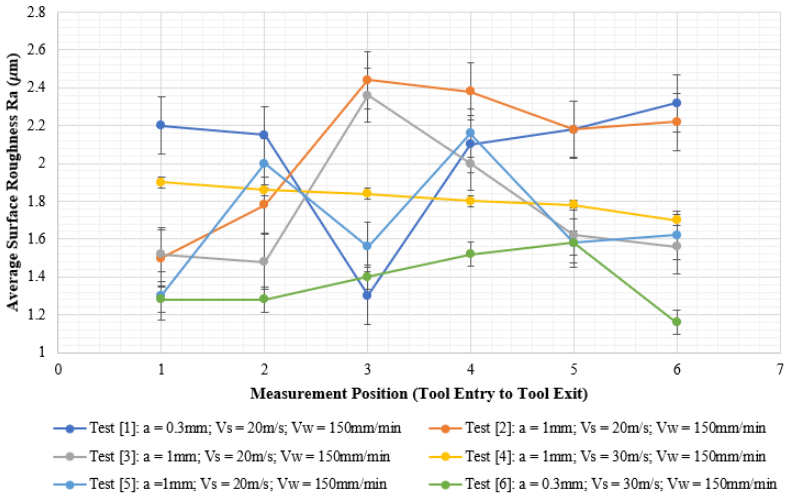



**Figure 6.4:** Average Surface Roughness vs. Position for Grinding Tests Conducted (Perpendicular)

Fig 6.5 provides the average surface roughness data perpendicular to the grinding path for Test [7] through to Test [10]. A further point of interest for all experimental trials is that a general linear trend of increasing $R_a$ value was observed across the entirety of the length evaluated.

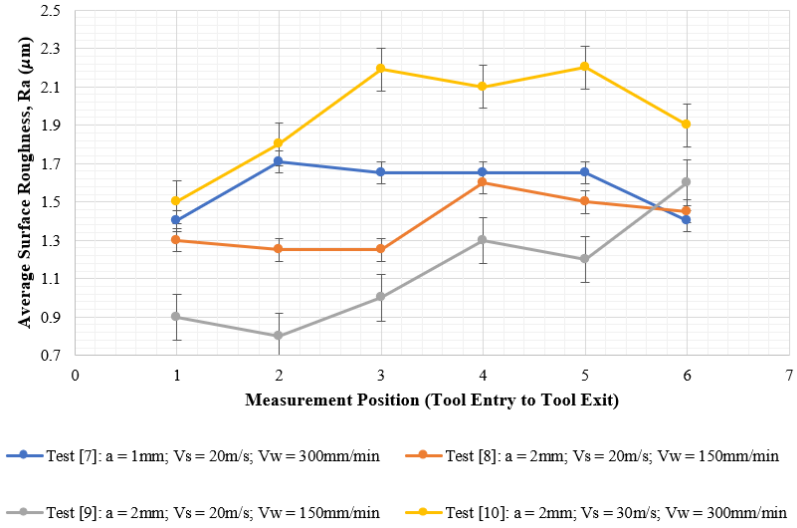



**Figure 6.5:** Average Surface Roughness vs. Position for Grinding Tests Conducted (Perpendicular)

Fig 6.6 details the average $R_a$ data for all tests regarding the perpendicular direction to the grinding pass.

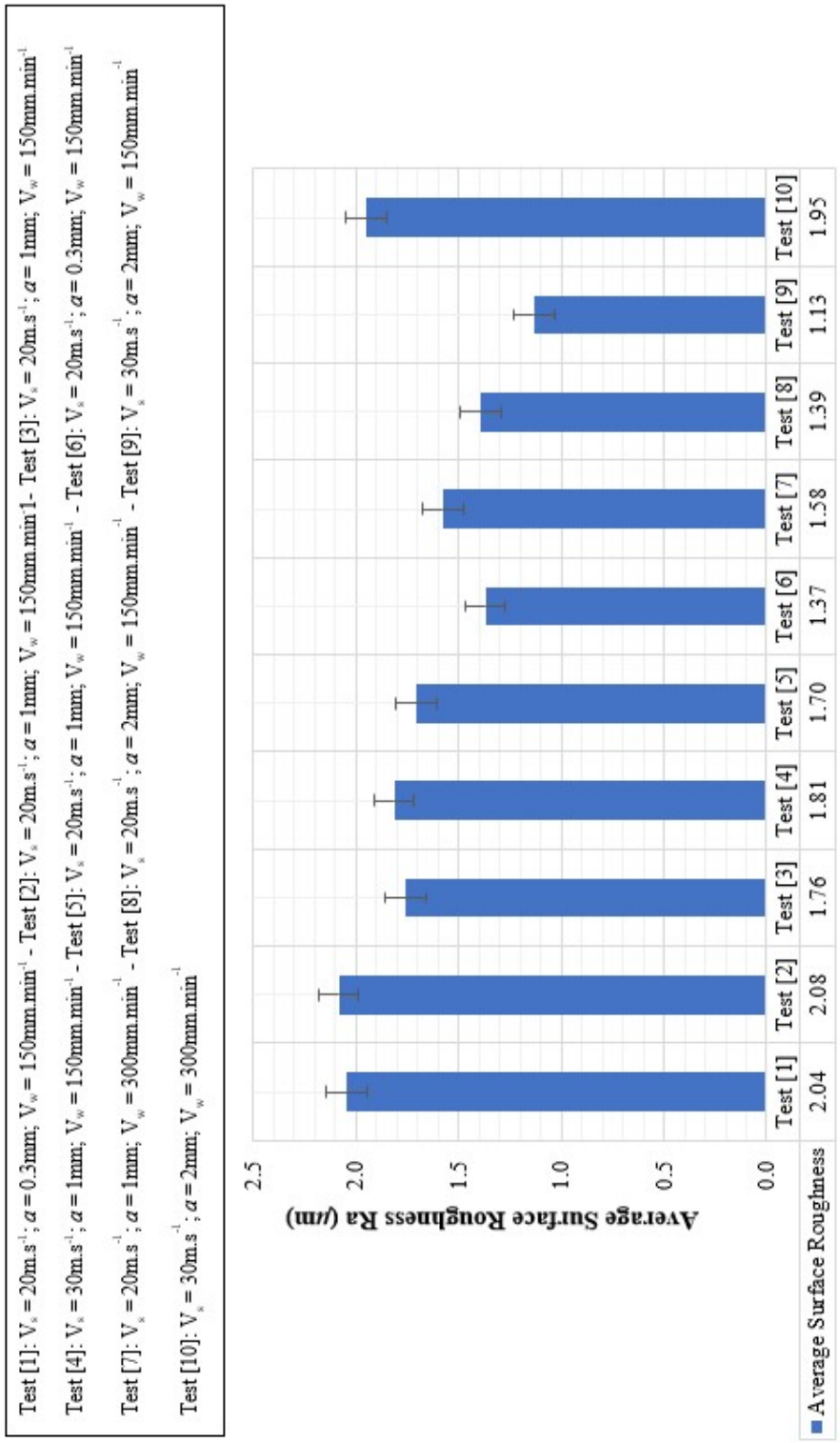



**Figure 6.6:** Average Surface Roughness Values across all Grinding Tests Conducted (Perpendicular)

### 6.1.2 Microstructural Interrogation

#### 6.1.2.1 Ground Surface

Fig 6.7, Fig 6.8 and Fig 6.9 detail the ground surface standard microscopy images for Test [1], Test [2] and Test [8] respectively. Generally, smooth surfaces can be observed which is indicative of the grinding process. This is due to grinding observing higher specific energies and therefore lower chip thickness values when compared to other machining processes such as milling (Rowe, 2009).

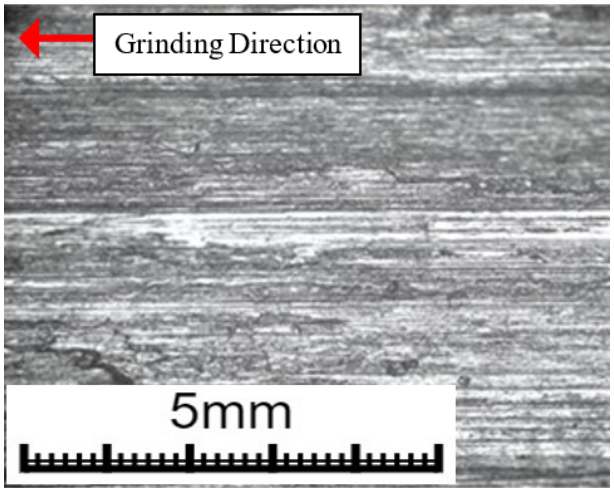



**Figure 6.7:** Ground Surface - Test [1] (Adjacent to TC 3)

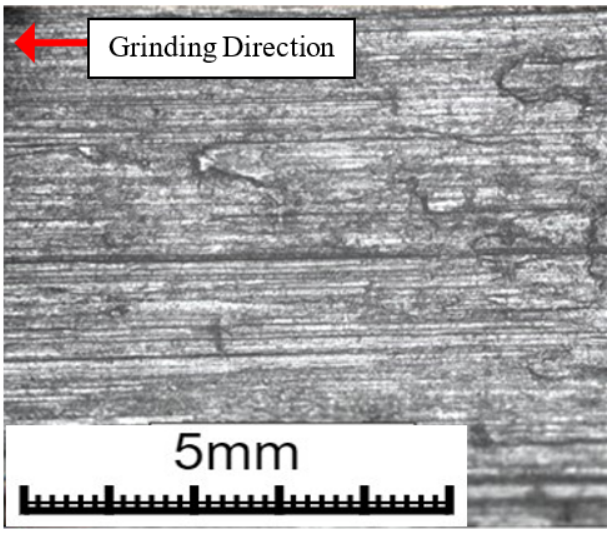



**Figure 6.8:** Ground Surface - Test [2]b (Between TC 2 and TC 3)

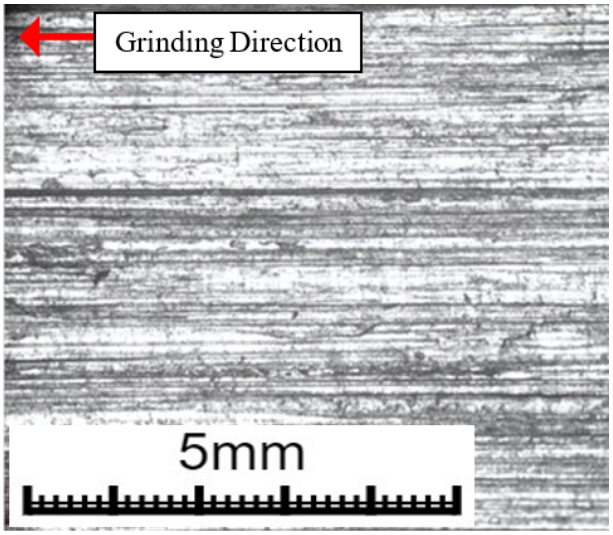



**Figure 6.9:** Ground surface - Test [8] (Adjacent TC 3)

#### 6.1.2.2 Subsurface

Fig 6.10 presents the standard microscopy images of the subsurface at increasing magnifications after Test [1] had been conducted. Clear subsurface regions relating to both the $\alpha$ and $\beta$ phases are apparent and is to be expected of the dual-phase, Ti-6Al-4V alloy being evaluated.

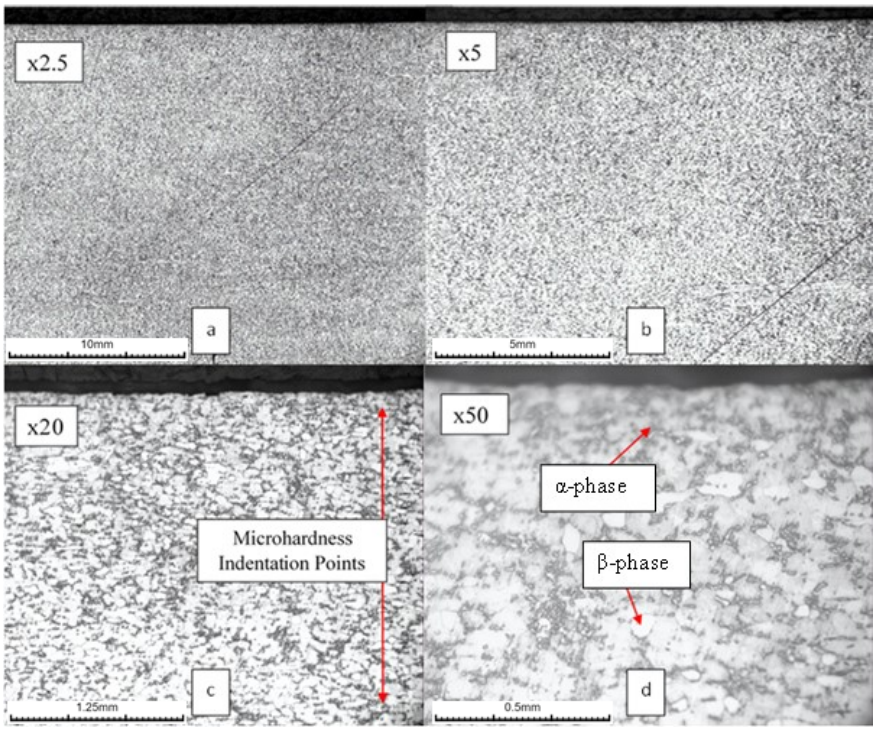



**Figure 6.10:** Thermocouple 3 Location Microstructure Micrographs for Test [1] at x2.5 magnification (a), x5 magnification (b), x20 magnification (c) and x50 magnification (d)

Fig 6.11 compares the workpiece substructure with the microhardness values measured associated with Test [1]. Some work hardening is observed close to the ground surface, before the microhardness value gradually reduces the further into the workpiece substrate being measured.

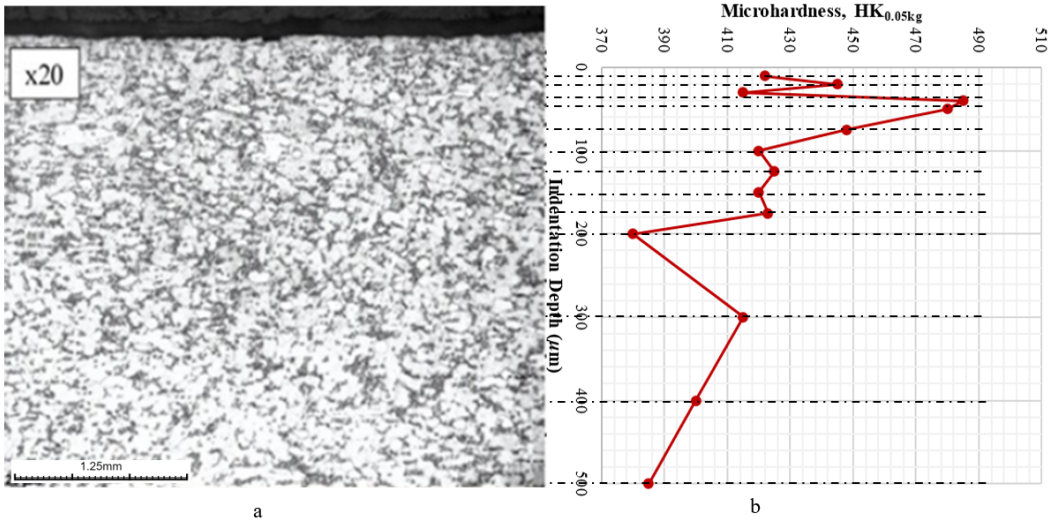



**Figure 6.11:** Thermocouple 3 Location Microstructure (a) and Microhardness (b) Comparison for Test [1]

Fig 6.12 details the W-EDM cut surface regarding Test [1] which displays clear evidence of severe subsurface damage.

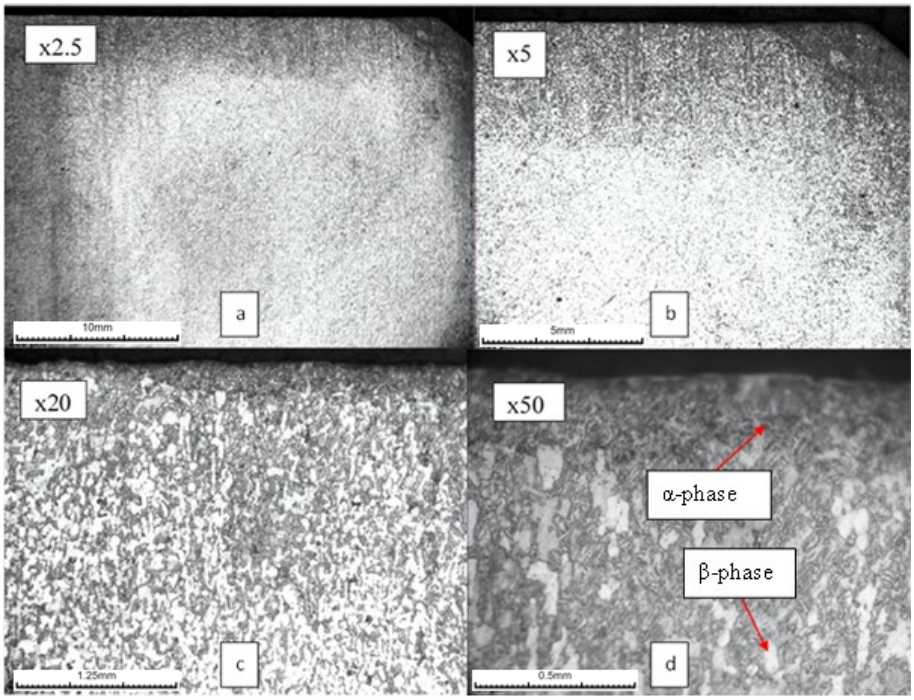



**Figure 6.12:** Thermocouple 3 Location Wire-EDM Surface Microstructure for Test [1] at x2.5 magnification (a), x5 magnification (b), x20 magnification (c) and x50 magnification (d)

Fig 6.13 further details the subsurface damage at differing magnifications relating to Test [2]. More extensive plastic deformation can be observed as a result of the increased depth of cut value evaluated.

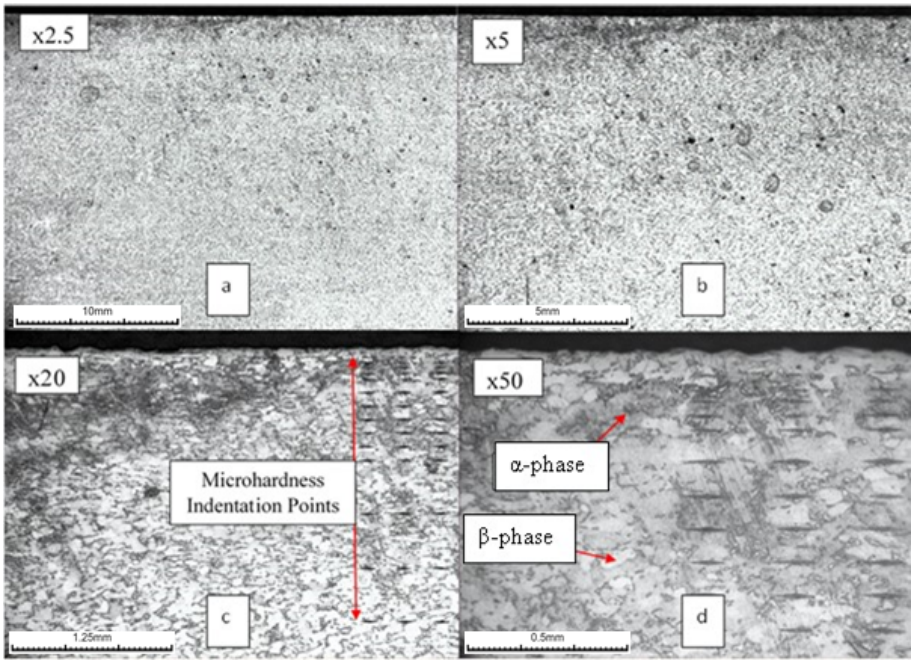



**Figure 6.13:** Thermocouple 3 Location Microstructure Micrographs for Test [2] at x2.5 magnification (a), x5 magnification (b), x20 magnification (c) and x50 magnification (d)

Fig 6.14 compares the subsurface damage against the microhardness plot obtained for Test [2]. Again, a similar response is observed as detailed in Fig 6.11, with it being noteworthy that a lower peak microhardness value was induced when evaluating a larger volume of material being removed from the workpiece.

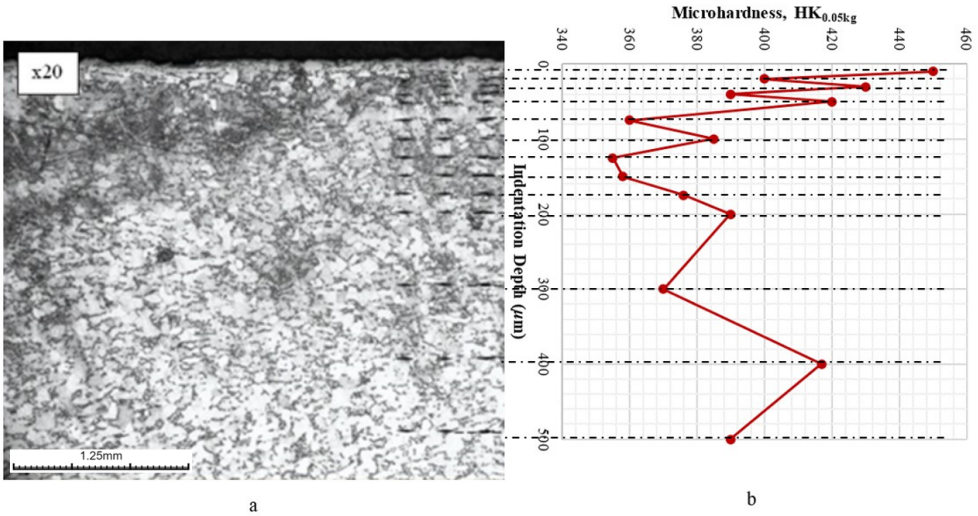



**Figure 6.14:** Thermocouple 3 Location Microstructure (a) and Microhardness (b) Comparison for Test [2]

Fig 6.15 details the W-EDM subsurface material at differing magnifications that relate to Test [2]. Evidence of the recast layer can be observed in sub-figure (d); something reported on by Welling (2014).

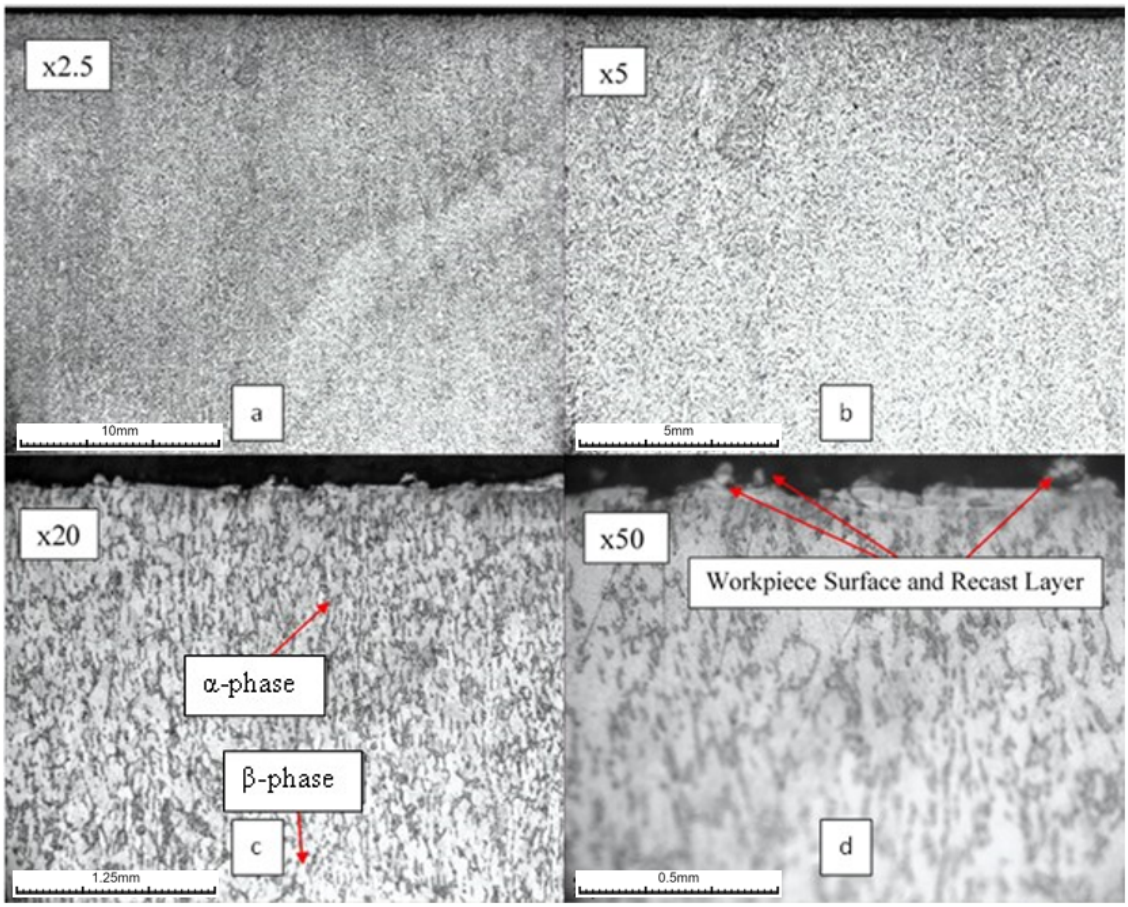



**Figure 6.15:** Thermocouple 3 Location Wire-EDM Surface Microstructure for Test [2] at x2.5 magnification (a), x5 magnification (b), x20 magnification (c) and x50 magnification (d)

Fig 6.16 highlights the subsurface damage at differing magnifications which pertain to Test [8]. Clear phase transition has resulted from more aggressive grinding parameters tested, with there also being evidence of residual workpiece damage as annotated in sub-figure (a) of the figure.

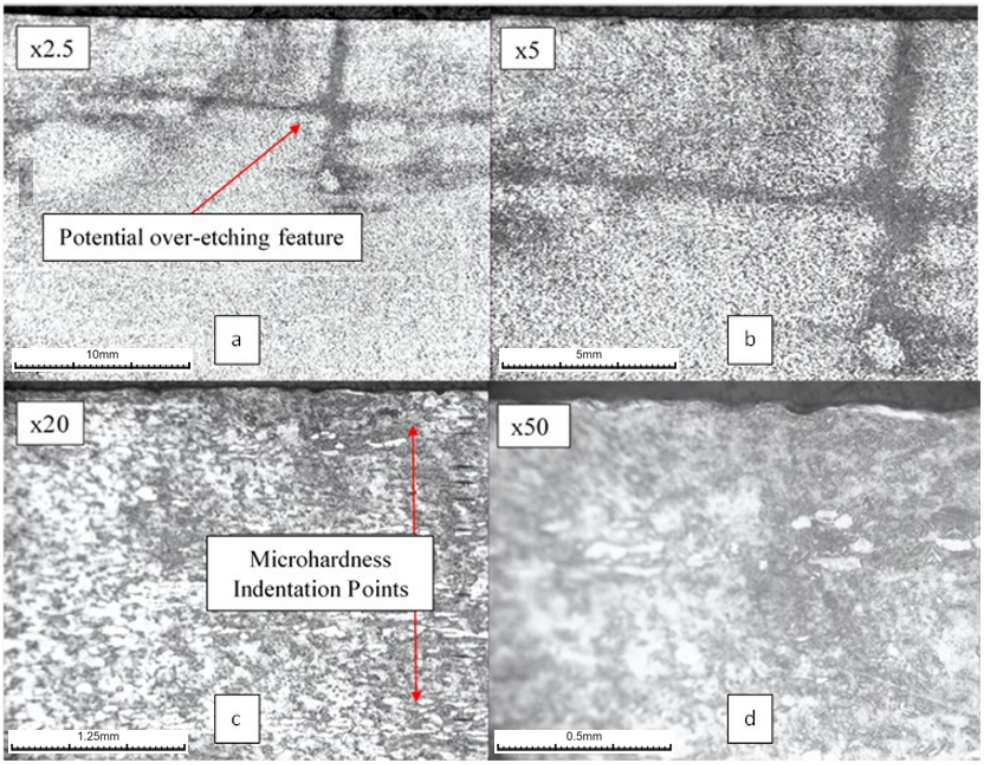



**Figure 6.16:** Thermocouple 3 Location Microstructure Micrographs for Test [8] at x2.5 magnification (a), x5 magnification (b), x20 magnification (c) and x50 magnification (d)

Fig 6.17 compares the subsurface damage with the microhardness plot associated with Test [8]. Variation in microhardness values is evident; however, more $\alpha$-phase is visibly present than $\beta$-phase indicating a lower workpiece temperature being present at that particular location.

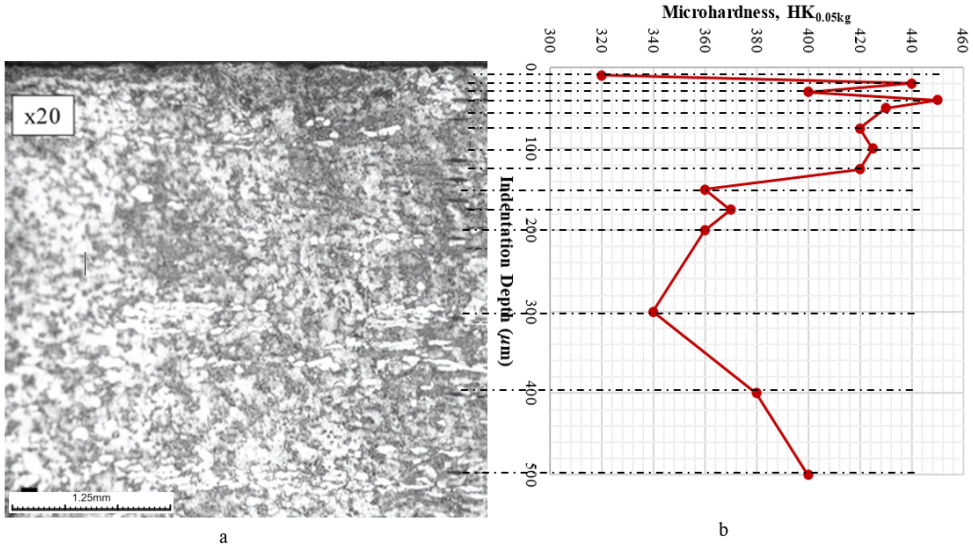



**Figure 6.17:** Thermocouple 3 Location Microstructure (a) and Microhardness (b) Comparison for Test [8]

Fig 6.18 details the subsurface damage at differing magnifications which relate to Test [10]. Thermal softening close to the ground surface is clearly visible in sub-figure (b), in addition to work hardening deeper into the workpiece substrate as demonstrated by the lighter, $\beta$ regions present.

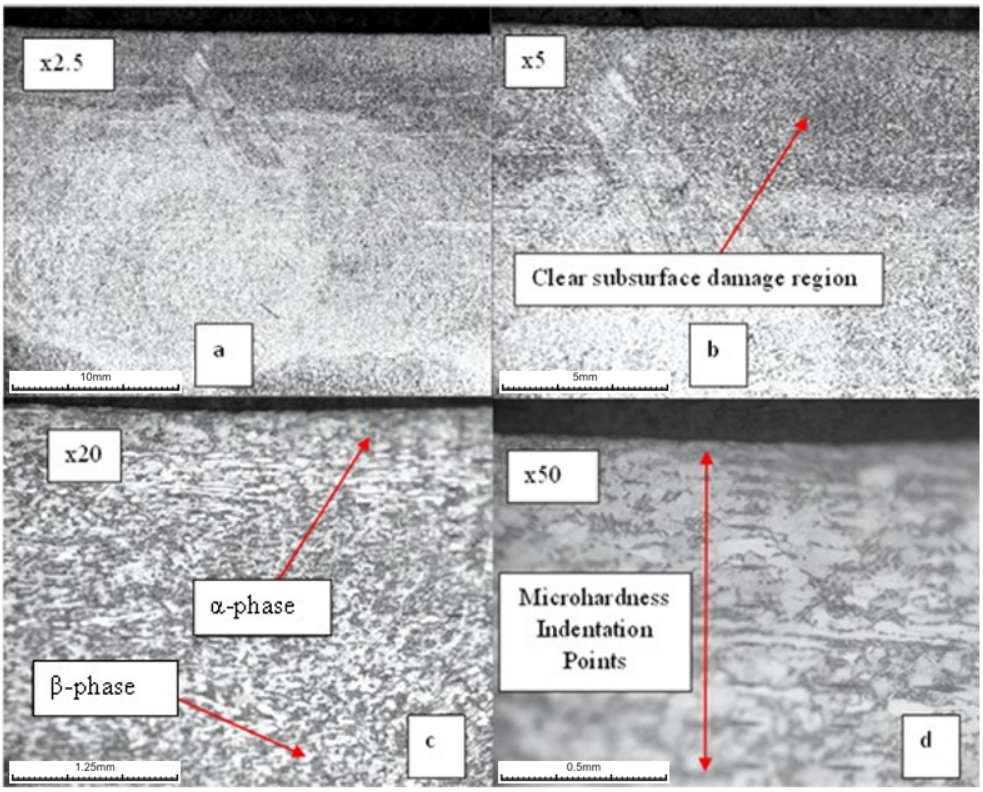



**Figure 6.18:** Thermocouple 3 Location Microstructure Micrographs for Test [10] at x2.5 magnification (a), x5 magnification (b), x20 magnification (c) and x50 magnification (d)

Fig 6.19 compares the subsurface damage against the microhardness values pertaining to Test [10]. High microhardness values were obtained from the test procedure (peaking at $HK_{0.05kg}$ = 500HK); again, something to be expected due to Test [10] using the most aggressive combination of grinding parameters evaluated.

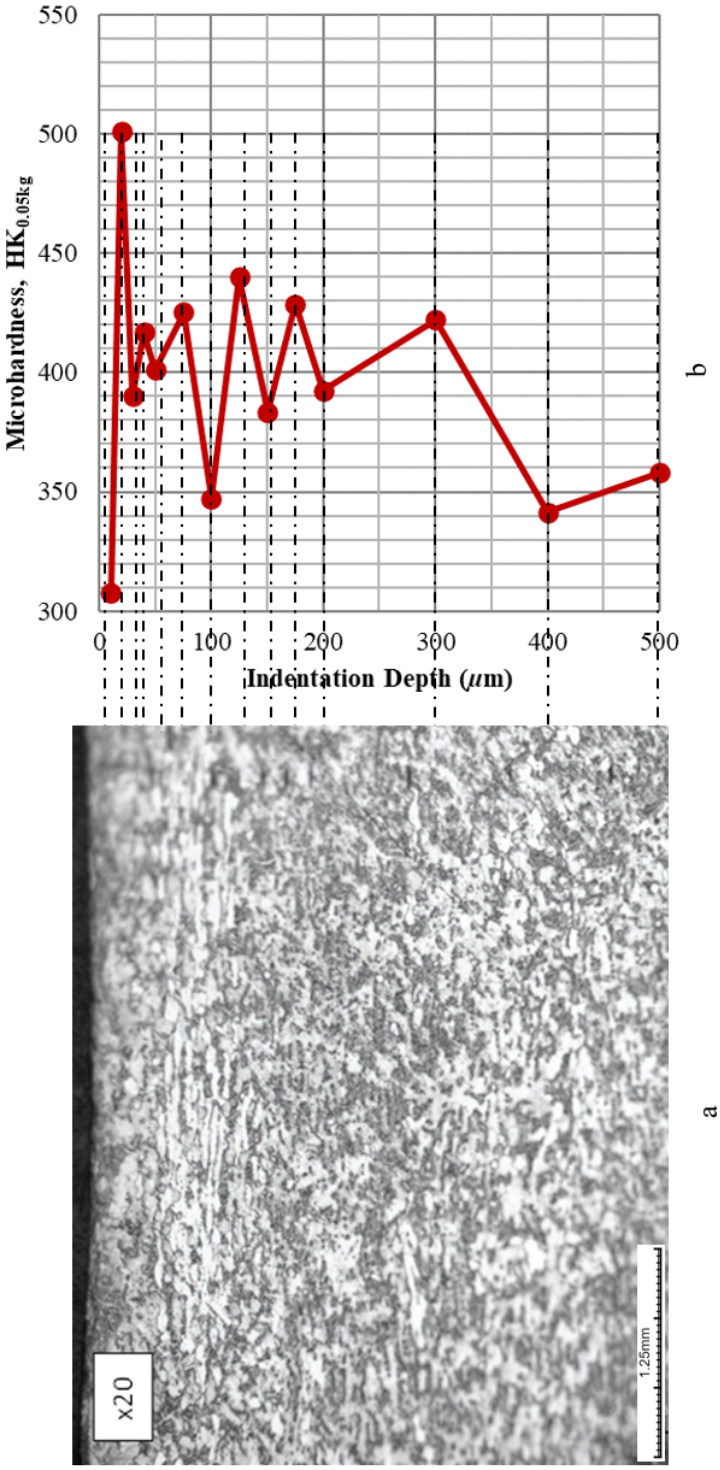



**Figure 6.19:** Thermocouple 3 Location Microstructure (a) and Microhardness (b) Comparison for Test [10]

#### 6.1.2.3 SEM Imaging

Fig 6.20 introduces the SEM images at the locations of TC1, TC2 and TC3 respectively (sub-figures (a), (b) and (c)) with regards to Test [1]. Little to no visible difference in subsurface damage can noted between these locations. Conversely, sub-figures (d) and (e) appear to show examples of smearing and grooving on the workpiece surface; an expected response when grinding a relatively high ductile alloy such as Ti-6Al-4V even at modest cutting parameters (Whittaker and Hess, 2015).

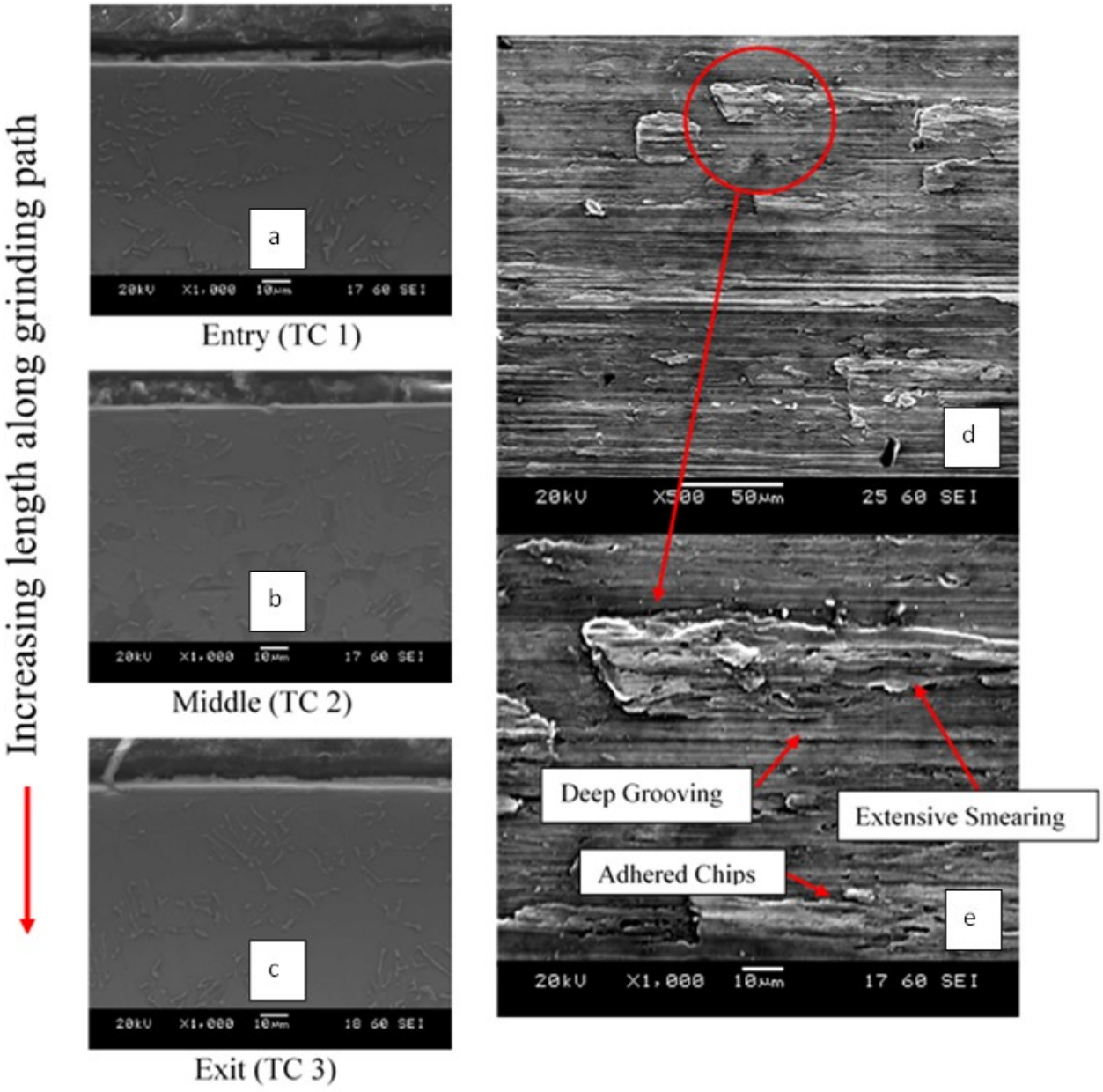



**Figure 6.20:** SEM Image of Subsurface (a-c) and Ground Surface (d-e) - Test [1]

Fig 6.21 presents a higher resolution SEM cross section image of the subsurface damage induced during Test [1]. A clear distinction can be drawn between the darker, $\alpha$-phase regions and the lighter, $\beta$-phase regions.

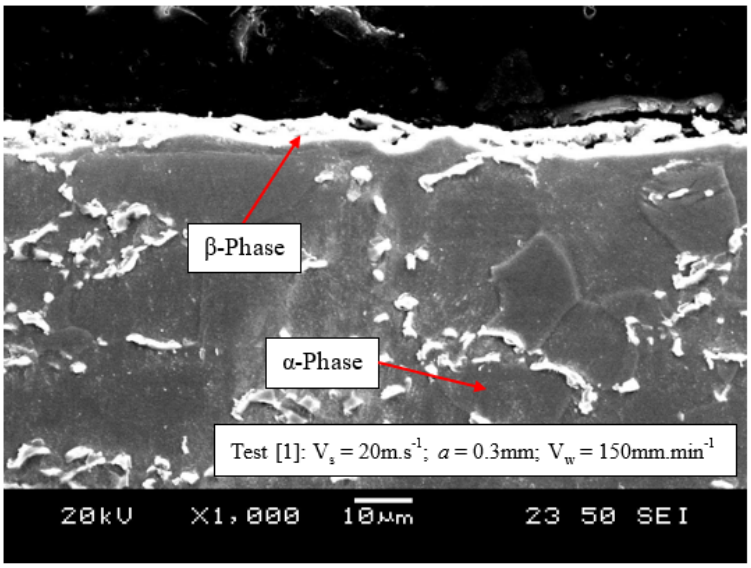



**Figure 6.21:** SEM Image of Subsurface - Test [1]

Fig 6.22 details the equivalent SEM image of the subsurface damage made after the W-EDM process used during the manufacture of the Test [1] workpiece. A clear distinction can be drawn between the two, with microcracks and the recast layer being evident on the W-EDM surface whilst no such features are apparent on the ground surface.

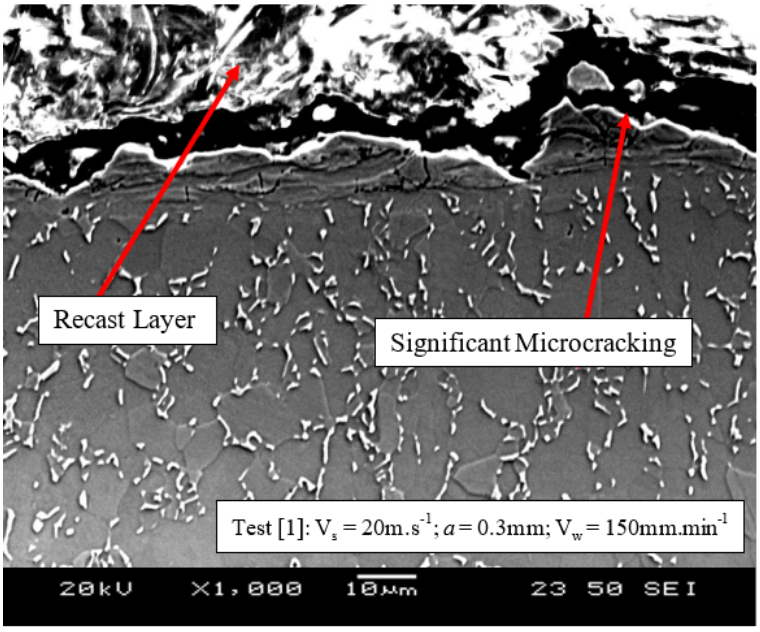



**Figure 6.22:** SEM Image of the Wire-EDM Subsurface - Test [1]

Fig 6.23 presents SEM images of subsurface damage pertaining to Test [6]. Obvious points of interest are the clear irregularities that were already present in the workpiece. These results could clearly have influenced this particular test case and adds further evidence to the causation of the somewhat anomalous data obtained during Test [6].

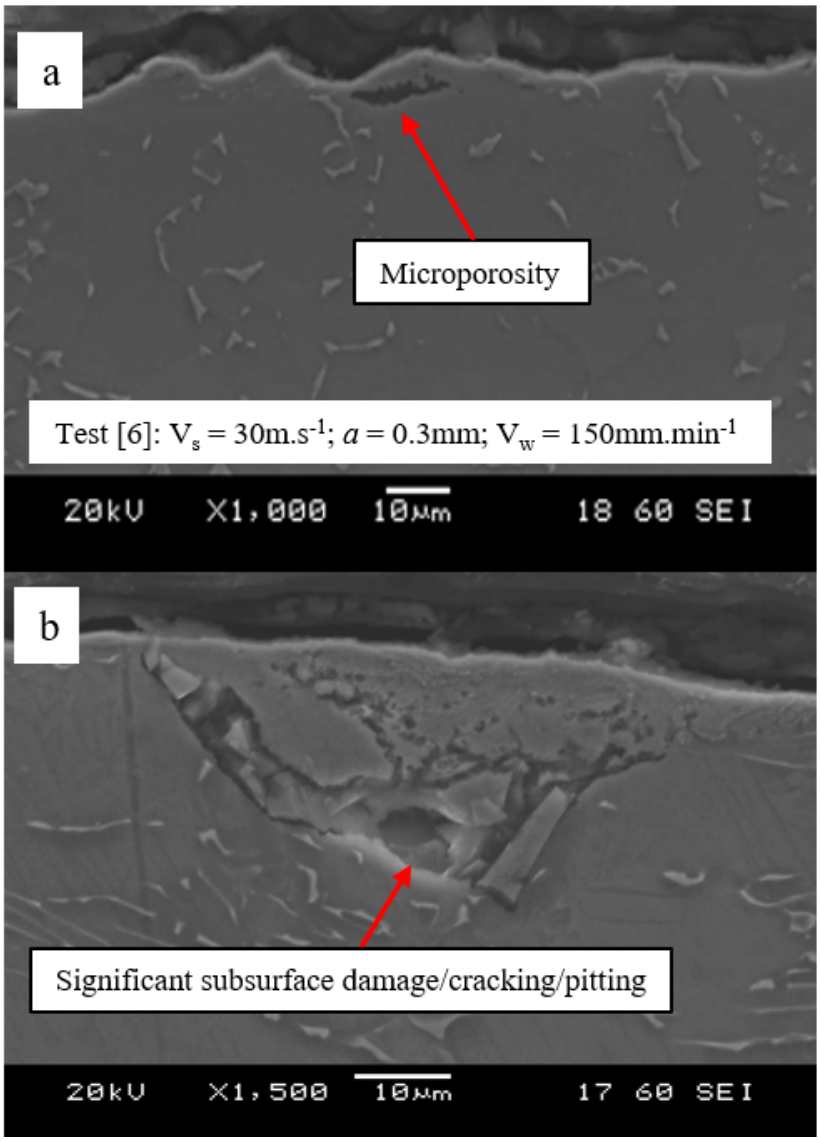



**Figure 6.23:** SEM Image of the Subsurface Damage at entry to the workpiece (a) and exit of the workpiece (b) - Test [6]

Fig 6.24 comprises of SEM images detailing the subsurface microstructural changes associated with Test [9]. Both sub-figures (a and b) were taken at the position of thermocouple one. An expected $\alpha$ phase is evident as at this position in the cut, the workpiece temperature had already increased, but was far below the transus temperature for Ti-6Al-4V, thus resulting in minimal subsurface plastic deformation.

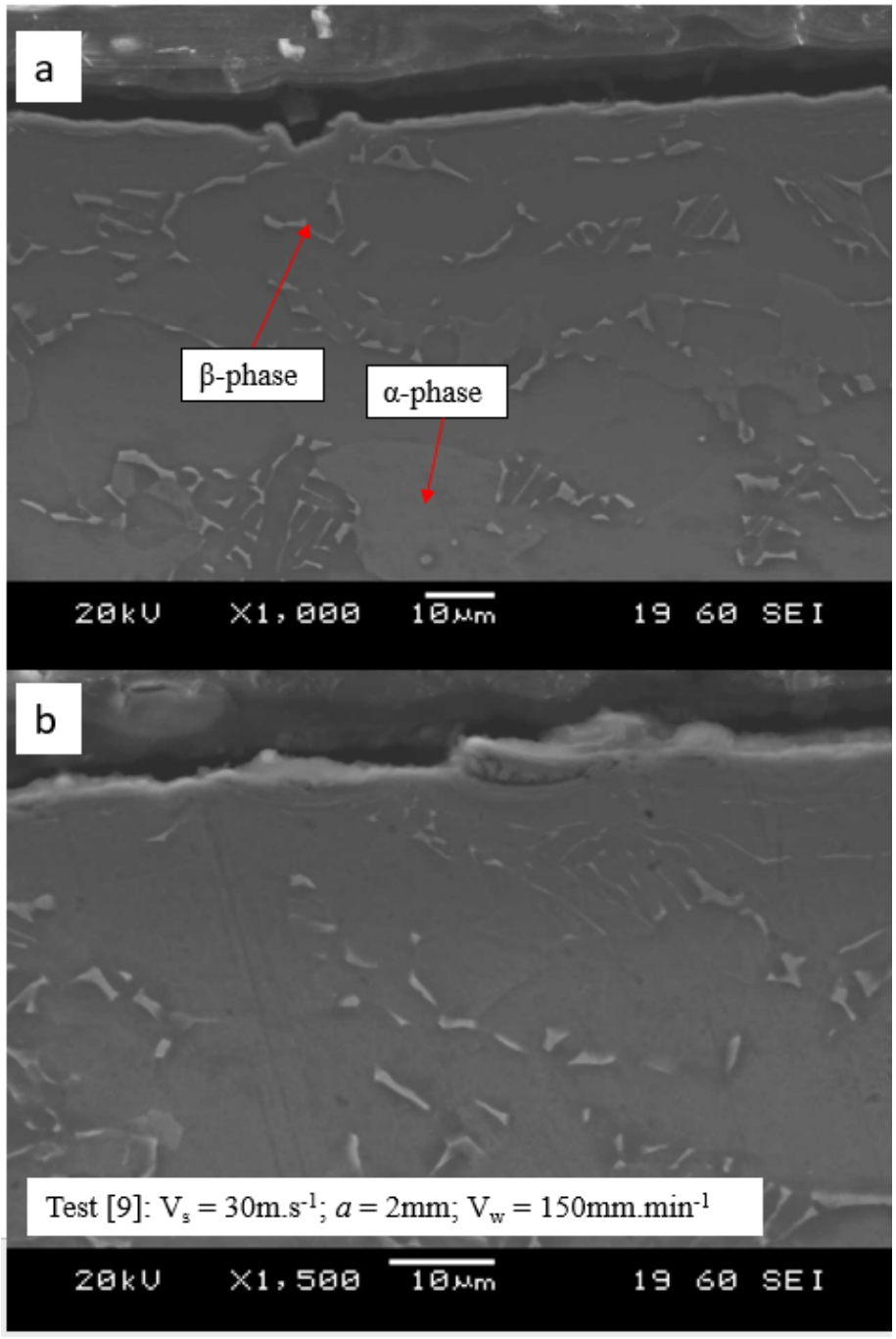



**Figure 6.24:** SEM Image of Subsurface Damage at entry to the workpiece x1000Mag (a) and entry of the workpiece x1500Mag (b) - Test [9]

Fig 6.25 introduces the standard camera images taken at the locations of TC1, TC2 and TC3 respectively which relate to Test [9] and Test [10]. As was previously presented in Fig 5.42 and Fig 5.43, the workpiece temperature increased across the grinding path at these positions, thus resulting in greater subsurface deformations at these locations. Fig 6.25 further explores this point, with the deformations visible following this trend.

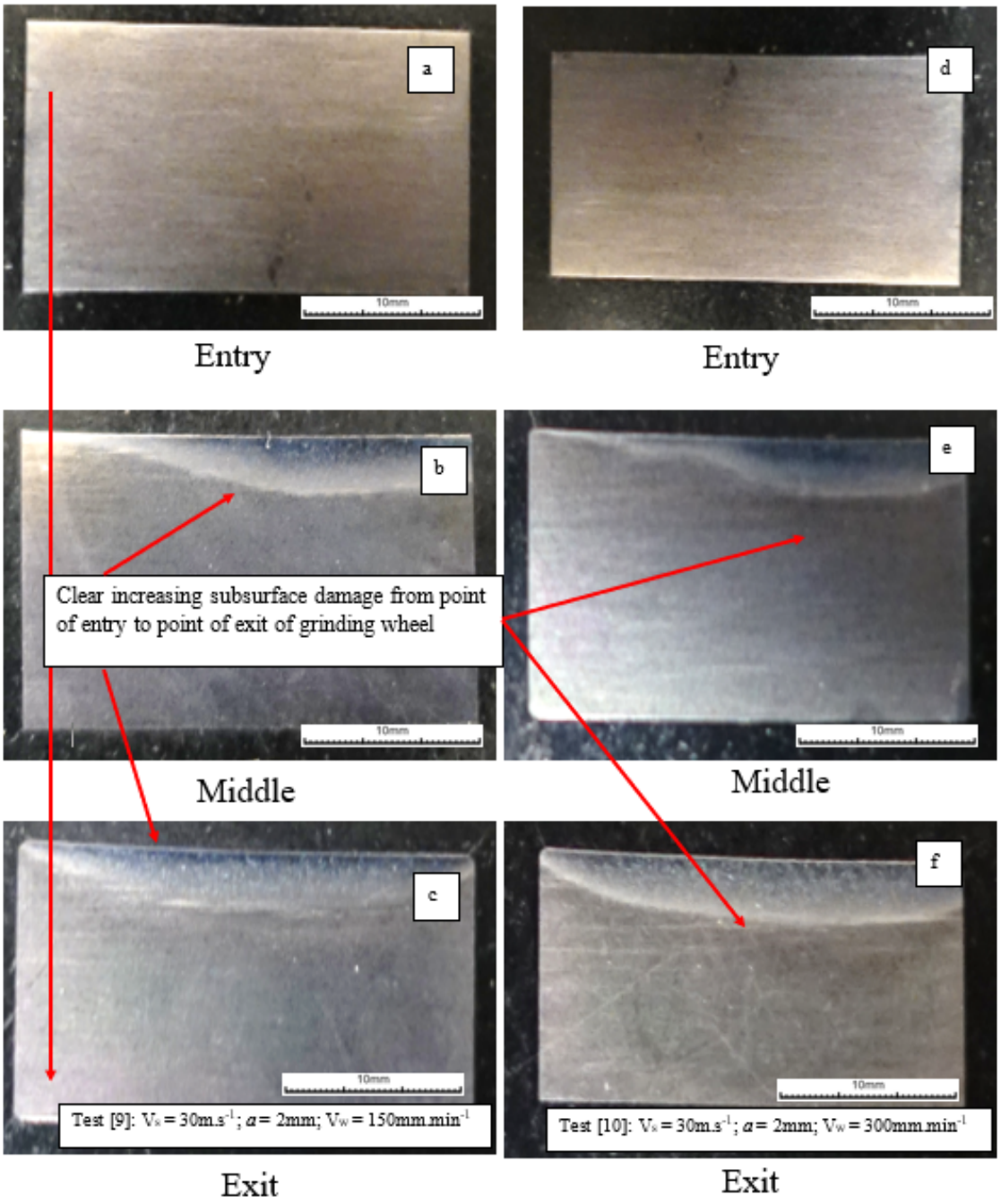



**Figure 6.25:** Conventional Camera Image of Subsurface Damage for Test [9] at the entry, middle and exit of the workpiece (a-c) and Test [10] (d-f) at locations of TC 1, TC 2 and TC 3

Fig 6.26 outlines the ground surface SEM images and subsurface damage images which were evaluated in regards to Test [10]. Obvious surface features include smearing and subsequent re-adhesion of ground surface chips back onto the cutting face as shown sub-figures (a), (b) and (c), whilst clear $\alpha$ and $\beta$ regions are apparent in sub-figures (d), (e) and (f).

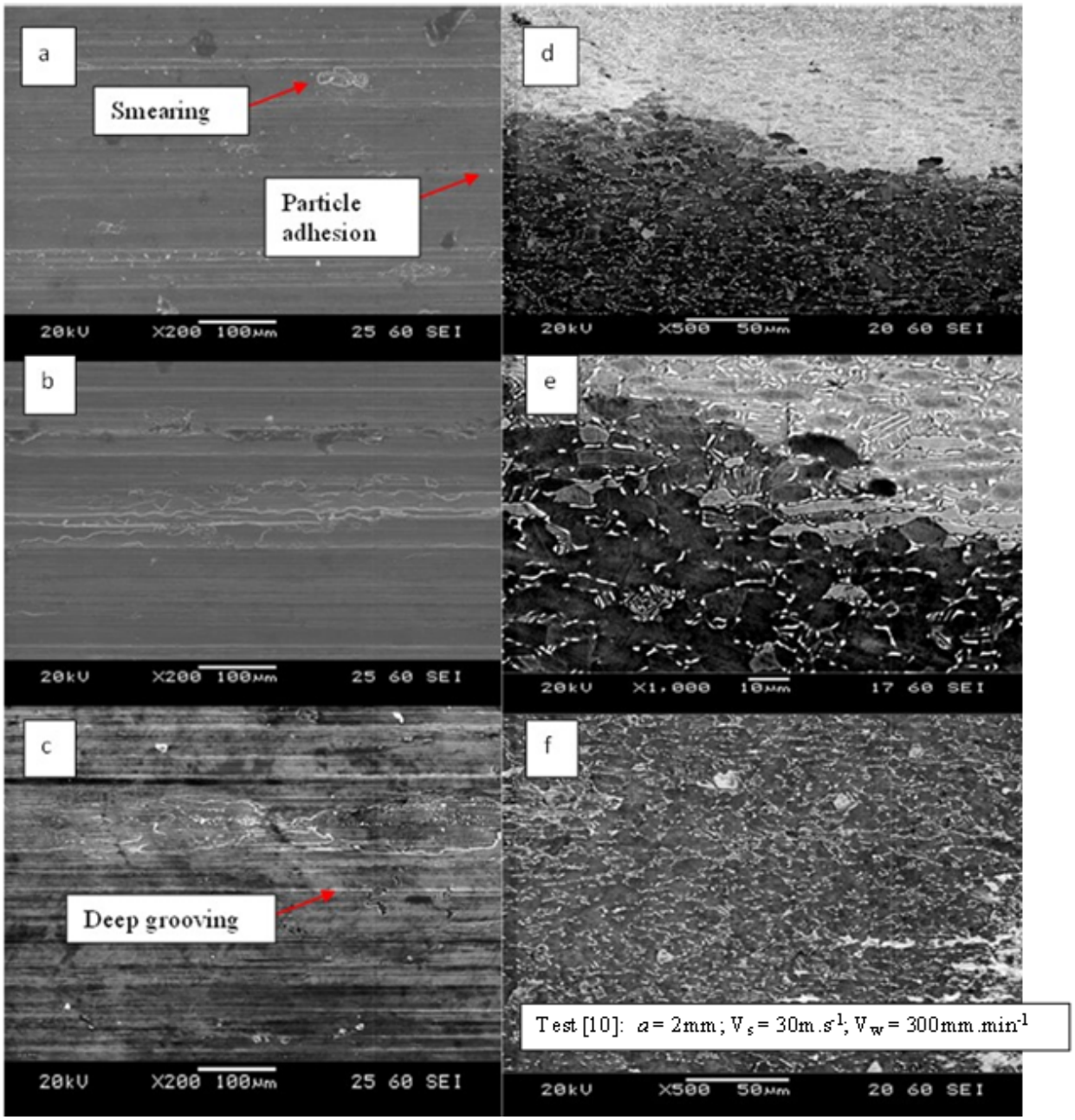



**Figure 6.26:** Ground Surface SEM Image for Test [10] (a-c) and Subsurface Damage for Test [10] (d-f)

### 6.1.3 Microhardness

Fig 6.27 presents the microhardness vs. indentation plot for Test [9]. The trace highlights four key zones; a thermally softened subsurface layer, a hard subsurface layer, a hardened subsurface layer and the bulk hardness layer. The relationship demonstrated here has also been proposed previously by Mathohol *et al.*, (2018) during milling and Hood (2010) during grinding.

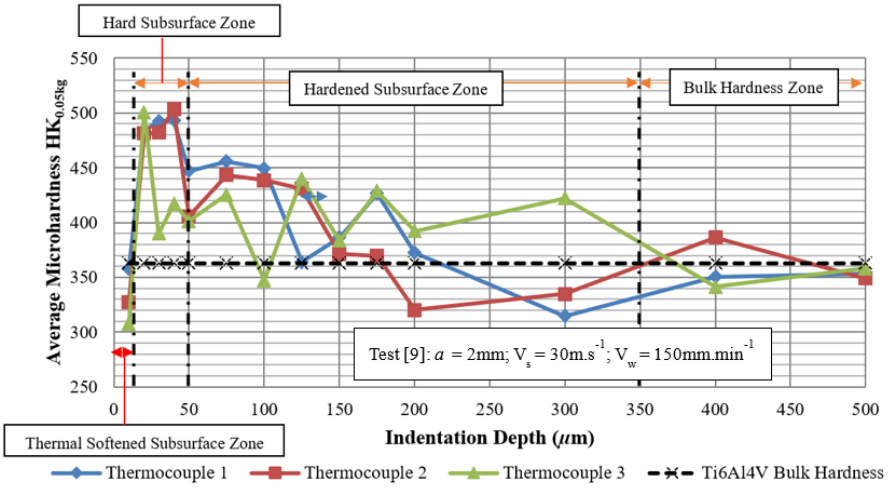



**Figure 6.27:** Microhardness vs. Indentation Depth for Test [9]

Fig 6.28 details the microhardness values at the location of TC1, TC2 and TC3 during Test [9]. Results indicate that the workpiece temperature increased across the length of the grinding pass; something also apparent in other experimental trials.

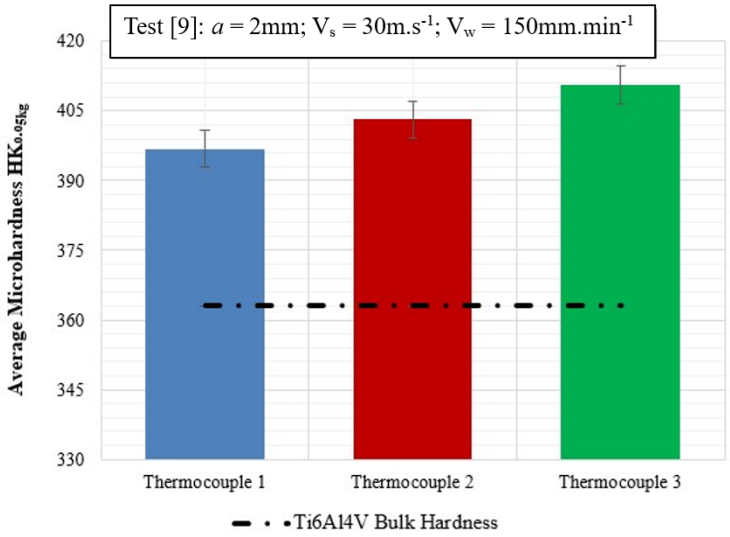



**Figure 6.28:** Average Microhardness per Thermocouple Location for Test [9]

Fig 6.29 details the microhardness vs. indentation depth plot that relates to Test [8]. Although not as clear a relationship between these two variables as was apparent in Fig 6.27 presents itself, the microhardness value does appear to vary across the thermocouple locations, and ultimately reverts back to the bulk microhardness of Ti-6Al-4V (≈360HK) at a depth of 300$\mu$m.

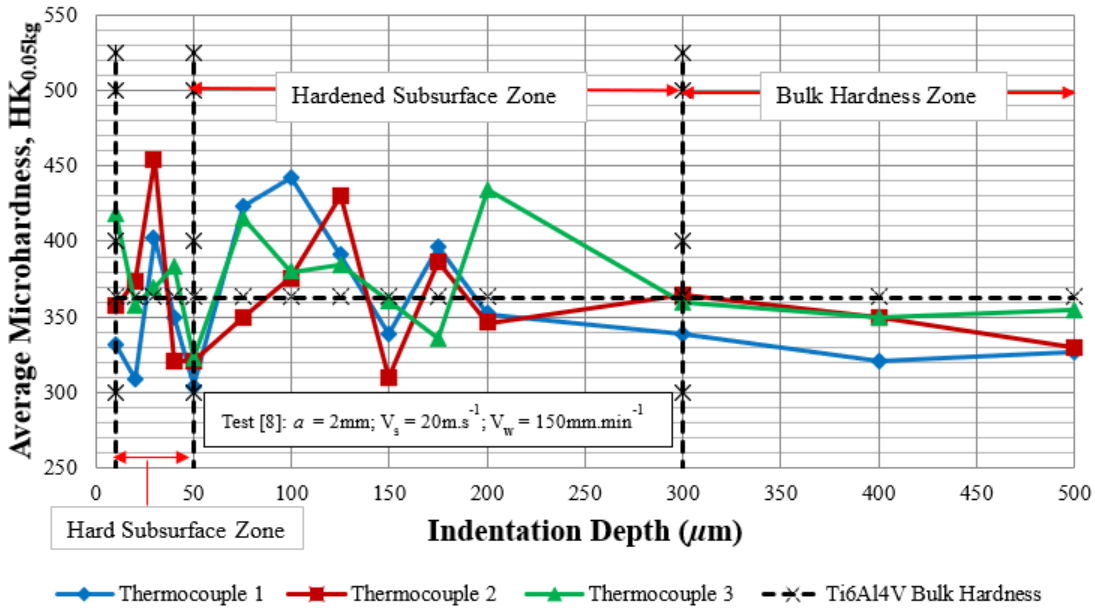



**Figure 6.29:** Microhardness vs. Indentation Depth for Test [8]

Fig 6.30 outlines the average microhardness values at the location of TC1, TC2 and TC3 respectively in regards to Test [8]. Again, the same trend can be determined as was demonstrated in Fig 6.28.

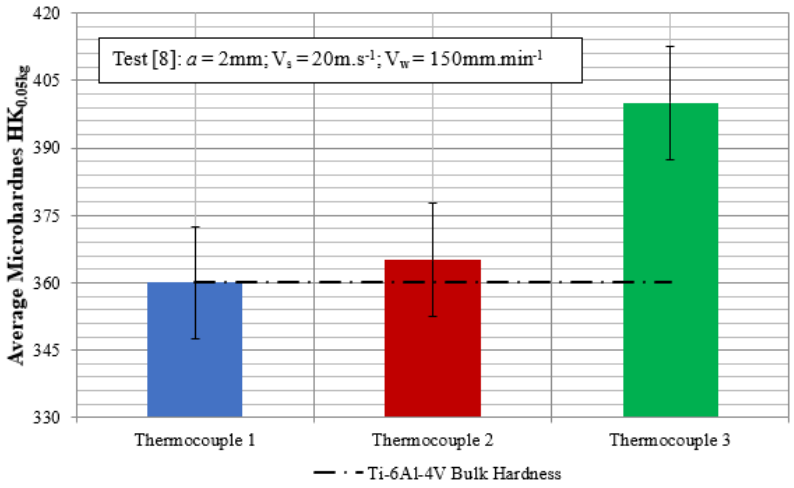



**Figure 6.30:** Average Microhardness per Thermocouple Location for Test [8]

Fig 6.31 summarises the average microhardness values for Test [1] through to Test [5]. A wide range of data points can be determined from the plot; however, an interesting point to note is that for all tests other than Test [1], the bulk hardness of the Ti-6Al-4V workpiece was not reached, even at 500$\mu$m into the workpiece substrate.

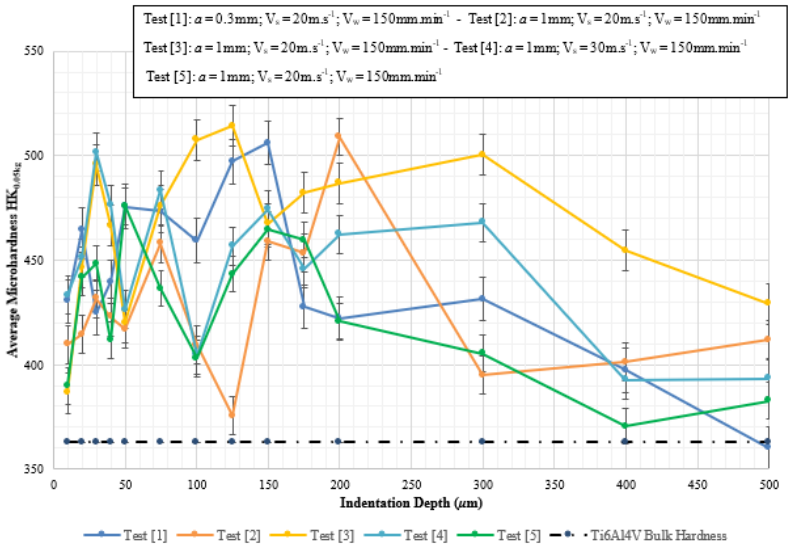



**Figure 6.31:** Average Microhardness vs. Indentation Depth for all Tests Conducted

Fig 6.32 summarises the average microhardness values for Test [7] through to Test [10]. As can be determined from the plot, Test [10] observed extremely deep microhardness changes until 500$\mu$m into the substrate. Higher workpiece temperatures were also evaluated during this test due to the most aggressive grinding parameter magnitudes being assessed.

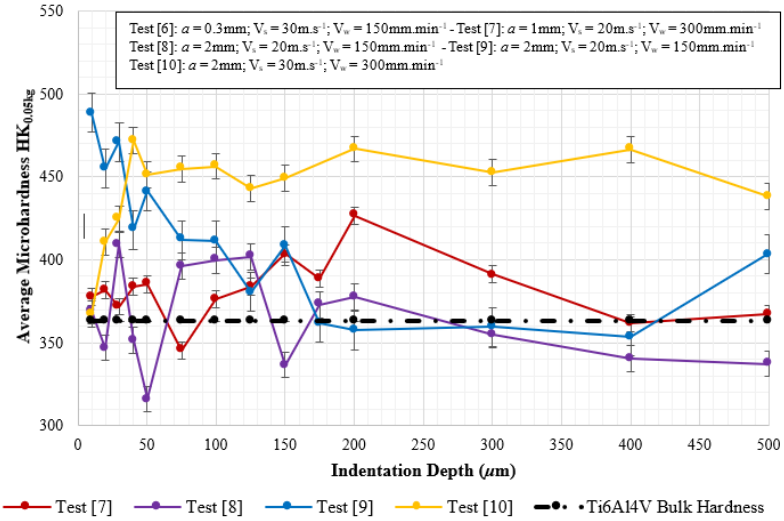



**Figure 6.32:** Average Microhardness vs. Indentation Depth for all Tests Conducted

Fig 6.33 presents a full summary of all the average microhardness values gathered for all grinding tests conducted. A similar magnitude across all trials can be determined; something which deserves additional research as grinding parameters have been reported to have a significant effect on the grinding temperature, and thus the final surface integrity condition (Field and Kahles, 1964).

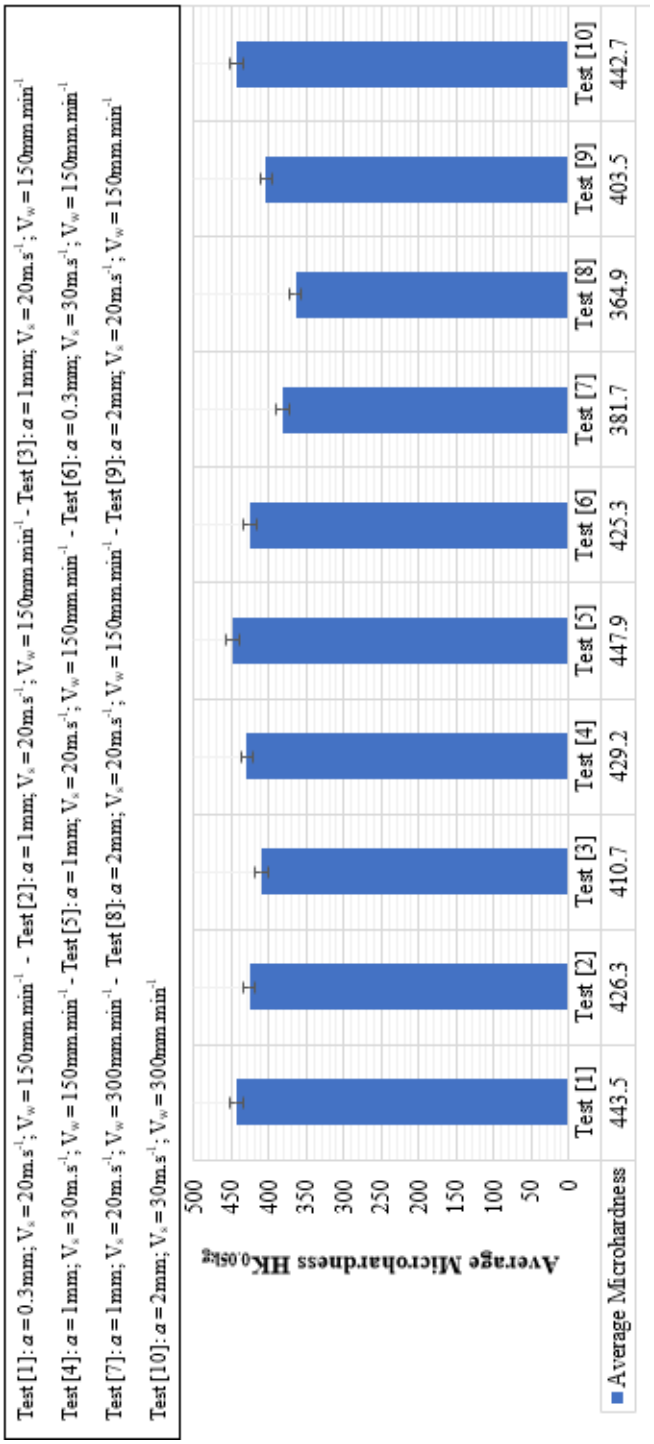



**Figure 6.33:** Average Microhardness across all Tests Summary

### 6.1.4 Residual Stress

Fig 6.34 presents the residual principal stress data as a function of depth into the workpiece for Test [1], Test [2] and Test [8]. As can be easily determined from the figure, Test [1] and Test [2] result in relatively low depths of induced residual stresses before normalizing at $\approx 75\mu$m into the substrate. Test [8], however, induces significant tensile residual stresses far deeper into the workpiece.

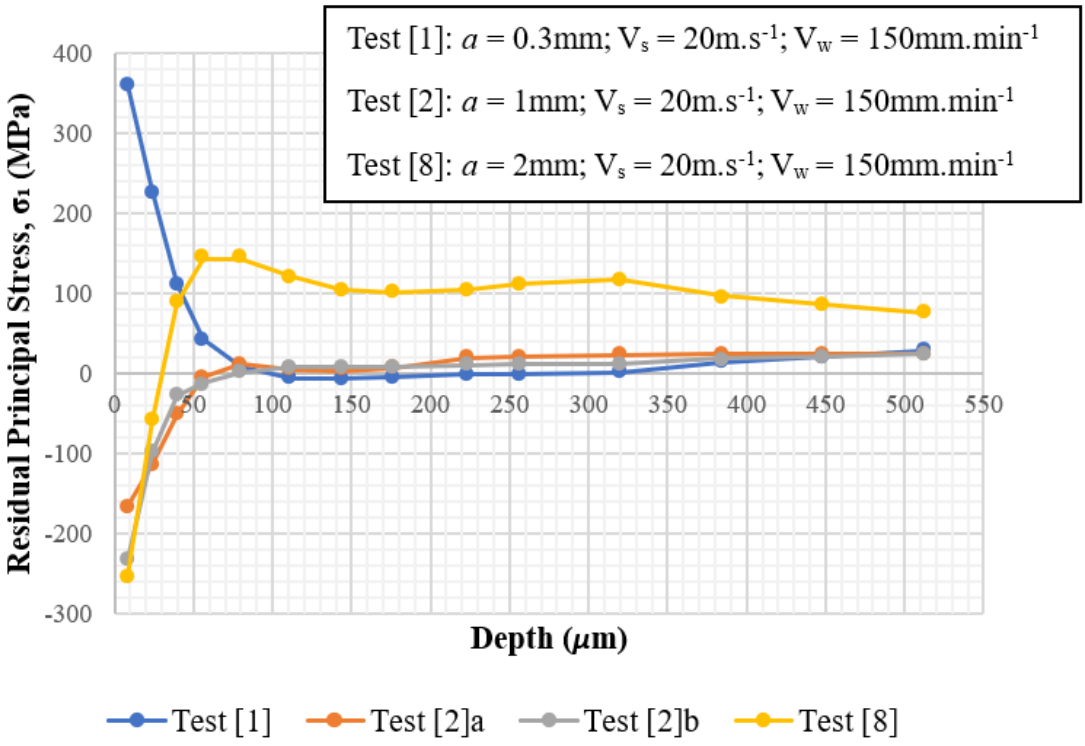



**Figure 6.34:** Residual Principal Stress $\sigma_1$ vs. Depth (Grinding Direction)

Fig 6.35 highlights the variance in both the desired compressive and undesired tensile residual stresses induced in the grinding direction as the depth of cut increased across Test [1], Test [2] and Test [8]. The compressive stress component is clearly observed to increase as the depth of cut increased, whilst conversely, the tensile stress component indicated more variance in magnitude across the tests.

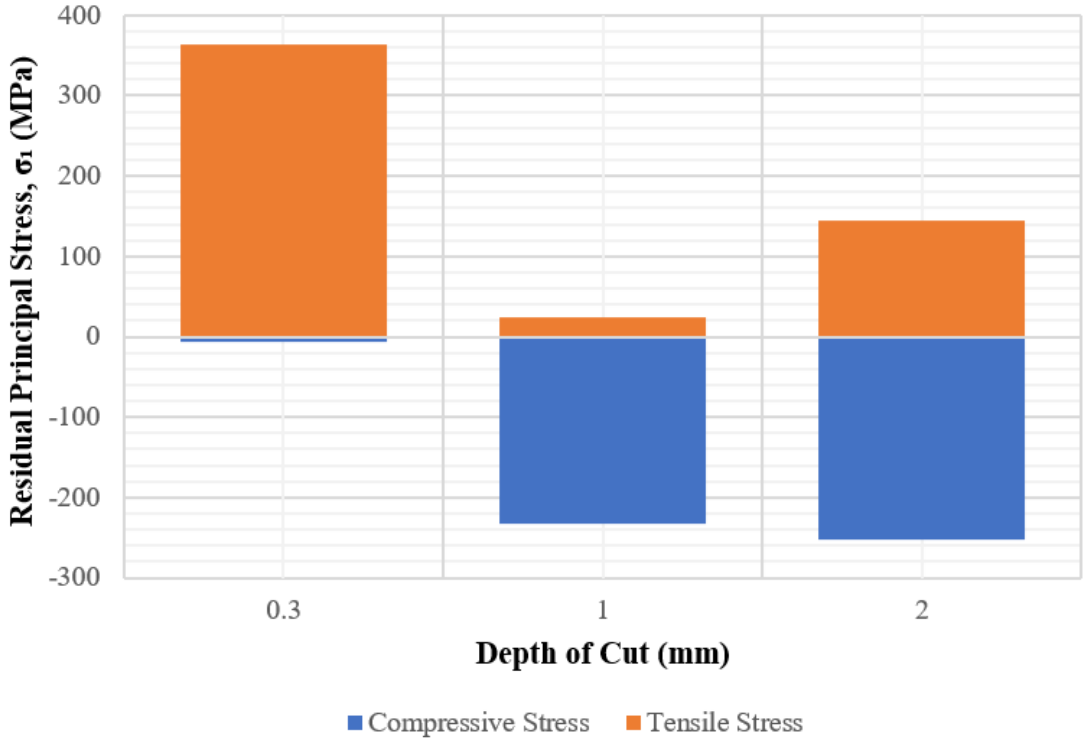



**Figure 6.35:** Residual Principal Stresses $\sigma_1$ for all Depths of Cut Analysed (Grinding Direction)

Fig 6.36 details a phase transition temperature plot for Ti-6Al-4V obtained from Majumdar *et al.*, (2019). As can be easily ascertained from the literature, the $\alpha$-phase to $\beta$-phase transition within Ti-6Al-4V is dependent on both the $\alpha$ stabilizing element (aluminium) and the $\beta$ stabilizing element (vanadium) percentage content. The $\alpha$ stabilizer increases the $\alpha$-phase to $\beta$-phase transition temperature, whilst the $\beta$ stabilizer increases the melting point and strength of the alloy (Callister and Rethwish, 2008).

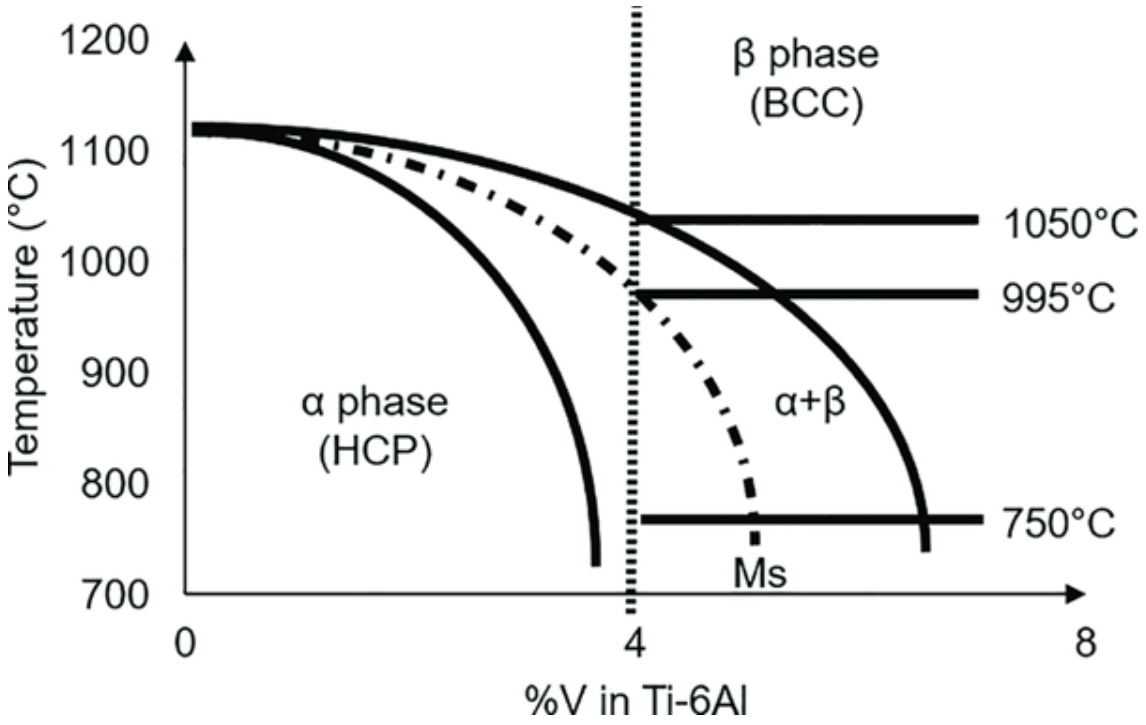



**Figure 6.36:** Typical Phase Transition Plot for varying percentage Vanadium Content within Ti-6Al-4V (Majumdar *et al.*, 2019)

Fig 6.37 introduces the changes in residual principle stresses induced during Test [1], Test [2] and Test [8] in the transverse direction to the grinding path. Again, Test [8] observed significant, undesirable tensile stresses. The plot also indicates that the transverse direction observed a greater overall stress magnitude for Test [8] when compared against the equivalent axial direction stress profile.

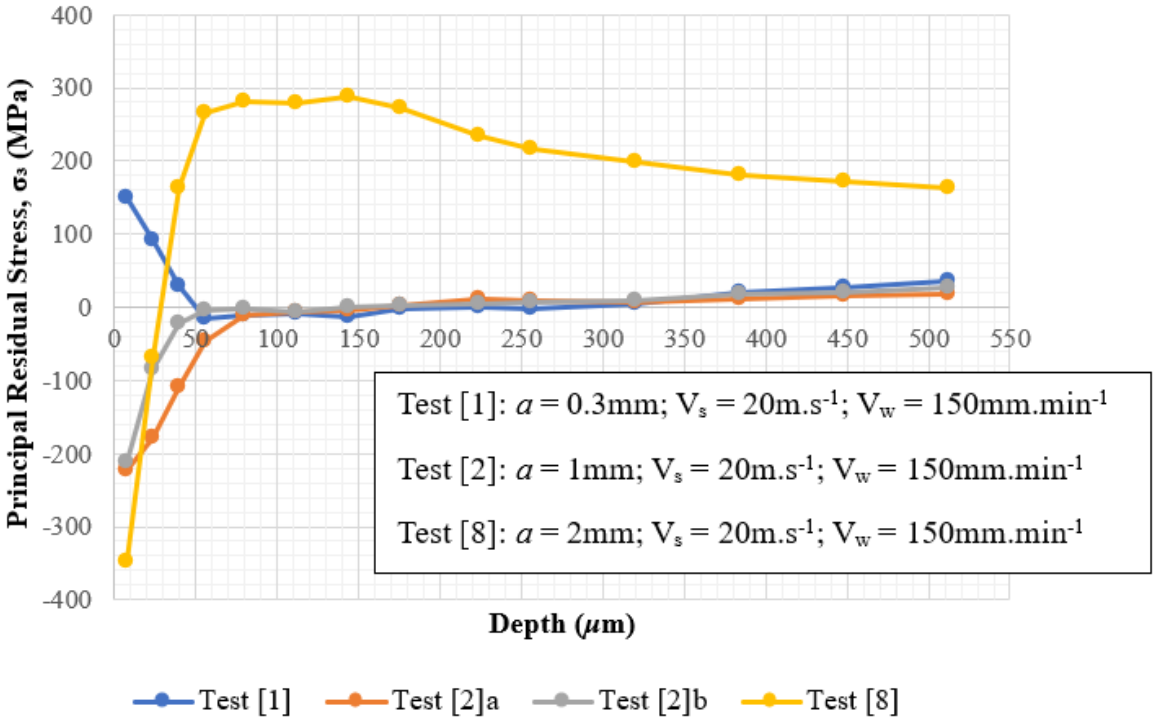



**Figure 6.37:** Residual Principal Stress $\sigma_3$ vs. Depth (Transverse Direction)

Fig 6.38 details the compressive and tensile residual stresses induced in the transverse direction for Test [1], Test [2] and Test [8]. In a similar manner to the data presented in Fig 6.35, the compressive stress component of the residual stresses induced increased as the depth of cut was increased, with the tensile stress component again showing more variation.

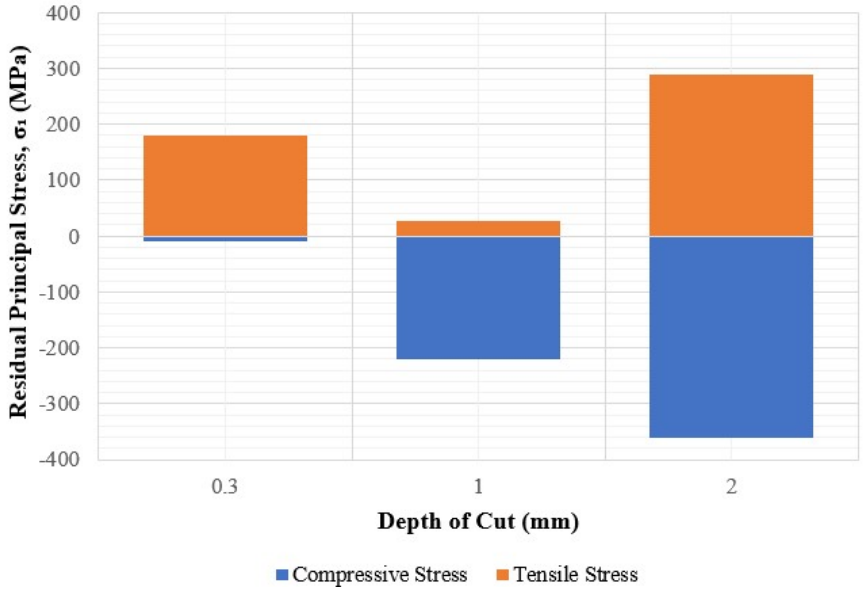



**Figure 6.38:** Residual Principal Stresses $\sigma_3$ for all Depths of Cut Analysed (Transverse Direction)

Fig 6.39 presents the residual shear stress profiles induced during Test [1], Test [2] and Test [8]. Unlike the tensile and compressive residual stress traces, the shear stress traces appear to indicate more variation the deeper into the workpiece the variable was measured. However, it is still apparent that Test [8], which induced higher workpiece temperatures than either Test [1] or Test [2], still indicated tensile shear stress values from ≈250$\mu$m into the subsurface depth.

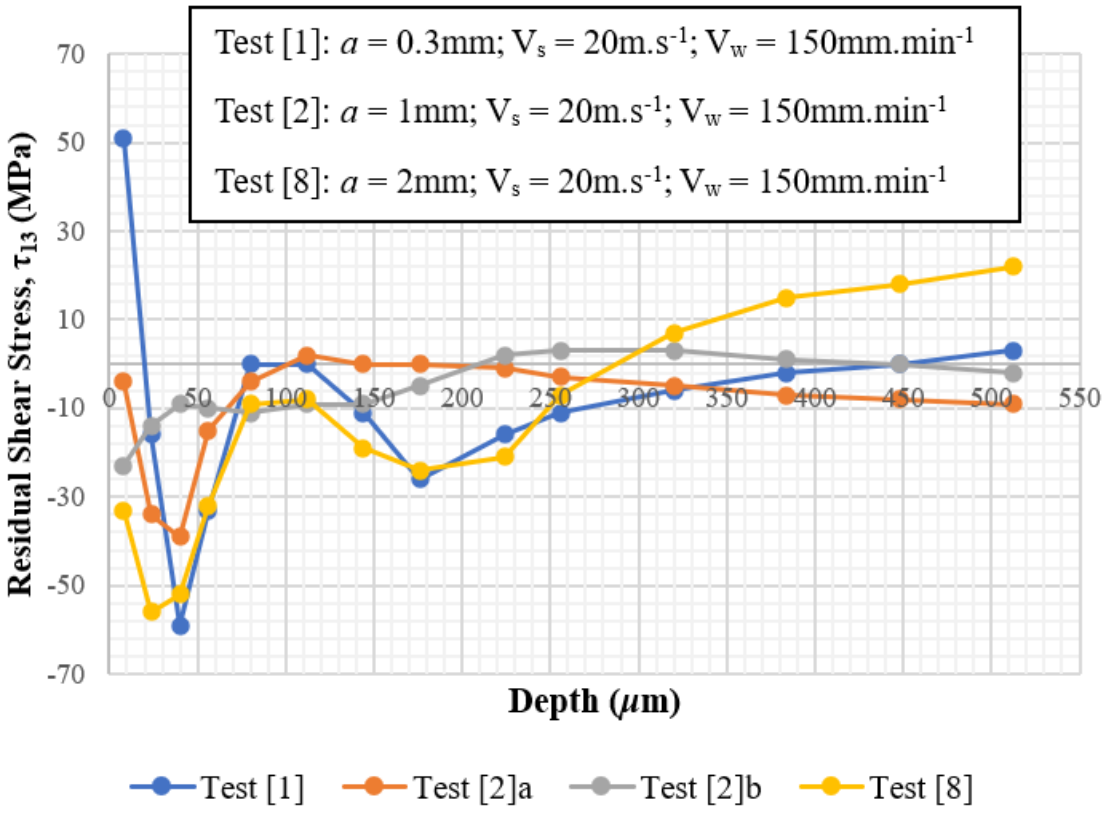



**Figure 6.39:** Residual Shear Stress vs. Depth

Fig 6.40 defines the compressive and tensile components of the residual shear stresses induced during Test [1], Test [2] and Test [8]. Unlike the previous compressive and tensile plot relating to the normal residual stresses, no clear relationship can be determined as the depth of cut was increased from 0.3mm, to 1mm, and finally to 2mm.

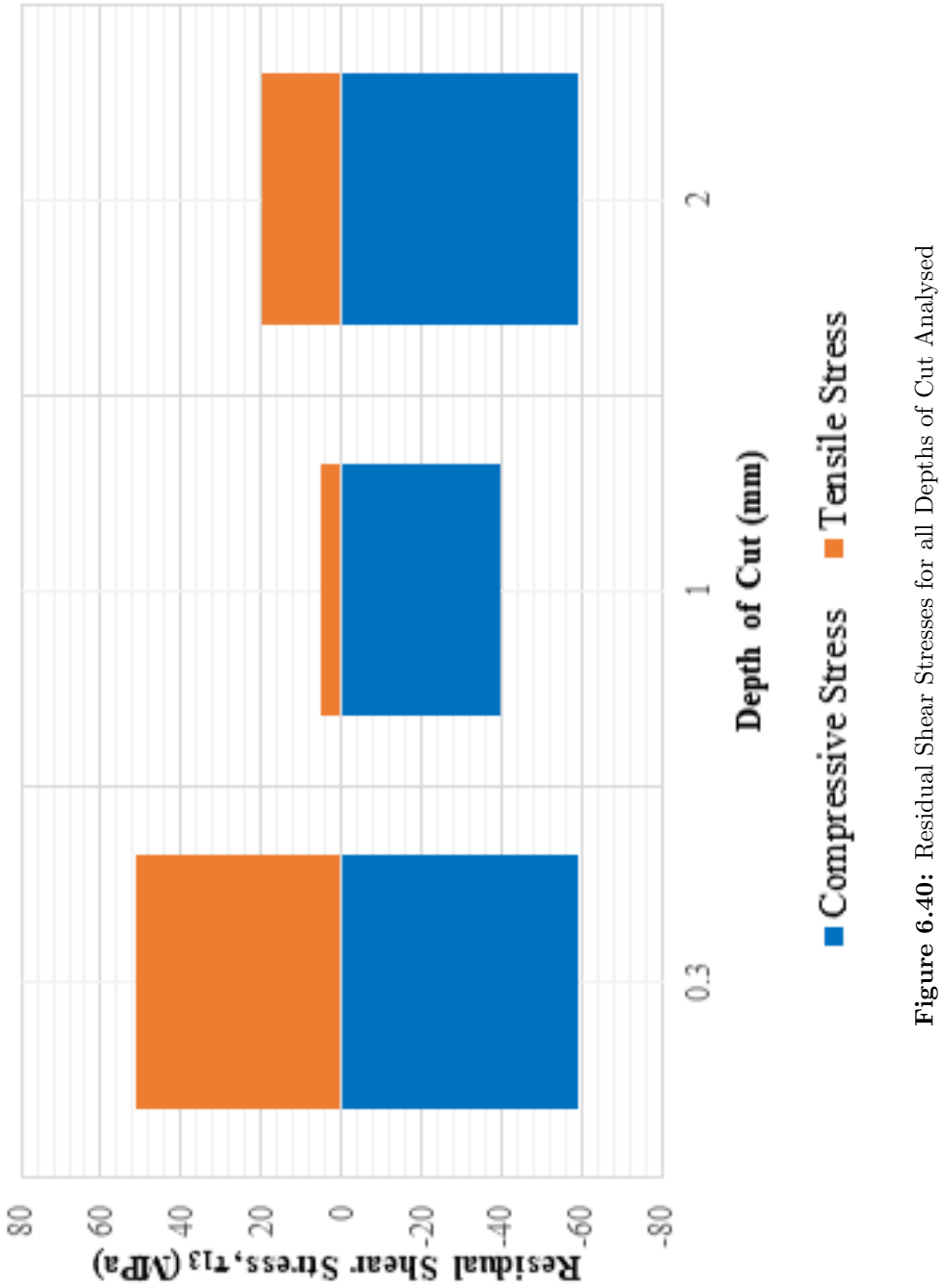



**Figure 6.40:** Residual Shear Stresses for all Depths of Cut Analysed

## 6.2 Discussion

### 6.2.1 Surface Roughness

The initial surface integrity assessment considered measuring the average surface roughness ($R_a$) value for the given workpieces post-grinding. The $R_a$ values were thus obtained for all test cases, both parallel and perpendicular to the grinding direction. Fig 6.1 details the $R_a$ values parallel to the grinding direction for the first six test cases conducted, whilst Fig 6.2 details the $R_a$ values parallel to the grinding direction for the final four test cases conducted.

As can be determined from Fig 6.1, the $R_a$ values across the first six grinding test cases varied between $0.26\mu\text{m} < R_a < 1.12\mu\text{m}$; a range of 76.8%. These $R_a$ values can be categorized as consistent for the reported ranges suggested in the literature by the likes of Puerto *et al.*, (2013), for example, who claimed grinding should achieve values across a wide range of $0.1\mu\text{m} < R_a < 2\mu\text{m}$. This percentage was increased significantly by the apparent outlying $R_a$ result of position six from Test [1]. This result appears to be inconsistent with other results and can possibly be explained by the high cutting forces (900N) acting on the tooling before the end of that pass.

When comparing Test [1] to Test [6], where the only change in test parameter was an increase in wheel speed from $20\text{m.s}^{-1}$ to $30\text{m.s}^{-1}$, the $R_a$ value decreased significantly, and is contradictory to the likes of Patil *et al.*, (2016) who claimed $R_a$ increases with an increase in wheel speed. However, when comparing this finding with the chip formation equation (Eqn. 4.1), one would expect to find $R_a$ would decrease with an increase in $V_s$, and so this finding is comparable. This result is interesting when one considers that the faster wheel speeds studied in this example induced a lower workpiece temperature (52°C) than the slower wheel speed tested (72°C). This is in part due to the workpiece temperature induced during grinding being proportional to the specific energy within the system, with a better surface finish being a trade-off between excellent $R_a$ values and high specific energies as was reported by Badger *et al.*, (2021). Additional analysis also confirms a varied response in terms of $R_a$ values along the length of the grinding pass from point of wheel entry to point of wheel exit, i.e.,

during Test [1], a gradual increase in $R_a$ value was observed (54.7%), whilst during Test [2], a similar, although less marked, trend (25.7%) was apparent. Again, both Test [4] and Test [5] also observed increases (42% and 60.4% respectively). Meanwhile, Test [3] and Test [10] both observed decreases in $R_a$ value across the grinding path of 51.4% and 38.6% respectively.

An interesting point to note in Fig 6.2 is the significant increase in $R_a$ value at position three during Test [7]. As can be attested by the error bar on the plot, there appears to be a larger error than with other traces on the figure, indicating a larger degree of variance and therefore some uncertainty from this result. Additionally, Test [6], Test [7] and Test [9] all demonstrated approximately linear $R_a$ responses across the length of the grinding path of 0.17%, 1.4% and 8.1% respectively.

Interestingly, Fig 6.2 also indicates that when comparing Test [8] and Test [9], whereby the only change is an increase in wheel speed, the $R_a$ value was observed to decrease considerably. Again, this observation is expected and explainable via the interaction between the grinding wheel and the workpiece causing wear of the tooling which thus results in a reduction in the magnitude of the chip thickness (Lubis, Darmanwan and Ericson, 2019). When comparing Test [9] with Test [10], where the feed rate was increased whilst all other grinding parameters were held constant, the $R_a$ value was 22.7% higher when utilising faster feed rates than slower feed rates. Again, this relationship is consistent with the literature, with more aggressive grinding parameters resulting in greater thermal softening of the workpiece, thus resulting in higher surface roughness, lower microhardness and greater plastic deformation beneath the ground surface, as was proposed by the work of Patil *et al.*, (2016).

With the issue regarding surface integrity being addressed by several sources previously mentioned, as workpiece temperatures are observed to increase, the $R_a$ value has been found to increase. However, the inverse relationship was found in some cases, i.e., Test [9]. In general, however, the expected trend was observed. For instance, Test [10], which observed the highest workpiece temperature (800°C and workpiece surface burn), observed

higher $R_a$ values than Test [9]. This observation has also been observed in nickel superalloys previously (Chen *et al.*, 2004). In conclusion, the key point to note from the parallel $R_a$ measurement data collected is that tests with the most aggressive grinding parameters, i.e., Test [7], Test [8], Test [9] and Test [10], observed better surface roughness ($0.26\mu\text{m} < R_a < 0.54\mu\text{m}$), whilst tests using the least aggressive parameters achieved similar, albeit covering a wider range ($0.3\mu\text{m} < R_a < 1.1\mu\text{m}$), $R_a$ values. The author therefore proposes more test cases be studied using faster feed rates to fully verify this claim.

Fig 6.3 details a summary of the average surface roughness measurements (parallel to the grinding pass) gathered across all tests conducted, with the test parameters for each being detailed in Table 3.2. As can be determined from the plot, there is a clear decrease in average $R_a$ value, with a select number of tests being contradictory to this observation, i.e., Test [7] and Test [10]. Interestingly, this observable decrease in $R_a$ as the tested grinding parameters became more aggressive is contradictory to the work of Rowe (2009), who stated that surface roughness increases with an increase in workpiece temperature through the use of increased feed rates, wheel speeds and depths of cut. It is an interesting point to highlight that the data set regarding Test [10] average surface roughness presented in Fig 6.2 demonstrated the inverse of what has been reported in the literature, and as such, further research should be conducted to investigate this finding.

Regarding the perpendicular $R_a$ performances which are presented in Fig 6.4 and Fig 6.5 respectively, it is clearly apparent that there is a significant increase in surface roughness values when compared to the parallel $R_a$ values. Peak $R_a$ performance across the case studies tested varied between $1.16\mu\text{m} < R_a < 2.4\mu\text{m}$; a 51.6% difference. The perpendicular $R_a$ values are in-keeping with the expected trend due to the increased tooling wear rates across the face of the wheel fluctuating more than the wheel wear rate parallel to the cutting plane. These findings were also highlighted in the $G$-ratio analysis data provided in section 4.1.2.1. It can be proposed that higher $R_a$ values are thus being observed at lower specific energies and, by definition, experience higher workpiece temperatures. It can also be clearly noted that the $R_a$ responses perpendicular to the grinding direction appear more

sensitive than those parallel to the grinding path.

In Fig 6.5, the $R_a$ values for the more aggressive grinding parameters indicate a clear, positive trend across the workpiece surface. The author proposes this is due to considerable wheel wear occurring across the wheel surface, as can be observed via the increasing $R_a$ values from position one through to position six. This is consistent with the previously referenced works relating the relationship between increased surface roughness and workpiece temperature (Patil *et al.*, 2016), i.e., surface roughness increases with an increase in workpiece temperature as the grinding tool wears (Rowe, 2009). Interestingly, whilst this relationship has been established during creep feed grinding, the opposite has been found during HEDG, and is therefore a result on which future research work could be based.

Conversely, Fig 6.1 indicates that a larger $R_a$ was found towards the exit of the workpiece when grinding parameters were the least aggressive. It was also established that during the test, the workpiece temperature and cutting forces were the lowest obtained from the experimental trials. This is surprising as less aggressive grinding parameters have been reported to induce a lower $R_a$. However, this has been counter-claimed by Suhail *et al.*, (2011), who claimed that as the feed rate increases, workpiece temperature decreases, thus resulting in an increase in $R_a$ value. When compared to Test 2, whereby the only alteration in test parameter was an increase in the depth of cut value whilst all other parameters were kept constant, a decrease in $R_a$ at the same position is apparent. Although an increase in the depth of cut significantly increased both the workpiece temperature and the cutting force response, it has been reported by Zhang *et al.*, (2020), that the depth of cut is the least important parameter that affects $R_a$, with the wheel speed being the most significant, followed by the feed rate and lastly the depth of cut. Additionally, higher cutting forces are often observed in relation to highly negative rake angles of the tooling than when utilising positive rake angles as wheel speed increases (Günnay *et al.*, 2004). This would also result in a higher workpiece temperature. A worsened $R_a$ value could therefore be a result of the grits breaking resulting in rake angles of the abrasive grains becoming negative, in addition

to a greater microhardness depth and unwanted tensile residual stresses also being induced.

Finally, as is demonstrated in Fig 6.6, the average surface roughness for all grinding tests perpendicular to the grinding path indicate a general reduction as the grinding parameters became more aggressive. The grinding parameters for each test described in the figure are presented in Table 3.2. This trend mirrors that demonstrated by Fig 6.3. However, in a similar manner to that presented within the parallel average $R_a$ values for Test [10] (i.e., the most aggressive grinding test conducted), an increase in $R_a$ value perpendicular to the grinding surface was observed, and is demonstrative of the trend proposed by Rowe (2009). Surface roughness values are also known to worsen significantly with materials that have a low thermal conductivity or high thermal expansion coefficients such as Ti-6Al-4V, and adds weight to the data collected regarding this response.

### 6.2.2 Microstructural Interrogation

#### 6.2.2.1 Ground Surface

The following micrographs detail the samples adjacent to those sent for etching with the grinding surface being clearly visible. Fig 6.7, Fig 6.8 and Fig 6.9 detail the images taken from Test [1], Test [2]b and Test [8] respectively.

As can be observed for the three tests, the ground surface is as expected, i.e., linear grinding marks. Taking Test [1] one can surmise that if the subsurface were to be analysed, darker HCP $\alpha$ phase would appear within the lighter BCC $\beta$ phase matrix due to less aggressive grinding parameters resulting in lower workpiece temperatures and therefore less subsurface damage. With it being known that the $\beta$ phase is harder than the $\alpha$ phase constituent, the microstructure phases should appear to be evenly distributed. This is explainable and due to the test parameters used, i.e., low level, or 'finishing' grinding parameters. Low temperatures were observed ($T < 100°C$) and therefore subsequent negligible changes in $R_a$, microhardness value and microstructural deformation should be

induced. This is due to the temperature being significantly lower than the $\alpha + \beta \longrightarrow \beta$ transition temperature of $\approx$ 840°C - 900°C (Wang *et al.*, 2020).

#### 6.2.2.2 Subsurface

As Test [1] utilised the least aggressive grinding parameters tested, it should have been expected to find the microstructure only marginally affected due to the lowest workpiece temperatures measured (75°C), and thus minimal subsurface damage being induced. This is precisely what was found as detailed in Fig 6.10 (a, b c and d). This result is visible throughout all magnification plots captured, whereby a mixed $\alpha$ and $\beta$ phase is evident within the bulk of the sample material. This result agrees with Mathohol *et al.*, (2018), and adds further weight to their claims. When the result contained in Fig 6.10 is compared with the microhardness plots at the location of thermocouple 3 in Test [1] as presented in Fig 6.11 (a and b), the author's claims regarding the microhardness results are verified by the micrographs which indicate some $\alpha$ to $\beta$ phase transition nearer to the grinding surface.

A further distinction can be drawn when assessing the Wire-EDM micrographs associated with Test [1] presented in Fig 6.12 (a, b, c and d). A clear trend can be observed whereby the $\alpha$ phase constituent is visible close to the wire cut surface i.e., an indication of obvious thermal-softening. This observation then moves towards a $\beta$ phase constituent within the bulk material of the workpiece, indicating little to no subsurface damage due to the workpiece temperature being lower at this subsurface depth than at the cutting surface.

Fig 6.13 (a, b, c and d) details the four magnification microstructure images taken at the thermocouple 3 position from the final pass during Test [2]. As discussed previously in this thesis, it was at this final position within the thermocouple configuration where the highest workpiece temperature was observed. In this test case, a workpiece temperature of 475°C was induced from the given grinding parameters utilised. When assessing the micrographs for this location, it is clear that there is a proportion of $\beta$ phase constituent and $\alpha$ phase constituent closer to the grinding surface ($<200\mu$m) than deeper into the sample subsurface ($>500\mu$m). This indicates that some work hardening of the

material is occurring closer to the grinding surface, whilst thermal softening occurs deeper into the workpiece, thus confirming the work of Mathohol *et al.*, (2018).

Additional analysis of the thermocouple 3 location during Test [2] is provided in Fig 6.14 (a and b). A direct comparison of the microhardness values is presented against the microstructure micrographs. As expected, the darker, $\alpha$ phase constituent is observable closer to the ground workpiece surface, i.e., the position of the highest workpiece temperature and thus greater work-hardening from material recrystallization. This in turn results in a greater microhardness value. This relationship alters a greater proportion of $\alpha$ phase constituent deeper into the material subsurface, i.e., thermal softening, and therefore results in a lower microhardness value as reported by Ginting and Nouari (2009).

An interesting result can be drawn when comparing the Wire-EDM cut edge of the sample created when preparing the workpiece prior to being mounted in the Bakelite powder. In Fig 6.15, the $\alpha$ and $\beta$ phases appear to be somewhat more consistent throughout the sample from the Wire-EDM face than the ground face. This is explainable due to the grinding temperatures induced being significantly higher than those induced via the Wire-EDM process; something also reported by Koyano *et al.*, (2018). Although not directly related to this thesis or analytically evaluated, the surface quality from the Wire-EDM machining process can be clearly observed to be worse than the ground surface which has been evaluated and critiqued in this section. At x50 magnification, particles and the recast layer on the workpiece surface is evident, indicating clear potential issues in relation to microcracking from pores and residual stresses.

When considering Test [8], which utilised the same grinding parameters as Test [2] excepting a doubling of the depth of cut from 1mm to 2mm, the subsurface damage appears less pronounced as presented in Fig 6.16. This is surprising as increasing the depth of cut has been demonstrated to increase the workpiece temperature significantly from 75°C to 710°C. However, it can be noted from Fig 6.16 (a, b, d and c) that there is a significant feature apparent in the microstructure, possibly due to over-etching of the Ti-6Al-4V

workpiece. Moreover, although previous studies by Bentley, Goh and Aspinwall (2001) claimed that subsurface layers could be free from any Heat Affected Zone (HAZ) when using $\gamma$-titanium aluminide workpieces whilst reciprocal grinding, the data presented here indicates that Ti-6Al-4V does not behave in such a manner when the grinding parameters are significantly aggressive.

The microhardness test data and microstructure analysis comparison for Test [8] can be observed in Fig 6.17 (a and b). A clear and more consistent relationship in relation to the mixed $\alpha$ and $\beta$ phase is evident throughout the workpiece sample. The microstructure microscopy does appear to offer sound additional weight to the microhardness data and assessment which pertains to a greater microhardness throughout the subsurface when using more aggressive grinding parameters. It should be noted that this appears more localised for Test [8] than in previous tests.

Fig 6.18 (a, b, c and d) details the microstructure at the location of thermocouple 3 used during Test [10]. Here, $\alpha$ phase material is observable close to the grinding surface as can be expected due to the high workpiece temperature induced (790°C) and therefore thermal softening occurring from utilising the most aggressive grinding parameters evaluated ($V_s$ = 30m.s$^{-1}$, $V_w$ = 300mm.min$^{-1}$ and $a$ = 2mm). $\beta$ phase constituents are clearly visible deeper into the sample's substrate confirming the work of Guo *et al.*, (2011). It is also interesting to note that Test [10] doesn't appear to have induced as much subsurface damage as previous tests (i.e., Test [8]) when considering that the highest workpiece temperature would have been expected to cause greater phase transition than lower workpiece temperatures. However, some degree of variance can be expected during experimental trials. Subsequently, increased microhardness and higher residual tensile stress would also be expected. Fig 6.19 details the microhardness plot at the location of thermocouple 3 against the microstructural analysis.

When analysing the microstructure responses of all the samples detailed herein, and especially when utilising the most aggressive grinding parameters which are detailed for both Test [8] and Test [10], the highest workpiece temperatures were observed (710°C and 790°C

respectively). This is due to the most severe plastic deformation occurring during those test cases resulting from the most significant level of friction between the grinding wheel and the workpiece (Guo *et al.*, 1999; Guo *et al.*, 2011). Conversely, as the results from both Test [1] and Test [2] indicate, a lower microhardness was found closer to the grinding surface (i.e., more $\alpha$ phase material), with a higher microhardness deeper into the material (i.e., more $\beta$ phase material). However, this hardness appears to reduce again towards the inner region of the sample. This phenomena can be explained via Ti-6Al-4V having a low thermal conductivity ($6.9 \mathrm{W.m^{-1}.K^{-1}}$), thus meaning the grinding surface increases in temperature, whilst the bulk material beneath the ground surface remains cooler due to poor temperature propagation throughout the substrate.

From basic metallurgical theory, it is known that when the phase transition temperature is breached (i.e., when the grinding temperature is above the phase transition temperature), a phase transformation occurs (Callister and Rethwish, 2008). This was found during this study, with subsurface damage more evident closer to the grinding surface than below it, as is observable in the micrographs presented. It is also clear from the micrographs that Ti-6Al-4V has a coarse equiaxed microstructure, indicating that it has a superior ability to withstand creep and fatigue crack propagation as discussed by Guo *et al.*, (2011). Finally, it can be concluded from the study that where grinding temperatures were higher, i.e., when using more aggressive grinding parameters including deeper depths of cut, the microstructure indicated greater subsurface damage as indicated by Test [10] when compared against less aggressive parameters as in Test [1]. This is an important result to realise when one considers the importance of having a material with as little plastic deformation as possible for performance and safety concerns in safety critical components. This is due to components with greater levels of subsurface plastic deformation being more brittle and thus more likely for potentially catastrophic failure during service. The results found and detailed in this surface integrity study therefore provides a sound analysis of Ti-6Al-4V components after being ground to extremely high temperatures up to approximately 800°C. The normal force acting on the grinding wheel is also observed to have a significant impact upon the workpiece integrity. This is in part due to its relation to friction and subsequent

heat generation within the workpiece. Conversely, the tangential force mainly affects the grinding power requirements and therefore is primarily associated with the chip formation mechanism (Li, Liu and Li, 2001). Chip formation also results in both mechanical and thermal induced effects. This can therefore explain why within Test 9 and Test 10, higher workpiece temperatures also observed higher cutting force magnitudes.

It is known that Ti-6Al-4V is a bi-modal alloy at room temperature. Within the matrix there is a mixture of equiaxed alpha phase and alternating alpha and beta phases. A phase transformation plot pertaining to when these phase changes occur is given in Fig 6.36. Within the SEM images presented in section 6.1.2.3, the darker regions are the alpha phase, whilst the beta phase are the lighter regions. The bi-modal structure of a given alloy of this nature can be altered when undergoing intense thermomechanical processing within the alpha-beta phase region described in the phase transformation diagram. Machining, and therefore grinding, thus alters the microstructure significantly due to the magnitude of heat generated within the grinding zone (Villa *et al.*, 2019).

#### 6.2.2.3 SEM Imaging

Fig 6.20 presents the ground and subsurface SEM image for Test [1]. There are extensive visible smearing marks associated with the test. Additionally, there appears to be a significant amount of adhered material to the workpiece surface. Smearing during grinding indicates that plastic deformation is occurring over a larger cross-sectional area and can be attributed to the lack of lubricant within the cutting zone or contamination of the grinding tooling and/or the polishing cloth. The smearing effect is normally associated with material surrounding the abrasive particles being pushed out of the tooling and pulled along the workpiece surface. The redeposition of the particles onto the workpiece surface is then observed, with adhesion between the two being a result of friction welding. In this particular case, the smearing markings could also be attributed to the relatively high ductility of the workpiece material, or possibly due to the grinding wheel and acting as if 'blunt', thus adding to the smearing effect observed. High redeposition phenomenon during flood cooling

was found by Naskar, Choundhary and Paul (2020) and so this result further ratifies their findings, and those of de Mello *et al.*, (2015), who observed significant striations on the ground Ti-6Al-4V workpiece surface when using SEM analysis.

Fig 6.21 (a, b and c) details a SEM image of the cross-sectional area of Test [1], whilst Fig 6.21 (d and e) details the ground surface of the sample. The increased accuracy of the image can be reconciled with the standard microscopy image presented in Fig 6.10 and Fig 6.11, i.e., significant $\alpha$ phase material near the ground surface (as expected due to much lower grinding temperatures occurring during this test), with a fairly distributed $\alpha$ and $\beta$ phase deeper into the bulk Ti-6Al-4V workpiece. This general plastic behaviour of Ti-6Al-4V workpieces was proposed by Moussaoui *et al.*, (2013), despite their claims of limitations of measuring bulk microhardness via current standard procedures as discussed previously.

For completeness, Fig 6.22 illustrates the subsurface damage due to the Wire-EDM manufacturing process. This adds further weight to the image captured via standard microscopy as presented in Fig 6.12 which illustrated far greater subsurface damage than the ground surface, i.e., greater areas of $\beta$-phase close to the cut edge. The SEM image of the Wire-EDM face shows more clearly the recast layer referred to in Fig 6.12. As theorised when discussing that image regarding the potential of microcracking being present, Fig 6.22 clearly provides evidence of significant microcracking and is an important note to mention regarding this manufacturing method in relation to Ti-6Al-4V workpieces. This observation has also been previously reported by Wang (2000) when assessing subsurface damage via the SEM method.

Fig 6.23 (a and b) details two images pertaining to the entry point of the workpiece (i.e., close to thermocouple 1) and the exit point of the workpiece (i.e., close to thermocouple 3) for Test [6]. These SEM images were captured at x1000 and x1500 magnifications respectively. There is clear evidence of microporosity in the workpiece at the entry point of the workpiece. Additionally, it can be observed that significant subsurface damage/cracking

and pitting is apparent close to the exit of the workpiece. This is an interesting and surprising result when one considers the test parameters associated with Test [6] ($V_s$ = 30m.s$^{-1}$, $a$ = 0.3mm and $V_w$ = 150mm.min$^{-1}$) induced a lowest temperature of approximately 50°C as detailed in Fig 5.33. As was proposed by Mackenzie (2017), cracking occurs when the residual stresses are at a maximum, which is generally associated with more aggressive grinding parameters, i.e., deeper depths of cut resulting in a greater MRR. More likely, this phenomenon is associated with the material during its initial manufacture and not with the grinding process itself. Conversely, microcracking was also observed during the work by de Mello *et al.*, (2015).

Fig 6.24 (a and b) details the cross-section images associated with Test [9] at the entry of the workpiece (i.e., close to thermocouple 1). Here, two different magnifications were used; again, x1000 and x1500 levels. Despite being one of the most aggressive grinding tests evaluated, there appears to be little surface damage through the cross section. When assessed in conjunction with Fig 6.25 (a-f), which evaluated the level of subsurface damage via a conventional camera approach for both Test [9] and Test [10], the entry point of the workpiece also indicated very little noticeable subsurface deformation. This is due to there being very little heat within the system at this position of the grinding pass and therefore little to no $\alpha \longrightarrow \beta$ transition as can be expected (Moussaoui *et al.*, 2013).

Despite it being clearly evident that there appears to be little subsurface damage at the entry point of the workpiece (i.e., close to the position of thermocouple 1), the level of subsurface plastic deformation progressively increases further along the pass to the middle of the workpiece (at the position of thermocouple 2), before reaching a maximum at the exit of the workpiece (position of thermocouple 3) for both Test [9] and Test [10]. This finding substantiates the author's previous findings presented within Fig 5.42 and Fig 5.43, where the workpiece temperature was observed to increase between the location of thermocouple 1 and thermocouple 3, i.e., an expected increase in subsurface plastic deformation. Fig 6.28 and Fig 6.30 also adds further evidence to this claim, whereby the microhardness for Test [9] and Test [8] increase from the location of thermocouple 1 through to the location of

thermocouple 3. Finally, the plastic deformation observable from the cross-section images corresponds to the burn on the workpiece surface, i.e., deeper subsurface damage where more burn is present and hence the off-centre profile (Badger and Torrence, 2000). The deformed material section is also clearly thinner at each of the ends which is also commonly observed and is something that has been reported when grinding $\gamma$-titanium aluminide by Nelson *et al.*, (1997) and Murtagian *et al.*, (2010).

Fig 6.26 (a-c) details the ground surface for Test [10]. The captured images detail smearing, abrasive adhesion and grooving which appear on the left-hand side of the figure. When assessing the subsurface SEM images pertaining to Test [10], i.e., the most aggressive grinding test analysed, significant levels of subsurface plastic deformation is apparent. Fig 6.26 (d-f) highlights these observations. The $\alpha$-phase to $\beta$-phase transition is apparent on the right-hand side of the figure. This is also to be expected as microstructural changes occur due to an increase in workpiece temperature. Workpiece temperature increases with the MRR (i.e., deeper depths of cut), which also leads to an increase in greater tensile residual stresses. Additionally, as has been reported in section 4.1.2.2, as the grinding wheel progresses along its path from entry to exit, the workpiece temperature is observed to increase with thermocouple 3 in the series registering the highest reading. This has been suggested as being due to film boiling of the coolant, which results in a worsening of subsurface deformation. Higher wheel speeds also result in higher strain rates of the workpiece material, higher specific energies and high temperature gradients. This would result in lower workpiece temperatures and is what was observed during tests which involved the higher wheel speeds during the experimental trials. Lower surface roughness would thus be induced, as well as less subsurface damage depth as was observed in Test 1 and which was inverse to Test 10.

In conclusion, using more aggressive grinding parameters results in a greater level of subsurface damage. This has been substantiated through three studies in this thesis via both conventional microscopy, SEM and standard conventional camera apparatus. Moreover, this has been reported in the literature, i.e., higher workpiece temperatures result

in worsening of surface integrity (Badger and Torrance, 2000). This issue is heightened further when considering the relatively high ductility of Ti-6Al-4V workpieces, which is observable via the intensive smear marks on the ground surface of the samples. Increases in the subsurface deformation is reinforced by the microhardness plots when moving from thermocouple 1 via thermocouple 2 and thermocouple 3, whereby the higher the workpiece temperature at a given location, the greater the microhardness. There is also an observable increase in residual tensile stress thus resulting in greater plastic deformation of the workpiece.

### 6.2.3 Microhardness

As can be observed in Fig 6.27 which details the microhardness results for Test [9], the microhardness of the sample increases initially (10$\mu$m) into the test piece until a maximum of 500HK$_{0.05kg}$ at approximately 40$\mu$m into the subsurface. After this measured depth, a significant reduction in microhardness response can be determined at additional depths until 400$\mu$m whereby the microhardness appears to reach the bulk microhardness of Ti-6Al-4V (approximately 363HK$_{0.05kg}$). This can be expected and has been reported in the literature (Wang and Liu, 2020). Fig 6.27 also clearly indicates that this relationship can be observed across all three thermocouple locations studied.

When one considers the percentage difference in microhardness measurements across the range of the depths studied, thermocouple 1 indicated a 31.2% difference, thermocouple 2 a 37.9% variation whilst thermocouple 3 observed a 38.6% total change. This indicates an increase in total variation in microhardness across the same range of depths along the grinding path studied per thermocouple location of 19.7%; not an insignificant result. This relationship in microhardness and penetration depth can be gleaned from the literature and confirms the work of Kekade *et al.*, (2016). Additionally, the microhardness of the subsurface material at 10$\mu$m below the ground surface was found to be 30% higher than the bulk hardness of the material, something explainable by Ti-6Al-4V work hardening, which, despite being significantly lower than for conventional steels for example, still occurs whilst machining this particular alloy. The same observation regarding three distinct

subsurface layers in the microstructure can also be determined as discussed by Ginting and Nouari (2009); namely, the hard-subsurface layer, the hardened-subsurface layer and the bulk microhardness of the material.

This observation is explainable by the material science regarding Ti-6Al-4V and its dual hexagonal close packed (HCP) $\alpha$ and body centred cubic (BCC) $\beta$ microstructure, as well as the aggressive grinding conditions utilised during Test [9], i.e., a deep depth of cut, fast feed rate and fast wheel speed. These grinding conditions were found to induce the highest workpiece temperatures of between 500°C and 800°C, and cutting forces (500N and 1500N), which, when one also considers the low thermal conductivity of Ti-6Al-4V, causes higher microhardness values to become established at points of contact with the highest temperature (Mathohol *et al.*, 2018). It can also be stated that when metallic workpieces are subjected to high workpiece temperatures such as those found during Test [9], as discussed in this thesis, both work-hardening and thermal softening occur simultaneously, therefore altering the microstructure of the workpiece through recrystallization of the $\alpha$ and $\beta$ phases, and thus inducing an increased microhardness. However, this has been questioned by Patil *et al.*, (2016), who suggested that thermal softening is more dominant than work hardening when using less aggressive machining parameters. The latter relationship was found within this sample up to 10$\mu$m whereby thermal softening was observed to occur.

Having calculated the average microhardness at each thermocouple location across all indentation depths studied, Fig 6.28 displays a clear increasing trend in microhardness across the length of the grinding pass (i.e., with an increase in workpiece temperature) and adds additional evidence to support the work of Ginting and Nouari (2009), i.e., at the initial temperature reading at the location of thermocouple 1, the microhardness is at a minimum (396.8$HK_{0.05kg}$), before increasing to 403.1$HK_{0.05kg}$ at thermocouple 2, and measuring a maximum at thermocouple 3 (410.5$HK_{0.05kg}$). The average microhardness across all thermocouple locations studied therefore indicates a 3.3% increase across the pass, and thus were found to be within the margin of error of 5%.

More generally across the samples prepared, there appeared more irregularity when assessing the average microhardness values at the depths studied. There is evidence in the literature as to why this might be the case, such as that which was discussed by Moussaoui *et al.*, (2013). Specifically considering Ti-6Al-4V, their study observed several irregularities when considering the microhardness at varying subsurface depths. A key conclusion drawn was the limitation of the microhardness indenter due to its significantly larger size in relation to the 20$\mu$m grain sizes of the Ti-6Al-4V workpiece studied. This poses significant challenges when hoping to take measurements at a single, specific grain, with the indenter often taking measurements over several grains at once. This, in addition to Ti-6Al-4V being a dual $\alpha$ and $\beta$ phase material, with the $\beta$ phase being harder than the $\alpha$ phase, can mean further irregularities occurring when measuring the microhardness of the substrate. This issue can be compounded further when one considers the possibility of the grain boundaries being included in the measurement method. It was suggested that the experimental method used was not suited to the given Ti-6Al-4V material and could therefore result in such irregularities in microhardness measurements.

When one compares the microhardness results from Test [9] to the microhardness results pertaining to Test [8] where the grinding conditions were less aggressive as is presented in Fig 6.29, the peak microhardness at the initial subsurface recrystallization layer is 460HK$_{0.05kg}$; an 8% variance. Again, the same trend as can be observed in Fig 6.29 can be determined from Fig 6.27.

Similarly for Test [8], the gradual increase in average microhardness at each thermocouple location along the grinding path can be observed in Fig 6.30. Microstructural changes resulting from less aggressive grinding parameters (i.e., wheel speed) are evident, with the lower workpiece temperatures inducing significantly less subsurface plastic deformation and therefore substantially lower microhardness values of 7.3% when compared to Test [9]. Another interesting point to note is the total percentage change in microhardness across the grinding pass. Test [8] observed an 8.8% increase compared to Test [9] which noted an 8% change. This indicates that more aggressive grinding parameters induce less variation

in microhardness across the length of the pass than less aggressive grinding parameters.

For completion, the entire set of microhardness data gathered from each test are presented in Fig 6.31 and Fig 6.32 respectively. These plots also detail the average microhardness at each thermocouple location for each test case studied. The trends in the earlier tests in the experimental programme as provided by Fig 6.31 indicate a significant variation in the shallower indentation depths measured (up to approximately 200$\mu$m), after which there appears to be a gradual decrease in the measured microhardness values. This observation is consistent with the works of Wang & Liu (2020) and Kekade *et al.*, (2016), whereby subsurface layers indicate a reduced microhardness the further away one studies from the cutting surface. A clear conclusion that can be drawn as suggested by Moussaoui *et al.*, (2013), and also found through this study, is that more research would be required regarding microhardness measurement methods when analysing Ti-6Al-4V due to the inherent difficulties associated with the complex microstructure of the bulk material. Additionally, as can be determined from the Test [3] plot in Fig 6.31, a large range of microhardness results are visible. Here we have error bars that do not indicate significant variance in the measured data which indicates the physical plastic deformation after conducting that test didn't cause a significant change in microhardness. This could be due to inconsistent thermal softening and work-hardening of the workpiece.

As can be observed in Fig 6.32, extremely high microhardness values can be determined deep into the material subsurface for Test [10], clearly indicating that more aggressive grinding parameters (and therefore higher workpiece temperatures and greater plastic deformation) have a strong effect on the microhardness of the ground component, and should therefore be considered when grinding parts depending on their in-service application. This microhardness response is observable at far deeper depths than the other tests conducted, with little error apparent at each indentation depth tested, thus adding further confidence in the data presented.

Considering Fig 6.27, where aggressive grinding parameters were utilised, high workpiece temperatures and cutting forces were observed. Higher workpiece temperatures induce greater levels of subsurface damage and is something easily discernible by the given plot. Conversely, Test 9 had a lower $R_a$ value at thermocouple position 3 (i.e., at the point of exit of the workpiece where the workpiece temperature peaked due to the film boiling of the coolant from the grinding zone); a result seemingly in accordance with Suhail *et al.*, (2011). Additionally, further research could be conducted on the micro-hardening of the subsurface layer in future tests by considering Barkhausen Noise Analysis (BNA) to try and improve upon and further ratify the data presented herein. BNA would thus enable both the tempered portion of the material (i.e., the over tempered martensitic/thermally softened areas) as well as the un-tempered/thermally hardened martensitic sections of the workpiece to be detected. The un-tempered martensitic layer is observable in Fig 6.23 which used SEM to detail the subsurface for Test 9, and Fig 6.24 which detailed cross sectional damage using a conventional camera. The added benefit of this measurement method is that it would allow for a NDT measurement to be performed which could prevent any unwanted parameters influencing the outcome of the test in addition to removing any potential mechanical stresses from the system before continuing to conduct residual stress testing. A recent example of where BNA has been applied previously include the work by Srivastava *et al.*, (2020), who monitored surface damage when grinding hardened steel.

It is also clear from the microhardness plots detailed in section 6.1.3 that the output is not consistent along the length of the grinding pass. This is due to the increased level of workpiece temperature due to the film boiling effect as the grinding wheel completes its route across the workpiece. This has significant ramifications for post-grinding heat treatments which would need to be applied to normalise this unwanted response. It is therefore evident that greater microhardness values are induced when greater workpiece temperatures are induced, with the highest magnitude of temperature value being closest to the cutting plane (Dai *et al.*, 2020).

In conclusion from the microhardness data gathered, Fig 6.33 details the average microhardness values per test studied, with the test parameters for each detailed in Table 3.2. As can be observed when comparing the average microhardness values, a similar response can be determined across most of the test cases studied. Conversely, the lowest microhardness values were measured during both Test [7] and Test [8], which observed the second most aggressive grinding conditions. This is contradictory to the works of Rowe (2009), who has repeatedly reported that more aggressive grinding conditions induce higher workpiece temperatures (i.e., in these two test cases, the measured workpiece temperatures were 380°C and 700°C respectively), resulting in thermal softening and re-hardening of the material, which thus causes the build-up of white layers, cracking, and therefore an increased microhardness.

### 6.2.4 Residual Stress

Fig 6.34 and Fig 6.37 detail the test data for the axial and transversal residual principle stresses, whilst Fig 6.39 details the residual shear stress data obtained. Here, $\sigma_1$ relates to the grinding direction, $\sigma_3$ relates to the transversal direction and $\tau_{13}$ relates to the shear stress values.

As can be determined from Fig 6.34, when regarding Test [1], high tensile residual stresses are observed (360MPa), before reducing to approximately 0MPa at 80$\mu$m into the sample. This trend is the opposite to what was found for the other grinding tests which utilised deeper depths of cut, yet is one that has been found previously when milling aluminium alloys (Li *et al.*, 2015). Possible reasons for high tensile residual stresses are high wheel wear. It should be noted that the overall residual stress is constituted of three parts, namely; mechanical stresses, thermal stresses and material phase transformation effects (Sun *et al.*, 2020). In terms of these tests, it can be stated that the data pertains to that presented by previous research when grinding (Hamdi, Zahouani and Bergheau, 2004; Youseff *et al.*, 2011 and more recently, Shao *et al.*, 2016). An example of when the phase transition changes occur within Ti-6Al-4V when grinding is presented in Fig 6.36. This is surprising

as Test [1] utilised the least aggressive grinding parameters, i.e., a 0.3mm depth of cut, experienced the lowest workpiece temperature and therefore the least plastic deformation induced across the tests considered here. Comparatively, compressive residual stresses are observed for Test [2]a and Test [2]b up to a maximum measured depth of 75$\mu$m, whereby the residual principal stresses reach approximately 0MPa in magnitude. A greater maximum compressive stress is apparent for Test [2]b than for Test [2]a, i.e., -230MPa and -160MPa respectively (a 30.4% difference). This is the expected trend as was proposed by Ding *et al.*, (2020). When assessing these plots for both the Test [2]a and Test [2]b samples, the medium level depth of cut of 1mm was utilised, whilst $V_s$ and $V_w$ were held constant as 20m.s$^{-1}$ and 150mm.min$^{-1}$ respectively. Moreover, as the samples were taken at the beginning and end of the grinding pass of the same test, higher compressive stresses were found at the location along the pass which observed the lowest workpiece temperature, before moving towards an $\approx$+20MPa in this test case. It can also be stated that the residual stresses detailed in the previous figures are a result of highly complex thermomechanical loading (Fergani, 2014).

Evaluating the relationship found regarding Test [8], the same compressive residual principal stress trace is found up to approximately 30$\mu$m into the test piece, at which point tensile stresses are observed, reaching a maximum of +135MPa. Additionally, very high compressive stresses are observable towards the surface of the workpiece, before generally becoming tensile further into the workpiece subsurface. This is an interesting result and poses the question what the trace would be beyond a 500$\mu$m depth. This relationship is to be expected due to the highest workpiece temperatures being observed during this test (approximately 800°C), with peak tensile residual stresses being a function of workpiece temperature as found by Fergani *et al.*, (2014). When assessing the theory of how residual stresses are formed during machining processes, three separate mechanisms are noted: namely, via thermal expansion and contraction, phase transformation and plastic deformation. In these test cases, all three mechanisms are apparent, with Test [8] having the greatest levels of plastic deformation as a result of significant workpiece temperature (due to the deepest 2mm depth of cut being used). This is also a key component for the high residual stresses occurring. This level of tensile residual stress is significant and

should be noted as a key finding from this study due to tensile residual stresses having a highly negative influence on a component's stiffness, corrosion resistance, fatigue strength and in-service lifespan (Marogu & Jin, 2017). This finding suggests that when using more aggressive grinding parameters such as those used for Test [8], subsequent suitable heat treatment should be considered, as even at depths above 500$\mu$m beneath the ground surface, residual tensile stresses remain at magnitudes +90MPa. Fig 6.35 additionally summarises the compressive and tensile residual principal stresses across the range of depths of cut analysed.

When assessing the principal stresses found transversally to the grinding direction as presented in Fig 6.37, a similar trend is observed as previously. During Test [1], where the minimum 0.3mm depth of cut was utilised, an initial high residual tensile stress of +170MPa was found, before being observed to reduce to approximately 0MPa at 50$\mu$m into the sample, 25$\mu$m shallower than in the axially ground direction. Additionally, a lower residual tensile stress was observed within the transversal direction when compared to the axial grinding direction (+360MPa and +175MPa respectively; a 51.3% difference). This lower residual tensile stress in the transverse direction compared to the axial direction indicates that the workpiece temperature was lower radially into the workpiece from the cutting plane than axially and is certainly the expected result based on the workpiece temperatures discussed previously. The principal stress data obtained from both the Test [2]a and Test [2]b samples indicates a similar response when comparing the axial responses. Peak compressive residual stresses reached a maximum of -220MPa and -210MPa for the beginning and end locations of the pass respectively. Finally, even greater compressive residual stresses were observed during Test [8] of -350MPa before increasing significantly to a residual tensile stress of +290MPa at 50$\mu$m into the sample. This is greater than the +144MPa tensile stress observed in the axial direction, indicating an increase of 50.3%. This result suggests that more aggressive grinding parameters which result in higher workpiece temperatures not only cause higher unwanted residual tensile stresses in components, but for this test case, the residual tensile stress was significantly higher in the transverse direction. This can be explained via residual stress being a function of both $F_N$ and $F_T$, whereby an increase in $F_T$

results in an increase in unwanted residual tensile stress. However, the inverse relationship can be observed across the cutting force plots for Test [1] and Test [2] presented in this thesis. These findings are also complementary to other works, such as Ding *et al.*, (2020), who found higher residual compressive stresses in the axial direction than transversally.

When addressing the residual stress profiles obtained from the grinding tests, Test 8 observed high tensile residual stresses induced extremely deep into the workpiece. This is to be expected as Test 8 used a significant depth of cut (resulting in a high workpiece temperature) when compared to Test 1 and Test 2 data which observed shallow subsurface damage depths. However, the temperature increase could also be attributed to grinding wheel wear resulting from mechanical and thermal loading and physicochemical wear (Sisodiya, Viswanathan and Dinakaran, 2016). Once blunting of the grinding wheel occurs, the grinding tooling's cutting face becomes smoother than when the tooling is new and/or been properly dressed to resharpen the abrasive grains (Linke and Klocke, 2010; Baseri *et al.*, 2008a; Baseri *et al.*, 2008b). This results in a larger contact area, i.e., grinding zone, and an increase in temperature transferred to the workpiece. Higher workpiece temperatures also can be a result of the chip formations from the machining process becoming fixated *in situ* within the exposed grinding wheel's porosity after undergoing grain fracture due to fatigue failure of the abrasive grains in the wheel's matrix from high mechanical loading (Linke, 2015). SiC is also more friable than other conventional grinding wheels such as $Al_2O_3$ which results in an increased likelihood of grain fracture occurring; a factor that can also be explained by its increased hardness value. Once the chips are imbedded in the grinding wheel, increased depths of subsurface damage are thus observable. This phenomenon is therefore more enhanced when using the more abusive grinding parameters. However, the author believes that the more likely explanation for the increased residual stresses is due to the wheel's material properties and the grinding parameters evaluated than wheel wear as intermittent dressing between passes was conducted to ensure a sharp a wheel as possible. It can be suggested that post-processing of Ti-6Al-4V workpieces should undergo a form of conventional stress relief such as annealing or normalizing (Rae and Rahimi, 2018) or more novel methods such as Thermal Vibratory Stress Relief (TVSR) processes as reported by

Gao *et al.*, (2022), who applied the process to Ti-6Al-4V. Results indicated a 45% decrease in tensile residual stresses when compared to Vibratory Stress Relief (VSR) alone.

Although residual stresses appear highly pronounced within Test 8, it has been reported that the feed rate variable has little influence over the result, with depth of cut, sparkout, wheel wear and the mode of dressing utilised being more influential during cylindrical grinding operations (Capello and Semeraro, 2002). Again, this would explain why high tensile residual stresses are observed during the test at deeper subsurface depths. Additionally, higher wheel wear also induces unwanted tensile residual stresses, whilst lower wheel wear rates induce compressive residual stresses. This is further presented for Test 8 in Fig 6.34 and Fig 6.37. Additionally, high grinding temperatures can cause thermal damage to the cutting tool, which can increase the frictional forces between the wheel and the workpiece, leading to higher cutting forces as observed during Test [8] where aggressive grinding parameters were assessed. This ultimately will have a negative influence over the induced tensile residual stresses at greater subsurface depths as observed in Fig 6.34 and Fig 6.37 which details the response in the axial and transverse directions respectively. Again, this trend was reported on by Malkin (1989). Similar results have also been reported by Sai *et al.,* (2015) who proposed that increases in cutting forces results in an increase in unwanted residual stresses. Therefore, it's important to control grinding temperature to ensure optimal cutting conditions and prevent excessive wear and damage to the grinding wheel.

Concluding, Fig 6.38 summarises the associated compressive and tensile residual stresses induced within each sample across the range of depths of cut analysed in the transverse direction. Finally, for completeness, Fig 6.39 details the residual shear stresses ($\tau_{13}$) obtained for all four samples tested, whilst Fig 6.40 indicates the associated compressive and tensile components of those shear stresses for all three depths of cut analysed.

# Chapter 7

# Dimensional Analysis Numerical Models

## 7.1 Results

### 7.1.1 Peak Workpiece Temperature

Here, the numerical calculations of the Buckingham-$\pi$ groups for predicting changes in the peak workpiece temperature as a function of feed rate, wheel speed and depth of cut are presented. Table 7.1 details the variables and base dimensions used for the analysis.

$$\Delta \mathrm{T} = f\ (V_w;\ V_s;\ a;\ c_w;\ \lambda_w;\ \tau_w;\ \lambda_s;\ c_s;\ \tau_s)$$

**Table 7.1:** Variables used for Buckingham-$\pi$ Group Derivations

| **Variable** | $\Delta$T | $V_w$ | $a$ | $V_s$ | $c_w$ |
|---|---|---|---|---|---|
| **Dimension** | $\theta_1$ | $LT_1^{-1}$ | $L$ | $T_1^{-1}$ | $L^2T_1^{-2}\theta_1^{-1}$ |
| **Variable** | $\lambda_w$ | $\tau_w$ | $c_s$ | $\lambda_s$ | $\tau_s$ |
| **Dimension** | $MLT_1^{-3}\theta_1^{-1}$ | $ML^{-1}T_1^{-2}$ | $L^2.T_1^{-2}\theta_1^{-1}$ | $MLT_1^{-3}\theta_1^{-1}$ | $ML^{-1}T_1^{-2}$ |

Therefore, the number of fundamental dimensions, n, = 4 [$M$;$L$;$T_1$;$\theta_1$].

The number of variables, m, = 10 [$\theta_1$; $LT_1^{-1}$; $L$; $T_1^{-1}$; $L^2T_1^{-2}\theta_1^{-1}$; $MLT_1^{-3}\theta_1^{-1}$; $ML^{-1}T_1^{-2}$; $L^2.T_1^{-2}\theta_1^{-1}$; $MLT_1^{-3}\theta_1^{-1}$; $ML^{-1}T_1^{-2}$].

Using the expression to calculate the number of Buckingham-$\pi$ groups, r = m - n; $\Rightarrow$ r = 10 – 4 = 6, and so six Buckingham-$\pi$ groups.

To ensure the relationship between $\Delta$T and $V_w$ can be determined, $\Delta$T and $V_w$ are kept separate from one another in $\pi_1$ Group. Therefore $\pi_1 = [a; V_s; c_w; \lambda_w]$ for $[L, T_1, \theta_1, M]$, respectively. This can be expressed as in Eqn. 4.1;

$$\pi_1 = [a^a.{V_s}^b.{c_w}^c.\lambda_w^d].\Delta T \qquad \text{(Eqn. 4.1)}$$

Therefore, expanding indices, collecting terms and equating indices yields Group Buckingham-$\pi_1$ as presented in Eqn. 4.2;

$$Buckingham - \pi_1 = \frac{T_{Max}.c_w}{a^2{V_s}^2} \qquad \text{(Eqn. 4.2)}$$

Using the same method as before, the remaining five Buckingham-$\pi$ groups were derived. These are also detailed in Table 7.2 for completion.

**Table 7.2:** Derived Buckingham-$\pi$ Groups for Peak Workpiece Temperature using Dimensional Analysis

| Buckingham-$\pi$ Group | Dependent Variable | Equation |
|---|---|---|
| $\pi_1$ | $\Delta$T | $\frac{T_{Max}.c_w}{a^2V_s^2}$ |
| $\pi_2$ | $V_w$ | $\frac{V_w}{aV_s}$ |
| $\pi_3$ | $\tau_w$ | $\frac{\tau_w c_w}{V_s \lambda_w}$ |
| $\pi_4$ | $c_w$ | $\frac{c_s}{c_w}$ |
| $\pi_5$ | $\lambda_s$ | $\frac{\lambda_s}{\lambda_w}$ |
| $\pi_6$ | $\tau_s$ | $\frac{\tau_s.c_w}{V_s \lambda_w}$ |

From these Buckingham-$\pi$ group derivations, the final form for peak workpiece temperature can therefore be expressed using the power law as presented in Eqn. 4.3.

$$\pi_1 = k_{constant}[\pi_2^{c2}.\pi_3^{c3}.\pi_4^{c4}.\pi_5^{c5}.\pi_6^{c6}] \qquad \text{(Eqn. 4.3)}$$

However, Eqn. 4.3 can therefore be expressed in log form as detailed by Eqn. 4.4:

$$log\pi_1 = logk_{constant} + c_2 log\pi_2 + c_3 log\pi_3 + c_4 log\pi_4 + c_5 log\pi_5 + c_6 log\pi_6 \qquad \text{(Eqn. 4.4)}$$

Furthermore, using regression analysis, the regression equation form of Eqn. 4.4 can be written in the form as presented in Eqn. 4.5;

$$y = k_1 + c_2 A + c_3 B + c_4 C + c_5 D + c_6 E \qquad \text{(Eqn. 4.5)}$$

However, as the experimental test programme only considered three independent variables, i.e., $V_s$, $V_w$ and $a$, this means that Eqn. 4.4 can be reduced to Eqn. 4.6:

$$log\pi_1 = logk_{constant} + c_2 log\pi_2 + c_3 log\pi_3 + c_4 log\pi_4 \quad \text{(Eqn. 4.6)}$$

When using the experimental test workpiece temperature data and applying $\pi_2$, we derive Eqn. 4.7;

$$\pi_1 = k_{constant}[\frac{V_w}{aV_s}]^{c_2} \quad \text{(Eqn. 4.7)}$$

Hence, solving for $k_{constant}$ and $c_2$ using simultaneous equations we can derive Eqn. 4.8 and Eqn. 4.9:

$$130 = k_{constant}[150]^{c_2} \quad \text{(Eqn. 4.8)}$$

and

$$350 = k_{constant}[300]^{c_2} \quad \text{(Eqn. 4.9)}$$

The unknowns become:

$k_{constant} = 0.10107$

and

$c_2 = 1.428$

Substituting theses values back into Eqn. 4.7 yields Eqn. 4.10;

$$\pi_1 = 0.10107[\frac{V_w}{aV_s}]^{1.428} \qquad \text{(Eqn. 4.10)}$$

Henceforth, plotting the empirical temperature data alongside the DA prediction a relationship as presented in Fig 7.1 becomes clearly evident i.e., the dimensional analysis prediction for workpiece temperature when increasing feed rate magnitudes results in an almost perfect, like-for-like, result. Both indicate a positive linear trend, in addition to the DA prediction suggesting identical magnitudes to the experimental data.

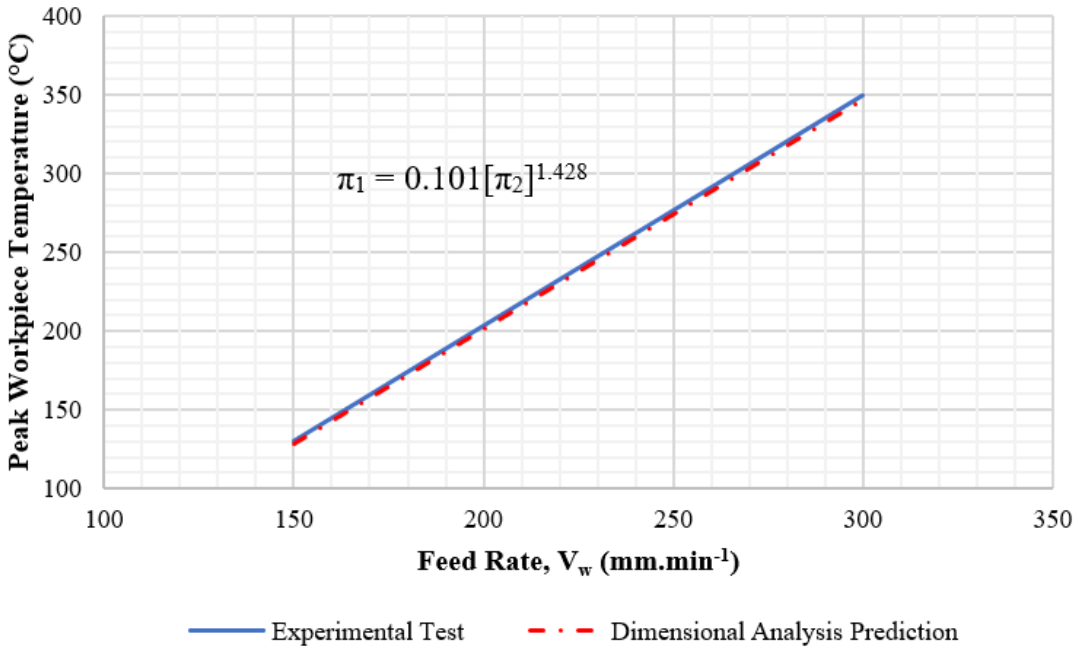



**Figure 7.1:** Dimensional Analysis Workpiece Temperature Prediction Derived Equation ($V_w$ Variable)

Using the same method, the DA prediction for changes in wheel speed and depth of cut are presented in Fig 7.2 and Fig 7.3, respectively. Within Fig 7.2, a similar response regarding DA accuracy is evident, with a clear decrease in workpiece temperature as the wheel speed is increased which matches extremely well with the empirical data.

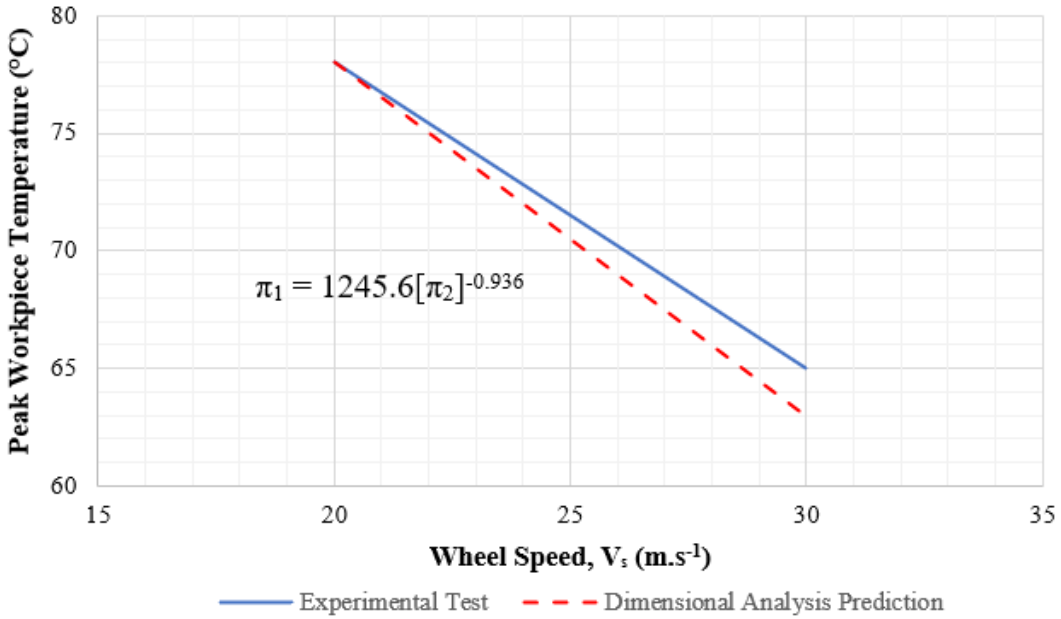



**Figure 7.2:** Dimensional Analysis Workpiece Temperature Prediction Derived Equation ($V_s$ Variable)

Meanwhile, Fig 7.3 indicates a suitable DA prediction when assessing depth of cut increases for workpiece temperature assessment. Again, a linear response is evident, with agreeable magnitudes for workpiece temperature being forecast.

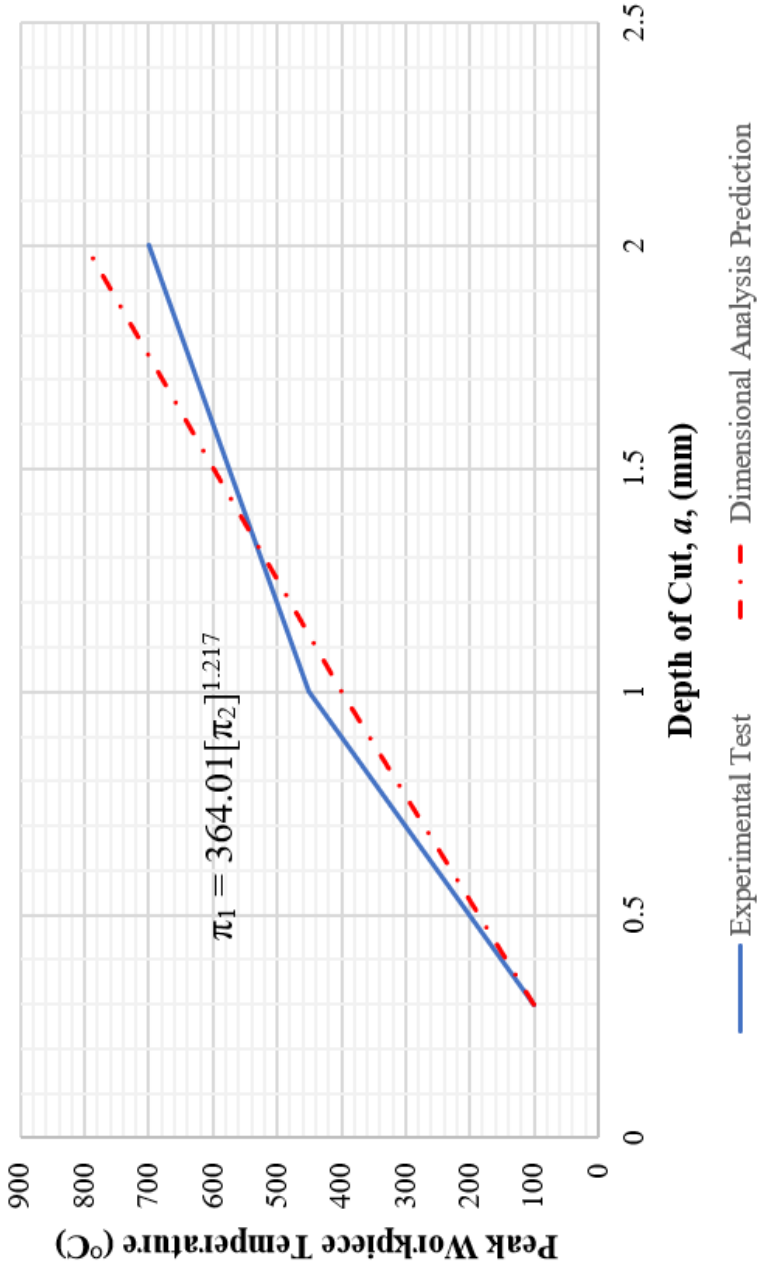



**Figure 7.3:** Dimensional Analysis Workpiece Temperature Prediction Derived Equation ($a$ Variable)

### 7.1.2 Peak Cutting Forces

Here, the numerical calculations of the Buckingham-$\pi$ groups for predicting changes in the peak cutting force as a function of feed rate, wheel speed and depth of cut are presented, with Table 7.3 summarising the base quantities and dimensions for the variables analysed.

$$\Delta F = f(V_w; V_s; a; c_w; \lambda_w; \tau_w; c_s; \lambda_s; \tau_s)$$

**Table 7.3:** Variables used for Buckingham-$\pi$ Group Derivations

| **Variable** | $\Delta$F | $V_w$ | $a$ | $V_s$ | $c_w$ |
|---|---|---|---|---|---|
| **Dimension** | $MLT_1^{-2}$ | $LT_1^{-1}$ | $L$ | $T_1^{-1}$ | $L^2T_1^{-2}\theta_1^{-1}$ |
| **Variable** | $\lambda_w$ | $\tau_w$ | $c_s$ | $\lambda_s$ | $\tau_s$ |
| **Dimension** | $MLT_1^{-3}\theta_1^{-1}$ | $ML^{-1}T_1^{-2}$ | $L^2.T_1^{-2}\theta_1^{-1}$ | $MLT_1^{-3}\theta_1^{-1}$ | $ML^{-1}T_1^{-2}$ |

Therefore, the number of fundamental dimensions, n, = 4 [$M$;$L$;$T_1$;$\theta_1$].

The number of variables, m, = 10 [$MLT_1^{-2}$; $LT_1^{-1}$; $L$; $T_1^{-1}$; $L^2T_1^{-2}\theta_1^{-1}$; $MLT_1^{-3}\theta_1^{-1}$; $ML^{-1}T_1^{-2}$; $L^2.T_1^{-2}\theta_1^{-1}$; $MLT_1^{-3}\theta_1^{-1}$; $ML^{-1}T_1^{-2}$].

Using the expression to calculate the number of Buckingham-$\pi$ groups, r = m - n; $\Rightarrow$ r = 10 – 4 = 6, and so six Buckingham-$\pi$ groups.

To ensure the relationship between $\Delta$F and $V_w$ can be determined, $\Delta$F and $V_w$ are kept separate from one another in $\pi_1$ Group. Therefore: $\pi_1$ = [$a$; $V_s$; $c_w$; $\tau_w$] for [$L$, $T_1$, $\theta_1$, $M$], respectively. This can be expressed as in Eqn. 4.11

$$\pi_1 = [a^a.{V_s}^b.{c_w}^c.\tau_w^d].\Delta F \qquad \text{(Eqn. 4.11)}$$

Expanding indices, collecting terms and equating indices yields Group Buckingham-$\pi_1$ as is shown in Eqn. 4.12;

$$Buckingham - \pi_1 = \frac{F_{Max}}{a^2 \tau_w} \qquad \text{(Eqn. 4.12)}$$

Using the same method as previously, the remaining five Buckingham-$\pi$ groups were derived and are presented in Table 7.4. By applying the same analysis approach used for assessing the validity of the workpiece temperature predictions, the cutting force responses were also evaluated. Fig 7.4, Fig 7.5 and Fig 7.6 detail these results.

**Table 7.4:** Derived Buckingham-$\pi$ Groups for Peak Cutting Force using Dimensional Analysis

| Buckingham-$\pi$ Group | Dependent Variable | Equation |
|---|---|---|
| $\pi_1$ | $\Delta$F | $\frac{F_{Max}}{a^2 \tau_w}$ |
| $\pi_2$ | $V_w$ | $\frac{V_w}{aV_s}$ |
| $\pi_3$ | $\tau_w$ | $\frac{\tau_w c_w}{V_s \lambda_w}$ |
| $\pi_4$ | $c_w$ | $\frac{\tau_s}{\tau_w}$ |
| $\pi_5$ | $\lambda_s$ | $\frac{\lambda_s}{\lambda_w}$ |
| $\pi_6$ | $\tau_s$ | $\frac{\tau_s . c_w}{V_s \lambda_w}$ |

Fig 7.4 presents the dimensional analysis prediction for total cutting force when increasing the feed rate value. The experimental test data is also included for comparison. A good prediction from the DA can be determined from the figure, with the numerical approach indicating an almost identical trend, with only a small deviation in predicted magnitude.

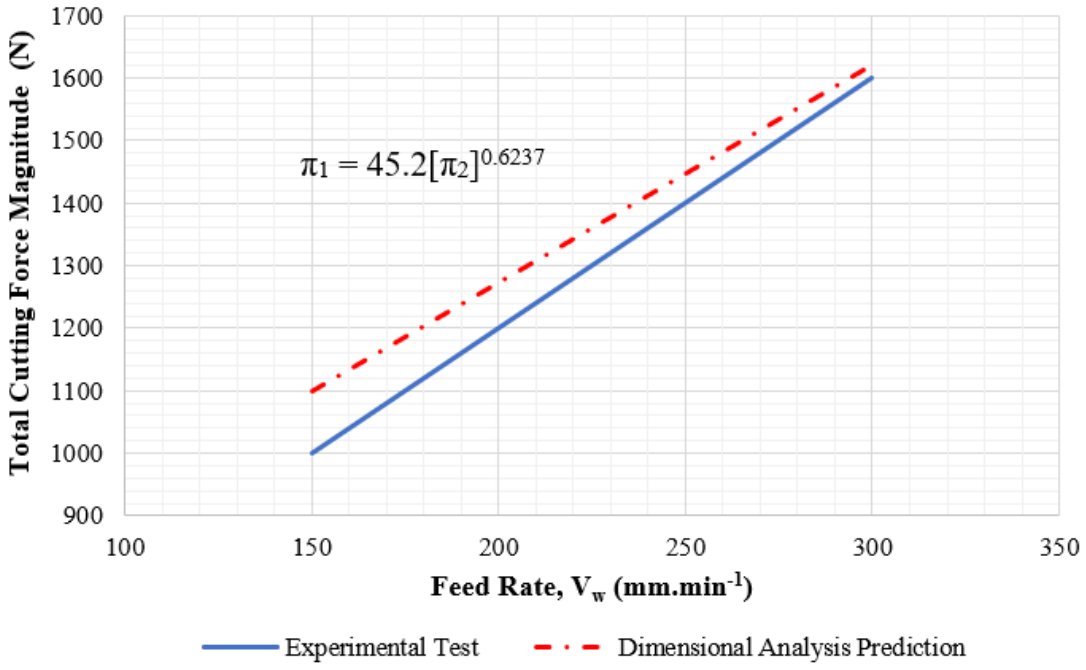



**Figure 7.4:** Dimensional Analysis Cutting Force Prediction Derived Equation ($V_w$ Variable)

Fig 7.5 outlines a comparison between the experimental cutting force magnitudes with the DA prediction of cutting force for increases in wheel speed. An excellent correlation between the data sets is again evident, adding further confidence to the methodology of applying dimensional analysis for predictive modelling.

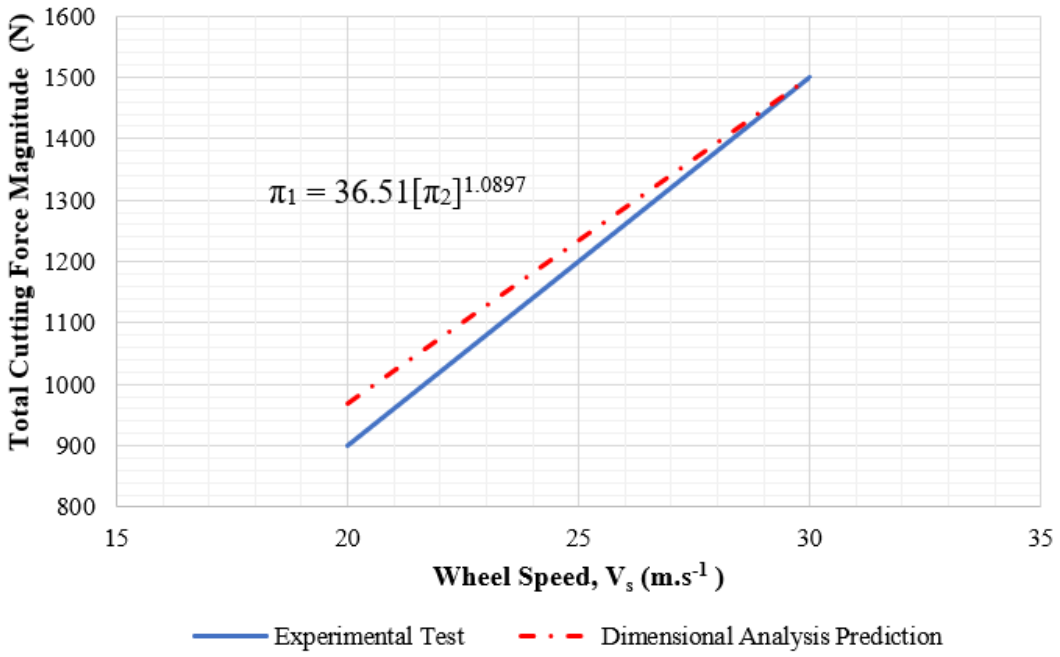



**Figure 7.5:** Dimensional Analysis Cutting Force Prediction Derived Equation ($V_s$ Variable)

Fig 7.6 presents the cutting force dimensional analysis prediction when plotted against the experimental data in regards to increases in depth of cut value. Again, an excellent comparison between the data sets can be readily determined, with only marginal deviations in predicted force magnitude when using larger depths of cut being evident.

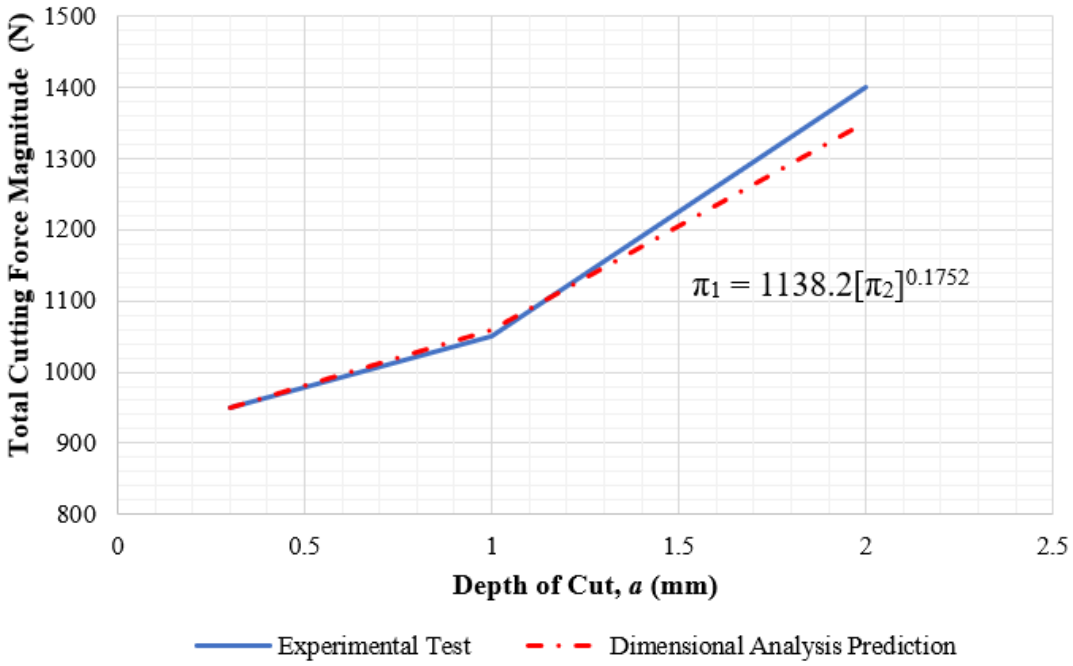



**Figure 7.6:** Dimensional Analysis Cutting Force Prediction Derived Equation ($a$ Variable)

## 7.2 Discussion

Once the experimental tests had been analysed, a subsequent DA of the same grinding test programme outlined in Table 3.2 was also undertaken in an attempt to verify the test programme further. This was evaluated to determine if the output variables requested (i.e., peak workpiece temperature and cutting forces) could be predicted using higher/lower degrees of magnitude. The results of the preliminary peak workpiece temperature response across a range of $V_w$, $V_s$ and $a$ values are presented in Fig 7.1, Fig 7.2 and Fig 7.3 respectively. In terms of the approach applied, with both the workpiece temperature and cutting force upon the tool being the required output, the six Buckingham-$\pi$ groups were derived using the Exponent Method for both responses, with the base quantities in relation to the analysis of grinding temperature and cutting forces being Mass, $(M)$, Length, $(L)$, Time, $(T_1)$ and Temperature $(\theta_1)$. Additionally, the variables considered when deriving the workpiece temperature and cutting force Buckingham-$\pi$ groups were feed rate, $(V_w)$, depth of cut, $(a)$, wheel speed, $(V_s)$, the specific heat capacity of the workpiece, $(c_w)$, the thermal conductivity of the workpiece, $(\lambda_w)$, the shear strength of the workpiece, $(\tau_w)$, the specific heat capacity of the wheel, $(c_s)$, the shear strength of the wheel, $(\tau_s)$ and the thermal conductivity of the wheel $(\lambda_s)$. These variables are summarised in Table 4.5. Once the DA had been undertaken, a basic power-law evaluation had to be conducted before a regression analysis on the data was able to be determined. This subsequently allowed for trends to be plotted comparing the predicted DA data for both peak workpiece temperature and cutting forces when observing changes in feed rate, wheel speed and depth of cut against that of the experimental data pertaining to the same variables.

### 7.2.1 Peak Workpiece Temperature

It can be clearly observed that there is a negative trend of workpiece temperature when plotted against increasing feed rates, with a decrease of 20.8% when increasing the feed rate from 150mm.min$^{-1}$ to 300mm.min$^{-1}$. This result was obtained from the experimental trials and further ratified by the DA of the data set. As the DA predictions were almost identical to the experimental trial results, it can be claimed that this trend is an accurate critique of the grinding system, and should be excepted as standard.

Using the same method, the influence of $V_s$ on workpiece temperature was determined as detailed in Fig 7.2. Again, in a similar manner to the comparative feed rate data, the DA predictions appear to provide an excellent comparable data set. Here, an almost like-for-like relationship can be derived, with the workpiece temperature appearing to reduce by 37.5% when increasing wheel speed from 20m.s$^{-1}$ to 30m.s$^{-1}$. From this result, it is advised that further work for assessing workpiece temperature and feed rate when grinding should be initiated by applying the DA and the Buckingham-$\pi$ method as a first point of analysis.

Finally, when the DA method was applied for a depth of cut trend, a highly similar result became apparent as shown in Fig 7.3. Although not a perfect, like-for-like trend as was the case with both the feed rate and wheel speed predictions, it certainly provided an adequate response when assessing changes in workpiece temperature as the depth of cut was increased. When compared against the experimental trial data, the DA predictions indicated a 90.7% increase as the depth of cut was increased from 0.3mm to 2mm, whilst the experimental trial found an 88.6% increase across the same depth of cut range; a variation of less than 5%. These disparities in the data sets are easily within the allowable range of approximated error and therefore DA can be deemed a powerful approach for predicting changes in workpiece temperature when increasing the depth of cut whilst grinding. This relationship has been reported in the literature, which adds further evidence to the trial data obtained, and the predictive DA approach used throughout this comparison for predicting changes in workpiece temperature when grinding more generally (Mahamani and Jawahar, 2018).

### 7.2.2 Peak Cutting Forces

When assessing the DA approach for modelling the cutting force response with changes in feed rate, a clear and accurate representation is observed. Again, an almost 'like for like' relationship of the two independent data sets present themselves, adding further credence to the DA modelling method and the experimental data gathered. Although little work has been conducted when applying DA to machining processes, this trend has been presented

in the literature as published by Phate and Toney (2019), Kumar and Kamba (2010) and Alauddin and Zhang (2007).

When analysing the data gleaned from the experimental test study, the DA predictions relating to wheel speed as demonstrated by Fig 7.5 appear to offer an excellent method for being able to predict both the trend and actual magnitudes gathered from the physical test. This is again unsurprising as all the changes thus far analysed, i.e., workpiece temperature for all altered parameters indicated an excellent correlation as the method utilises a base quantity approach. These results prove that DA can and should be applied more broadly when attempting to model and assess machining processes.

Finally, when assessing the DA predictions for the depth of cut variable, a reliable relationship presents itself as demonstrated by Fig 7.6. Although not as reliable as the predictions for feed rate and wheel speed, a solid and sound trend and order of magnitude were attained when using the analysis method, with a less than 10% difference in experimental and DA predicted value from the data compared and analysed in this section. DA therefore clearly offers a powerful analysis tool from which to investigate mechanical systems such as machining. These findings have many highly interesting ramifications for DA being applied to the grinding process moving forward. This is due to the highly complex nature of grinding cutting mechanics, with any form of simplification or deriving predictive models for workpiece temperature and cutting forces being highly valued.

# Chapter 8

# Overall Discussion and Conclusions

The overall aim of the project was to assess the grindability of Ti-6Al-4V, with the specific objective to experimentally evaluate the peak workpiece temperature. Additionally, the development of a process model for predicting both workpiece temperature and cutting forces via the Dimensional Analysis method was undertaken to further substantiate the experimental data obtained. These aims were achieved as demonstrated via this thesis. Successful experimental testing and measurement of workpiece temperature and cutting forces were undertaken, as were the corresponding DA prediction models of the grinding temperature and the associated cuttings forces being derived. Moreover, the objectives which were stated at the beginning of this thesis are thus assessed against the work combined herein, with conclusions and recommendations based on the preceding work.

**1. Conduct a comprehensive literature review of relevant past research on grinding of Ti-6Al-4V alloy including both experimental based studies and simulation; specifically, those relating to workpiece temperature and cutting force predictions and measurement.**

This objective was achieved. This thesis contains an accurate and up to date critical assessment of approximately two hundred and fifty references from academic and industrial sources that relate to well-established grinding mechanics; traditional and recent advances of the grinding process such as CFG and VIPER; workpiece temperature and

cutting force measurement and data acquisition instrumentation systems and numerical approaches (including current limitations) for predicting workpiece temperature and associated cutting forces when analysing the Ti-6Al-4V alloy. The review found notable areas for improvement in acquisition of workpiece temperature data when grinding Ti-6Al-4V due to it being one of the more challenging materials to grind. Additionally, it has subsequent use amongst temperature critical components and its inherent low thermal conductivity value (approximately 6.9W.m$^{-1}$.K$^{-1}$) are also critical to this machining issue. If the workpiece temperatures for hard to machine materials can therefore be determined, then that sets the limits for additional research to be conducted. The literature review provided significant scope for improvement in the assessment of grinding wheel abrasive grits, both for industrial wheel production efficiency and grinding surface integrity improvements.

**2. Investigation of the peak workpiece temperature and cutting forces via a valid test program and a novel thermocouple placement configuration.**

Physical testing was conducted using Ti-6Al-4V workpieces to assess the peak workpiece temperatures and cutting forces involved whilst grinding this particular alloy. A variety of different cutting conditions were considered to determine how these responses altered when going from rough, larger stock removal processes to fine surface finishing. The test programme consisted of using a novel, multiple in-series, thermocouple configuration to ensure an accurate peak workpiece temperature response could be determined. During the experimental phase, the author was able to prove beyond reasonable doubt that workpiece temperature readings using only a singular thermocouple is insufficient for purpose. Configurations of at least three thermocouples in-series are needed as large peaks in workpiece temperature are observed at the final thermocouple location due to a build-up of ambient heat in the workpiece, as well as film boiling of the coolant. The maximum workpiece temperature and the associated cutting forces were observed to be almost identical to those predicted via the DA method. This indicates that the DA method has been under-represented and utilised when assessing the grinding process, and to the machining research arena more broadly. The author therefore concludes that DA could have

a vital part to play for future machining research and should be utilised more frequently as this thesis has proven it a powerful tool for analysis.

### 3. Effect of Workpiece Temperature and Cutting Forces on Surface Integrity

Findings from the experimental test programme displayed a clear, negative increase in workpiece temperature and cutting force when the depth of cut was increased. Similarly, the same relationship was observed when the feed rate was increased. However, the inverse was observed when the wheel speed was increased, with a positive decrease being observed. This indicates that when wishing to improve surface integrity performance when grinding Ti-6Al-4V, i.e., surface roughness, microhardness etc., higher wheel speeds would prove a better approach. This result was confirmed by the surface roughness plots presented in this thesis adding validity to this claim. Additionally, the $G$-ratio was observed to be significantly higher when using less aggressive grinding parameters than when using more aggressive grinding parameters, indicating reduced wheel wear during finishing operations such as surface grinding than for SRG operations such as CFG. More aggressive grinding parameters resulted in higher levels of plastic deformation within the workpiece, resulting in a more compromised part. This result was further ratified by the individual thermocouple placement assessment, whereby the third thermocouple in the series was found to subsequently have the higher microhardness value. These results therefore indicate that, where possible, lower depths of cut, faster wheel speeds and slower feed rates should be used to reduce workpiece temperature. Additionally, lower cutting forces were observed when using shallower depths of cut, slower feed rates and higher wheel speeds. Using these grinding conditions would thus result in an improved surface integrity condition for safety-critical Ti-6Al-4V components whilst being manufactured.

**4. Development of new Buckingham-$\pi$ predictive models to evaluate the grinding process regarding peak workpiece temperatures and cutting forces under a wealth of operating conditions.**

After the experimental test programme had been conducted, a theoretical evaluation via Dimensional Analysis using the experimental data was conducted to determine if predictive models for both workpiece temperature and cutting forces could be derived. From the data presented in this thesis, this objective was met comfortably, with the twelve new and innovative predictive models derived by the author being highly representative of the grinding process for both workpiece temperature and cutting force when assessed across ranges of depth of cut, feed rate and wheel speed. When assessing both feed rate and wheel speed, the predictive DA approach was found to be within <5% error of the experimental data, indicating that the DA method should be the first analytical approach utilised when wishing to evaluate the grinding process when assessing workpiece temperature. The depth of cut prediction also indicated a good response, albeit one which varied more than the feed rate and wheel speed prediction. Here the variance appeared to increase as the depth of cut increased, with 11.1% difference at $a$ = 1mm and 12.5% at $a$ = 2mm. A highly identical trend was observed for changes in wheel speed, feed rate and depth of cut when analysing the cutting force response. Here an 8.3% error was observed between the DA prediction and experimental test for the feed rate variable, whilst less than 5% variance was observed for the wheel speed and depth of cut variable. From this study, therefore, it can be concluded that Dimensional Analysis offers an excellent solution for predicting accurate magnitudes for workpiece temperature and the associated cutting forces acting on the grinding wheel tooling during machining.

**5. Analysis, implementation and integration of state-of-the-art data logging equipment into the manufacturing architecture available at the University of Birmingham.**

The author was able to utilise state-of-the-art data logging equipment after undertaking and assessing thermocouple implantation within Ti-6Al-4V workpieces for temperature acquisition. This form of data retrieval is rarely seen within grinding research as temperature measurements of any form are rare. The need for fast response time data loggers is evident when wishing to ensure accurate temperature readings and is certainly a consideration that any future researchers in the area must contemplate. Additionally, the author was aware of the limitations of the thermocouple and OMEGA data logger set up. Due to the inherent nature of the thermocouple, faster feed rate temperature measurements might prove difficult. As such, the author additionally developed a Simulink Laplace Transform for application in any post-processing of temperature data from any further experimental testing. For the slow feed rates examined in this thesis, however, the set up was proven to suffice through several boiling water temperature trials outlined in Appendix C.

# Chapter 9

# Suggestions for Further Work

Here, the author proposes some logical and suggestive avenues to expand upon the current work presented.

**1. Expansion of the experimental test plan developed.**

The thermocouple configuration that was developed by the author which considered three thermocouples in-series has opened up some very interesting questions to be answered. Developing a more expansive test plan which considers further aerospace materials such as Inconel 718, or CMSX-4, for example, would allow a host of opportunities for exciting research. Additionally, the testing of a wider range of the parameters discussed in this thesis could be proposed including $Al_2O_3$, diamond or cBN wheels.

**2. Expansion of the Dimensional Analysis approach to the grinding process.**

This thesis considered the peak workpiece temperature and cutting forces as the requested outputs when deriving the Buckingham-$\pi$ equations. There also remains further scope to apply this method for being able to predict surface integrity responses. As such, additional Buckingham-$\pi$ groups could be derived to predict surface roughness or residual stresses for example. Such research would add additional knowledge to the

literature and allow for further advances in grinding research to be made without the need for time-intensive testing to be conducted at the initial point of study.

**3. Development of a 'Direct Injection' approach for applying thermal cements.**

During the physical testing and subsequent analysis, anomalies in the data were surmised by the author to be one arising from issues regarding thermocouple implantation; in particular, being able to apply the thermal cement consistently and accurately. The author proposes research be conducted into the development of a direct injection approach, i.e., via a nozzle under an applied pressure thus allowing for a more highly precise application of the cement into the thermocouple hole. If this mode of application were to be developed, it would allow for a cleaner and more consistent application method of the thermal cement, thus enabling a more consistent outcome in workpiece temperature response.

**4. Optimisation of the thermocouple pilot hole.**

Prior to the thermocouple embedding process, two holes were manufactured via carbide drills. The first was a pilot hole for the thermocouple node, whilst the second was a larger, relief hole for the thermal cement. If both this and recommendation three can be developed in tandem, then any potential failure of the cement could be reduced, and so improvements in the experimental system could developed and improved upon thus minimising any outliers in the data collected.

**5. Apply the developed Laplace Transform to the thermocouple temperature responses.**

Due to the thermocouples used having an inherent lag in their ability to register a response, independently of the data logger used, the author developed a Laplace Transform in Simulink to filter the data to ensure an accurate reading when undertaking experimental work where high feed rates are utilised, i.e., $V_w > 300\text{mm.min}^{-1}$. This approach is presented in Appendix C. The data presented herein, and due to time constraints, however, did not need this Laplace Transform due to testing only considering slower feed rates, i.e., $150\text{mm.min}^{-1} < V_w < 300\text{mm.min}^{-1}$. The author proposes that any future results obtained from the data retrieval system where high feed rates are utilised, i.e., $V_w > 300\text{mm.min}^{-1}$, apply such an approach post data acquisition.

# Chapter 10

# References

3M solutions. (2015) http://solutions.3m.com [online] Available from *http* : *//solutions.3m.com/wps/portal/3M/en*$_U$*S/3MIndustrial/Abrasives/Products/Abrasives−Product − Catalog/Abrasive − Wheels*, Accessed [10th March 2015].

Abdolahi, A., Risto, M., and Haas, R. (2018) 'Non-Dimensional Analysis and optimization of EDM Drilling process, using an innovative function', *Procedia CIRP*, 68, pp. 248-253.

Alagan, N., Hoier, P., Beno, T., Klement, U., and Wretland, A. (2020) 'Coolant boiling and cavitation wear – a new tool wear mechanism on WC tools in machining alloy 718 with high-pressure coolant', *Wear*, 452-453, Article Number: 203284.

Alagumurthi, N., Palaniradja, K., and Soundararajan, V. (2006) 'Optimization of Grinding Process Through Design of Experiment (DOE) — A Comparative Study', *Materials and Manufacturing Processes*, 21 (1), pp. 19-21.

Alauddin, M., and Zhang, L.C. (2007) 'Grinding force modelling: combining dimensional analysis with response surface modelling', *International Journal of Technology and Management*, 12 (1-3), pp. 299-310.

Alexandre, F., Lopes, W., Ferreira, F., Dotto, F., Aguiar, P., and Bianchi, E. (2018) 'Chatter Vibration Monitoring in the Surface Grinding Process through Digital Signal Process of Acceleration Signal', *Proceedings*, 2 (3), pp. 1-5.

Alhama, F., and Madrid, C. (2007) 'Discriminated Dimensional Analysis versus Classic Dimensional Analysis and Application to Heat Transfer and Fluid Dynamics', *Chinese Journal of Chemical Engineering*, 15 (5), pp. 626-631.

Altintas, Y., and Weck, M. (2004) 'Chatter stability of metal cutting and grinding', *CIRP Annals of Manufacturing Technology*, 53 (2), pp. 619–642.

Amritkar, A., Prakash, C., and Kulkarni, A. (2012) 'Development of temperature measurement setup for machining', *World Journal of Science and Technology*, 2 (4), pp. 15-19.

Anderson, D., Warkentin, A., and Bauer, R. (2008a) 'Comparison of numerically and analytically predicted contact temperatures in shallow and deep feed dry grinding with infrared measurements', *Journal of Materials Processing Technology*, 204, pp. 320-328.

Anderson, D., Warkentin, A., and Bauer, R. (2008b) 'Experimental validation of numerical thermal models for dry grinding', *Journal of Materials Processing Technology*, 204, pp. 269-278.

Andrew, C., Howes, T., and Pearce, T. (1985) *Creep Feed Grinding*. United States: Industrial Press Inc.

Anthony, J. (2014) *Design of Experiments for Engineers and Scientists*. 2nd Edition, London, UK: Elsevier.

Ashman, D. (1987) *High-speed Performance of a Hydrostatic Thrust Bearing.* PhD Thesis. Wolverhampton Polytechnic, Wolverhampton, UK.

Aslan, D., and Budak, E. (2014) 'Semi-analytical force model for grinding operations', *Procedia CIRP*, 14, pp. 7-12.

Aspinwall, D., Soo, S.L., Curtis, D.T., and Mantle, A.L. (2007) 'Profiled Superabrasive Grinding Wheels for the Machining of a Nickel Based Superalloy', *Annals of the CIRP*, 56 (1), pp. 335-338.

Assarzadeh, S., and Ghoreishi, M. (2013) 'The Application of Piezoelectric Materials in Machining Processes', in Ebrahimi, F. (ed.) *Piezoelectric Materials and Devices – Practice and Applications*, INTECH: Croatia.

Axinte, D., Stepanian, J., Kong, M., and McGourlay, J (2009) 'Abrasive water-jet turning - An efficient method to profile and dress grinding wheels', *International Journal of Machine Tools and Manufacture*, 40, pp. 351-356.

Badger, J., Murphy, S., and O'Donnell G. (2021) 'Big-and-dull or small and sharp: A comparison of specific energy, wheel wear, surface generation mechanisms and surface characteristics when grinding $Al_2O_3$ and CBN to achieve a given surface roughness', *Journal of Materials Processing Technology*, 288, Article Number: 116825.

Badger, J., and Torrance, A. (2000) 'Burn Awareness', *Cutting Tool Engineering*, 52 (12), pp. 16-19.

Baksa, T., Farsky, J., Hronek, O., and Zetek, M. (2018) 'Impact of Cutting Speed on Grinding Wheel Wear and Cutting Force when Grinding Cermet', *Manufacturing Technology*, 18 (5), pp. 699-703.

Baseri, H., Rezaei, S., Rahimi, A., and Saadat, M. (2008a) 'Analysis of the Disc Dressing Effects on Grinding Performance – Part 1: Simulation of the Disc Dressed Wheel Surface', *Machining Science and Technology: An International Journal*, 12, pp. 183-196.

Baseri, H., Rezaei, S., Rahimi, A., and Saadat, M. (2008b) 'Analysis of the Disc Dressing Effects on Grinding Performance – Part 2: Effects of the Wheel Topographical Parameters on the Specific Energy and Workpiece Surface Roughness', *Machining Science and Technology: An International Journal*, 12, pp. 197-213.

Batako, A., Rowe, W., and Morgan, M. (2005) 'Temperature measurement in high efficiency deep grinding', *International Journal of Machine Tools and Manufacture*, 45, pp. 1231-1245.

Bentley, S., Mantle, A., and Aspinwall, D. (1999) 'The effect of machining on the fatigue strength of a gamma titanium aluminide intermetallic alloy', *Intermetallics*, 7, pp. 967-969.

Bentley. S., Goh, N., and Aspinwall, D. (2001) 'Reciprocating surface grinding of gamma titanium aluminide intermetallic alloy', *Journal of Materials Processing Technology*, 118, pp. 22-28.

Beranoagirre, A., and Lopez de Lacelle, L. (2013) 'Grinding of Gamma TiAl Intermetallic Alloys', *Procedia Engineering*, 63, pp. 489-498.

Bhaduri, D., Soo, S.L., Aspinwall, D., Novovic, D., Harden, P., Bohr, S., and Martin, D. (2012) 'A study on ultrasonic assisted creep feed grinding of nickel based superalloys', *Procedia CIRP*, 1, pp. 359-364.

Bhaduri, D., Soo, S.L., Novovic, D., Aspinwall, D., Harden, P., Waterhouse, C., Bohr, S., Mathieson, A., and Lucas, M. (2013) 'Ultrasonic assisted creep feed grinding of Inconel 718', *Procedia CIRP*, 6, pp. 615-620.

Bhaduri, D., Soo, S., Aspinwall, D., Novovic, D., Bohr, S., Harden, P., and Webster, J. (2017) 'Ultrasonic assisted creep feed grinding of gamma titanium aluminide using conventional and superabrasive wheels', *CIRP Annals*, 66 (1), pp. 341-344.

Bienkowski, K. (1993) 'Coolants and lubricants: part 1 – The Truth'. *Manufacturing Engineering*, 110 (3), pp. 90-96.

Bisacre, F., and Bisacre, G. (1947) 'The Life of Carbide-tipped Turning Tools', *Proceedings of the Institution of Mechanical Engineers*, 157 (1), pp. 452 - 469.

Brehl, D., and Dow, T. (2008) 'Review of vibration assisted grinding', *Precision Engineering*, 2, pp. 153-172.

Brinksmeier, E., Heinzel, C., and Wittmann, M. (1999) 'Friction, Cooling and Lubrication in grinding', *Annals of the CIRP*, 48 (2), pp. 581-598.

Butler-Smith, P., Axinte, D., and Daine, M. (2011) 'Ordered diamond micro-arrays for ultra-precision grinding – An evaluation in Ti-6Al-4V', *International Journal of Machine Tools and Manufacture*, 51, pp. 54-66.

Caggiano, A., and Teti, R. (2013) 'CBN Grinding Performance in Aircraft Engine Components Manufacture', *Procedia CIRP*, 9, pp. 109-114.

Callister, W., and Rethwish. D. (2008) *Materials Science and Engineering: An Introduction.* 8th Edition, New Jersey: John Wiley & Sons Inc.

Capello, E., and Semeraro, Q. (2002) 'Process Parameters and Residual Stresses in Cylindrical Grinding', *Journal of Manufacturing Science and Engineering*, 124 (3), pp. 615-623.

Carslaw, S., and Jaeger, J. (1959). *Conduction of heat in solids.* London: Oxford University Press.

Che-Haron, C.H., and Jawaid, A. (2005) 'The effect of machining on surface integrity of titanium alloy Ti-6% Al-4% V', *Journal of Materials and Processing Technology*, 166, pp. 188-192.

Chen, C., and Feng, Z.M. (2003) 'Effectiveness of laser cleaning for grinding wheel loading', *Key Engineering Materials*, 238-239, pp. 289-294.

Chen, X. (2002) 'The sharpness of grinding wheels: an important measure of grinding behaviour', *Proceedings of the Institute of Mechanical Engineers, Part B: Journal of Manufacture*, 216, pp. 829-832.

Chen, X., and Öpöz, T. (2016) 'Effect of different parameters on grinding efficiency and its monitoring by acoustic emission', *Production & Manufacturing Research*, 4 (1), pp. 190-208.

Chen, M., Lee, Y., Sun, F., and Yang, S. (2004) 'Surface Quality Studies with Respect to Grinding Burn of New Typical Nickel-based Superalloy', *Key Engineering Materials*, 256-260, pp. 233-238.

Chestnut, J.C. (1992) Titanium Aluminides for Aerospace Applications. *Superalloys 1992.* The Minerals, Metals and Materials Society; Warrendale, PA, United States, 20th-24th Sep, pp. 381-389.

Childs, T.H.C., Maekawa, K., Obikawa, T., and Tamane, Y. (2000) *Metal Machining – Theory and Applications*. London: Arnold.

Childs, T. (2013) *Encyclopaedia of Tribology*. Boston, Springer Link.

Chitali, A., and Gupta R. (2007) *Product Design and Manufacturing*. India: Prentice Hall of India.

Conradie, P.J.T., Oosthuizen, G.A., Treurnicht, N.F., and Al Shaalane, A. (2012) 'Overview of work piece temperature measurement techniques for machining Ti6Al4V', *South African Journal of Industrial Engineering*, 23 (2), pp. 116-130.

Cook, R.D., Malkus, D., Plesha, M., and Witt, R. (2007) *Concepts and Applications of Finite Element Analysis*. New York: John Wiley & Sons.

Cool Grind Nozzles (2020): Available at [https://cool-grind.com/collections].

Cotton, J.D., Clark, L.P., and Phelps, H.R. (2002) 'Titanium Alloys on the F-22 Fighter Airframe', *Advanced Materials & Processes*, 160 (5) pp. 25–28.

Curtis, D., Aspinwall, D., Soo, S.L., Kitchin, D., and Mantle, A. (2007) 'In-process electrical discharge dressing (IEDD) of metal bonded superabrasive grinding wheels', *Proceedings of the 15th International Symposium on Electro-Machining (ISEMXV)*, Pittsburgh, USA. Apr. 23rd-27th.

Dai, X., Zhuang, K., Pu, D., Zhang, W., and Ding, H. (2020) 'An Investigation of the Work Hardening Behavior in Interrupted Cutting Inconel 718 under Cryogenic Conditions', *Materials*, 13 (9), pp. 1-15.

Davies, M., Ueda, T., M'Saoubi, R., Mullany, B., and Cooke, A. (2007) 'On The Measurement of Temperature in Material Removal Processes', *Annals of the CIRP*, 56 (2), pp. 581-604.

Davim, J. (2010) *Surface Integrity in Machining*. New York: Springer.

Davim, J. (2011) *Machining of Hard Materials*. New York: Springer.

de Mello, A., Da Silva, B., Guimaraes, C., de Paiva, R., Armques, A., Gelamo, R., and de Freitas. (2015) 'A Contribution To Grinding Of Titanium Ti-6Al-4V alloy With Various Coolant Delivery Techniques'. *23rd ABCM International Congress of Mechanical Engineering*. Rio de Janeiro, RJ, Brazil, Dec. 6th-11th.

Demichela, M., Barresi, A., and Baldissone, G. (2018) 'The Effect of Human Error on the Temperature Monitoring and Control of Freeze Drying Processes by Means of Thermocouples', *Frontiers in Chemistry*, 6 (419), pp. 1-11.

de Paiva, R., de Souza Ruzzi, R., and da Silva, B. (2021) 'An Approach to Reduce Thermal Damages on Grinding of Bearing Steel by Controlling Cutting Fluid Temperature', *Metals*, 11 (10), pp. 1160-1174.

Dhavlikar, M., Kulkarni, M., and Mariappan, V. (2003) 'Combined Taguchi and dual response method for optimisation of a centreless grinding operation', *Journal of Materials Processing Technology*, 132, pp. 90-94.

Dillon, H., Emery, A., Cochran, R., and Mescher, A. (2010) 'Dimensionless versus Dimensional Analysis in CFD and Heat Transfer', *Proceedings of the COMSOL Conference 2010*. Boston, USA, Oct.

Ding, W., Xu, J., Chen, Z., Su, H., and Fu, Y. (2010) 'Grinding and Surface Integrity of Case Nickel-based Superalloy in Creep Feed Grinding with Brazed CBN Abrasive Wheels', *Chinese Journal of Aeronautics*, 23, pp. 501-510.

Ding, Z., Jiang, X., Guo, M., and Liang, S. (2018) 'Investigation of the grinding temperature and energy partition during cylindrical grinding', *International Journal of Advanced Manufacturing Technology*, 97, pp. 1767-1778.

Ding, Z., Sun, G., Guo, M., Jiang, X., Li. B., and Liang, S. (2020) 'Effect of phase transition on micro-grinding residual stress', *Journal of Materials Processing Technology*, 281, Article Number: 116647.

Donovan, T., Murray, D., and Torrance, A. (2006) 'Jet Heat Transfer in the Vicinity of a Rotating Grinding Wheel', *Proceedings of the Institute of Mechanical Engineers, Part C: Journal of Mechanical Engineering Science*, 220, (6), pp. 837-845.

Dowson, D., and Higginson, G.R. (1959) 'A Numerical Solution to the Elasto-Hydrodynamic Problem', *Journal of Mechanical Engineering Science*, 1, pp. 6–15.

Dowson, D., and Higginson, G.R. (1960) 'The Effect of Material Properties on the Lubrication of Elastic Rollers', *Journal of Mechanical Engineering Science*, 2, pp. 188–194.

Dowson, D., and Higginson, G.R. (1966) *Elasto-Hydrodynamic Lubrication.* Oxford, UK: Pergamon Press.

Drucker, C., and Ekstein, H. (1950) 'A Dimensional Analysis of Metal Cutting', *Journal of applied Physics*, 21 (2), pp. 104-107.

Du, Y., Mukherjee, T., Finch, N., De, A. and DebRoy, T. (2022) 'High-throughput screening of surface roughness during additive manufacturing', *Journal of Manufacturing Processes*, 81, pp. 65-77.

Durakovic, B. (2017) 'Design of Experiments Application, Concepts, Examples: State of the Art', *Periodicals of Engineering and Physical Sciences*, 5 (4), pp. 421-439.

Durgumahanti, P., Singh, V., and Rao, Ventakeswara. (2010) 'A new Model for the Grinding Force Prediction and Analysis', *International Journal of Machine Tools and Manufacture*, 50, pp. 231-240.

Durivage, M. (2016) *Practical Design of Experiments (DoE): A Guide for Optimising Designs and Processes*. Wisconsin, USA: ASQ Quality Press.

El Wakil, S., and Azab, N. (2010) 'Effect Of Process Parameters On The Grinding Of Polymeric Composites', *13th European Conference on Composites Materials*. Stockholm, Sweden, Sept, pp. 1-7.

Esnault, V., and Roux, J. (2013) '3D numerical simulation study of quasistatic grinding process on a model granular material', *Mechanics of Materials*, 66, pp. 88-109.

Farahani, S.D. (2019) 'Estimation of Distribution of Moving Heat Source During Milling of AISIH13 By Inverse Heat Conduction Method', *Journal of Theoretical and Applied Mechanics*, 57 (4), pp. 1080-1093.

Fathima, K., Kumar, A., Raham, M., and Lim, H.S. (2003) 'A study on wear mechanism and wear reduction strategies in grinding wheels used for ELID grinding', *Wear*, 254, pp. 1247-1255.

Fergani, O., Shao, Y., Lazoglu, I., and Liang, S. (2014) 'Temperature Effects on Grinding Residual Stress', *Procedia CIRP*, 14, pp. 2-6.

Field, M., and Kahles, J. (1964) The surface integrity of machine and ground high strength steels. *DMIC Report*, 210, October, pp. 54-77.

Gao, H., Li, X., Li, B., Wu, Q., Ma, Y., Jian, X., Song, H., and Chen, S. (2022) 'Residual stress and microstructure of Ti6Al4V treated by thermal-vibratory stress relief process', *Journal of Materials Research and Technology*, 18, pp. 5161-5181.

Ghani, J., Choudhury, I., and Hassan, H. (2004) 'Application of Taguchi method in the optimization of end milling parameters', *Journal of Materials Processing Technology*, 145, pp. 84-92.

Ghosh, S., Chattopadhyay, A., and Paul, S. (2008) 'Modelling of specific energy requirement during high-efficiency deep grinding', *International Journal of Machine Tools and Manufacture*, 48, pp. 1242-1253.

Gift, F., and Misiolek, W. (2004) 'Fluid Performance Study for Groove Grinding a Nickel Based Superalloy using Electroplated Cubic Boron Nitride (CBN) Grinding Wheels', *Journal of Engineering Science and Technology*, 126, pp. 451-458.

Ginting, A., and Nouari, M. (2009) 'Surface integrity of dry machined titanium alloys', *International Journal of Machine Tools and Manufacture*, 49, pp. 325-332.

Giraud, M., Gatumel, C., Vaudez, S., Nos, J., Gervais, T., Bernard-Granger, G., and Berthiaux, H. (2021) 'Investigating grinding mechanisms and scaling criteria in a ball mill by dimensional analysis', *Advanced Powder Technology*, 32 (8), pp. 2988-3001.

Godino, L., Pombo, I., Sanchez, J., and Izquierdo, B. (2018) 'An Original Tribometer to Analyze the Behaviour of Abrasive Grains in the Grinding Process', *Metals*, 8 (557), pp. 1-11.

Grimmert, A., Pachnek, F., and Wiederkehr, P. (2023) 'Temperature modeling of creep-feed grinding processes for nickel-based superalloys with variable heat flux distribution', *CIRP Journal of Manufacturing Science and Technology*, 41, pp. 441-489.

Günnay, M., Aslan, E., Korkut, C., and Seker, S. (2004) 'Investigation of the effect of rake angle on main cutting force', *International Journal of Machine Tools and Manufacture*, 44 (9), pp. 953-959.

Guo, C., Attia, H., Shi, Z., and McIntosh, D. (2007) 'Power and Wheel Wear for Grinding Nickel Alloy with Plated CBN Wheels', *Annals of the CIRP*, 56 (1), pp. 343-346.

Guo, C., and Malkin, S. (2000) 'Energy Partition and Cooling During Grinding', *Journal of Manufacturing Processes*, 2 (3), pp. 151-157.

Guo, C., Wu, Y., Varghese, V., and Malkin, S. (1999) 'Temperatures and Energy Partition for Grinding with Vitrified CBN Wheels', *CIRP Annals*, 48 (1), pp. 247-250.

Guo, G., Liu, Z., An, Q., and Chen, M. (2011) 'Experimental investigation on conventional grinding of Ti-6Al-4V using SiC abrasive', *Journal of Advanced Manufacturing Technology*, 57, pp. 135-142.

Gviniashvili,V., Woolley, N., and Rowe, W. (2004) 'Useful coolant flowrate in grinding', *International Journal of Machine Tools and Manufacture*, 44, pp. 629-636.

Hadad, M., and Sadeghi, B. (2012) 'Thermal analysis of minimum quantity lubrication-MQL grinding process', *International Journal of Machine Tools and Manufacture*, 63, pp. 1-15.

Hahn, R. (1962) 'On the nature of the grinding process', *Proceedings of the Third International Conference on Machine Tool Design and Research.* Birmingham, Sept, pp. 129-164: Pergamon Press.

Hamdi, H., Zahouani, H., and Bergheau, J.M. (2004) 'Residual stresses computation in a grinding process', *Journal of Materials Processing Technology*, 147, pp. 277-285.

Hood, R. (2010) *The Machinability of a Gamma Titanium Aluminide Intermetallic.* PhD Thesis. The University of Birmingham, Birmingham, UK.

Hood, R., Aspinwall, D., and Voice, W. (2007a) 'Creep feed grinding of titanium aluminide intermetallic alloy using SiC abrasives', *Journal of Materials Process Technology*, 191, pp. 210-214.

Hood, R., Lechner, F., Aspinwall, D., and Voice, W. (2007b) 'Creep feed grinding of titanium aluminide and burn resistant titanium alloys using SiC abrasives', *International Journal of Machine Tools and Manufacture – Design, Research and Application*, 47, pp. 1486-1492.

Hou, Z.B., and Komanduri, R. (2003) 'On the mechanics of the grinding process – Part I. Stochastic nature of the grinding process', *International Journal of Machine Tools and Manufacture*, 43, pp. 1579-1593.

Hou, Z.B., and Komanduri, R. (2004a) 'On the mechanics of the grinding process, Part II – thermal analysis of fine grinding', *International Journal of Machine Tools and Manufacture – Design, Research and Application*, 44, pp. 247-270.

Hou, Z.B., and Komanduri, R. (2004b) 'On the mechanics of the grinding process, Part III – thermal analysis of the abrasive cut-off operation', *International Journal of Machine Tools and Manufacture – Design, Research and Application*, 44, pp. 271-289.

Howes, T. (1990) 'Avoiding Thermal Damage in Grinding', *Joint Industry Conference of the Abrasive Engineering Society.* May 16th-18th, Cleveland, Ohio, USA.

Hryniewicz, P., Szeri, A., and Jahanmir, S. (2000) 'Coolant flow in surface grinding with non-porous wheels', *International Journal of Mechanical Sciences*, 42, pp. 2347-2369.

Hryniewicz, P., Szeri, A., and Jahanmir, S. (2001a) 'Application of Lubrication Theory to Fluid Flow in Grinding: Part I – Flow Between Smooth Surfaces', *Transactions of the ASME*, 123, pp. 94-100.

Hryniewicz, P., Szeri, A., and Jahanmir, S. (2001b) 'Application of Lubrication Theory to Fluid Flow in Grinding: Part II – Influence of Wheel and Workpiece Roughness', *Transactions of the ASME*, 123, pp. 101-107.

Huang, Q., and Ren, J. (1991) 'Surface integrity and its effects on the fatigue life of the nickel-based superalloy GH33A', *International Journal of Fatigue*, 13 (4), pp. 322-326.

Ichida, Y., Sato, R., Morimoto, Y., and Inoue, Y. (2006) 'Profile Grinding of Superalloys with Ultrafine-Crystalline cBN Wheels', *The Japan Society for Mechanical Engineers*, 49 (1), pp. 94-99.

Inasaki, I., Karpushchewski, B., and Lee, H-S. (2001) 'Grinding Chatter - Origin and Suppression', *CIRP Annals*, 50 (2), pp. 515-534.

Inasaki, I., and Tönshoff, H. (2001) *Sensors in Manufacturing.* Wiley-VCH. Weinheim. New York.

Irani, R., Bauer, R., and Warkentin, A. (2005) 'A review of cutting fluid application in the grinding process', *International Journal of Machine Tools and Manufacture: Design, Research and Application*, 45, pp. 1696-1705.

Jackson, M., and Davim, J. (2011) *Machining with Abrasives*. New York: Springer.

Jadam, T., Rakesh, M., and Datta, S. (2020) 'Machinability of Ti-6Al-4V Superalloy: Performance of Dry Cutting and Nanofluid MQL (MWCNT-Added Rice Bran Oil)', *Arabian Journal for Science and Engineering*, 45, pp. 5673-5695.

Jaeger, J.C. (1942) 'Moving Sources of Heat and the Temperature at Sliding Contacts', *Journal and Proceedings of the Royal Society of New South Wales*, 1, pp. 203-224.

Jalili, M., Fazel, R., and Abootorabi, M. (2017) 'Simulation of chatter in plunge grinding process with structural and force nonlinearities', *International Journal of Manufacturing Technology*, 89, pp. 2863-2881.

Jawahir, I., Brinksmeier, E., M'Sauobi, R., Aspinwall, D., Outeiro, J., Meyer, D., Umbrello, D., and Jayal, A. (2011) 'Surface integrity in material removal processes: Recent advances', *CIRP Annals – Manufacturing Technology*, 60, pp. 603-626.

Jin, T., Rowe, W., and McCormack, D. (2002) 'Temperatures in deep grinding of finite workpieces', *International Journal of Machine Tools and Manufacture: Design, Research and Application*, 42, pp. 53-59.

Jin, T., Stephenson, D., and Rowe, W. (2003) 'Estimation of the convection heat transfer coefficient of coolant within the grinding zone', *Proceedings of the Institute of Mechanical Engineers Part B – Journal of Engineering Manufacture*, 217, pp. 397-407.

Judkins, M., and Uecker, W. (1933) 'Cemented Carbide Cutting Tools', *American Machinist*, 7, pp. 325-364.

Kadivar, M., Azarhoushang, B., Daneshi,A., and Krajnik, P. (2020) 'Surface integrity in micro-grinding of Ti6Al4V considering the specific micro-grinding energy', *Procedia CIRP*, 87, pp. 181-185.

Kaelani, Y., and Syaifudin, A. (2021) 'Mathematical model of wear volumes due to sliding speed using Buckingham Pi Model', *IOP Conference Series: Materials Science and Engineering*, 1034, 2nd International Conference on Mechanical Engineering Research and Application (iCOMERA 2020) 7th–9th October 2020, Malang, Indonesia.

Kaiser, Dr. (2012) Dressing of Grinding Wheels. Available at https://www.drkaiser.com/service/downloads.html [Online] (Accessed: 26th September 2021).

Kalita, P., Malshe, A., Arun Kumar, S., Yoganath, V., and Gurumurthy, T. (2012) 'Study of specific energy and friction coefficient in minimum quantity lubrication grinding using oil-based nanolubricants', *Journal of Manufacturing Processes*, 14 (2), pp. 160-166.

Kalpakjian, S., and Schmid, S.R. (2008) *Manufacturing Processes for Engineering Materials*. 5th edn. Singapore: Prentice Hall.

Kamble, Y., Rajiv, B., and Jadhav, P. (2021) 'Experimental investigation and dimensional analysis of friction drilled hole on 6062 aluminium pipe using hardened M2 centre drill', *Materials Today: Proceedings*, (42), pp. 1239-1243.

Keeg, R.L. (1983) 'Industrial Problem in Grinding', *Annals of the CIRP*, 32 (2), pp. 559-561.

Kekade, S., Patil, S., Phapale, K., Jadhav, S., Powar, A., Supare, A., and Singh, RKP. (2016) 'Effect of Quench Delay on Subsurface integrity during machining of Titanium Alloy Ti6Al4V', *Procedia Manufacturing*, 6, pp. 148-153.

Kim, T.Y., Woo, J., Shin, D., and Kim, J. (1999) 'Indirect cutting force measurement in multi-axis simultaneous NC milling processes', *International Journal of Machine Tools and Manufacture*, 39, pp. 1717-1731.

Klocke, F. (2009) *Manufacturing processes 2 – Grinding, Honing, Lapping.* Germany: Springer.

Klocke, F., Barth, S., and Matfield, P. (2016) 'High Performance Grinding', *Procedia CIRP*, 46, pp. 266-271.

Kopac, J., and Kranjnik, P. (2006) 'High-performance grinding - A Review', *Journal of Materials Processing Technology*, 175, pp. 278-284.

Koyano, T., Takahashi, T., Tsurutani, S., Hosokawa, A., Furumoto, T., and Hashimoto, Y. (2018) 'Temperature Measurement of Wire Electrode in Wire EDM by Two-colour Pyrometer', *Procedia CIRP*, 68, pp. 96-99.

Kronenberg, M. (1966) 'Machining Science and Application'. Oxford, UK: Pergamon Press.

Kumar, K. (1990) 'Superabrasive Grinding of Titanium Alloys', *SME Technical Paper, Code: MR90-505*, pp. 1-17.

Kumar, J., and Kamba, J. (2010) 'Modelling the material removal rate in ultrasonic assisted machining of titanium using dimensional analysis', *International Journal of Advanced Manufacturing Technology*, 48, pp. 103-119.

Kwak, J-S. (2005) 'Application of Taguchi and response surface methodologies for geometric error in surface grinding process', *International Journal of Machine Tools and Manufacture: Design, Research and Application*, 45, pp. 327-334.

Kyas, K., Stanek, M., Manas, D., Manas, M., Ovsik M., Skrobak, A., and Krumal, D. (2011) 'Thermal Effects on Steels at Flame Cutting', *Annals of DAAAM: Proceedings of the 22nd International DAAAM Symposium*, 22 (1), pp. 737-738.

Lane, B., Whitenton, E., Madhaven, V., and Donmez, A. (2013) 'Uncertainty of temperature measurements by infrared thermography for metal cutting applications', *Metrologia*, 50, pp. 637-653.

Lebedev, V., Chumachenko, T., Klymenko, N., Frolenkova, O., and Yevtifieiev, S. (2021) *Penetration Depth of the Critical Temperature into the Workpiece Material During Grinding.* In "Advances in Design, Simulation and Manufacturing IV", Springer, New York.

Levi, P. (2000) *The Periodic Table.* Translated by R. Rosenthal. London, England: Penguin Classics.

Li, B., Jiang, X., Yang, Y., and Liang, S. (2015) 'Effects of depth of cut on the redistribution of residual stress and distortion during the milling of thin-walled part', *Journal of Materials Processing Technology*, 216, pp. 223-233.

Li, H., Yu, T., Wang, Z., Zhu, L., and Wang, W. (2017) 'Detailed modelling of cutting forces in grinding process considering variable stages of grain-workpiece micro interactions', *International Journal of Mechanical Sciences*, 126, pp. 319-339.

Li, H., Liu, K., and Li, X. (2001) 'A new method for determining the undeformed chip thickness in milling', *Journal of Materials Processing Technology*, 113, pp. 378-384.

Li, L., Fu, J., and Peklenik, P. (1980) 'A Study of Grinding Force Mathematical Model', *CIRP Annals – Manufacturing Technology*, 29 (1), pp. 245-249.

Lindsay, R., and Hahn, R. (1971) 'On the basic relationships between grinding parameters', *Annals of the CIRP*, 19, pp. 657-666.

Linke, B. (2008) 'Dressing process model for vitrified bonded grinding wheels', *CIRP Annals*, 57 (1), pp. 345-348.

Linke, B. (2015) 'Review on grinding tool wear with regard to sustainability', *Journal of Manufacturing Science and Engineering*, 137 (5). Available [Online]. doi:10.1115/1.4029399.

Linke, B., and Klocke, F. (2010) 'Temperatures and wear mechanisms in dressing of vitrified bonded grinding wheels', *International Journal of Machine Tools and Manufacture*, 50, pp. 552-558.

Linke, B., Duscha, M., Klocke, F., and Dornfield, D. (2011) 'Combination of Speed Stroke Grinding and High Speed Grinding with Regard to Sustainability', *Green Manufacturing and Sustainable Manufacturing Partnership, Proceedings of the 44th CIRP International Conference on Manufacturing Systems*. Madison, WI, USA, June 1st-3rd.

Liu, D., Wang, G., Nie, Z., and Rong, Y. (2016) 'An in-situ infrared-measurement method with back focusing on surface for creep-feed grinding', *Measurement*, 94, pp. 645-652.

Liu, Q., Chen, X., and Gindy, N. (2007a) 'Assessment of $Al_2O_3$ and superabrasive wheels in nickel-based alloy grinding', *International Journal of Advanced Manufacturing Technology*, 33, pp. 940-951.

Liu, Q., Chen, X., and Gindy, N. (2007b) 'Evaluation of superalloy heavy-duty grinding based on multivariate tests', *Proceedings of the Institute of Mechanical Engineers, Part B: Journal of Engineering Manufacture*, 221, pp. 1421-1430.

Liu, Q., Chen, X., and Gindy, N. (2008) 'Robust design and optimisation of aerospace alloy grinding by different abrasive wheels', *International Journal of Advanced Manufacturing Technology*, 39, pp. 1125-1135.

Liu, Q., Chen, X., Wang, Y., and Gindy, N. (2008) 'Empirical modelling of grinding force based on multivariate analysis', *Journal of Materials Processing Technology*, 203, pp. 420-430.

Lockheed Martin (2023). Available at [https://www.lockheedmartin.com/en-us/products/f-22.html].

Lubis, S., Darmawan, S., and Ericson, A. (2019) 'Effect of cutting speed on temperature cutting tools and surface roughness of AISI 4340 steels', *IOP Conference Series: Materials, Science and Engineering.* 508, Article Number: 012053.

Mackenzie, D.S. (2017) 'Metallurgical Reasons for Grinding Cracks and Their Detection', *Gear Solutions*, 5, pp. 25–27.

Mackerle, J. (1999) 'Finite-element analysis and simulation of machining: a bibliography (1976-1996)', *Journal of Materials Processing Technology*, 86, pp. 17-44.

Madopothula, U., Vijayaraghavan, L., Ramesh Babu, N., and Pradeev, E. (2017) 'Prediction of Temperature Distribution in the Workpiece during Multi-Pass Grinding by Finite Volume Method', *International Journal of Precision Engineering and Manufacturing*, 18 (11), pp. 1485-1493.

Mahamani, A., and Jawahar, S. (2018) 'Influence of grinding parameters on grinding force and temperature in grinding of AA60661-TiB2/ZrB2 in-situ composite', *IOP Conference Series: Materials Science and Engineering.* 390: 1-7.

Majumdar, T., Bazin, T., Riberio, E., and Frith, J. (2019) 'Understanding the effects of PBF process parameter interplay on Ti-6Al-4V surface properties', *PLoS ONE*, 14 (8), pp. 1-24.

Maksoud, T., and Wong, L. (2000) 'In-process automatic dressing system for grinding wheels', *Proceedings of the Institute of Mechanical Engineers, Part B: Journal of Engineering Manufacture*, 214, pp. 799-803.

Malkin, S. (1989) *Grinding Technology: Theory and Applications of Machining with Abrasives*, England: Ellis Horwood Ltd.

Malkin, S., and Cook, N. (1971a) 'The Wear of Grinding Wheels, Part 1 – Attritious Wear', *Journal of Manufacturing Science and Engineering*, 93 (4), pp. 1120-1128.

Malkin, S., and Cook, N. (1971b) 'The Wear of Grinding Wheels, Part 2 – Fracture Wear', *Journal of Manufacturing Science and Engineering*, 93 (4), pp. 1129-1133.

Malkin, S., and Guo, C. (2007) 'Thermal Analysis of Grinding', *CIRP Annals*, 56 (2), pp. 760-782.

Manas, D., Stanek, M., Manas, M., Ovsik, M., Pata, V., and Cerny, J. (2011) 'Thermal Effects on Metals at Laser Cutting in Annals of DAAAM', *Proceedings of the 22nd International DAAAM Symposium*, 22 (1), 739-741.

Manimaran, G., and Kumar, M. (2013) 'Effect of cryogenic cooling and sol-gel alumina wheel on grinding performance of AISI 316 stainless steel', *Archives of Civil and Mechanical Engineering*, 13, pp. 304-312.

Marinescu, I., Hitchiner, M., Uhlmann, E., Rowe, W., and Inasaki, I. (2006) *Handbook of Machining with Grinding Wheels (Manufacturing Engineering and Materials Processing).* New York: CRC Press.

Marinescu, I., Rowe, W.B., Dimitrov, B., and Ohmori, H. (2013) *Tribology of Abrasive Machining Process.* 2nd edn: Elsevier.

Marogu, N.K., and Jin, X. (2017) 'Effects of Vibration Assistance on Surface Residual Stress in Grinding Ti6Al4V Alloy', *Procedia Manufacturing*, 10, pp. 171-182.

Mathohol, I., Akilabiln, E., Mubiayi, M., and Mbohwa, C. (2018) 'Effect of milling parameters on microhardness and microstructure during dry and flood milling of Ti-6Al-4V', *IOP Conference Series: Materials Science and Engineering.* 423, Article Number: 012161.

McManus, T., and Haddad, A. (2014) 'Use of Methanol as a Coolant During Dry Machining of Aluminium in a Shipbuilding Environment: A Failure to Assess and Manage Risk', *Advanced Materials Research*, 955-959, pp. 1061-1064.

Mihic, S., Cioc, S., Marinescu, I., and Weismiller, M. (2013) 'Detailed Study of Fluid Flow and Heat Transfer in the Abrasive Grinding Contact using Computational Fluid Dynamics Methods', *Journal of Manufacturing and Science Engineering*, 135 (4), Article Number: 041002.

Montgomery, D. (2013) *Design and Analysis of Experiments.* 8th edn., Minneapolis, USA: John Wiley & Sons, Inc.

Morgan, M., Rowe, W., Black, S., and Allanson, D. (1998) 'Effective thermal properties of grinding wheels and grains', *Proceedings of the Institute of Mechanical Engineers, Part B: Journal of Engineering Manufacture*, 212, pp. 661-669.

Morgan, M., and Baines-Jones, V. (2009) 'On the coherent length of fluid nozzles in grinding', *Key Engineering Materials*, 404, pp. 61-67.

Moussaoui, K., Mousseigne, M., Senatore, J., Chieragatti, R., and Monies, F. (2013) 'Influence of milling on surface integrity of Ti6Al4V — study of the metallurgical characteristics: microstructure and microhardness', *International Journal of Advanced Manufacturing Technology*, 67, pp. 1477–1489.

Murtagian, G. (2004) *Surface Integrity on Grinding of Gamma Titanium Aluminide Intermetallic Compounds*. PhD Thesis. Georgia Institute of Technology, Atlanta, USA.

Murtagian, G., Hecker, R., Liang, S., and Danyluk, S. (2010) 'Plastic deformation depth modeling on grinding of gamma Titanium Aluminides', *International Journal of Advanced Manufacturing Technology*, 49, pp. 89–95.

Nadolny, K., Wojtewicz, M., Sienicki, W., and Herman, D. (2015) 'An analysis of centrifugal MQL supply system potential in the internal cylindrical grinding process', *Archives of Civil and Mechanical Engineering*, 15 (3), pp. 639-649.

Nalbant, M., Gokkaya, H., and Sur, G. (2007) 'Application of Taguchi method in the optimisation of cutting parameters for surface roughness in turning', *Materials & Design*, 28, pp. 1379-1385.

Naskar, A., Choudhary, A., and Paul, S. (2020) 'Wear mechanism in high-speed superabrasive grinding of titanium alloy and its effect on surface integrity', *Wear*, 463-463, Article Number: 203475.

Nedić, P., and Erić. M (2014) 'Cutting Temperature Measurement and Material Machinability', *Thermal Science*, 18 (1), pp. 259-268.

Nee, A., and Tay, A. (1981) 'On the Measurement of Surface Grinding Temperature', *International Journal of Machine Tool Design and Research*, 21 (3-4), pp. 279-291.

Nelson, L., Xu, H., Danyluk, S., and Jahanmir, S. (1997) 'Subsurface Damage in Grinding Titanium Aluminide', *Machining Science and Technology*, (2), pp. 289-297.

Nigm, M., Sadek, M., and Tobias, S. (1977) 'Dimensional Analysis of the Steady State Orthogonal Cutting Process', *International Journal of Machine Tool Design and Research*, 17, pp. 1-18.

Nik, M., Mohammad, M., and Akbari, J. (2012) 'Ultrasonic-Assisted Grinding of Ti-6Al-4V Alloy', *Procedia CIRP*, 1, pp. 353-358.

Novikov, F., Hutorov, A., Yermolenko, O., Dytynenko, S., and Halahan, Y. (2022) *Evaluation of a Decrease in Temperature Conditions upon Intermittent Grinding.* In "Advanced Manufacturing Processes IV", Springer. New York.

Novikov, F., Polyansky, V., Shkurpiy, V., and Novikov, D. (2019) 'Determining the conditions for decreasing cutting force and temperature during machining', *Eastern European Journal of Enterprise Technologies*, 6 (1), pp. 41-50.

Ohkubo, C., Watanabe, I., Ford, J., Nakajima, H., Hosoi, T., and Okabe, T. (2000) 'The machinability of cast titanium and Ti-6Al-4V', *Biomaterials*, 21, pp. 421-428.

Oliveira, J., Elrado, J., Guo, C., and Fukuo, H. (2009) 'Industrial challenges in grinding', *CIRP Annals – Manufacturing Technology*, 58, pp. 663-680.

Öpöz, T.T., and Chen, X. (2010) 'Numerical Simulation of Single Grit Grinding', *Proceedings of the 16th International Conference on Automation and Computing.* 11th Sept. Birmingham, UK.

Oraon M., and Sharma V. (2022) 'Deriving the functional relation of input parameters in single-point incremental forming through dimensional analysis', *Frontiers in Mechanical Engineering*, 8: Article Number 1003456.

Osorio, A., Bustamante, M., Restrepo, G., Lopez, M., and Menedez-Aguado, J. (2019) 'A Study of the Effect of Medium Viscosity on Breakage Parameters for Wet Grinding', *Symmetry*, 11, pp. 1-11.

Österle. W., Li, P., and Nolze, G. (1999) 'Influence of surface finishing on residual stress depth profiles of a coarse-grained nickel-base superalloy', *Materials Science Engineering: A*, 262, pp. 308-311.

Outwater, J., and Shaw, M. (1952) 'Surface Temperatures in Grinding', *Transactions of the American Society of Mechanical Engineers*, 74 (1), pp. 73-81.

Paknejad, M., Abdullah, A., and Azarhoushang, B. (2017) 'Effects of high power ultrasonic vibration on temperature distribution of workpiece in dry creep feed up grinding', *Ultrasonics – Sonochemistry*, 39, pp. 392- 402.

Patil, S., Jadhav, S., Kekade, S., Supare, A., Powar, A., and Singh, RKP. (2016) 'The Influence of Cutting Heat on the Surface Integrity during Machining of Titanium Alloy Ti6Al4V', *Procedia Manufacturing*, 5, pp. 857-869.

Phate, M., and Toney, S. (2019) 'Modelling and prediction of WEDM performance parameters for Al/SiCp MMC using dimensional analysis and artificial neural network', *Engineering Science and Technology: An International Journal*, (22), pp. 468-476.

Pratap, A., Gorodkova, A., Patra, K., and Dyakonov, A. (2023) 'Finite difference numerical modeling and experimental validation of workpiece surface temperature in micro-grinding', *Machining Science and Technology*, 27 (1), pp. 42-62.

Puerto, P., Fernandez, R., Madariaga, J., Arana, J., and Gallego, I. (2013) 'Evolution of Surface Roughness in Grinding and its Relationship with the Dressing Parameters and Radial Wear', *Procedia Engineering*, 63, pp. 174-182.

Quintana, G., and Ciurana, J. (2011) 'Chatter in machining processes: a review', *International Journal of Machine Tools and Manufacture*, 51 (5), pp. 363–376.

Rabiey, M., Walter C., Kuster, F., Stirnimann, J., Pude, F., and Wegener, K. (2012) 'Dressing of Hybrid Bond CBN Wheels Using Short-Pulse Fibre Laser', *Journal of Mechanical Engineering*, 58 (7-8), pp. 462-469.

Rae, W., and Rahimi, S. (2018) 'Evolution of Microstructure and Residual Stress in Hot Rolled Ti-6Al-4V Plates Subjected to Different Heat Treatment Conditions', *Conference: European Conference on Residual Stresses 10 (ECRS10) - Materials Research Proceedings 6*, pp. 171- 176.

Rane, K., and Date, P. (2021) 'A dimensional analysis based model to predict completion of solvent debinding step for Metal Injection Moulded parts', *Advances in Materials and Processing Technologies*, 7 (2), pp. 241–261.

Rascalha, A., Filo, S., Lauro, C., and Brandäo, L. (2017) 'Effects of different cutting strategies on G-ratio in through-feed centerless grinding', *Acta Scientiarum – Technology*, 39 (1), pp. 45-49.

Reddy, P., and Ghosh, A. (2014) 'Effect of cryogenic cooling on spindle power and G-ratio in grinding of hardened bearing steel', *Procedia Materials Science*, 5, pp. 2622-2628.

Ribeiro, F., Lopes, J., Garcia, M., Sanchez, L., Mello, H., Aguiar, P., and Bianchi, B. (2020) 'Grinding assessment of workpieces with different interrupted geometries using aluminium oxide wheel with vitrified bond', *The International Journal of Advanced Manufacturing Technology*, 108, pp. 931–941.

Rodriguez, R., Lopes, J., Hildebrandt, R., Perez, R., Diniz, A., de Ângelo Sanchez, L., Rodrigues, A., de Mello, H., de Aguiar, P., and Bianchi E. (2019) 'Evaluation of grinding process using simultaneously MQL technique and cleaning jet on grinding wheel surface', *Journal of Materials Processing Technology*, 271, pp. 357–367.

Rowe, W.B., Black, S., Mills, B., Qi, A., and Morgan, M. (1995) 'Experimental Investigation of Heat Transfer in Grinding', *Annals of the CIRP*, 44 (1), pp. 329-332.

Rowe, W.B. (2001) 'Temperature case studies in grinding including an inclined heat source model', *Proceedings of the Institute of Mechanical Engineers, Part B: Journal of Engineering Manufacture*, 214, pp. 473-491.

Rowe, W. (2009) *Principles of Modern Grinding Technology*. United States: Elsevier.

Rugg, D. (2003) 'The Current Status of Titanium Use in Aerospace Engines', *Proceedings of the 10th World Conference on Titanium (Ti-2003).* Hamburg, Germany, 13th-17th July, 4, pp. 2727-2753.

Sadeghi, M., Haddad, M., Tawakoli, T., and Emani, M. (2009) 'Minimal quantity lubrication-MQL in grinding of Ti-6Al-4V titanium alloy', *The International Journal of Advanced Manufacturing Technology*, 44, pp. 487-500.

Sai, S., Kumar, K., and Ghosh, A. (2015) 'Assessment of spray quality from an external mix nozzle and its impact on SQL grinding performance', *International Journal of Machine Tools and Manufacture*, 89, pp. 132-141.

Seco-Nicolás, M., Alarćon, M., and Alhama, F. (2018) 'Thermal behaviour of fluid within pipes based on discriminated dimensional analysis. An improved approach to universal curves', *Applied Thermal Engineering*, 131, pp. 54-69.

Sedov, S. (1959) 'Similarity and Dimensional Methods in Mechanics', London, UK: Academic Press.

Seker, U., Kurt, A., and Ciftci, I. (2004) 'The effect of feed rate on the cutting forces when machining with linear motion', *Journal of Materials Processing Technology*, 146 (3), pp. 403-407.

Setti, D., Yadav, N., and Ghosh, S. (2014) 'Grindability improvement of Ti-6Al-4V using cryogenic cooling', *Journal of Engineering Manufacture*, 225 (9), pp. 1131-1137.

Shafto, G., Howes, I., and Andrew, C. (1975) 'Thermal Aspects of Creep-feed Grinding', *Proceedings of the 16th International MTDR Conference*, January, Manchester, UK.

Shaji, S., and Radhakrishnan, V. (2002a) 'An investigation on surface grinding using graphite as a lubricant', *International Journal of Machine Tools and Manufacture*, 42, pp. 733-740.

Shaji, S., and Radhakrishnan, V. (2002b) 'Investigations on the application of solid lubricants in grinding', *Proceedings of the Institute of Mechanical Engineers, Part B: Journal of Engineering Manufacture*, 216, pp. 1325-1343.

Shaji, S., and Radharkrishnan, V. (2003) 'Analysis of process parameters in surface grinding with graphite as a lubricant based on the Taguchi method', *Journal of Materials Processing Technology*, 141, pp. 51-59.

Shao, Y., Fergani, O., Li, B., and Liang, S. (2016) 'Residual stress modeling in minimum quantity lubrication grinding', *The International Journal of Advanced Manufacturing Technology*', 83, pp. 743–751.

Shaw, M.C. (1985). *The Theory of Metal Cutting.* In: Tobias, S.A. (eds) Proceedings of the Twenty-Fifth International Machine Tool Design and Research Conference. Palgrave, London.

Shaw, M.C. (1988) 'The importance of temperature in grinding', *Journal of Mechanical Working Technology*, 17, pp. 343-355.

Shaw, M.C. (1994) 'A Production Engineering Approach to Grinding Temperatures', *Journal of Materials Processing Technology*, 44, pp. 159-169.

Shaw, M. (1996a) *Principles of Abrasive Processing.* New York: Oxford University Press.

Shaw, M. (1996b) 'Energy Conservation in Cutting and Grinding', *Annals of the CIRP*, 45 (1), pp. 101-104.

Shaw, M.C. (2003) 'The Size Effect in Metal Cutting', *Sandhana*, 28 (5), pp. 875-896.

Shaw, M., and Oxford Jr., C. (1957) 'On the drilling of metals, the torque and thrust in drilling', *Transactions on ASME*, 79, pp. 139–148.

Shen, B., Xiao, G., Guo, C., Malkin, S., and Shih, A. (2008) 'Thermocouple Fixation Method for Grinding Temperature Measurement', *International Journal of Science and Engineering*, 130 (5), pp. 1-8.

Shen, B., and Xiao, G. (2011) 'A Heat Transfer Model Based on Finite Difference Method for Grinding', *Journal of Manufacturing Science and Engineering*, 133, pp. 1-10.

Shi, Y., Chen, L., Xi., H., and Yu, T. (2020) 'Investigation on the grinding properties of high thermal conductivity vitrified bond CBN grinding wheel for titanium alloy', *The International Journal of Advanced Manufacturing Technology*, 107, pp. 1539–1549.

Singh, R., and Khamba, J. (2009) 'Mathematical modelling of surface roughness in ultrasonic machining of titanium using Buckingham-$\pi$ approach: a review', *International Journal of Abrasive Technology*, 2 (1), pp. 3-24.

Singleton, R. (2014) *Utilisation Of Chip Thickness Models In Grinding.* PhD Thesis. University of Sheffield, Sheffield, UK.

Sisodiya, G., Viswanathan, K., and Dinakaran, D. (2016) 'Study on Factors Influencing Wheel Wear in Grinding Process', *International Journal of Advance Research and Innovative Ideas in Education*, 3 (2), pp. 301-307.

Souza, A.M., and Silva, E.R. (2019) 'Global strategy of grinding wheel performance evaluation applied to grinding of superalloys', *Precision Engineering*, 57, pp. 113-126.

Spina, R., and Cavalcante, B. (2020) 'Thermal Analysis of PA66', *Procedia Manufacturing*, 47, pp. 910-914.

Spriggs, G. (2002) 'Properties of diamond cubic boron nitride' in Beiss, P. *et al.*, (ed). *Powder Metallurgy Data. Refractory, Hard and Intermetallic Materials, 2A2.* Berlin, Heidelberg: Springer-Verlag.

Srivastava, A., Awale, A., Vashista, M., and Yusufzai, M. (2020) 'Monitoring of thermal damages upon grinding of hardened steel using Barkhausen noise analysis', *Journal of Mechanical Science and Technology*, 34, pp. 2145-2151.

Stanek, M., Manas, D., Manas, M., Ovsik, M., Skrobak, A., and Krumal, M. (2011) 'Thermal Effects on Metals at Plasma Cutting in Annals of DAAAM', *Proceedings of the 22nd International DAAAM Symposium*, 22 (1), pp. 742-744.

Stein, J., and Huh, K. (2002) 'Monitoring Cutting Forces In Turning: A Model-Based Approach', *Transactions of the ASME*, 124, pp. 26-31.

Steffen, J., Warkentin, A., Bauer, R.J., and Becze, C. (2005) 'Effect of Jet Coherency on Workpiece Burn for Non-continuous dress creep feed grinding of Inconel 718', *Journal of Advanced Manufacturing Systems*, Vol. 4 (2), pp. 117-130.

Sterrett, S. (2009) 'Similarity and Dimensional Analysis' in Sterrett, S. *In Philosophy of Technology and Engineering Sciences*. Amsterdam: Elsevier.

Stone, W., and Kurfess, T. (2007) 'Grinding titanium aluminide: subsurface damage', *International Journal of Manufacturing Technology and Management*, 12 (1-3), pp. 200-224.

Suhail. A., Ismail, N., Wong, S., and Jalil, N. (2011) 'Workpiece Surface Temperature for In-process Surface Roughness Prediction using Response Surface Methodology', *Journal of Applied Sciences*, 11 (2), pp. 308-315.

Sun, C., Liu, Z., Lan, D., Duan, J., and Xiu, S. (2018) 'Study on the influence of the grinding chatter on the workpiece's microstructure transformation', *The International Journal of Advanced Manufacturing Technology*, 96, pp. 3861–3879.

Sun, C., Xiu, S., Hong, Y., Kong, X., and Lu, Y. (2020) 'Prediction on residual stress with mechanical-thermal and transformation coupled in DGH', *International Journal of Mechanical Sciences*, 179, Article Number: 105629.

Sunarto, Y. (2001) 'Creep feed profile grinding Ni-based superalloys with ultrafine-polycrystalline cBN abrasive grits', *Precision Engineering*, 25, pp. 274-283.

Tahvilian, A.M., Liu, Z., Champliaud, H., and Hazel, B. (2013) 'Experimental and finite element analysis of temperature and energy partition to the workpiece whilst grinding with a flexible robot', *Journal of Materials Processing Technology*, 213, pp. 2292-2303.

Tang, J., Du, J., and Chen, Y. (2009) 'Modelling and experimental study of grinding forces in surface grinding', *Journal of Materials Processing Technology*, 209, pp. 2847-2854.

Tarasov, L.P. (1952) 'How to grind titanium', *American Machinist*, 96 (23), pp. 135-146.

Tawakoli, T. (1990) 'Requirements for high-efficiency deep grinding', *Industrial Diamond Review*, 50, pp. 1-9.

Tawakoli, T., and Azarhoushang, B. (2008) 'Influence of ultrasonic vibrations on dry grinding of soft steel', *International Journal of Machine Tools and Manufacture*, 45, pp. 1585-1591.

Tawakoli, T., Hadad, M., and Sadeghi, M. (2010) 'Investigation on minimum quantity lubricant - MQL grinding of 100Cr6 hardened steel using different abrasive and coolant-lubricant types', *International Journal of Machine Tools and Manufacture*, 50 (8), pp. 698-708.

Tawakoli, T., Hadad, M., Sadeghi, M., Daneshi, A., and Sadeghi, B. (2011) 'Minimum quantity lubrication in grinding: effects of abrasive and coolant-lubricant types', *Journal of Cleaner Production*, 19 (17-18), pp. 2088-2099.

Tawakoli, T., Reinecke, H., and Vesali, A. (2012) 'An Experimental Study on the Dynamic Behaviour of Grinding Wheels in High Efficiency Deep Grinding', *Procedia CIRP*, 1, pp. 382-387.

Teicher, U., Ghosh, A., Chattopadhyay, A., and Künanz, K. (2006) 'On the grindability of titanium alloy by brazed type monolayered superabrasive grinding wheel', *International Journal of Machine Tools and Manufacture*, 46, pp. 620-622.

Teicher, U., Künanz, K., Ghosh, A., and Chattopadhyay, A. (2008) 'Performance of diamond and CBN single-layered grinding wheels in grinding titanium', *Materials and Manufacturing Processes*, 23, pp. 224-227.

Telford, J. (2007) 'A Brief Introduction to Design of Experiments', *John Hopkins APL Technical Digest*, 27 (3): 224-232.

Tönshoff, H., Peters. J., and Paul, T. (1992) 'Modelling and Simulation of Grinding Processes', *CIRP Annals – Manufacturing Technology*, 41 (2), pp. 677-688.

Tooling and Production (2014) http://toolingandproduction.com [online] Available from http://www.toolingandproduction.com/cms/tap/opens/articleview. Accessed [26th March 2015].

Toth, M. (2020) *On the dynamic stability of surface grinding: the role of the specific energy in regenerative chatter.* PhD Thesis. University of Sheffield, South Yorkshire, UK.

Turley, D.M. (1985) 'Factors affecting surface finish when grinding titanium and a titanium alloy (Ti-6Al-4V)', *Wear*, 104 (4), pp. 323-335.

Ulutan, D., and Ozel, T. (2010) 'Machining induced surface integrity in titanium and nickel alloys: A review', *International Journal of Machine Tools and Manufacture*, 51 (1), pp. 250-280.

Umino, K., and Shinozaki, N. (1972a) 'Elastic modulus and bending strength of grinding wheel–study on grinding wheels by ultrasonic pulse method, Part IV', *Journal of the Japan Society for Precision Engineering*, 38 (447), pp. 349-354.

Umino, K., and Shinozaki, N. (1972b) 'New grade tester of grinding wheel using ultrasonic pulse method—study on grading of grinding wheels by ultrasonic pulse method, Part V', *Journal of the Japan Society for Precision Engineering*, 38 (449), pp. 485-488.

Umino, K., Yamanaka., R,. and Shinozaki, N. (1972) 'On the estimation of grade of fine-grain-size grinding wheel–study on grinding wheels by ultrasonic pulse method, Part III', *Journal of the Japan Society for Precision Engineering*, 38 (445), pp. 161-166.

Urgoiti, L., Barrenetxea, D., Sánchez, J., Pombo, I., and Álvarez, J (2018). 'On the Influence of Infra-Red Sensor in the Accurate Estimation of Grinding Temperatures', *Sensors*, 18, pp. 1-10.

Valíček, J., Držík, M., Hloch, S., Ohlídal, M., Miloslav, L., Gombár, M., Radvanská, A., Hlaváček, P., and Páleníková, K. (2007) 'Experimental Analysis of Irregularities of Metallic Surfaces generated by Abrasive Water', *International Journal of Machine Tools and Manufacture: Design, Research and Application*, 47, pp. 1786 – 1790.

Vashisht, R., and Kapila, A. (2008) 'A Comparative Study of Coolants Based on the Cooling Time of Injection Molding', *International Journal of Emerging Technology and Advanced Engineering*, 4 (6), pp. 830-834.

Vashista, M., and Paul, S. (2008) 'Study of the effect of process parameters in high-speed grinding on surface integrity by Barkhausen noise analysis', *Proceedings of the Institute of Mechanical Engineers, Part B: Journal of Engineering Manufacture*, 222, pp. 1625-1637.

Villa, M., Brooks, J.W., Turner, R.P., Wang, H., Boitout, F., and Ward, R. (2019) 'Microstructural Modeling of the $\alpha + \beta$ Phase in Ti-6Al-4V: A Diffusion-Based Approach', *Metallurgical and Materials Transactions B*, 50, pp. 2898–2911.

Vinay, P.V., and Rao, C.S. (2013) 'Grinding Mechanics and Advances – A Review', *Journal of Mechanical Engineering and Technology* 5 (2), pp. 41-74.

Walsh, D., and Torrance, A. (1999) 'Influence of form on surface temperatures in form grinding', *Proceedings of the Institution of Mechanical Engineers, Part C: Journal of Mechanical Engineering Science*, 213 (6), pp. 601-611.

Wang, S. (2000) *Investigation into the Grinding of Titanium Alloys.* PhD Thesis. Cranfield University, Bedfordshire, UK.

Wang, C., and Chen, C. (2002) 'Three dimensional inverse heat transfer analysis during the grinding process', *Proceedings of the Institute of Mechanical Engineers, Part C: Journal of Mechanical Engineering Science*, 216, pp. 199-212.

Wang, C., Feng, L., Ding, C., Chang., H, and Zhou, L. (2020) Investigation of phase transition in Fe microalloyed Ti6Al4V alloy during heating process. MATEC Web of Conferences, *The 14th World Conference on Titanium*: 1-8.

Wang, Y., Lin, B., Cao, X., and Wang, S. (2014) 'An experimental investigation of system matching in ultrasonic vibration assisted grinding for titanium', *Journal of Materials Processing Technology*, 214, pp. 1871-1878.

Wang, Z., and Liu, Y. (2020) 'Study of surface integrity of milled gamma titanium aluminide', *Journal of Manufacturing Processes*, 5, pp. 806-819.

Webster, J. A. (2007) 'Improving surface integrity and economics of grinding by optimum coolant application, with consideration of abrasive tool and process regime', *Proceedings of the Institute of Mechanical Engineers, Part B: Journal of Engineering Manufacture*, 221 (12), pp. 1665-1675.

Webster, J., Brinksmeier, E., Heinzel, C., Wittmann, M., and Thoens, K. (2002) 'Assessment of Grinding Fluid Effectiveness in Continuous-Dress Creep Feed Grinding', *CIRP Annals – Manufacturing Technology*, 51 (1), pp. 235-240.

Wegener, K., Hoffmesister, H., Karpuschewski, B., Kuster, F., Hahmann, W., and Rabiey, M. (2011) 'Conditioning and monitoring of grinding wheels', *CIRP Annals – Manufacturing Technology*, 60, pp. 757-777.

Welling, D. (2014) 'Results of Surface Integrity and Fatigue Study of Wire-EDM compared to Broaching and Grinding for demanding Jet Engine Components made of Inconel 718', *Procedia CIRP*, 13, pp. 339-344.

Wen, Y., Tang, J., Zhou, W., and Zhu, C. (2019) 'Study on contact performance of ultrasonic-assisted grinding surface', *Ultrasonics*, 91, pp. 193-200.

Wetton, A.G. (1969) 'A Review of the Theories of Material Removal in Grinding', *Journal of Mechanical Engineering Science*, 11 (4), pp. 412-425.

Whitenton, E. (2012) 'An introduction for machining researchers to measurement uncertainty sources in thermal images of metal cutting', *International Journal of Machining and Machinability of Materials*, 12 (3), pp. 195-214.

Whittaker, J., and Hess, D. (2015) 'Ductility of Titanium Alloy and Stainless Steel Aerospace Fasteners', *Journal of Failure Analysis and Prevention*, 15 (5), pp. 571-575.

Williams, J.C., and Starke, E.A. (2003) 'Progress in Structural Materials for Aerospace Systems', *Acta Materialia*, 51 (19), pp. 5775–5799.

Wu, C., Li, B., Yang, J., and Liang, S. (2017) 'Comparison of Machining Temperature in High Speed Grinding of Metallic Materials and Brittle Materials', *MATEC Web of Conferences*, 114, pp. 1-6.

Xi, X., Ding, W., Wu, Z., and Anggei, L. (2021) '$\gamma$ -TiAl intermetallics with electroplated diamond wheels', *Chinese Journal of Aeronautics*, 34 (6), pp. 100-109.

Xu, X., and Malkin S. (2001) 'Comparison of Methods to Measure Grinding Temperatures', *Journal of Manufacturing Science and Engineering*, 123 (2), pp. 191-195.

Xu, L., Shen, B., and Shih, A. (2006) 'Vitreous bond silicon carbide wheel for grinding of silicon nitride', *International Journal of Machine Tools and Manufacture - Design, Research and Application*, 46, pp. 631-639.

Xu, X., Yu, Y., Yu, Y., and Huang, H. (2003) 'Mechanisms of abrasive wear in the grinding of titanium (TC4) and nickel (K147) alloys', *Wear*, 225, pp. 1421-1426.

Yan, H., Deng, F., Qin, Z., Zhu, J., Chang, H., and Niu, H. (2023) 'Effects of Grinding Parameters on the Processing Temperature, Crack Propagation and Residual Stress in Silicon Nitride Ceramics', *Micromachines*, 14 (3). Available Online: DOI:10.3390/mi14030666.

Yang, Y., Jin, L., Zhu, J., Kong, J., and Li, L. (2022) 'Study on Cutting Force, Cutting Temperature and Machining Residual Stress in Precision Turning of Pure Iron with Different Grain Sizes', *Chinese Journal of Mechanical Engineering*, 33 (1), pp. 1-9.

Yang, C.T., and Shaw, M.C. (1955) 'The grinding of titanium alloys', *Transactions of the ASME*, 77, pp. 645-660.

Yang, W.W., and Tarng, Y.S. (1998) 'Design optimisation of cutting parameters for turning operations based on the Taguchi method', *Journal of Materials Processing Technology*, 84, pp. 122-129.

Yao, C., Jin, Q., Huang, X., Wu, D., Ren, J., and Zhang, D. (2013) 'Research on surface integrity of grinding Inconel 718', *The International Journal of Advanced Manufacturing Technology*, 65, pp. 1019-1030.

Yildiz, Y., and Nalbant, M. (2008) 'A review of the cryogenic cooling in machining processes', *International Journal of Machine Tools and Manufacture*, 45, pp. 947-964.

Youseff, S., Salem, W.B., Hamdi, H., and Brossem A. (2011) 'Residual stresses and metallurgic transformations induced by grinding', *International Journal of Machining and Machinability of Materials*, 9 (3-4), pp. 223-232.

Zeng, Q., Liu, G., Liu, L., and Qin, Y. (2015) 'Investigation into grindability of a superalloy and effects of grinding parameters on its surface integrity', *Proceedings of the Institution of Mechanical Engineers, Part B: Journal of Engineering Manufacture*, 229 (2), pp. 238-250.

Zeppenfield, C. (2006) 'Speed Stroke Grinding of $\gamma$-Titanium Aluminides', *Annals of the CIRP*, 55 (1), pp. 333-339.

Zhang, L. (1999) 'A Discussion On The Modelling Of Grinding And Polishing. Abrasive Technology', in Wang J., Scott W and Zhang L.C (ed.) *Abrasive Technology: Current Development And Applications I.* Brisbane, Australia: World Scientific Publication Ltd.

Zhang, L., Kang, M., and Tang W. (2020) 'Effects of Grinding Parameters on Surface Quality in High-Speed Grinding Considering Maximum Undeformed Chip Thickness' *SAE International Journal of Materials and Manufacturing*, 13 (2), pp. 139-150.

Zhang, L., Suto, T., Nouguchi, H. and Waida, T. (1993) 'Applied Mechanics in grinding part II: Modelling of Elastic Modulus of Wheels and Interface Forces', International Journal of Machine Tools and Manufacture, 33 (2): pp. 245-255.

Zhang, S., Yang, Z., Jiang, R., Jin, Q., Zhang, Q., and Wang, W. (2021) 'Effect of creep feed grinding on surface integrity and fatigue life of $Ni_3Al$ based superalloy IC10', *Chinese Journal of Aeronautics*, 34 (1), pp. 438-448.

Zhou, W., Tang, J., and Shao, W. (2020) 'Modelling of surface texture and parameters matching considering the interactions of multiple rotation cycles in ultrasonic assisted grinding', *International Journal of Mechanical Sciences*, 166, Article Number: 105246.

Zhu, X., Liu, Y., Zhang J., Wang, K., and Kong, H. (2020) 'Ultrasonic-assisted electrochemical drill-grinding of small holes with high quality', *Journal of Advanced Research*, 23, pp. 151-161.

# Appendices

## Appendix A: Post Surface Grinding Roughness Results

Fig A1 through to Fig A4 detail the normal and axial surface roughness measurements obtained by the author after the surface grinding preparation stage. Measurements taken included the average, ($R_a$), Root Mean Square, RMS, ($R_q$) and Peak-to-Valley ($R_z$) surface roughness values respectively. These measurements were obtained using the Mitutyou Surftest SJ-310-Series 178 Portable Surface Roughness Tester as referred to in section 3.1.2.

### A.1 - Normal to Grinding Direction

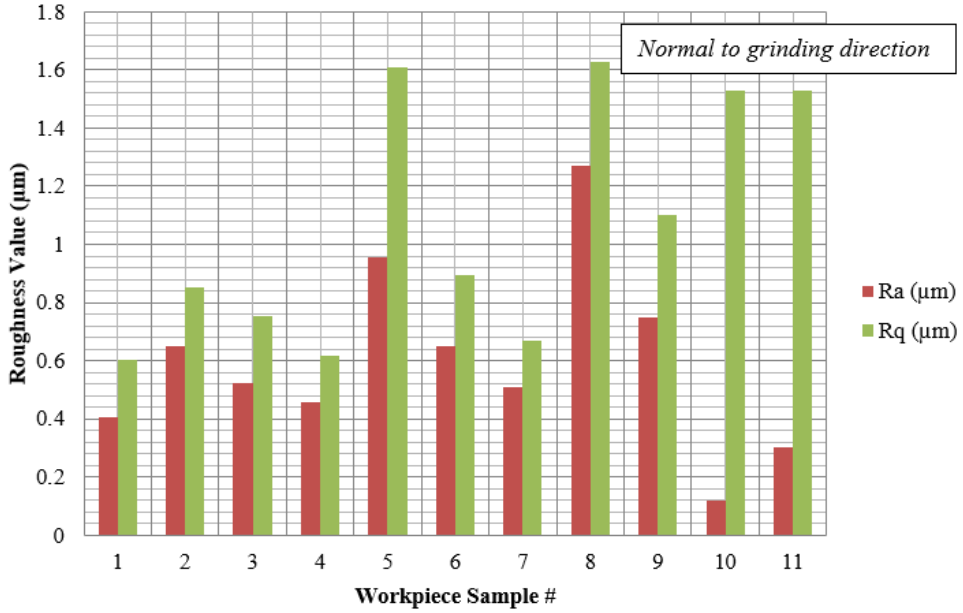



**Figure A1:** Normal to Grinding Direction Surface Roughness Measurements ($R_a$; $R_q$)




**Figure A2:** Normal to Grinding Direction Surface Roughness Measurements ($R_z$)

## A.2 - Axial to Grinding Direction

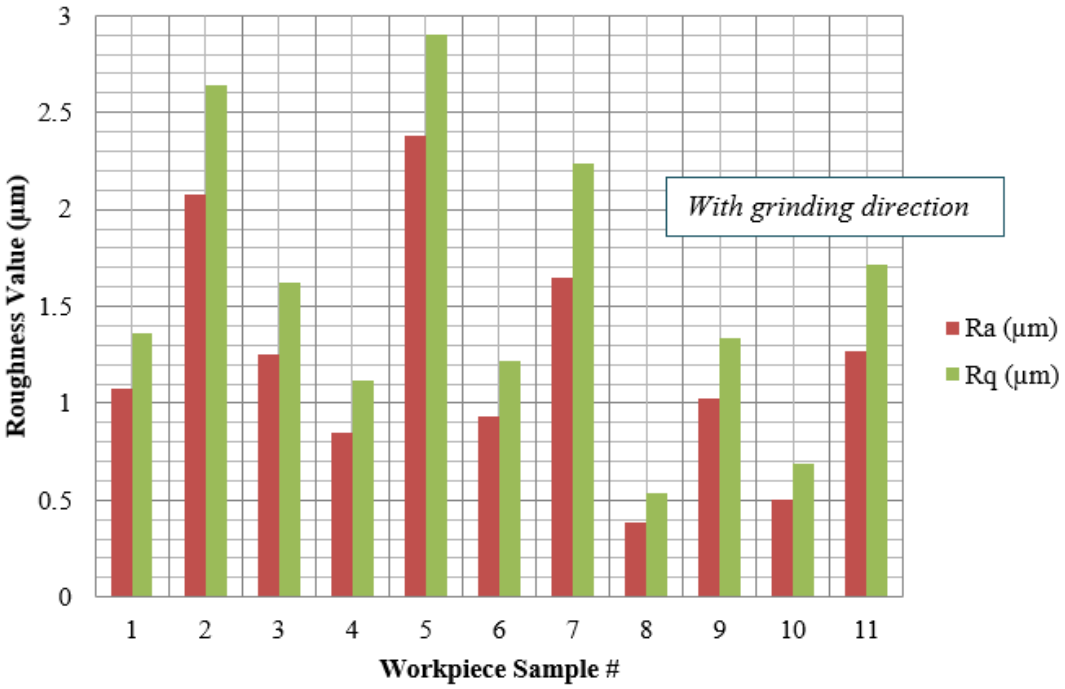



**Figure A3:** Axial to Grinding Direction Surface Roughness Measurements ($R_a$; $R_q$)

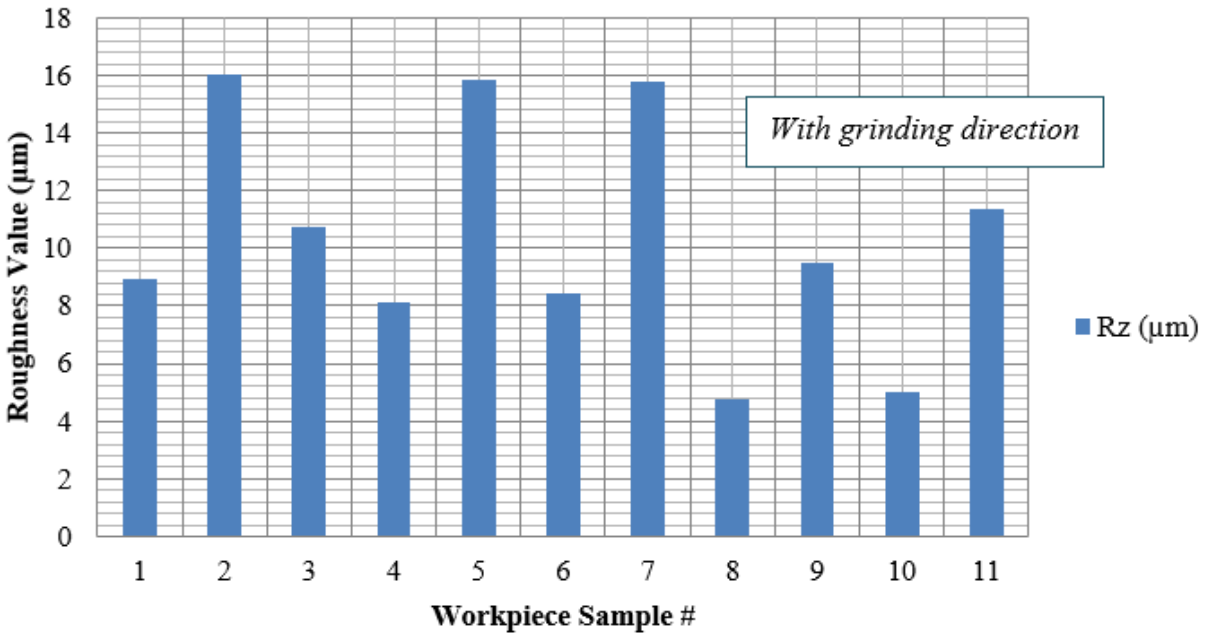



**Figure A4:** Axial to Grinding Direction Surface Roughness Measurements ($R_z$)

## A.3 - Position Variance Comparison

Additionally, the author conducted the same test again, this time varying the distance along the workpiece at which the roughness measurements were taken; namely, 22mm, 36mm and 50mm from the workpiece front edge. Both with the grinding pass and normal to the grinding pass measurements were recorded. This was undertaken to determine, if any, changes in surface roughness occurring along the axial and perpendicular directions of the grinding path. Fig A5 through to Fig A10 detail these findings.

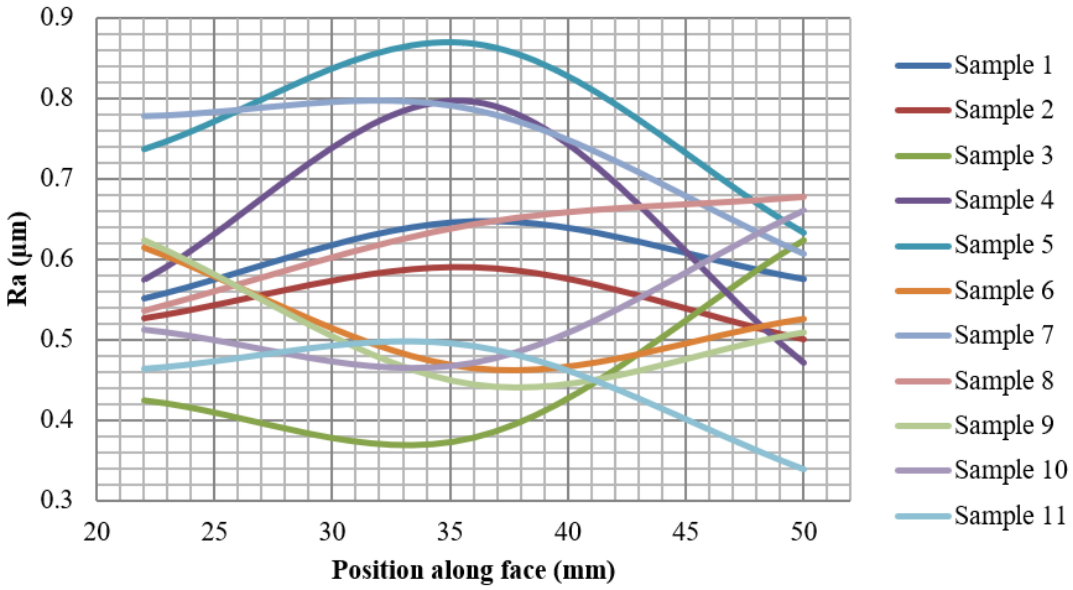



**Figure A5:** Position Variance of Surface Roughness Measurements ($R_a$)(with grinding pass)

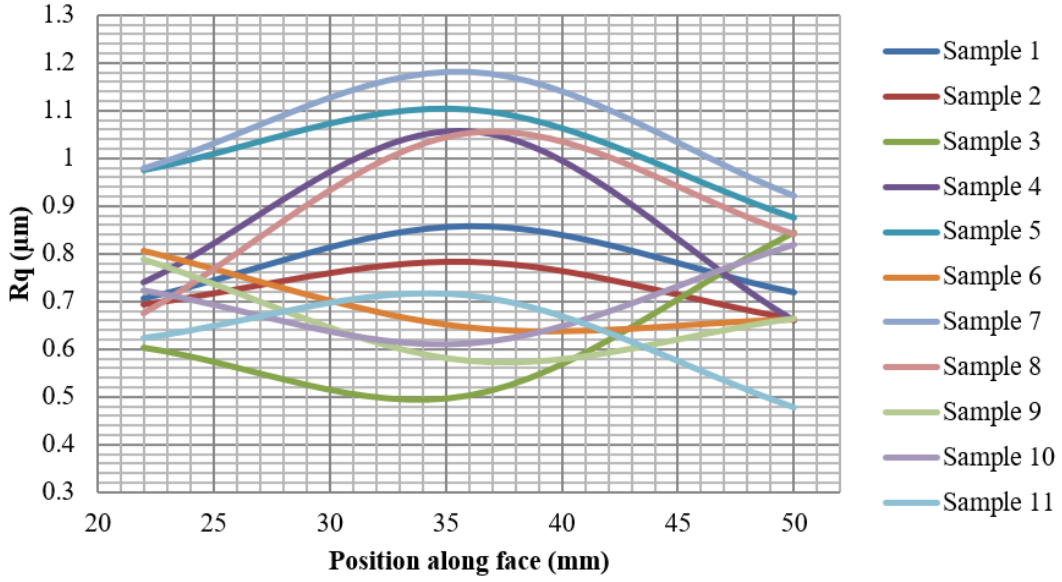



**Figure A6:** Position Variance of Surface Roughness Measurements ($R_q$)(with grinding pass)

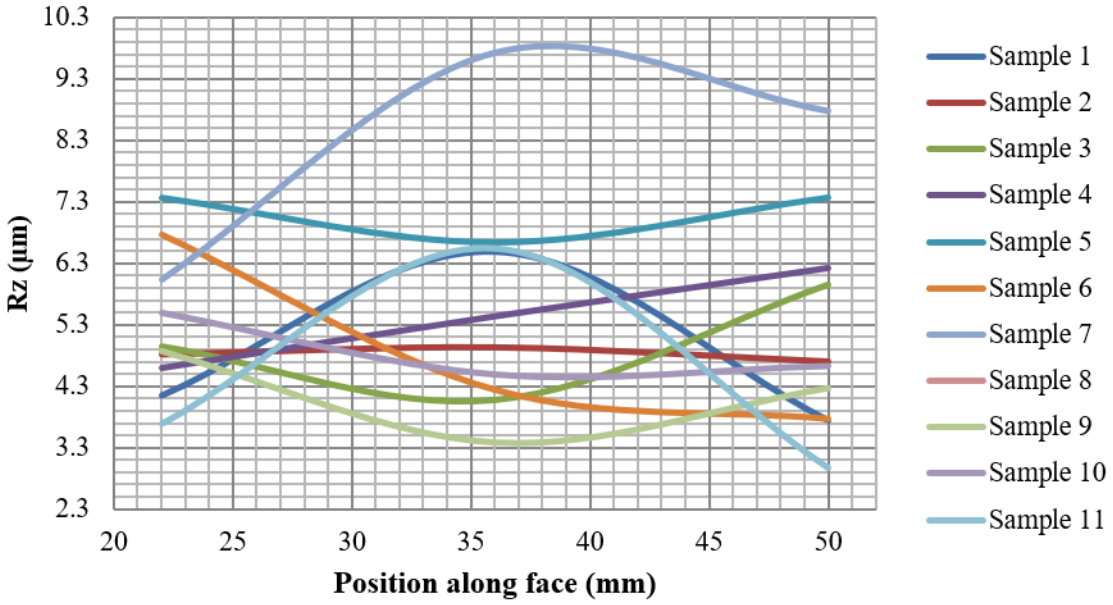



**Figure A7:** Position Variance of Surface Roughness Measurements ($R_z$)(with grinding pass)

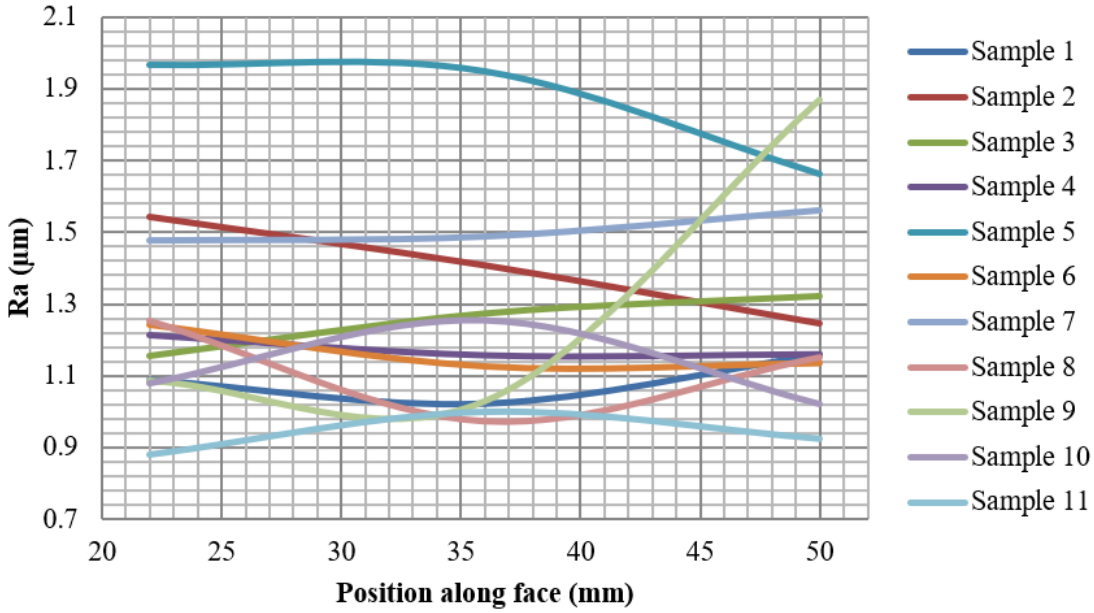



**Figure A8:** Position Variance of Surface Roughness Measurements ($R_a$)(against grinding pass)

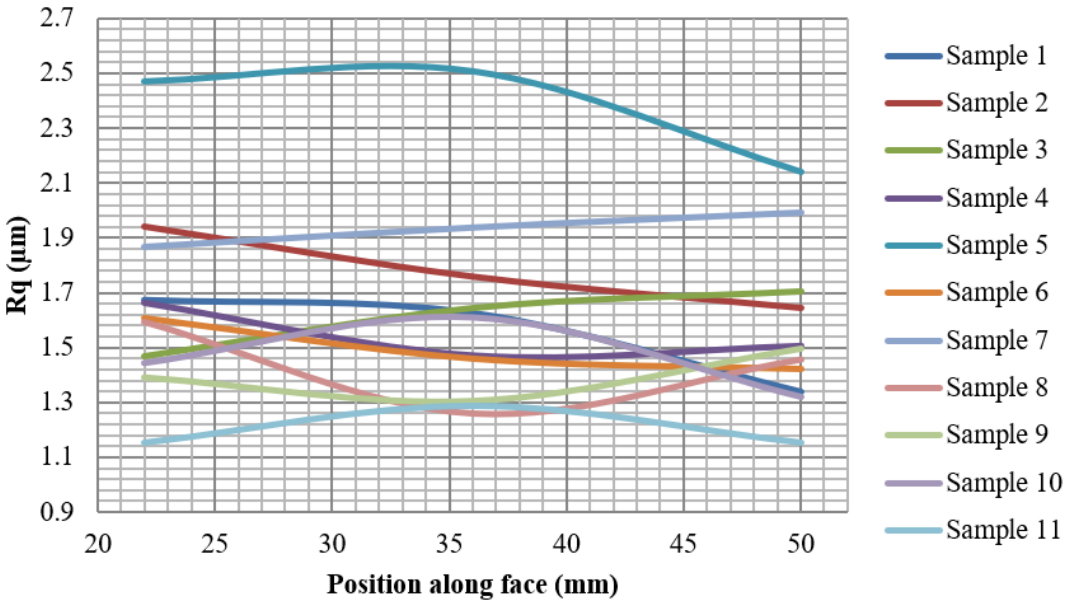



**Figure A9:** Position Variance of Surface Roughness Measurements ($R_q$)(against grinding pass)

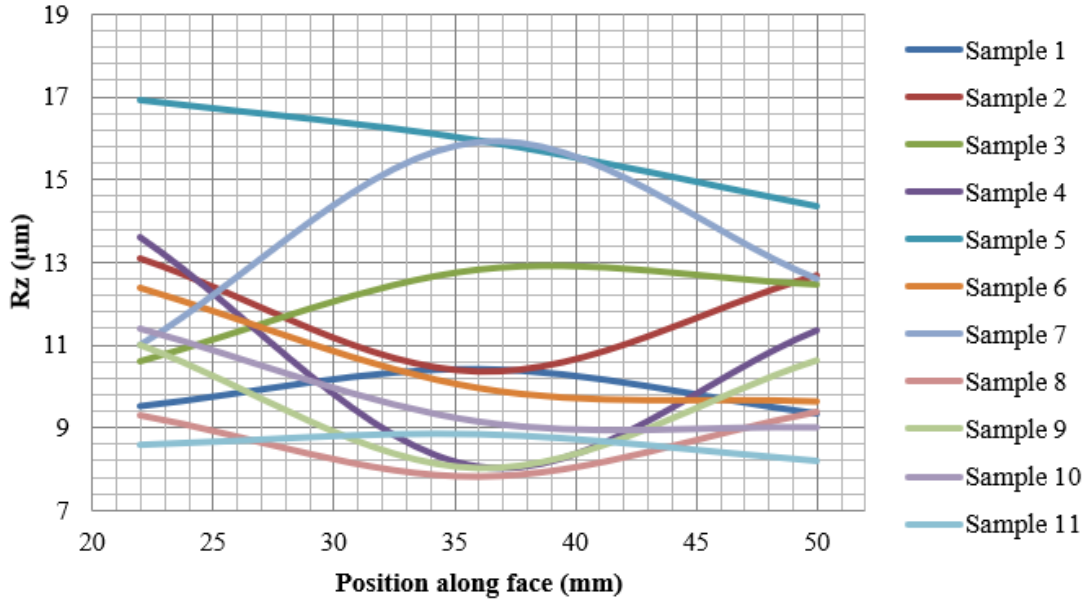



**Figure A10:** Position Variance of Surface Roughness Measurements ($R_z$)(against grinding pass)

## Appendix B: Grinding Wheel Modal Analysis

Additionally, the author conducted a basic modal analysis on a range of common grinding wheel materials. This analysis was conducted using the ANSYS Modal module. The study was undertaken to assess the natural frequency of the rotating tool. Two Taguchi L9 orthogonal arrays were assessed (L9a and L9b) which are detailed in Table B1 and Table B2. The graphics detailing the first six modes are listed in Table B3. Moreover, Fig B1 and Fig B2 detail the findings from the study.

**Table B1:** Grinding Wheel Modal Study Taguchi L9a Array

| **Exp** | **Grinding Wheel Material** | **Grinding Wheel Speed**, $V_s$ ($m.s^{-1}$) | **Element Size** (mm) | **Wheel Thickness** (mm) |
|---|---|---|---|---|
| 1 | SiC | 20 | 1.5 | 5 |
| 2 | SiC | 30 | 3.0 | 10 |
| 3 | SiC | 40 | 4.5 | 15 |
| 4 | $Al_2O_3$ | 20 | 3 | 15 |
| 5 | $Al_2O_3$ | 30 | 4.5 | 5 |
| 6 | $Al_2O_3$ | 40 | 1.5 | 10 |
| 7 | Diamond | 20 | 4.5 | 10 |
| 8 | Diamond | 30 | 1.5 | 15 |
| 9 | Diamond | 40 | 3 | 5 |

**Table B2:** Grinding Wheel Modal Study Taguchi L9b Array

| **Exp** | **Grinding Wheel Material** | **Grinding Wheel Speed**, $V_s$ ($m.s^{-1}$) | **Element Size** (mm) | **Wheel Thickness** (mm) |
|---|---|---|---|---|
| 1 | $Al_2O_3$ 92% | 20 | 1.5 | 5 |
| 2 | $Al_2O_3$ 92% | 30 | 3.0 | 10 |
| 3 | $Al_2O_3$ 92% | 40 | 4.5 | 15 |
| 4 | $Al_2O_3$ 96% | 20 | 3 | 15 |
| 5 | $Al_2O_3$ 96% | 30 | 4.5 | 5 |
| 6 | $Al_2O_3$ 96% | 40 | 1.5 | 10 |
| 7 | $Al_2O_3$ | 20 | 4.5 | 10 |
| 8 | $Al_2O_3$ | 30 | 1.5 | 15 |
| 9 | $Al_2O_3$ | 40 | 3 | 5 |

## B.1 - L9a Array

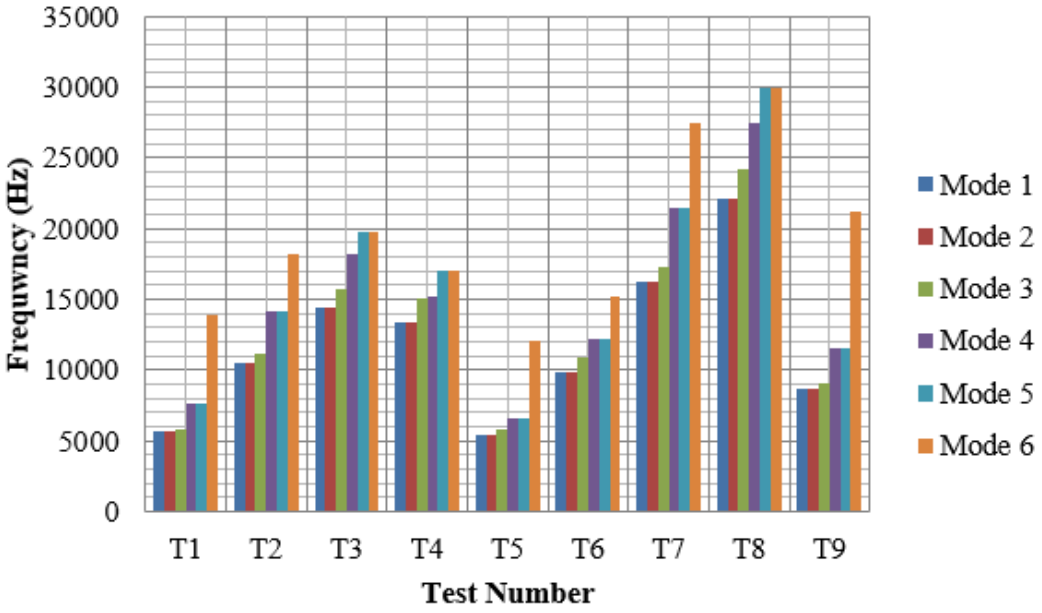
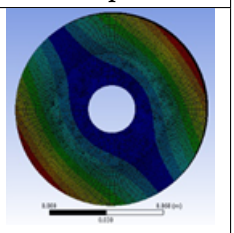
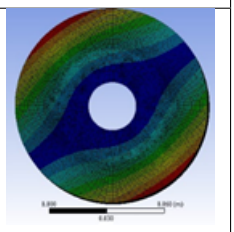
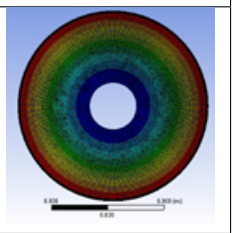
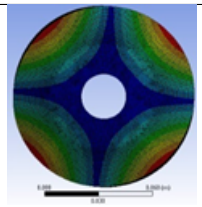
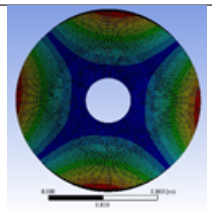
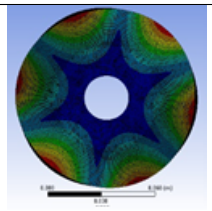



**Figure B1:** Grinding Wheel Mode Values (L9a OA)

**Table B3:** Sample First Six Mode Distributions

| Grinding Wheel Mode | Graphic |
|---|---|
| 1 |  |
| 2 |  |
| 3 |  |
| 4 |  |
| 5 |  |
| 6 |  |

## B.2 - L9b Array

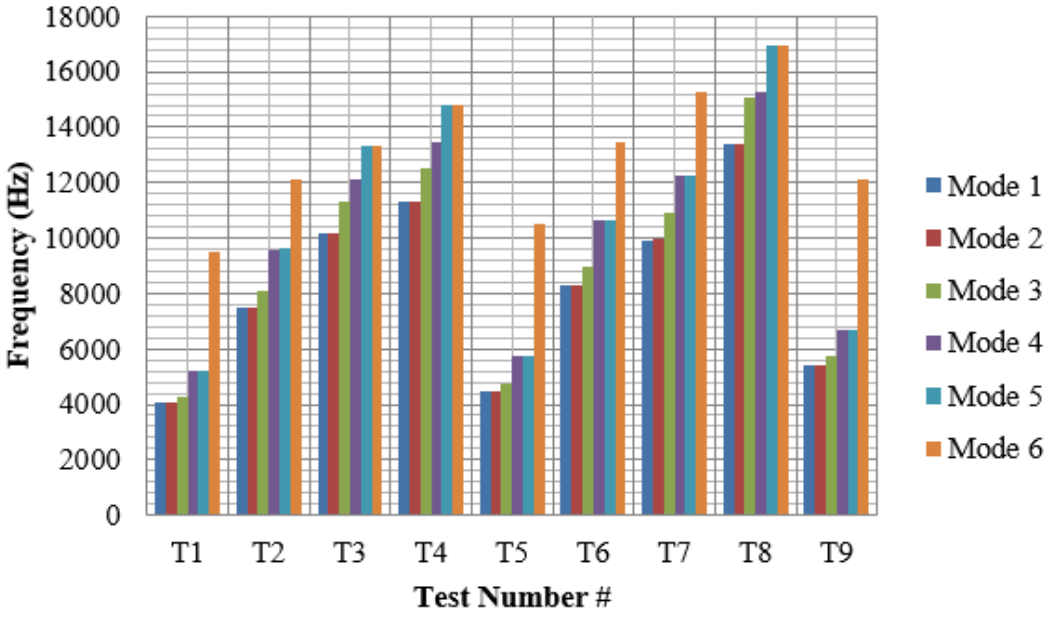



**Figure B2:** Grinding Wheel Mode Values (L9b OA)

## Appendix C: Thermocouple Response Time Tests

Herein are the response time calculations for the OMEGA high temperature k-type thermocouples used throughout this thesis. Two test cases were conducted, i.e., a repeated low temperature differential test via plunging the thermocouple into hot water. The response time of the thermocouples for these tests are detailed in Fig C1.

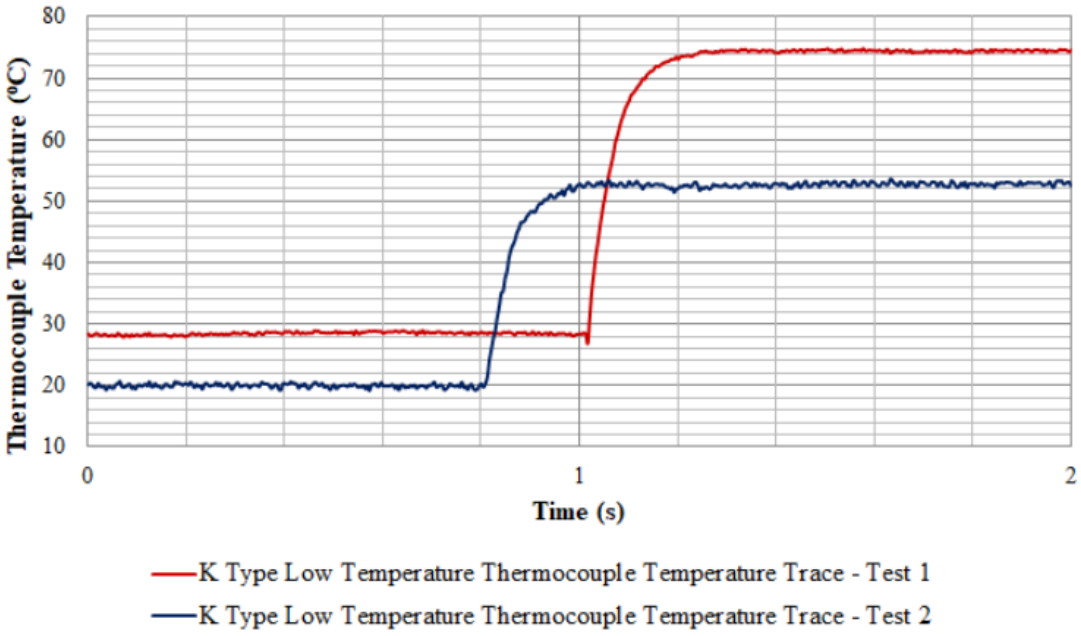



**Figure C1:** Low Temperature Thermocouple Response Time Trial Results

Once these tests had been conducted, the author additionally developed a Simulink Laplace Transfer code in an attempt to convert the thermocouple temperature readings into a more accurate response if faster feed rates were ever to be assessed. This was undertaken because the response time of the thermocouple may not be sufficient for higher feed rate temperature measurement. However, as presented in Table 3.2, the feed rates tested in the main body of this thesis were low, and so the response time for the thermocouples for this set-up were sufficient. The Laplace Transform for faster feeds was achieved by applying basic control theory to the thermocouple system. Through the use of a block diagram, the author was able to process the temperature readings through a control system and yield improved results. The block diagram related to this control system is detailed in Fig C2.

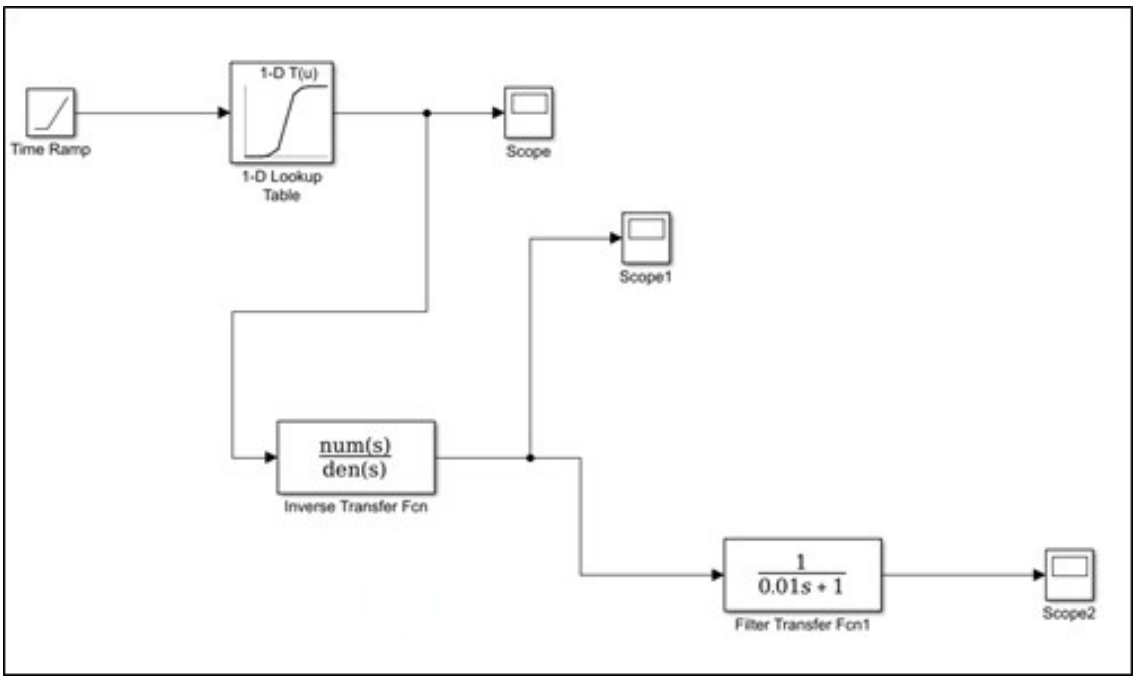



**Figure C2:** Laplace Transform System Developed

For this to be derived, the author had to first establish a value for the time constant, $\tau$, from the thermocouple temperature data. The thermocouple response can be easily modelled as a first order differential equation in the form of Eqn. C.1;

$$a_1 \frac{d_y}{d_t} + a_0.y = F(t) \qquad \text{(Eqn. C.1)}$$

where $y(t)$ is the response of the thermocouple and $F(t)$ is the forcing function. Alternatively, the equation can be proffered as Eqn. C.2;

$$\tau \frac{d_y}{d_t} + y = k_1.F(t) \qquad \text{(Eqn. C.2)}$$

In this instance, $\tau = \frac{a_1}{a_o}$, and is the time constant of the system, and $\mathrm{k}_1 = \frac{1}{a_o}$, and is deemed as the thermocouple's gain.

As the thermocouple instrumentation is a first order system, the time constant, $\tau$, can be found at the point when the temperature of the system reaches 63% of the final value. This was determined by plotting the temperature vs. time trace curve for the lower temperature differential tests. Fig C3 presents a more detailed version of the data presented in Fig C1.

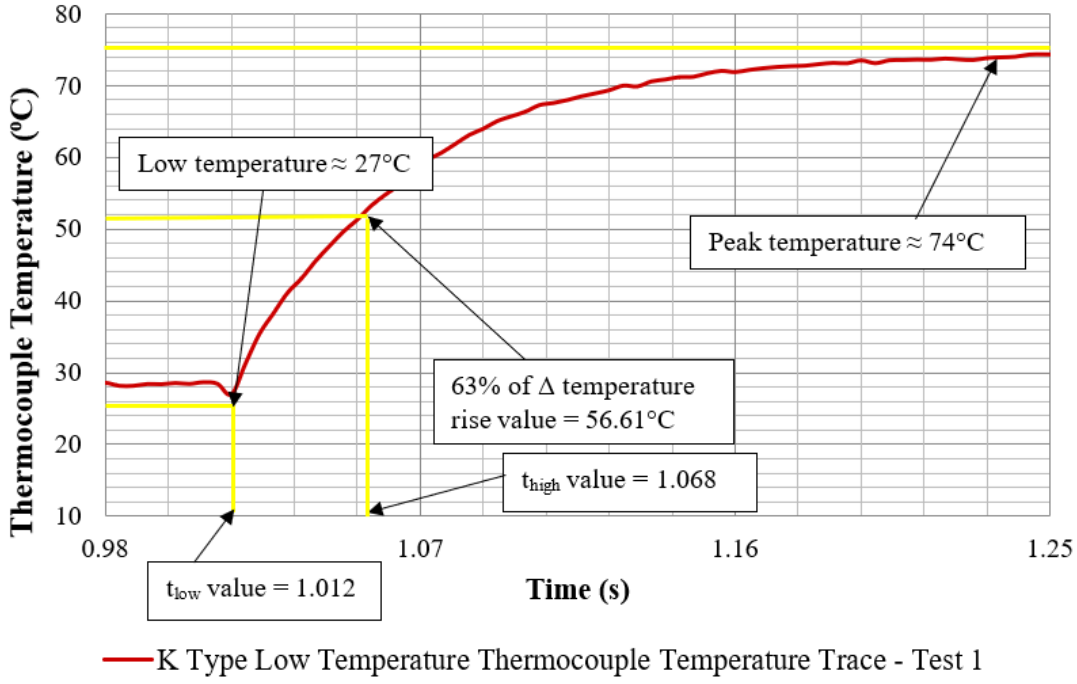



**Figure C3:** Low Temperature Thermocouple Response Time Trial Results

From Fig C3, maximum and minimum temperatures can be ascertained, and thus a ΔT rise can be calculated.

Peak Temperature ≈ 74°C.

Low Temperature ≈ 27°C.

ΔT = 74 - 27 = 47°C.

We therefore need the $T$ value at 63% of this value, i.e., (0.63)(47) = 29.61°C. But to align the data with the baseline temperature, the initial temperature needs to be added to this value. Thus, the actual temperature = 29.61 + 27 = 56.61°C.

Reading down to the associated $t$ value on the $x$-axis for 56.61°C, $t$ value = 1.068. Finally, the $\tau$ value can be found by calculating the Δt, i.e., $t_{high}$ value - $t_{low}$ value = 1.068 - 1.012 = 0.056.

# Appendix D: Engineering Drawings

## D.1 - Kistler 9257A Dynamometer Platform

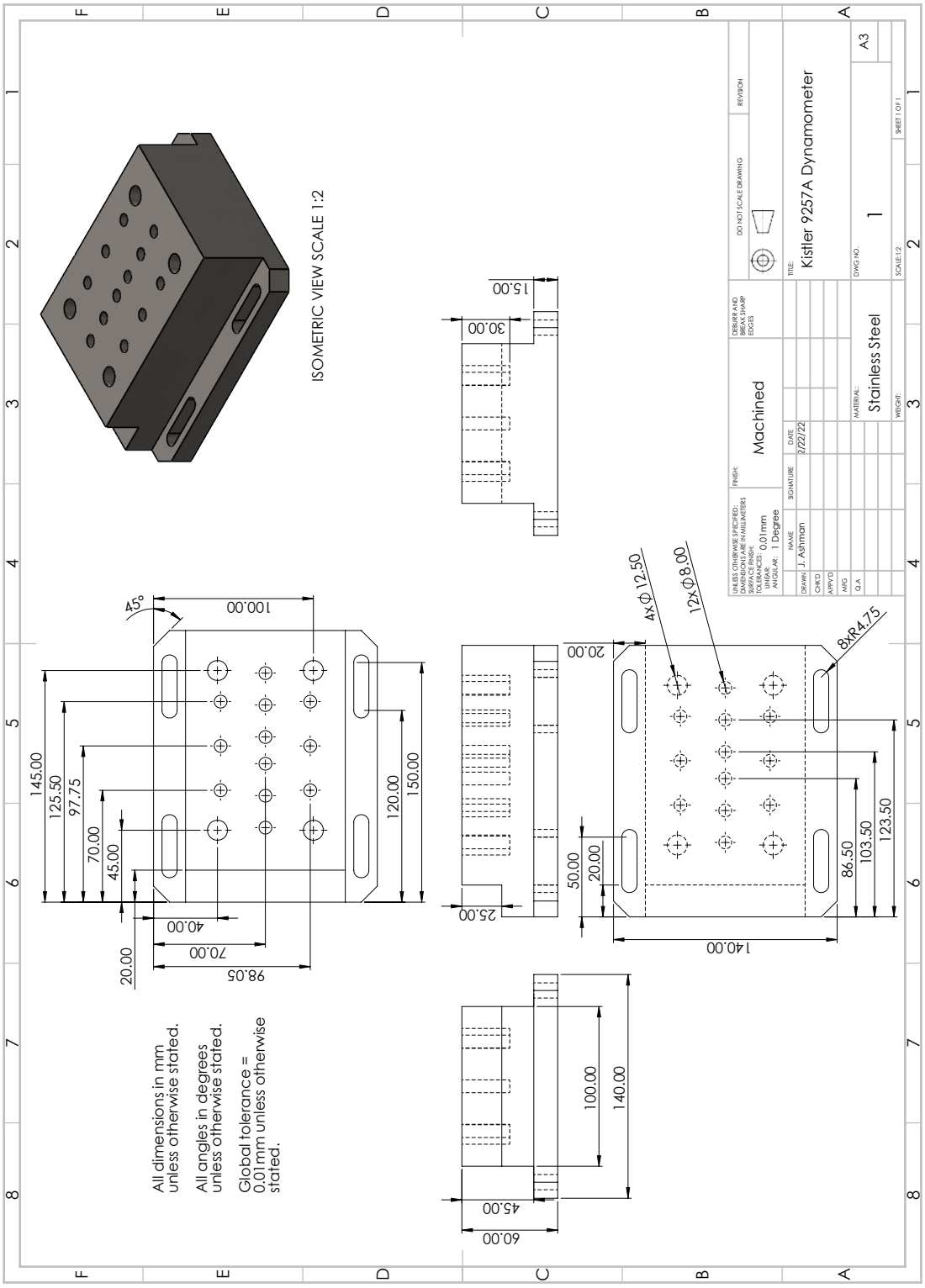



**Figure D1:** Kistler 9257A Dynamometer Platform

## D.2 - Thermocouple Extraction Plate

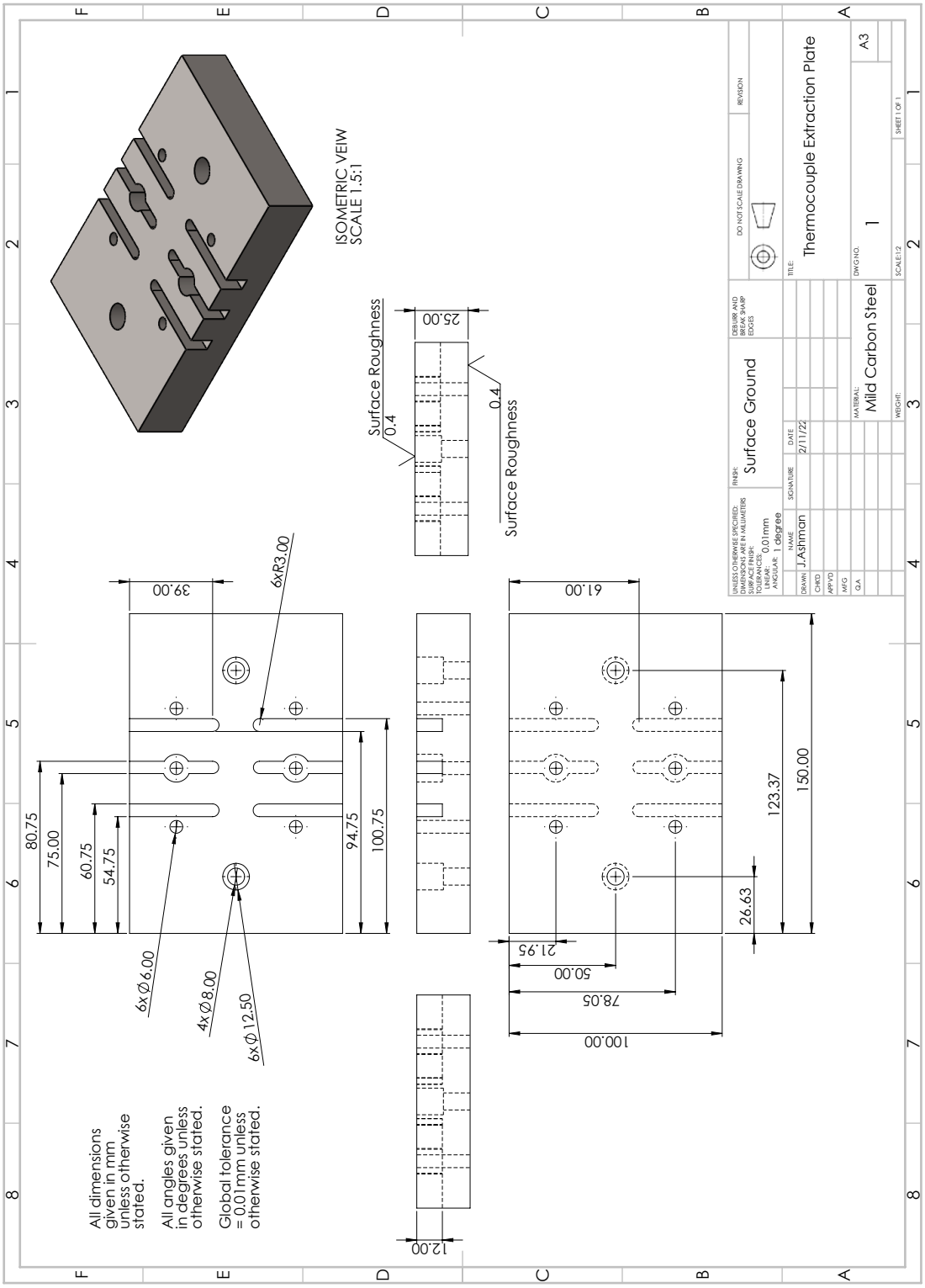



**Figure D2:** Thermocouple Extraction Plate

## D.3 - Embedded Thermocouple Workpiece

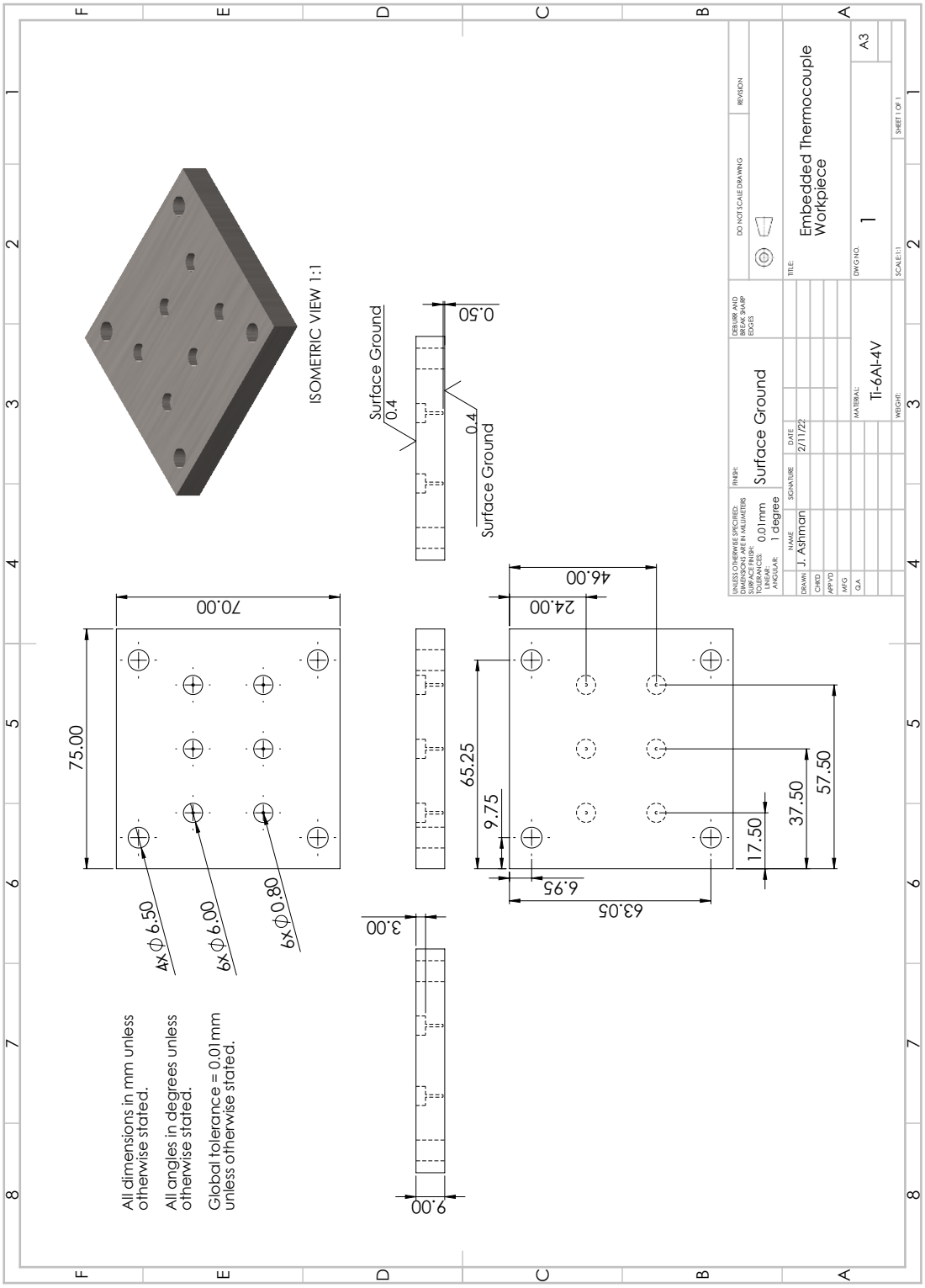
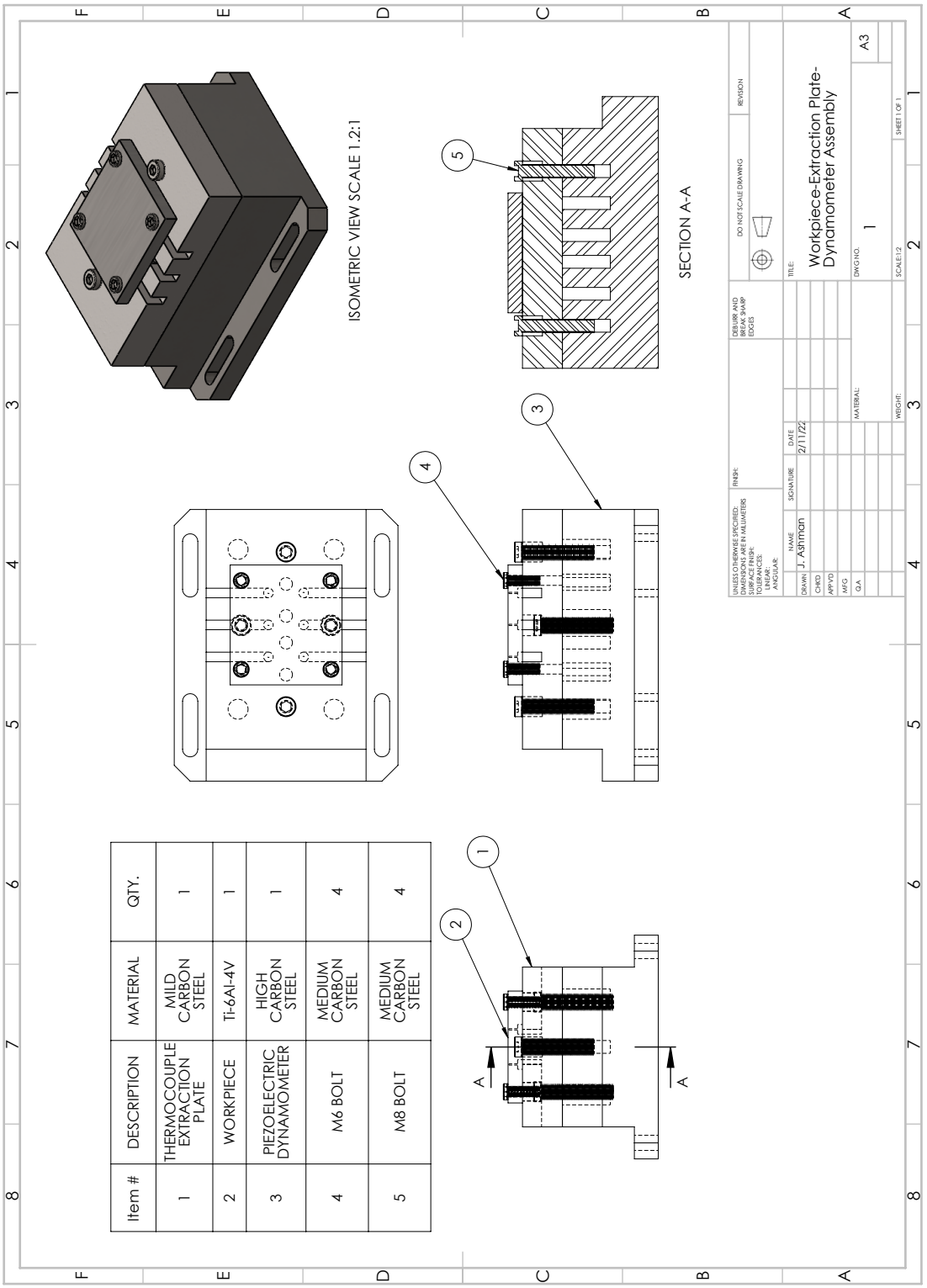



**Figure D3:** Embedded Thermocouple Workpiece

## D.4 - Cutting Force and Workpiece Temperature Data Acquisition Sub-Assembly Configuration




| Item # | DESCRIPTION | MATERIAL | QTY. |
|---|---|---|---|
| 1 | THERMOCOUPLE EXTRACTION PLATE | MILD CARBON STEEL | 1 |
| 2 | WORKPIECE | Ti-6Al-4V | 1 |
| 3 | PIEZOELECTRIC DYNAMOMETER | HIGH CARBON STEEL | 1 |
| 4 | M6 BOLT | MEDIUM CARBON STEEL | 4 |
| 5 | M8 BOLT | MEDIUM CARBON STEEL | 4 |

**Figure D4:** Cutting Force and Workpiece Temperature Data Acquisition Sub-Assembly Configuration

## D.5 - Cutting Force and Workpiece Temperature Data Acquisition Sub-Assembly Exploded View Configuration

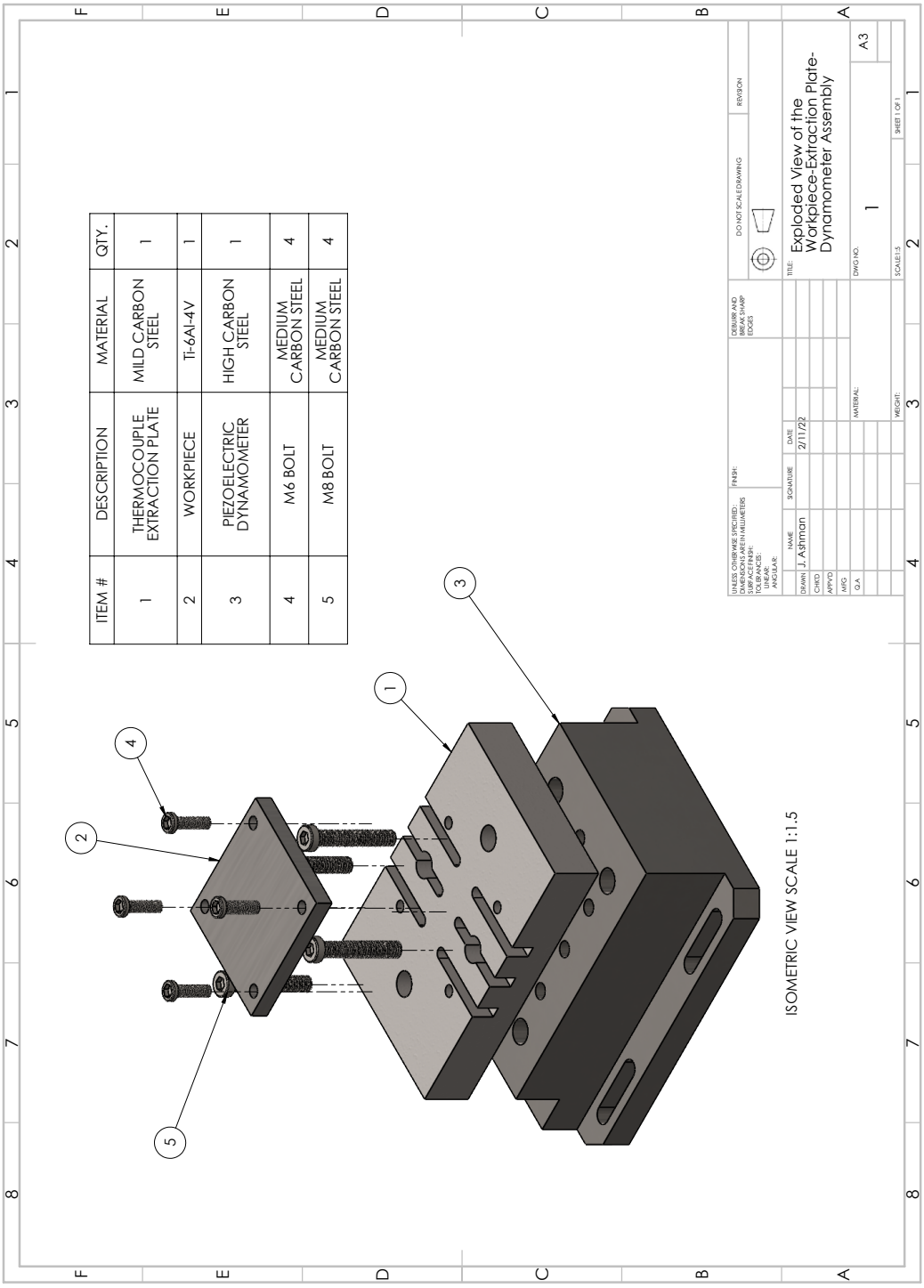



**Figure D5:** Cutting Force and Workpiece Temperature Data Acquisition Sub-Assembly Exploded View Configuration

## D.6 - SiC Grinding Wheel Tooling

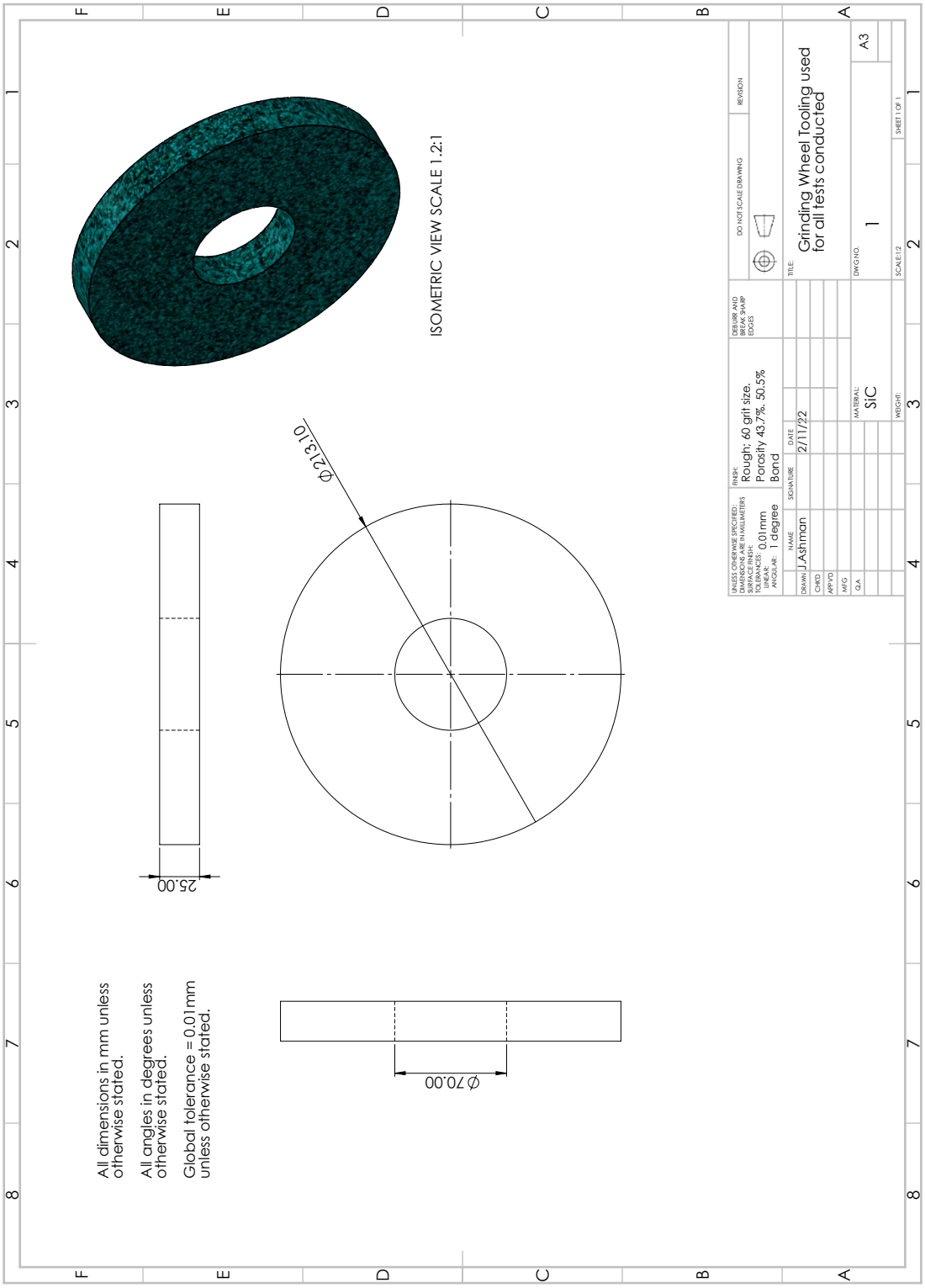



**Figure D6:** SiC Grinding Wheel Tooling

## D.7 - Wendt Mk IV Cantilever Dresser Roller Spindle Mounting Points

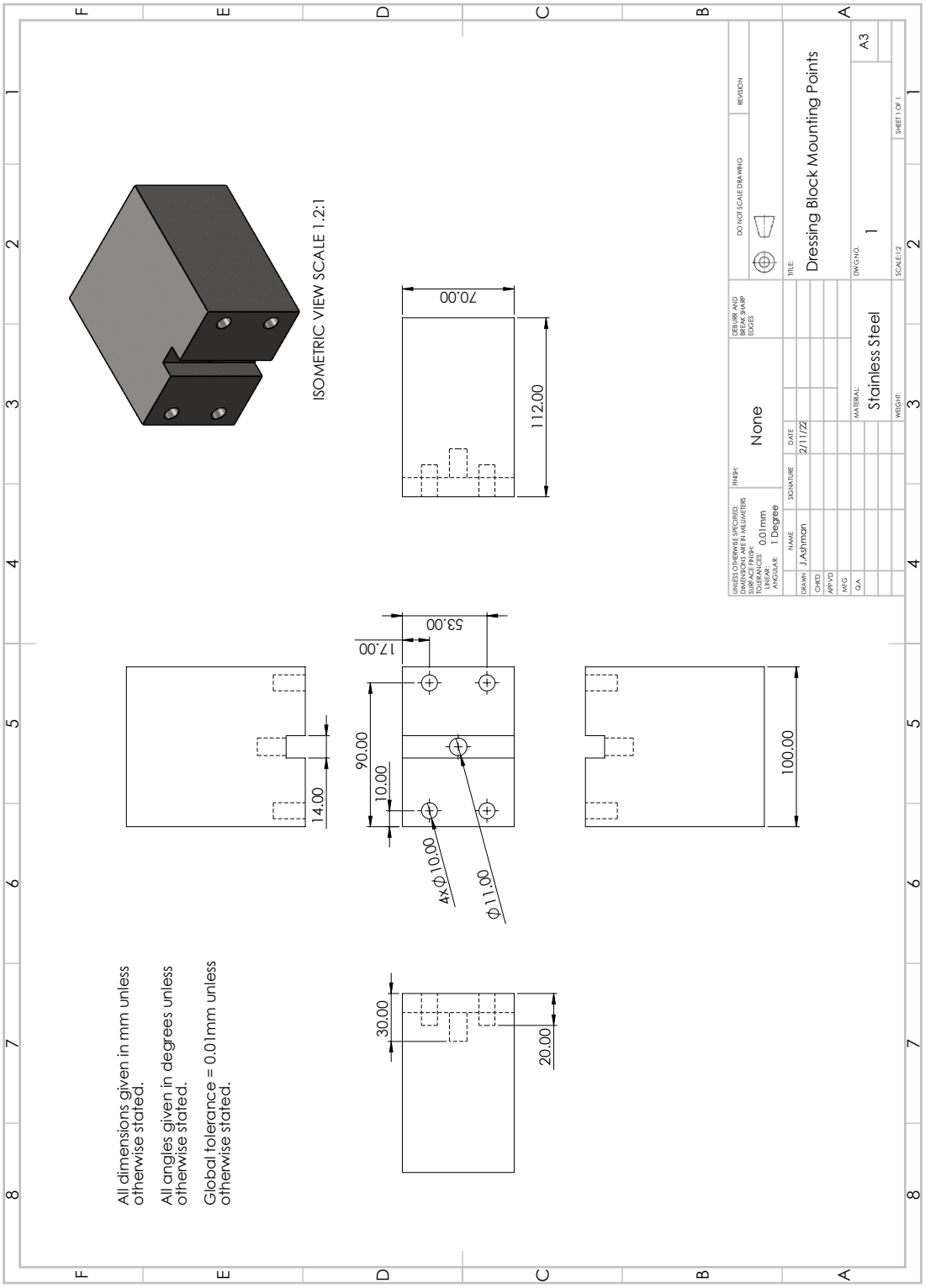



**Figure D7:** Wendt Mk IV Cantilever Dresser Roller Spindle Mounting Points

## Appendix E: Grinding Power Rate Profiles

The power delivered to the spindle during the grinding process has a fundamental impact on the MRR and $G$-ratio. As such, the grinding power can be expressed as a function of the cutting forces acting on the grinding wheel as defined in Eqn. E1;

$$Processing\ Power, P_c = F_T(V_s \pm V_w) + F_N.V_d + F_a.V_a \quad \text{(Eqn. E1)}$$

Or, more simplified in Eqn. E2;

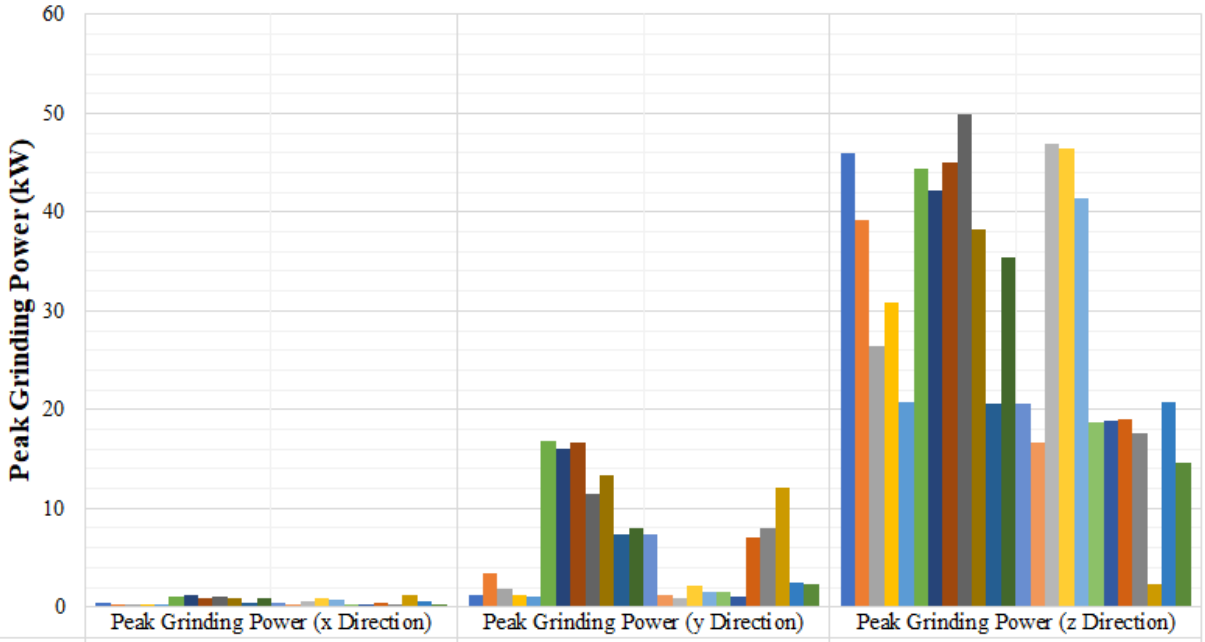
$$Processing\ Power, P_c = F_T.V_s \quad \text{(Eqn. E2)}$$

Or as expressed in Eqn. E3;

$$Processing\ Power, P_c = P_{SpindleTotal} - P_{SpindleIdle} \quad \text{(Eqn. E3)}$$

Where $P_c$ is the processing power, $F_T$ is the tangential cutting force, $V_s$ is the wheel speed, $V_w$ is the feed rate, $F_N$ is the normal cutting force, $V_d$ is the cross-feed rate, $F_a$ is the axial cutting force and $V_a$ is the axial feed rate. Finally, $P_{SpindleTotal}$ and $P_{SpindleIdle}$ are the total spindle power and the spindle idle power respectively.

Using Eqn. E2, and substituting the experimental values for $F_T$, the author was able to establish $P_c$ values for all experimental tests conducted. For completeness, these are presented in Fig E1.




| | Peak Grinding Power (x Direction) | Peak Grinding Power (y Direction) | Peak Grinding Power (z Direction) |
|---|---|---|---|
| Test [10] - Pass 1 | 0.41 | 1.24 | 46.00 |
| Test [9] - Pass 1 | 0.28 | 3.48 | 39.20 |
| Test [8] - Pass 1 | 0.22 | 1.86 | 26.40 |
| Test [7] - Pass 2 | 0.24 | 1.21 | 30.80 |
| Test [7] - Pass 1 | 0.22 | 0.99 | 20.80 |
| Test [6] - Pass 7 | 1.09 | 16.78 | 44.41 |
| Test [6] - Pass 6 | 1.15 | 16.09 | 42.19 |
| Test [6] - Pass 5 | 0.84 | 16.59 | 45.06 |
| Test [6] - Pass 4 | 1.13 | 11.41 | 49.93 |
| Test [6] - Pass 3 | 0.89 | 13.34 | 38.17 |
| Test [6] - Pass 2 | 0.50 | 7.31 | 20.62 |
| Test [6] - Pass 1 | 0.92 | 8.05 | 35.44 |
| Test [5] - Pass 2 | 0.50 | 7.31 | 20.62 |
| Test [5] - Pass 1 | 0.29 | 1.18 | 16.61 |
| Test [4] - Pass 3 | 0.55 | 0.90 | 46.91 |
| Test [4] - Pass 2 | 0.86 | 2.16 | 46.38 |
| Test [4] - Pass 1 | 0.80 | 1.58 | 41.42 |
| Test [2] - Pass 2 | 0.21 | 1.56 | 18.65 |
| Test [2] - Pass 1 | 0.21 | 1.07 | 18.80 |
| Test [1] - Pass 5 | 0.37 | 7.06 | 19.10 |
| Test [1] - Pass 4 | 0.32 | 7.97 | 17.63 |
| Test [1] - Pass 3 | 1.23 | 12.10 | 2.28 |
| Test [1] - Pass 2 | 0.53 | 2.46 | 20.78 |
| Test [1] - Pass 1 | 0.25 | 2.27 | 14.67 |

**Figure E1:** Grinding Power Rate Profiles for all Experimental Tests